Politecnico di Milano

Scuola di Ingegneria Industriale e dell'Informazione

Corso di Laurea Magistrale in Ingegneria Aeronautica

Design and Optimization of Acoustic Liners with Complex Cavities for Improved Broadband Noise Absorption

Relatore: Prof. Lorenzo Dozio

Correlatori: Ing. Marco Vercellesi, Dr. Paul B. Murray

Tesi di Laurea di:

Giuseppe Dilillo, n° Matricola 899675

Anno accademico 2019/2020

Ringraziamenti

Questa tesi di laurea conclude un percorso di studi faticoso ed estenuante iniziato ormai sei anni fa. Ricordo ancora l'ardore virgineo con cui avevo deciso di iscrivermi al Politecnico di Milano e la totale inconsapevolezza del destino travagliato che negli anni a venire avrei dovuto affrontare. Quelli appena trascorsi sono stati anni di sudore e fatica, fatti di ore di studio interminabili e di limitata vita sociale, ben riassumibili con la singolare variante della regola benedettina "labora et labora". Grazie alla brutalità del percorso però, questi anni di Politecnico sono stati una ineguagliabile palestra di vita, che mi ha introdotto forzatamente nel mondo reale e mi ha allenato ad affrontare le sfide più dure, insegnandomi a non arrendermi mai. Mi ha fatto sperimentare il dolore delle cadute e la gioia della vittoria, mi ha fatto assaporare la durezza dell'umiliazione e il piacere dell'orgoglio. Naturalmente però, prima della crescita personale, il Politecnico mi ha permesso quasi gratuitamente di acquisire un bagaglio tecnico e culturale immenso, di poter partecipare quotidianamente alle lezioni dei più importanti ingegneri e docenti italiani e di poter utilizzare illimitatamente e in maniera sconfinata le più sofisticate tecnologie attualmente esistenti. Sarà forse l'entusiasmo della fine ad animare le mie parole, ma garantisco che se mai dovessi tornare indietro, sceglierei sempre di intraprendere questo arduo ma straordinario percorso accademico.

Tutto questo è stato reso possibile grazie ai miei genitori Saverio e Giovanna e a mia sorella Martina, che sono sempre stati al mio fianco anche nei momenti più duri e non hanno mai smesso di sostenermi negli anni di università. Il traguardo che ho raggiunto con questa tesi è anzitutto merito loro e gliene sarò sempre, infinitamente grato.

Questo finale di percorso non sarebbe stato di certo così soddisfacente se non avessi avuto modo di lavorare a stretto contatto con il Dr. Paul B. Murray. Devo ringraziarlo per l'incommensurabile aiuto e la straordinaria dedizione con cui ha sostenuto il mio progetto di tesi, per la grande passione che mi ha trasmesso verso il mondo dell'acustica e per i suoi preziosissimi e memorabili insegnamenti. Qualunque sia il mio futuro impiego, spero davvero di poter sempre lavorare al fianco di persone come lui.

Assieme al Dr. Murray, devo ringraziare l'Ing. Marco Vercellesi e il Prof. Lorenzo Dozio, per la grandissima opportunità di svolgere la tesi di laurea in Leonardo Velivoli e per il loro continuo e immancabile sostegno. Non hanno mai smesso di supportare la mia attività dall'inizio alla fine, anche in un periodo arduo e provante come quello dell'epidemia di Coronavirus.

Ringrazio poi le mie nonne Filomena e Antonietta perché, parimenti ai miei genitori, mi sono sempre state vicino anche se abitano lontano da me. La loro presenza è stata indispensabile per affrontare questo percorso accademico.

Infine, per ultimi, ma non perché di ultima importanza, devo ringraziare tutti i miei amici. È grazie a loro se durante questi sei lunghi anni non sono impazzito completamente e ho pur vissuto nonostante la vita monastica, se ho riso a crepapelle anche nei momenti di più totale disperazione e se le mie giornate sono state comunque dense di felicità e spensieratezza. Dovrei fare un ringraziamento personale per ciascuno di loro, ma questo richiederebbe un volume di dimensioni probabilmente simili a quelle di questa tesi. Ringrazio allora sinteticamente per il loro fondamentale supporto: Giacomo, Luca, Riccardo, Giovanni, Alice, Mattia, Roberto, Francesco, Domenico, Alberto, Davide, Giovanni, Zakaria, Gabriele, Gianmarco, Alessandro, Sebastiano, Mateusz, Riccardo, Giulia, Roberto, Alberto, Letizia, Sofia, Giulia, Daniele, Stefania, Violeta.

Abstract

The recent advances in aircraft propulsion systems and in sound-absorbing technologies has caused broadband fan noise to become more prominent and the engine noise spectrum to shift towards lower frequencies. However, this evolving noise source cannot be attenuated adequately by the conventional acoustic treatments installed in aircraft nacelles. While traditional designs are indeed effective at reducing narrowband noise sources, the sound absorption at low frequencies is limited due to space and weight restrictions.

This thesis proposes an innovative configuration of acoustic liner that provides enhanced absorption of broadband sound sources, while also permitting the attenuation of the low-frequency noise. The configuration can be easily adjusted to any space reserved for acoustic liners in aircraft nacelles, so that the gain in acoustic performance can be obtained within an acceptable overall thickness. The concept may also be tuned to target an individual noise spectrum.

In the thesis, a liner design with complex cavities is optimised for two fixed overall depths, in order to maximise noise reduction between 500 Hz and 4000 Hz, in the absence of mean flow, and for a normally incident sound wave. Two scaled samples of these optimal liners were manufactured using stereolithography. Their measured acoustic impedances confirm the expected broadband sound absorption.

The thesis validates the use of COMSOL to predict the measured impedance of both conventional and innovative liners with complex configurations. Moreover, some relevant considerations are outlined which must be accounted for in the simulation of the acoustic treatment. The principal acoustic features of the proposed liner concept are investigated in detail and an analytical routine is validated for preliminary design.

Sommario

I recenti sviluppi dei sistemi propulsivi aeronautici e delle tecnologie per l'assorbimento del rumore hanno modificato il caratteristico spettro di frequenza del rumore generato dal motore turbofan. La componente in banda larga del rumore del fan ha acquisito un ruolo predominante e lo spettro del rumore del motore turbofan ha assunto frequenze caratteristiche sempre più basse. I trattamenti acustici tradizionalmente usati nelle gondole motore non sono adatti ad attenuare questo tipo di rumore, poiché assorbono efficacemente il rumore solamente in banda stretta. Inoltre, il limitato spazio disponibile e le restrizioni sulla massa dei trattamenti acustici impediscono un assorbimento efficiente del rumore a basse frequenze.

La seguente tesi di laurea propone una configurazione innovativa di pannello fonoassorbente che promette una significativa riduzione del rumore ad ampio spettro e a basse frequenze. La configurazione è facilmente adattabile a qualsiasi volume riservato nelle gondole motore ai pannelli e la geometria proposta prevede una attenuazione del rumore a basse frequenze, anche in trattamenti dallo spessore complessivo limitato.

Nell'elaborato, questa configurazione è ottimizzata per due spessori prestabiliti, al fine di massimizzare l'assorbimento sonoro tra 500 Hz e 4000 Hz, nell'ipotesi di onda sonora normale al pannello e in assenza di flusso medio. Due versioni ridotte di questi pannelli sono realizzate mediante stereolitografia e l'impedenza acustica misurata conferma la fono-assorbenza attesa nell'intervallo di frequenze considerato.

La tesi dimostra l'efficacia di COMSOL nella modellazione dell'impedenza acustica effettiva, sia nel caso di pannelli fonoassorbenti tradizionali, sia nel caso di pannelli dalla configurazione complessa. Lo studio propone considerazioni rilevanti per la modellazione numerica dei pannelli fonoassorbenti, convenzionali e non, e presenta le principali caratteristiche acustiche della configurazione presentata. Dimostra, inoltre, la validità di una formulazione analitica per una progettazione preliminare di pannelli dalla configurazione complessa.

Contents

List of figures

Nomenclature

α	=	Sound absorption coefficient
λ	=	Wavelength
k	=	Wavenumber
Γ	=	Complex reflection coefficient
p_{ref}	=	Reference threshold (pressure) of human hearing
p	=	Total pressure field
c	=	Speed of sound
ρ	=	Air density
V	=	Acoustic velocity
i	=	Imaginary unit $\sqrt{-1}$
M	=	Flow Mach number
ϕ	=	Incidence angle of sound pressure wave
C_D	=	Discharge coefficient
ϵ	=	Dimensionless end correction
$EPNL$	=	Effective perceived noise level
BPR	=	Bypass ratio
BPF	=	Blade passing frequency
Ω	=	Fan rotor angular velocity (in rpm)
SPL	=	Sound pressure level
$OASPL$	=	Overall sound pressure level
σ	=	Porosity of the plate
POA	=	Percentage open area
POA_{eff}	=	Effective percentage open area
$SDOF$	=	Single degree-of-freedom liner
$DDOF$	=	Double degree-of-freedom liner
f_{res}	=	Resonance frequency
Z	=	Liner impedance
R	=	Liner resistance
X	=	Liner reactance
X_{cav}	=	Cavity reactance
Z_{fs}	=	Face sheet impedance
R_{fs}	=	Face sheet resistance
X_{fs}	=	Face sheet reactance
Z_{septum}	=	Septum impedance
R_{septum}	=	Septum resistance
X_{septum}	=	Septum reactance

1. Regulatory and technical evolution of aircraft noise

The demand from communities living close to airports to reduce aircraft noise has been a continuing challenge to aircraft and engine manufacturers since the introduction of turbojet and turbofan-powered aircraft in civil aviation in the late 1960s and early 1970s. In order to face this critical issue, the international organizations ICAO (International Civil Aviation Organization) and FAA (Federal Aviation Administration), and local authorities involved in airport planning and air traffic management, imposed stringent aircraft noise requirements that have been tightened progressively over the subsequent decades. During this period, great technical progress has been made, succeeding in reducing aircraft noise at source and mitigating its effects by the introduction of noise reduction technologies.

The EC noise certification regulation in force is designated ICAO Annex 16, while the American equivalent is FAR 36. The ICAO regulation characterizes the noise of a specific aircraft operation using the Effective Perceived Noise Level (EPNL) metric, measured in EPNdB at three certifications points (see Figure 1.1): side-line, cutback and approach. The side-line point is located 450m laterally to the runway centreline as the aircraft takes off and climbs steeply at full power. The cutback point is located below the flight path, at 6500m from the end of the runway, as the aircraft cuts back to a slower rate of climb at a lower power setting (typically around 80% of maximum power). The aircraft altitude at cutback is a function of the climb rate, which, in turn, is a function of the number of engines. The approach point lies below the flight path at 2000m from the start of the runway, as the aircraft comes into land at a steady degree 3° glide angle, and an associated altitude of 120m [1].

The environmental impact of aircraft noise is essentially a local problem. It arises at departure and approach, and affects areas close to airports but it is not generally an issue during flight [2]. These considerations are essential in the certification of a commercial aircraft, because the aircraft industry can focus on the reduction of aircraft noise mainly at take-off and approach.

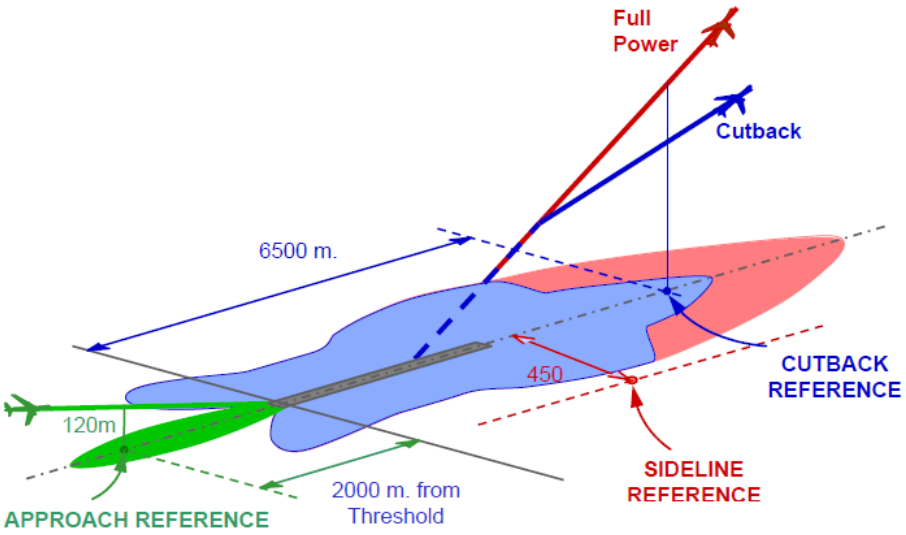

Figure 1.1.Noise certification points for ICAO Annex 16 and FAA FAR36 [2]

The noise of a given aircraft must lie below the certification limit, which depends on the aircraft mass, the number and the type of engines (at departure) and the year of its entrance into service. The certification limit is defined in terms of a cumulative noise margin, calculated using the three measured EPNL values assessed against maximum EPNL limits defined in [1] for each certification condition.

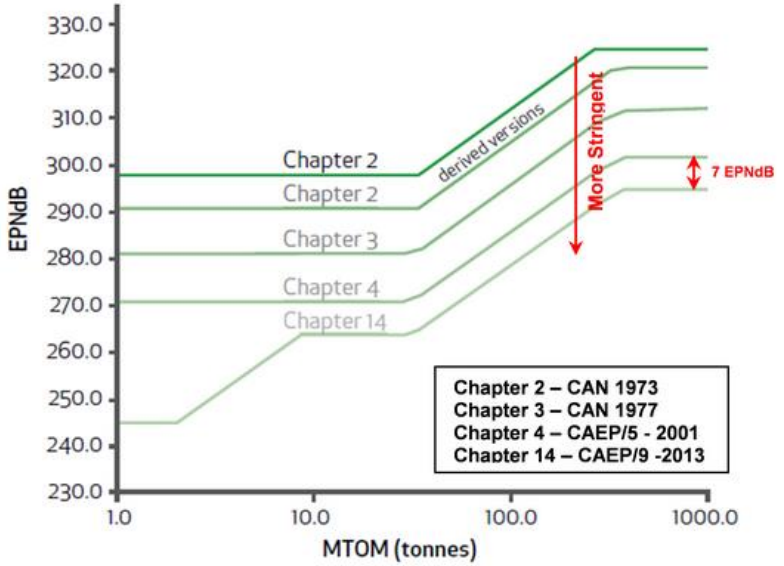

Figure 1.2. Historical trend of maximum EPNLs (in EPNdB) through the revisions of Annex 16

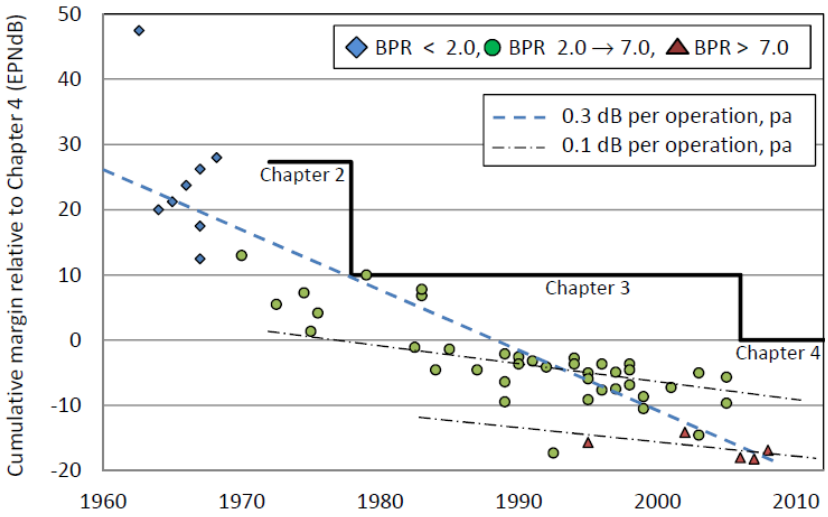

Figure 1.3. Historical trends in aircraft noise reduction as measured by cumulative noise levels per operation (EPNdB) for aircraft entering service 1960-2010 [2]

Figure 1.2 and Figure 1.3 show the historical evolution of the certification limits through the revisions of Annex 16 (in figure, Chapter 2, 3, 4 and 14). Moreover, Figure 1.3 provides the measured cumulative noise margins for a representative selection of aircraft, entering service between 1960 and 2010. These measured margins are separated into three categories based on the Engine Bypass Ratio (BPR) of the relevant turbofan engine; less than 2.0, between 2.0 and 7.0, and greater than 7.0. The BPR of a turbofan engine is defined as the ratio between the unburnt air mass flow (secondary flow) and the mass flow going through the core (primary flow) (see Figure 1.4).

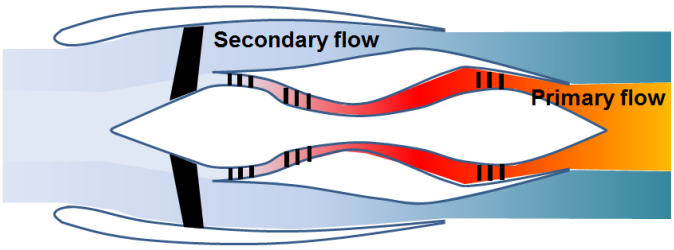

Figure 1.4. Bypass turbofan engine scheme [3]

In Figure 1.3, the overall trend line of aircraft noise reduction from 1960 to 2010 is drawn. It follows a noise reduction of approximately 0.3 dB per operation per year. Much of the reduction stems directly or indirectly from changes in the BPR. In 40 years, aircraft industry has reduced aircraft noise by 30 dB, that is equivalent to reducing the acoustic power to 0.1% of its level in the early 1960s [4]. This enormous reduction in noise power was achieved almost solely through the modification of the propulsion system. The migration from the straight jet to the modern, large diameter turbojet engine has yielded enormous increases in overall propulsive efficiency and has produced significant reductions in aircraft noise [4]. It should be noted that high BPR engines (6-11) are dominating the current propulsive scenario. They are adopted both by long-range airplanes (like A380, 747-8, 787, and A350) and shorter-range airplanes, (A320 NEO and 737 MAX). Moreover, the next generation of aircraft will adopt an Ultra High By-pass Ratio (UHBR) turbofan and they are expected to have a BPR close to 15 or 16.

The reduction in engine noise is not only due to the modification of the propulsion system. In Figure 1.3, within each aircraft generation, the weaker trend of noise reduction of approximately 0.1 dB per operation per year, reveals that a further noise reduction has been obtained independently from the increased BPR. It mainly depends on the significant advance in sound absorption technologies, the acoustic treatments lining the internal walls of nacelles, which further improved the attenuation of the aircraft noise [2].

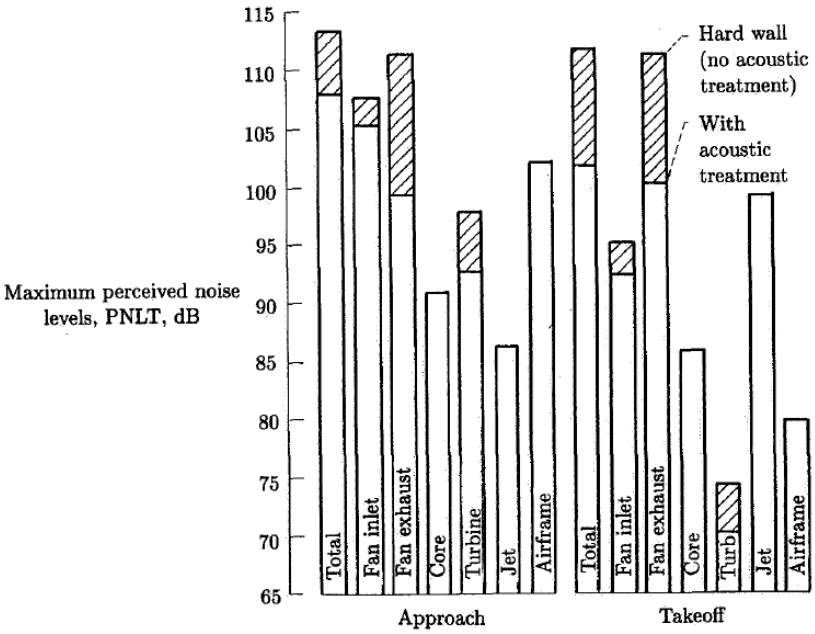

Figure 1.5. Take-off and landing noise levels for a high-bypass ratio turbofan [5]

Figure 1.5 shows the importance of sound-absorbing technologies in the attenuation of aircraft noise. This illustrates the typical distribution of noise levels for take-off and landing in a high BPR turbofan engine. The most prominent sources of noise are produced by the turbomachinery. The fan noise component dominates the total perceived noise both at the take-off and at the approach, but it is reduced dramatically thanks to the inclusion of acoustic treatments lining the internal walls of the aircraft nacelles. The treatments are usually mounted in the intake and in the aft by-pass duct, where the fan noise propagates. They may also be found in the core duct to attenuate turbine and combustion noise. As shown in Figure 1.6, the noise generated at the fan propagates to the forward arc through the intake and to the rear arc through the bypass duct, and then it is radiated to the atmosphere [6].

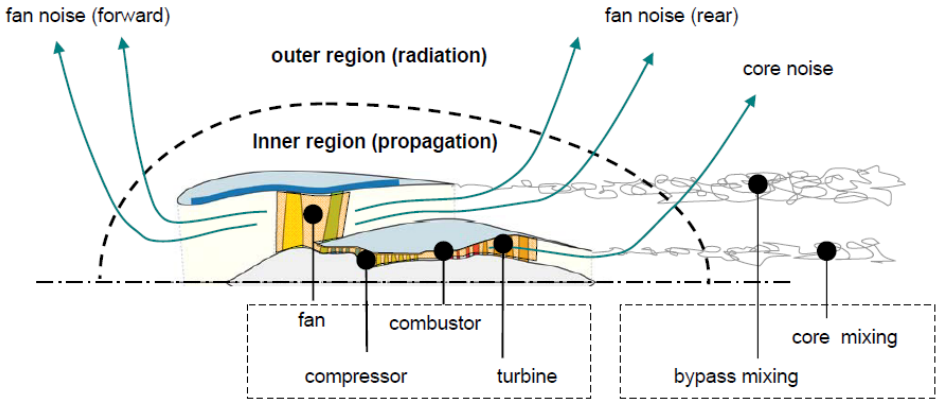

Figure 1.6. Noise sources and transmission paths in a turbofan engine [6]

Figure 1.5 suggests that, beside fan noise, jet noise is also a dominant source at departure. However, the increasing BPR has corresponded to a decreasing jet velocity, so that jet-mixing noise has been reduced and jet noise is a secondary source in current engines (see Figure 1.7 and Figure 1.8), though recent advances to very large engines have led to an increases in jet-flap interaction noise. At the same time, the advance of the noise reduction technologies has determined that on approach, the reduced levels of engine source noise leads to the engine contribution being comparable to the airframe contribution [4]. The airframe sources arise from the deflection of high lift devices (flaps, slats), and the deployment of the undercarriage. Finally, given the large dimensions of modern turbofans, efforts are made to reduce their length in order to reduce weight and fuel consumption, so the efficiency of acoustic treatments must increase in order to maintain the status quo.

.

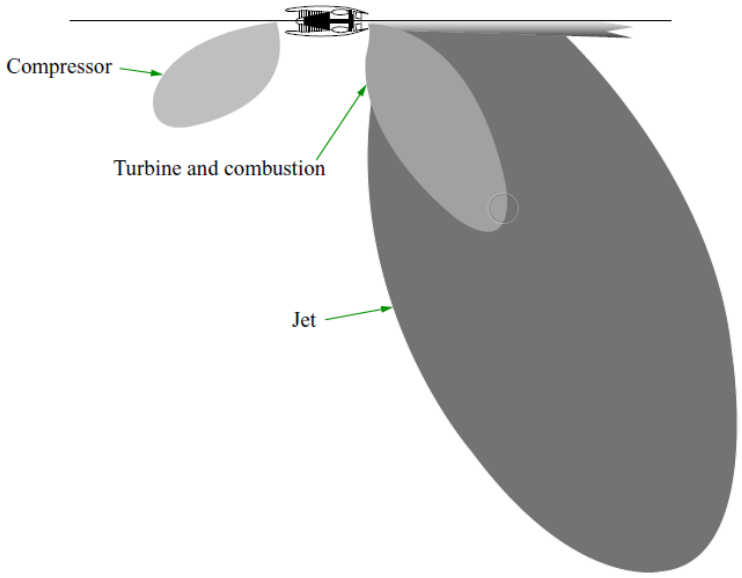

Figure 1.7. Representation of aircraft low BPR turbofan noise radiation in the half-plane below the engine axis [7]

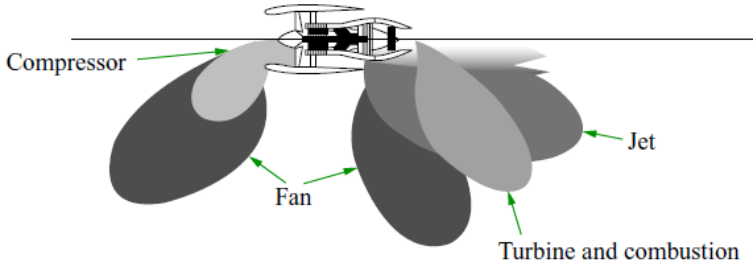

Figure 1.8. Representation of aircraft high BPR turbofan noise radiation in the half-plane below the engine axis [7]

1.1 Brief overview of fan noise generating mechanism

The current paragraph presents a general overview of the main features characterizing the propagation of fan noise in a nacelle. For a detailed and advanced understanding of the mechanisms governing the propagation and radiation of fan noise within and outside a cylindrical duct, the reader is referred to the pioneering work of J. M. Tyler and T. G. Sofrin [8].

The sound produced by an engine fan results from the interaction between the flow and the components of turbomachinery. The description of fan noise propagation must account for the presence of the duct surrounding the turbomachinery. The duct imposes its own boundary conditions on both the interior and the radiated sound field.

In a first approximation, the propagation of fan noise in the nacelle duct can be described by the wave equation in Equation 1.3. This is obtained by subtracting the time derivative of the mass conservation equation,

$$\frac{\partial \rho}{\partial t} + \frac{\partial \rho u_i}{\partial x_i} = 0 \tag{1.1}$$

from the divergence of the momentum conservation equation,

$$\frac{\partial}{\partial t}\rho u_i + \frac{\partial}{\partial x_j}\left(p_{ij} + \rho u_i u_j\right) = 0 \tag{1.2}$$

The wave equation is then given by,

$$\frac{\partial^2 p}{\partial t^2} - c^2 \nabla^2 p = 0 \tag{1.3}$$

In Eqs.1.1-1.3, ρ is the air density, c is the sound speed of air, and p is the total pressure field. The left-hand side of Equation 1.3 is the wave operator that governs the propagation of density fluctuations through the air. The flow is assumed to be unaffected by the sound as it radiates.

The sound produced by duct sources is most conveniently described in terms of the natural acoustic duct modes [9]. When the flow is confined within a wave guide, in fact, the acoustical energy accumulates into modes [10]. The acoustic pressure field p in Equation 1.3 can be effectively described as the weighted sum of modal solutions, whose weighting factors depend on the source distribution. At a single frequency, the general solution for the acoustic pressure p is written as [9]:

$$p(r, \theta, x, t) = \sum_{m=-\infty}^{+\infty} \sum_{n=-\infty}^{+\infty} \bar{p}_{mn} \Phi_{mn}(r, \phi) e^{j(\omega t - \alpha_{mn} k x)} \tag{1.4}$$

In Equation 1.4, r and ϕ are the radial and angular circumferential coordinates, ω is the circular frequency, $k = 2\pi f/c$ is the free-field wavenumber, and $\alpha_{mn}k$ is the axial propagation wavenumber. Each mode (m, n) has a pressure amplitude of $\bar{p}_{mn}$, and its spatial distribution in a cross-section of the duct is characterized by the function $\Phi_{mn}(r, \phi)$. The axial propagation wavenumber $\alpha_{mn}k$ is linked to the free-field wavenumber k, according to the dispersion equation:

$$\left(\frac{\kappa_{mn}}{k}\right)^2 + \alpha_{mn}^2 = 1 \tag{1.5}$$

where κ_{mn} is the transverse wavenumber of the (m, n) mode. The dispersion equation is linked with the excitation frequency f through $k = 2\pi f/c$.

At any frequency, the total propagating field in a duct comprises the superposition of singular modes, which travel at different speeds along the duct. Each mode may be regarded as a pressure pattern across the duct cross-section, which propagates axially along the duct at its own characteristic axial phase speed $c_{mn} = c/\alpha_{mn}$. For a given mode, a so-called cut-off frequency, $\omega_{mn} = c\kappa_{mn}$ [9] exists, below which α_{mn} is purely imaginary, and the mode decays exponentially with distance along the duct. Hence, at frequencies above ω_{mn}, the mode is cut-off or evanescent. The rate at which cut-off modes decay with distance increases with frequencies ratios ω_{mn}/ω greater than unity. In an infinite duct, the pressure and the particle velocities of single-frequency cut-off modes are in quadrature. Therefore, the time-averaged axial intensity flow is zero, and no acoustic energy is transmitted along the duct.

An essential condition for the propagation of the (m, n) mode in the ith direction, is that the modal phase speed in this direction must exceed the sound speed c,

$$c_i = \frac{\omega}{k_i} \geq c \tag{1.6}$$

The mode can propagate in the ith direction if the wavenumber component k_i is less than, or equal to k, so that α_{mn} is real. Equation 1.6 suggests that an essential requirement for efficient sound generation by ducted rotating sources is that their speed of rotation, either actual or effective (axial phase speed $c_{mn} = c/\alpha_{mn}$) is supersonic.

At a single frequency, only a finite number of modes can propagate unattenuated along a hard-walled duct, at their own characteristic axial phase speed. All other higher-order modes decay exponentially along the duct. The zero-order mode $(0,0)$ is called the plane wave. It propagates at all frequencies parallel to the duct axis, at the speed of sound in air.

.

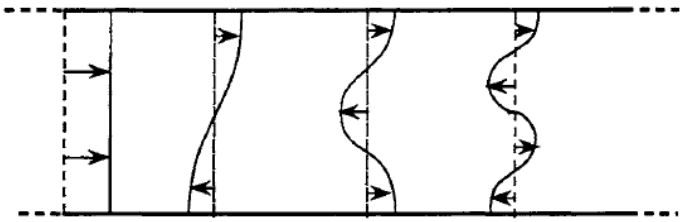

Figure 1.9. Scheme of transverse distributions of pressure and axial particle velocity at low-order modes along a rectangular duct – Side view [11]

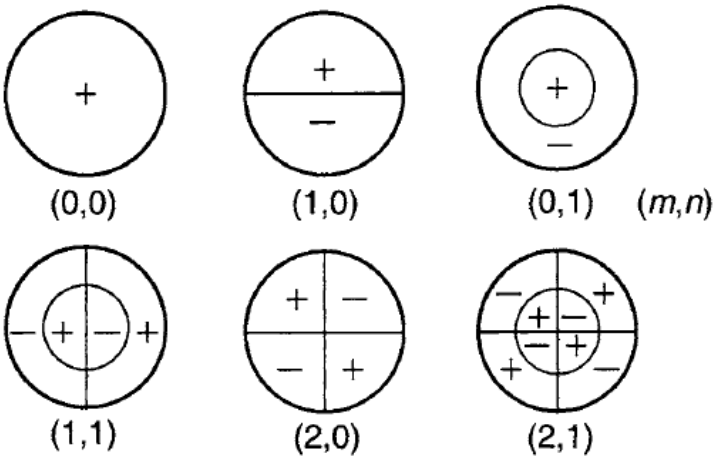

Figure 1.10. Regions of uniform phase in low-order modes of a uniform, cylindrical duct – Cross section, front view [11]

With this consideration in mind, the sound pressure field of the fan noise can be decomposed into tonal noise and broadband noise. The former usually comprises a few dominant modes centred on the blade passing frequency (BPF) and its integer multiples; the latter comprises a much larger number of modes of various amplitude over a wide frequency range. The blade passing frequency is dependent on the characteristics of the fan and it is given by

$$BPF = \frac{B}{60}\Omega \tag{1.7}$$

where B is the number of blades of the fan and Ω is the rotor angular velocity in rpm. Knowledge of the fan noise modal structure permits the prediction and control of sound propagation in the duct and the subsequent estimation of the radiation directivity patterns. Moreover, sound-absorbing liners can be designed to effectively abate specific modes of the fan noise [9].

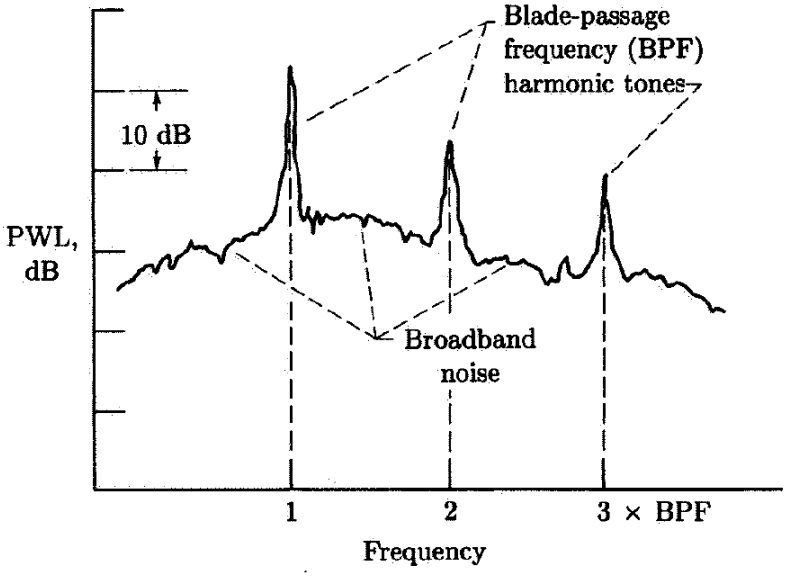

Figure 1.11. Typical fan sound power spectrum – Subsonic tip speed [5]

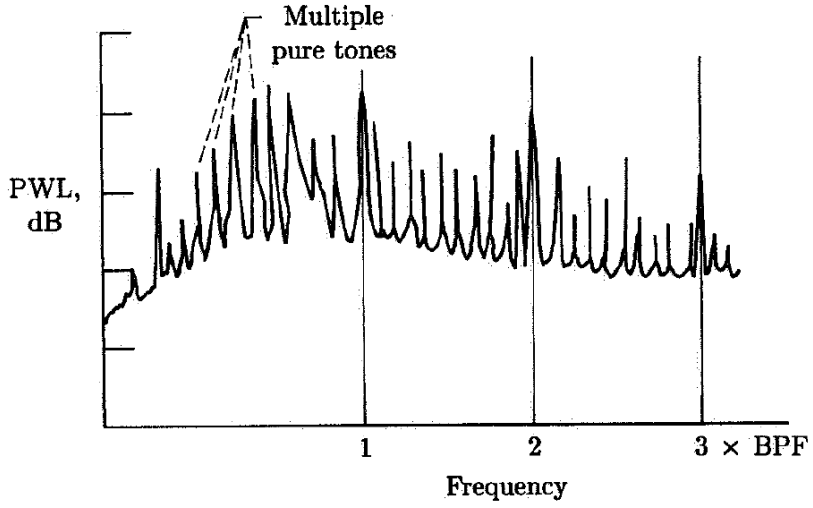

Figure 1.12. Typical fan sound spectrum – Supersonic tip speed [5]

1.1.1 Tonal fan noise

The tonal component of fan noise is mainly generated by the self-noise of the rotor and the noise caused by the aerodynamic interaction between the rotor and the stator [8]. Another source mechanism of tonal noise may be the distortion of the inlet steady flow impinging on the fan face. In each case, the resultant power sound spectrum is largely dependent on the speed at the rotor tips.

1.1.2 Self-noise rotor

In rotors with subsonic tip speeds, a dominant noise source is the pressure field deriving from the steady aerodynamic blade loading [8]. This pressure field acts on each rotor blade and it is repeated every $2\pi/B$ interval, and it rotates with the angular velocity Ω of the rotor. However, this source is cut-off, so it will not radiate for typical aircraft engine duct lengths. On the contrary, in rotors with supersonic tip speeds, a shock wave is produced ahead of each blade. The shock wave produces a sonic boom similar to that produced by an aircraft travelling at supersonic speeds. In this case, the pressure pattern has the shape of a regular saw-tooth, and it rotates with the rotor angular velocity Ω. For both subsonic and supersonic tip speeds, the self-noise of the rotor produces rotating pressure patterns, which are referred to spinning modes [8]. The periodicity of the fan blades causes most of the acoustic energy to be confined to the blade-passing frequency and its harmonics. However, in practice, small differences in blade geometry, and in the high-speed aero-elastic response between each blade, causes the pressure patterns to be irregular and no longer periodic. The original regular pressure pattern, with its peaks centred at the BPF and at its harmonics, is redistributed amongst a wider range of frequencies. This is because each blade generally has a unique shock strength, so each shock propagates at a different speed, creating a more distorted waveform as the wave propagates along the duct. By the end of the inlet duct, most of the acoustic energy has been spread into frequencies other than the BPF. It is noted that the energy transferred to higher frequencies (higher-order modes) is more readily dissipated. However, the resulting high-amplitude, low-frequency tones present a greater problem for noise engineers as they are more difficult to absorb with conventional acoustic liners, they propagate relatively unattenuated by the atmosphere, and they are also more easily transmitted through the walls of aircraft cabins.

1.1.1.1 Rotor-stator interaction noise

As discussed in 1.1.2, the modes generated by the fan rotors with subsonic tip speeds do not radiate efficiently to the far field, as they decay exponentially along the duct. Nonetheless, for certain combination of rotor blades and stator vanes, the subsonic rotor wakes impinging onto the downstream stator vanes can produce a disturbance at the BPF and its harmonics, as the effective speed of rotation of these interaction modes is supersonic around the stator. This disturbance couples to propagating duct modes, which then radiate to the far field. Similarly, noise is also produced by the interaction between the potential near field of the rotor and the stator. This potential field interaction can be neglected because of its rapid exponential decay with distance from the blades. However, it becomes significant for rotors and stators very close together, if the spacing is small compared to the acoustic wavelength.

The noise produced by the aerodynamic interaction between the rotor and the stator is largely dependent on the number of the rotor blades B and the number of the stator vanes V. B rotor blades adjacent to V stator vanes produce a pressure pattern occurring at s times the BPF, in m circumferential wavelengths. The order m of the spinning modes produced by this interaction can be calculated as [9]:

$$m = sB \pm qV \tag{1.8}$$

where q is any positive integer. The sign of m may be positive or negative; this indicates that the modes may spin in either direction relative to the stator or to the rotor. It is recalled that the necessary condition for modal propagation is that the modal phase speed in the circumferential direction should exceed, or be equal to, the sound speed

in that direction (see Equation 1.6). This condition can be expressed in terms of the ratio V/B between the number of stator vanes V and the number of rotor blades B using the following relation [9]

$$\frac{V}{B} \geq 1.1(1 + M_t)s \tag{1.9}$$

where M_t is the rotor tip Mach number. Hence, as it emerges from Equation 1.9, the spinning modes produced by the rotor-stator interaction can propagate only for certain combinations of the number of stator vanes V and rotor blades B.

1.1.2.1 Inlet steady flow distortion noise

The interactions between the distortions of the mean intake-flow velocity and the fan face of a subsonic rotor can excite duct modes propagating along the duct. Distortions of the intake-flow occur naturally in the atmosphere or may be produced by non-axisymmetric features within the duct. B rotor blades that interact with a harmonic circumferential variation p of the axial flow speed, produce a pressure pattern occurring at s times the BPF in m circumferential wavelengths. The order m of the spinning modes produced by this interaction is given by [9]

$$m = sB + p \tag{1.10}$$

This interaction mechanism is particularly important at the BPF. At BPF, the contribution to the fan noise due to the rotor-stator is usually designed to be cut-off using an appropriate selection of rotor blades B and stator vanes V. Hence, the noise produced by the interaction between the distorted mean intake-flow velocity and the fan face becomes significant.

1.1.3 Broadband fan noise

The broadband component of fan noise is mainly generated by the interaction between the various sources of turbulence present in the turbofan engine. Broadband noise is present over a wide frequency bandwidth and its control at source is extremely difficult. The number of distinct source mechanisms is large. All broadband sources generally excite all modes to varying degrees. The typical spectrum of broadband noise usually falls off slowly with increasing frequency (see Figure 1.11 and Figure 1.12).

The dominant broadband sources in the forward arc are [9]:

- The inlet turbulence impinging on the fan blades; the turbulence may be ingested from the atmosphere or may originate from the boundary layer on the duct walls.
- The turbulence of the blade boundary layer (see Figure 1.14), that is scattered into sound at the blade trailing edge.

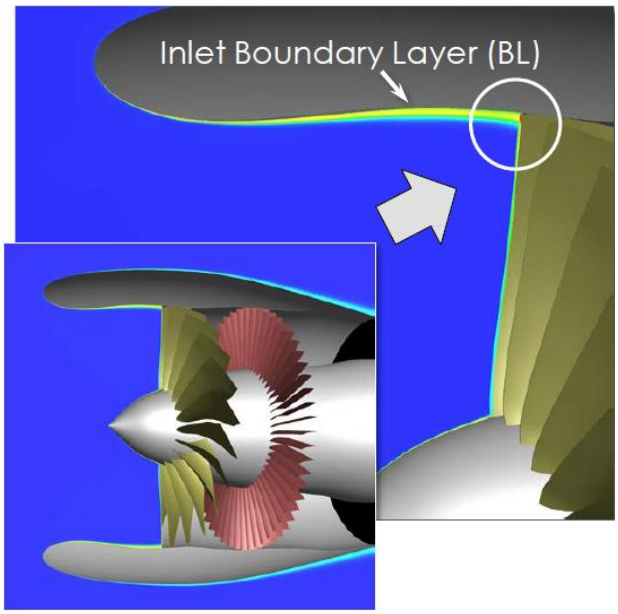

Figure 1.13. Inlet boundary layer [12]

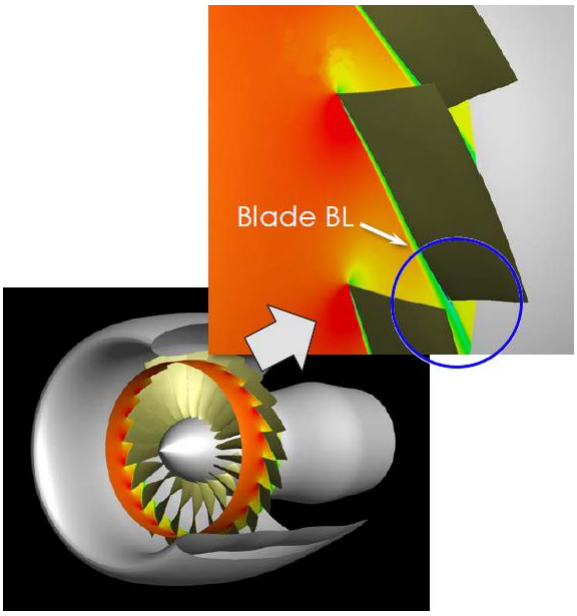

Figure 1.14. Fan blade boundary layer [12]

The dominant broadband sources in the rear arc are [9]:

- The turbulence of the inlet boundary layer impinging on the blade surface (see Figure 1.13), that is scattered into sound at the rotor blade tips.
- Turbulent wakes shed from the rotor impinging onto the stator (see Figure 1.15). The radiated power increases roughly in proportion to the number of stator vanes V.

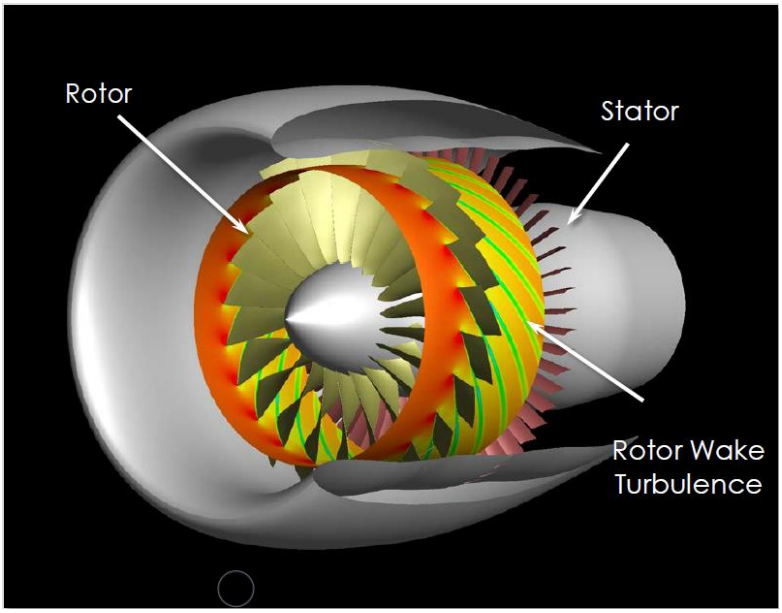

Figure 1.15. Interaction of the rotor wake turbulence with the fan exit guide vanes [12]

1.2 Fan noise reduction at the source and during propagation using sound-absorbing treatments

The reduction of fan noise can be achieved by either designing the fan to reduce noise at the source or by designing acoustic treatments to absorb the fan noise propagating along the duct.

As seen in 1.1, the rotor tip speed and the number of blades and vanes have an influence both on the noise source and on the achievable noise suppression. They can be selected to drive specific mode patterns, while degrading others. In general, it is desirable to have pressure mode patterns which are near cut-off, so that the sound is well attenuated by acoustic liners in the duct walls. Designing the fan to abate noise is described in 1.2.1 and 1.2.2. Key drivers include reduction of fan tip speed, design for rotor-stator mode cut-off, adding rotor sweep, and increasing the rotor-stator separation.

1.2.1 Reduction of the rotor-stator interaction noise

A conventional way of reducing the rotor-stator interaction noise consists in selecting an adequate ratio V/B between B rotor blades and V stator vanes to cut-off specific rotor-stator tones. The vane-blade count ratio may be selected to cut-off the pressure pattern propagating in the duct at a given multiple of the BPF (normally just BPF). From Equation 1.9, it is deduced that all modes at $1BPF$ and $2BPF$ ($s = 1$ and 2) are cut-off for numbers of stator vanes approximately equal to $V = 2B + 1$ and $V = 4B + 1$, respectively. Usually, second and higher harmonics require $V/B > 4$ to achieve cut-off [5]. If it is not possible to select V/B to cut-off a specific tone, an alternative way is to select V/B such that the wave propagation spiral angle in the duct is as close to $90°$ as possible, because cut-off corresponds to a spiral angle of $90°$. In this way, the residence time of the wave pattern in the duct is sufficiently long for the duct acoustic treatment to attenuate the tone as much as possible.

Alternatively, the rotor-stator interaction can be reduced by adequately designing the aerodynamic properties of the rotor blade. The downstream stator vanes see the impinging rotor wakes or the wake velocity defect as gusts. The wake gust amplitudes can be reduced by sweeping the blade and selecting the camber and incidence angle to provide minimum blade section drag coefficients and, hence, smaller wake defects. However, the degree of the possible noise reduction is not certain, because the precise behaviour of rotor wakes is difficult to predict, especially for rotors with transonic tip speeds.

In addition, the rotor wake gust amplitude can be reduced by also designing the rotor-stator axial spacing to be sufficiently large, so that the wake has largely decayed before reaching the stator vanes. Nonetheless, although effective in reducing noise, this option necessitates an increase in overall engine length, and therefore it imposes a weight penalty and a decrease in fan efficiency [5].

1.2.2 Reduction of other fan noise mechanisms

In a typical turbofan engine, frame struts (referred to as 102, 104, 106 and 108 in Figure 1.16 and Figure 1.17) and engine support pylons (referred to as 148 and 150 in Figure 1.16) are present in the duct, downstream of the fan. These struts and pylons produce static-pressure distortions which can be felt upstream in the vicinity of the rotor itself. The degree to which the rotor feels the circumferential variations in the static pressure is a function of the

axial location, number and size of the obstructions. The influence of these distortions can be lowered by designing the fan to have a large axial distance between the fan rotor and the downstream struts and pylons. This approach is effective, but it also introduces a weight penalty by increasing the length of the engine [5].

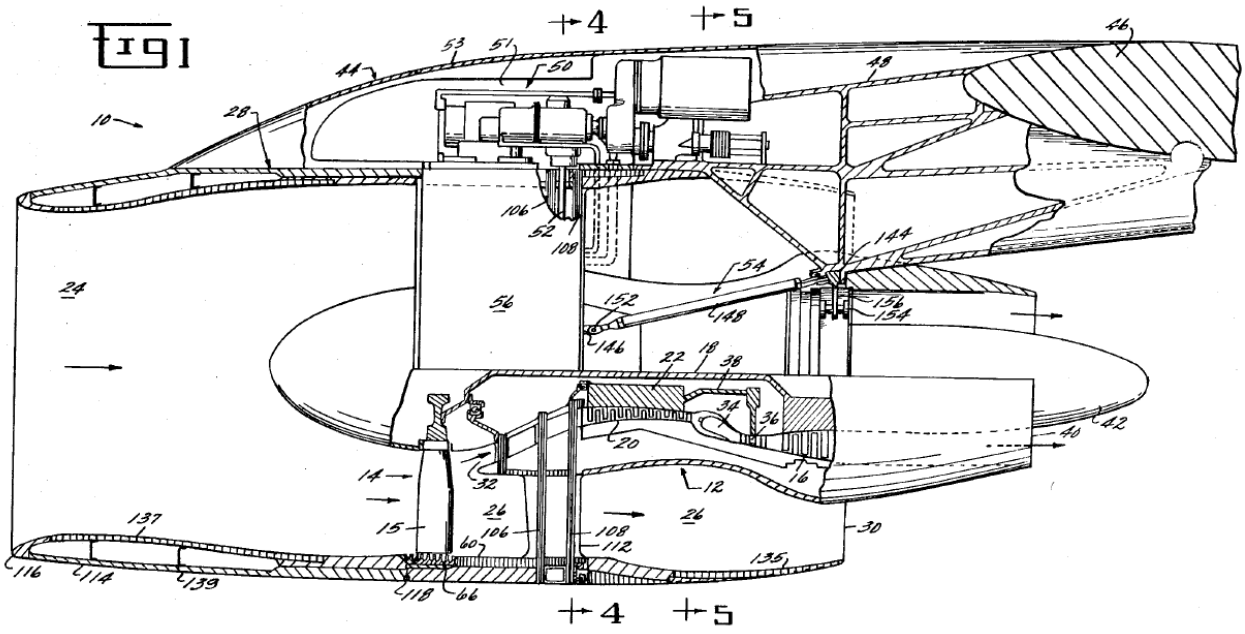

Figure 1.16. Schematic representation of a turbofan engine [13]

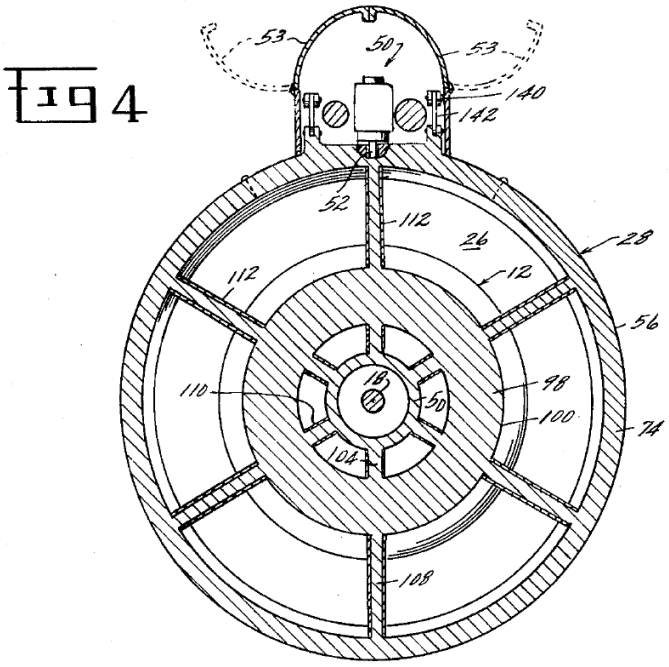

Figure 1.17. Cross-sectional view of the turbofan engine, taken along the line 4-4 of Figure 1.16 [13]

1.2.3 Sound-absorbing materials

Reducing the fan noise at source is the starting point for minimisation of engine noise. However, noise source reducing mechanisms may introduce weight penalties while design constraints may also restrict their implementation. Nonetheless, reduction only of the fan noise at the source is not sufficient to meet certification limits, so the internal walls of the nacelles must also be lined with sound-absorbing panels (referred to 136 and 137 in Figure 1.16). These passive devices are mounted in the walls of an aircraft nacelle inlet, aft-bypass duct, and core ducts, to absorb both tonal and broadband noise sources. It should be noted that the effectiveness of the treatment tends to deteriorate at frequencies and operating conditions away from the design condition, and the amount of noise suppression is predominantly a function of the fan design characteristics [5]. However, the acoustic treatments are usually designed to preferentially suppress fan noise at those frequencies that contribute most to the aircraft perceived noise level. In conventional turbofan engines, the treatments are tuned to absorb noise in a given frequency band at those operating conditions where the noise level is limited by regulations.

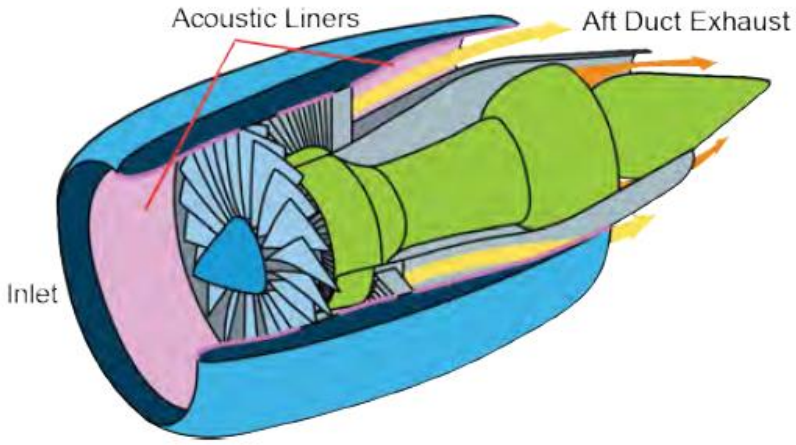

Figure 1.18. Aircraft nacelle of a turbofan engine. Detail on acoustic treatments lining the internal walls [14]

Generally, nacelle liners are selected to reduce community noise frequencies most effectively, typically between 500 Hz and 6000 Hz for full-scale engines [6]. Liners currently mounted in commercial aircraft nacelles are predominantly perforate-over-honeycomb structures. These are referred to as Single Degree-Of-Freedom (SDOF) and Double Degree-Of-Freedom (DDOF) structures.

An SDOF panel consists of a single-layer sandwich construction, with a resistive face sheet (a perforate plate, or a wire mesh supported by a highly open perforate) bonded onto resonating cavities (usually made of honeycomb core). It has a rigid back plate bonded to the rear of the honeycomb. A DDOF is a double-layer sandwich, which adds a second resistive (septum) layer and honeycomb.

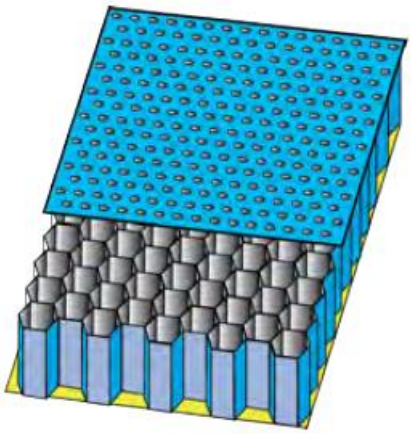

Figure 1.19. Scheme of a SDOF perforate liner [15]

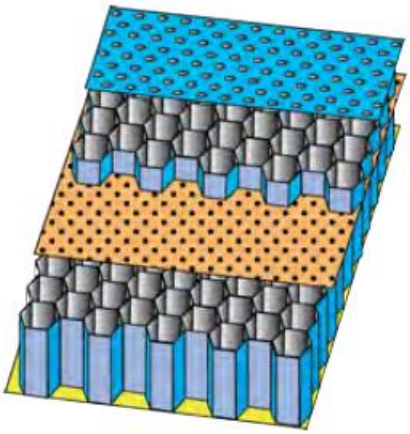

Figure 1.20. Scheme of a (perforate-perforate type) DDOF liner [15]

An SDOF liner can be effective in abating noise over a narrow range of frequencies. It is generally tuned to the frequency band containing the single fan tone of greatest concern. The useful bandwidth of the SDOF treatment is usually about one octave. A DDOF treatment has a wider useful bandwidth, being most effective typically for fan blade-passage frequency (BPF) and its first harmonic. The useful bandwidth of DDOF treatments, in fact, can be extended to cover the BPF and its next two harmonics (about two octaves) [16].

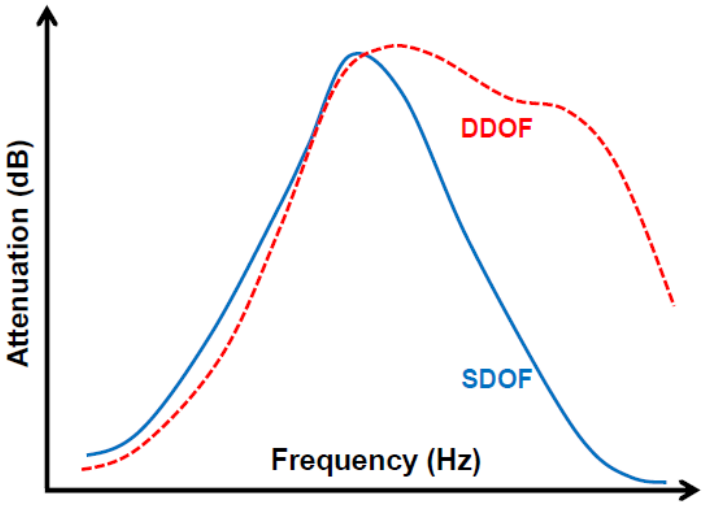

Figure 1.21. Attenuation spectra for a SDOF and a DDOF of the same total thickness [3]

Intake acoustic liners were originally manufactured in two or three curved segments (see Figure 1.23). For the decades prior to the 2000s, acoustic liners usually consisted of several large panel segments, separated by thin longitudinal strips of acoustically reflecting material, referred to as liner splices. Because of the constraints in the manufacturing process and the related costs, it had been difficult to fit single-piece liner barrels that cover the entire circumference of the duct (i.e. 0-splice liners, see Figure 1.24). However, despite the cost and manufacturing benefits, the inclusion of separate segments of liners has a large detrimental effect on forward fan noise. The extent of the noise penalty was not realised until the introduction of 3D sound propagation models. Longitudinal splices were shown to scatter energy from a given incident circumferential mode into a number of other neighbouring modes. In a spliced intake liner configuration, the hard-walled splices generate an additional parasitic noise source

compared to a splice-less configuration [17]. Hence, in addition to the lost acoustic areas from the splice, overall liner efficiency is also degraded.

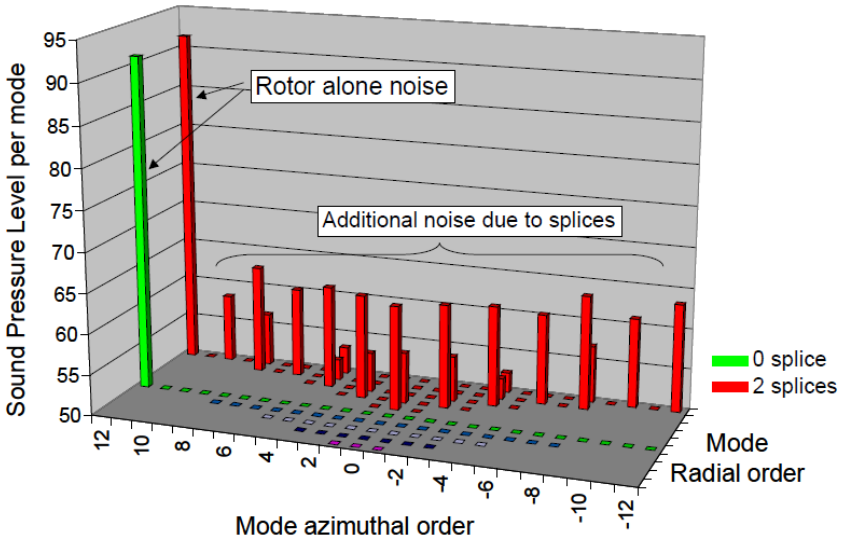

Figure 1.22. Induct noise for a 2 splices (red) and a 0 splice (green) intake liner configurations [17]

As shown in Figure 1.22, for a 0-splice intake, the noise generated by a single self-noise rotor acoustic mode can propagate as a unique acoustic mode along the duct. On the contrary, with splices, this mode is scattered into other modes which may be less well attenuated by the duct acoustic lining. Splices, in fact, break the circumferential symmetry of the intake waveguide. As a result, incident spinning modes that carry fan noise are scattered and other modes are generated. If scattered modes are cut-on more than the original mode, they will tend to be less well attenuated by the lining, so the existence of the splices becomes detrimental in terms of the overall noise attenuation. For these reasons, nowadays aircraft manufacturers insist on a single-piece inlet liner, which gives significantly better noise attenuation than a liner with two or three longitudinal splices [17] [18]. Zero-splice liners have been already installed in nacelles of long-range aircraft, such as the A380, A350, and B787 [2], in addition to medium-range single aisle aircraft including the A320 NEO and the B737 MAX, among others.

Figure 1.23. Two-splice liners [19]

Figure 1.24. Zero splice liner [12]

1.3 Acoustic features and design parameters of sound-absorbing treatments

Acoustic impedance is the key design parameter that drives the noise suppression yielded by an acoustic liner in a nacelle duct [16].

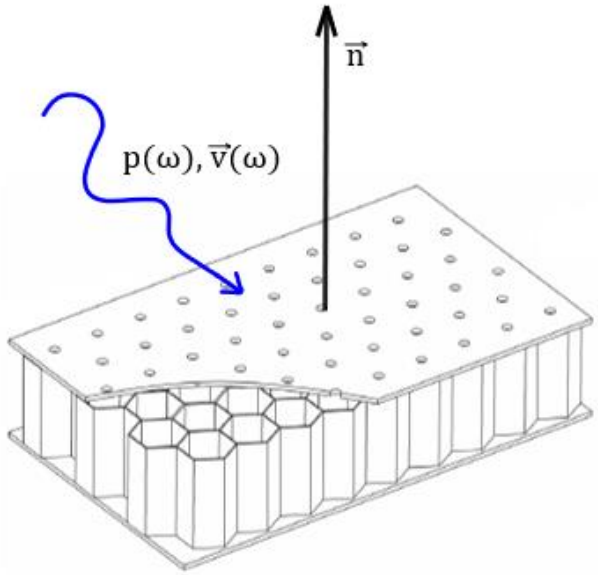

Figure 1.25. Scheme of the pressure wave incident on the surface of an SDOF liner

The acoustic impedance, Z, is defined as the complex ratio of the acoustic pressure $p(\omega)$ to the normal component of acoustic velocity, $\vec{v}\,(\omega)$, at a point on the liner surface [11]:

$$Z(\omega) = \frac{p(\omega)}{\vec{v}\,(\omega) \cdot \vec{n}} \tag{1.11}$$

In Equation 1.11, ω is the circular frequency $\omega = 2\pi f$, and $\vec{n}$ is the dimensionless vector, normal to the liner surface.

Both the acoustic pressure $p(\omega)$ and the acoustic velocity $\vec{v}\,(\omega)$ are frequency dependent. Consequently, both the impedance of an acoustic liner, and the corresponding sound absorption, are frequency dependent. Moreover, the impedance presented to a sound wave that impinges onto the liner surface depends upon the form and the direction of the incident wave. This is because the normal component of the particle velocity at any point on the interface is influenced not only by the local sound pressure, but also by the direction of the incident wave.

The acoustic liners used in aircraft engines contain internal walls (i.e. honeycomb core partitions) that prevent lateral propagation of the sound within the panel. In this way, it is reasonable to assume that the particle velocity generated by the incident sound at any point on the surface is directly related to the local sound pressure of the incident wave. The honeycomb cells ensure plane wave propagation inside the cells at the frequencies influencing EPNL. The facing sheet particle velocity is therefore independent of the form of the incident sound field and the panel is said to be locally reacting. As a result, the acoustic properties of the liner can be characterized by a uniform impedance along its surface [11]. On the contrary, in a non-locally reacting panel, the impedance at a point depends on the wave motion within the panel in an extended region around a point on the surface, and it varies with the incidence angles of the incoming waves Hence, it is not possible to define an impedance for a non-locally reacting panel, and the analysis of the design and performance of such panels must include the lateral propagation of sound waves inside the panel.

As a rule of a thumb, in locally reacting liners (such as SDOF and DDOF liners), the axial extent of the internal partitions should be less than the depth of the panel, and narrow enough to ensure plane wave propagation at the

frequency of interest. In conventional treatments, the partitions usually have an axial spacing of $3/8''$ ($\approx 9.5\ mm$). Conversely, the most common versions of an extended-reaction liners do not have partitions and the core is filled by foam or fibres [14]. The filling may be covered with a perforated face sheet or a wire mesh to protect the material from the flow over the liner. In these panels, the majority of the sound absorption is supplied by the filling and sound is transmitted in all directions within the liner. Most importantly, extended reaction liners tend not to be used in aircraft nacelle due to their tendency to hold fluids [7].

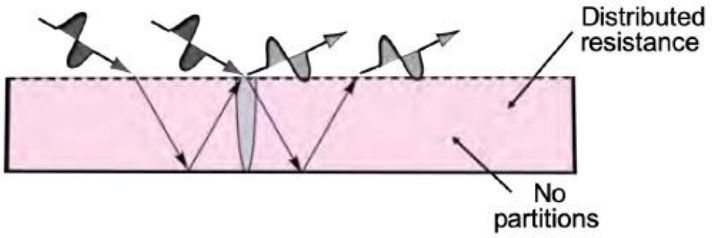

Figure 1.26.Sketch of an extended-reacting liner [14]

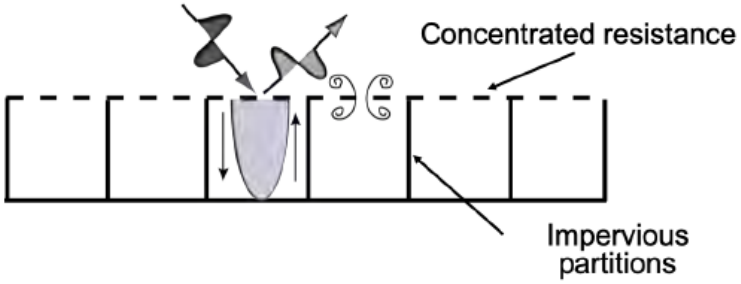

Figure 1.27. Sketch of a local-reacting liner [14]

As the acoustic pressure and acoustic velocity at the facing sheet of a liner are not necessarily in phase, the acoustic impedance Z is a complex number, whose real part R is referred to resistance, while the imaginary part X is referred to reactance,

$$Z = R + i\mathrm{X} \tag{1.12}$$

Z is usually normalized by the characteristic impedance of air, ρc, given by the product of the density of air ρ and the air speed of sound c.

The key parameters that relate the impedance of the panel to its physical construction can be identified in the mathematical models of the treatment impedances for each panel. For single-degree-of-freedom liners, the acoustic impedance can be modelled as [16],

$$\frac{Z}{\rho c} = \frac{R}{\rho c} + i\left(\frac{X_{fs}}{\rho c} + \frac{X_{cav}}{\rho c}\right) \tag{1.13}$$

where $R/\rho c$ is the normalized face sheet resistance, $X_{fs}/\rho c$ is the normalized face sheet reactance and $X_{cav}/\rho c$ the normalized cavity reactance. The normalized cavity reactance is given by,

$$\frac{X_{cav}}{\rho c} = -\cot(kh) \tag{1.14}$$

where h is the depth of the cavities of the honeycomb core, and k is the wavenumber $k = 2\pi f/c$. The reactance of the face sheet X_{fs} will be discussed further in 1.3.1.

The reactance of single-layer panels follows a slightly modified cotangent curve $X_{fs}/\rho c - \cot(kh)$ which governs the spectrum of the sound absorption. The normal incidence sound absorption is maximum at the frequency where the reactance is zero, called the resonance frequency f_{res}. The height of the core cells and the acoustic features of the porous face sheet may be chosen to tune the sound absorption in the desired frequency bandwidth.

In the case of an SDOF liner, the resonance frequency can be calculated from Equation 1.15,

$$\frac{X}{\rho c} = \frac{X_{fs}}{\rho c} - \cot(kh) = 0 \tag{1.15}$$

$$f_{res} = \frac{c}{2\pi h}\operatorname{atan}\left(\frac{\rho c}{X_{fs}}\right) \tag{1.16}$$

In the case where a face sheet is not bonded onto the liner surface ($X_{fs} = 0\ \rho c$ in Equation 1.15), the panel behaves as a quarter-wave resonator. The resonance frequency is given by,

$$f_{res} = \frac{c}{4h} \tag{1.17}$$

It is noted that the equations above are valid for a normal incidence plane wave in the absence of mean flow. Thus, they are not directly applicable to nacelle propagation where the sound wave is not normally incident upon the liner surface and the mean flow is not null (i.e. see 1.3.3 for liner impedance with grazing incident flow). In practice, the propagation is multi-modal, and each mode has its own propagation angle [3]. However, these equations permit the preliminarily design of the impedance of an acoustic liner.

The following figures show typical normalized impedance spectra of SDOF liners with a wire mesh (Figure 1.28) or with a perforate (Figure 1.29) face sheet. In the figures, the impedances are calculated for 130 dB pressure level at the liner surface and for frequencies ranging from 500 Hz to 5000 Hz, for a normally incident sound wave in the absence of mean flow.

An acoustic liner with a wire mesh face sheet is usually labelled as linear, because the pressure drop is almost linearly dependent on acoustic velocity ($\Delta p = k_1 V$), with the coefficient of proportionality (k_1) known as the DC flow resistance. On the contrary, the pressure drop across SDOF liners with perforated face sheets also has a non-linear dependence on acoustic velocity ($\Delta p = k_1 V + k_2 V^2$), and may exhibit a non-linear resistance peak near resonance frequency, where acoustic velocities peak (see Figure 1.29).

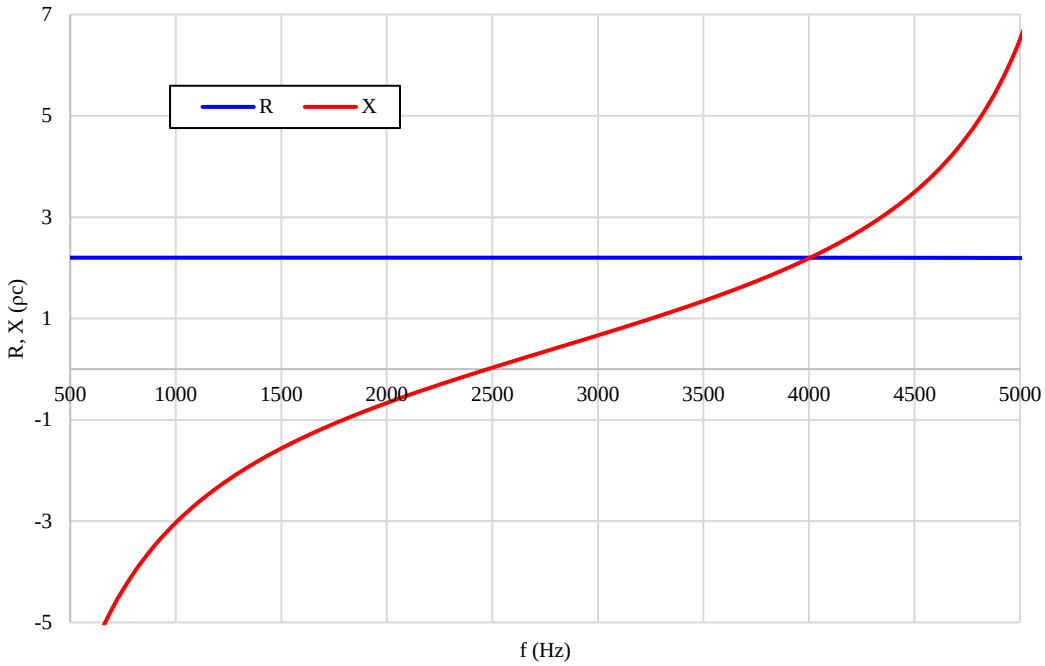

Figure 1.28. Typical normalized impedance of a linear SDOF plate at 130 dB SPL

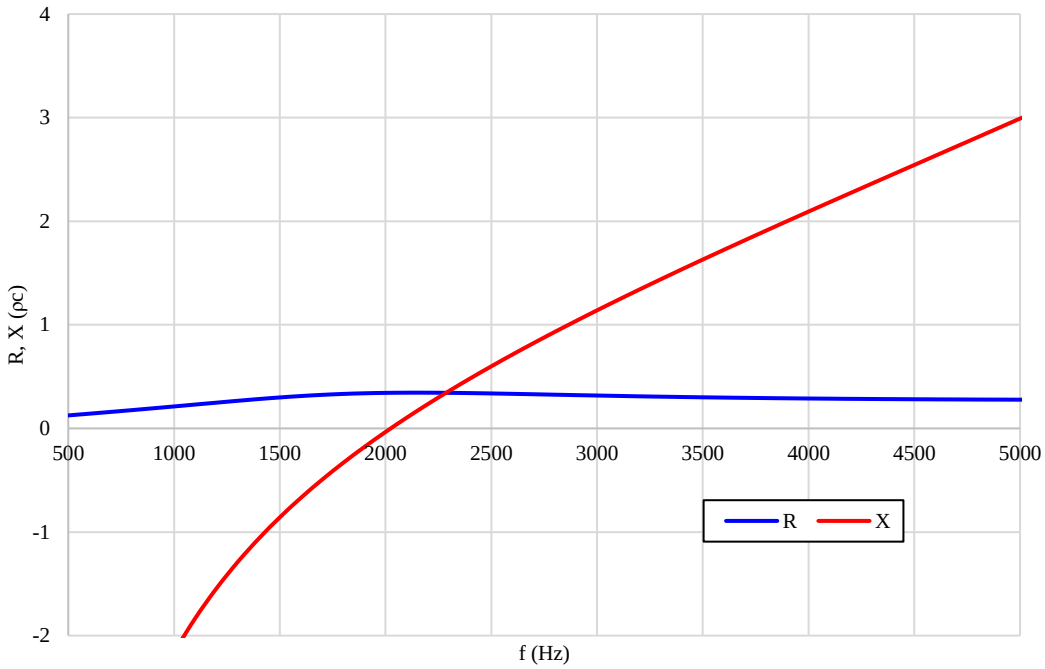

Figure 1.29. Typical normalized impedance of a perforate SDOF plate at 130 dB SPL

For two-degree-of-freedom panels, the acoustic impedance can be modelled as [16]

$$\frac{Z}{\rho c} = \frac{Z_1}{\rho c} + \frac{\frac{Z_2}{\rho c}\frac{\cos(k_1 h)\sin(kh_2)}{\sin(kh)} - i\cot(kh)}{1 + i\frac{Z_2}{\rho c}\frac{\sin(kh_1)\sin(kh_2)}{\sin(kh)}} \tag{1.18}$$

In Equation 1.18, the subscript 1 denotes the impedance of the face sheet, while the subscript 2 denotes that of the septum. These can be written as,

$$\frac{Z_1}{\rho c} = \frac{R_{fs}}{\rho c} + i\frac{X_{fs}}{\rho c} \tag{1.19}$$

$$\frac{Z_2}{\rho c} = \frac{R_{septum}}{\rho c} + i\frac{X_{septum}}{\rho c} \tag{1.20}$$

where $R_{septum}/\rho c$ is the normalized septum resistance, while $X_{septum}/\rho c$ is the normalized septum reactance.

Figure 1.30 illustrates an example of normalized impedance for a typical perforated DDOF liner. The impedance is calculated for 130 dB sound pressure level at the liner surface and in the frequency range between 1000 Hz and 5000 Hz, in the absence of mean flow and for a normally incident sound wave.

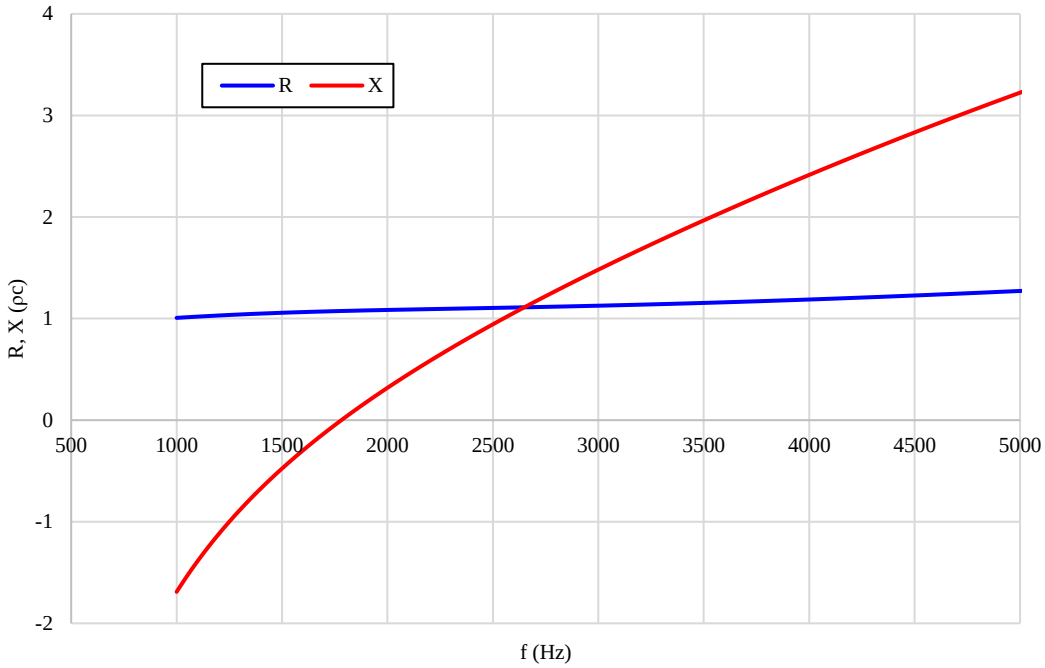

Figure 1.30. Typical normalized impedance of a DDOF liner at 130 dB source SPL

In DDOF liners, even with the use of perforate face sheets, linear properties can be approached (see Figure 1.30) because the septum controls most of the effective acoustic resistance of the panel. The linear properties of the DDOF liner are emphasised as the septum is designed to have almost linear acoustic properties. Septum linearity can be approached by using a perforated sheet with very small holes or by using a wire mesh.

1.3.1 Resistance and reactance of the face sheet

The resistance of a face sheet in the absence of mean flow (and the resistance of a septum) can be described by the following relation [16]

$$\frac{R}{\rho c} = A + BV \tag{1.21}$$

In Equation 1.21, A and B are constant values determined experimentally (see 2.1.2) and V is the acoustic velocity. The figure below illustrates a typical resistance-velocity curve of a perforate SDOF liner, for increasing pure tone SPLs, with a normally incident acoustic wave, and in the absence of mean flow.

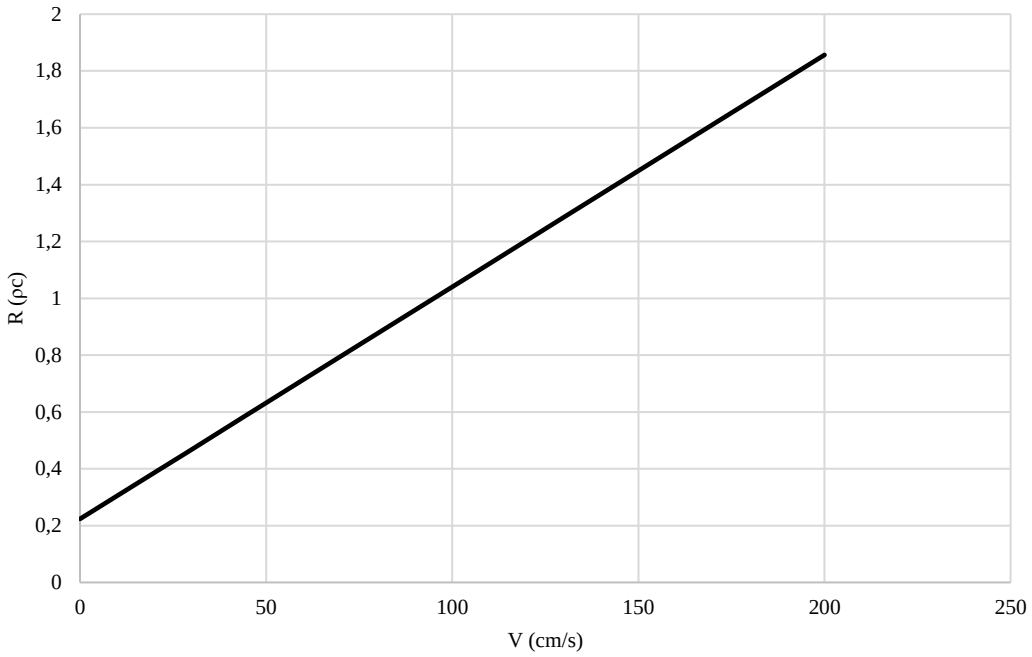

Figure 1.31. Typical R-V curve of a perforate SDOF plate at increasing pure tone SPL

In Equation 1.21, A represents the linear component of the resistance, while BV represents the non-linear component. The existence of the velocity-dependent term shows that the resistance a function of the pressure amplitude of the incident wave. In general, in wire mesh materials, the value of BV is low, and the resistive layer has predominantly a linear behaviour. On the contrary, for traditional perforated panels with hole diameters in the region of 1 mm, the value of A is negligible and the resistance is dominated by the term BV. The acoustic behaviour is essentially non-linear, and it is dependent on the magnitude of the excitation pressure.

In sound-absorbing panels, the parameters A and B can be modelled from fluid mechanics, considering the mechanism that causes the difference of pressure across the face sheet. A accounts for the pressure loss within the holes due to the viscous scrubbing losses. This term is typically low for traditional perforates, and it only dominates for micro-perforates when the hole diameter d is so small that the flow through the pores is laminar (typically d < 0.1 mm). On the contrary, BV is related to the dynamic head loss due to the turbulence that occurs at the entrance and exit of the hole edges. As a result, in the case of the wire-mesh materials, the term A is prominent because the flow across the plate is mainly laminar, while in the case of ordinary perforate plates at high incident sound levels, BV dominates because the flow in the holes is turbulent [16].

In [16], the resistance parameters A and B are calculated from the ratio between the pressure drop across the sample and the acoustic velocity V incident on the liner surface. The ratio of the pressure drop Δp across the face sheet to the air dynamic pressure q within the hole is given by:

$$\frac{\Delta p}{q} = \frac{Ft}{d} + K_i + K_e \tag{1.22}$$

In Equation 1.22, t is the thickness of the face sheet, d is the hole diameter, K_i and K_e are respectively the dimensionless entrance and exit loss coefficients. For commercially available perforate materials, experience has shown

that $K_i + K_e \approx 1$ as a first approximation. In the equation above, F is the friction factor for the pipe flow and it is defined as

$$F = \frac{a}{Re} = \frac{a\mu}{\rho V_h d} \tag{1.23}$$

where a is a dimensionless proportionality constant ($a = 64$), Re the Reynolds number, μ is the dynamic viscosity of the air, ρ is the air density, and V_h is the velocity in the orifice. The velocity within the orifice is used to calculate the dynamic pressure $q = \frac{1}{2}\rho V_h^2$. It is related to the incident acoustic velocity V according to the following relation.

$$V_h = \frac{V}{C_D \sigma} \tag{1.24}$$

As it will be discussed later, V_h represents the acoustic velocity in the vena contracta of the hole (see Figure 1.32), that is the region where the irrotational flow field is confined. The vena contracta is smaller than the theoretically available cross-sectional area of the hole. The contraction of the irrotational flow field is accounted for by the term C_D, that is the dimensionless orifice discharge coefficient, usually approximated by $C_D = 0.76$ [20]. This corresponds to the ratio of the cross-section area of the hole where the flow-field is irrotational S_{vena}, to the original cross-section area of the hole S_{hole}, and it is given by,

$$C_D = S_{vena}/S_{hole} \tag{1.25}$$

In Equation 1.24, σ is the porosity of the liner surface, and corresponds to the hole area across the liner surface. In the case of a perforate plate with n circular holes per unit of area, σ is given by:

$$\sigma = \frac{n\pi d^2}{4} \tag{1.26}$$

σ is more commonly normalized by the area of the liner surface S and, in the normalized version, it corresponds to the fraction of the hole area across the liner surface. It is usually expressed in terms of the percentage open area $POA = 100\sigma$.

Substituting Eqs.1.23-1.26 in Equation 1.22 and solving for $\Delta p/\rho c V$, the normalized resistance is given by

$$\frac{R}{\rho c} = \frac{\Delta p}{\rho c V} = \frac{a\mu t}{2\rho c(\sigma C_D)d^2} + \frac{K_i + K_e}{2c(\sigma C_D)^2} V \tag{1.27}$$

Comparing the terms of Equation 1.27 to the terms of the Equation 1.21, A and B are extracted:

$$A = \frac{a\mu t}{2\rho c(\sigma C_D)d^2} \tag{1.28}$$

$$B = \frac{K_i + K_e}{2c(\sigma C_D)^2} \tag{1.29}$$

The above relations clarify that A depends on both the temperature (through c, μ ad ρ) and the pressure of air (through ρ), while B depends only on the temperature (through c). It should be noted that the values of a, C_D, and $K_i + K_e$ may change with the material type of face sheet (or septum), being a wire mesh or a perforate plate.

As far as the face sheet reactance X_{fs} is concerned, this is given by,

$$\frac{X_{fs}}{\rho c} = \frac{k(t + \epsilon d)}{\sigma} \tag{1.30}$$

In Equation 1.30, ϵ is the dimensionless end correction, and it depends on the type of face sheet (or septum) material. Early literature suggests that the end correction can be approximated using $\epsilon = 0.85$ or by a function dependent on the plate porosity σ, $\epsilon = 0.85\left(1 - 0.7\sqrt{\sigma}\right)$. However, as will be discussed in 2.1.3, ϵ can depend both on the sound pressure level SPL and the wave frequency f.

For the sake of brevity, the normalized impedance $Z/\rho c$, and its real, $R/\rho c$, and imaginary, $X/\rho c$, parts will be hereinafter simply indicated as Z, R, and X.

1.3.2 Physics of the sound absorption mechanism

Panel impedance is the key parameter to use in the design of the sound absorption performance of a liner. It depends on many factors, such as the sound wave frequency, the pressure magnitude, or the liner geometry. Its real component, the resistance, is a measure of the forces that dissipate the acoustic energy within the panel. Its imaginary part, the reactance, accounts for the oscillation of air across the panel and it determines the frequencies for which the energy conversion process is optimal.

A general comprehension of the physics that rules the sound absorption in acoustic liners passes through the description of the sound absorption mechanism of a Helmholtz resonator. Locally reactive acoustic liners, in fact, act like arrays of Helmholtz resonators [21]. Furthermore, the mutual interaction between the resonators can be implicitly neglected if each resonator is sufficiently far from the resonators nearby. In this way, the micro-fluid flow-field of a resonator perturbed by an incident sound wave can be studied in two-dimensions.

The archetypal Helmholtz resonator consists in a small opening on a rigid surface connected through a tiny pipe to an air cavity, that is terminated by a rigid plane.

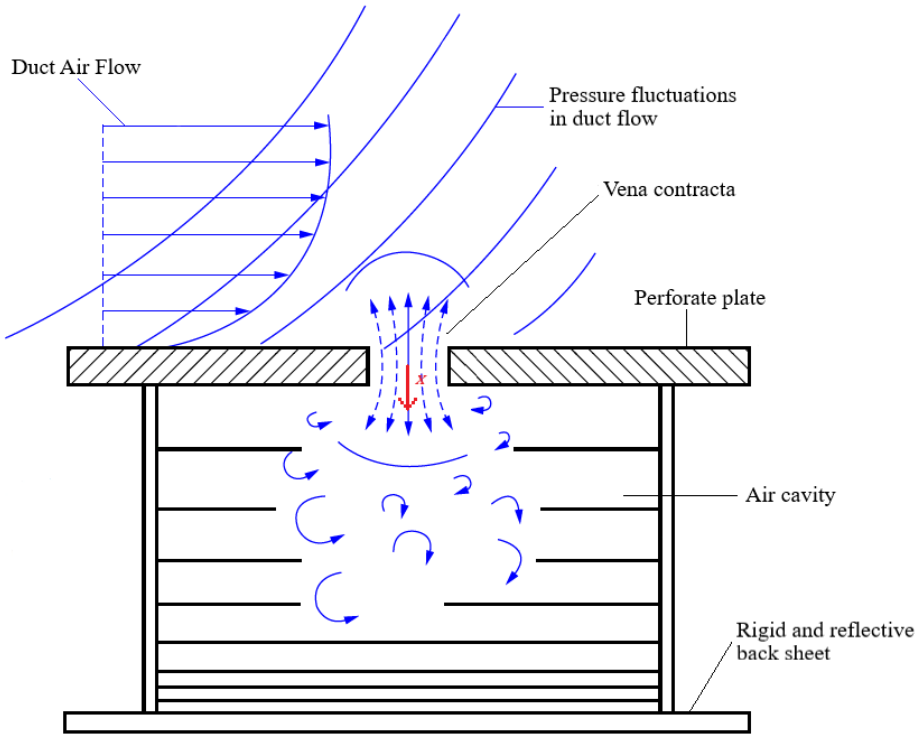

Figure 1.32. Helmholtz resonator [7]

At frequencies for which the acoustic wavelength k greatly exceeds the cavity depth h (i.e. $kd \ll 1$), the air in the cavity behaves as a spring [11]. Without any loss of generality, the impedance of the air in the cavity can be studied by supposing that a face sheet is not bonded over the Helmholtz surface, and considering a normally incident sound wave, in the absence of mean flow. In this case, the cavity is referred to quarter-wave resonator. With these hypotheses, the total pressure p in the air cavity acts along the longitudinal cavity axis $\vec{x}$ and it corresponds to the summation of the pressure $p_i = p^+ e^{-ikx}$ incident on the resonator and the pressure $p_r = p^- e^{ikx}$ reflected from the resonator termination [22]. It should be noted that the sound-wave frequency is assumed to be below the first cut-on frequency in the cavity, so that only a plane wave can propagate in the cavity. This hypothesis holds for the frequencies of interest, considering the usual axial extent of the internal partitions in a honeycomb core ($\approx 9.5\ mm$). The total pressure is given by,

$$p = p^+ e^{-ikx} + p^- e^{ikx} \tag{1.31}$$

where p^+ and p^- are the unknown magnitude of the incident and the reflected pressure. In the cavity, the incident acoustic velocity v is obtained from the Fourier transform of Equation 1.2, expressed along the axis $\vec{x}$.

$$j\omega\rho v = -\frac{\partial p}{\partial x} \tag{1.32}$$

$$v = \frac{1}{\rho c}(p^+ e^{-ikx} - p^- e^{ikx}) \tag{1.33}$$

At the reflective back sheet ($x = h$), the hard wall boundary condition is imposed ($v = 0$). With this consideration, the magnitude of the reflected pressure is obtained from Equation 1.33:

$$p^- = \frac{e^{-ikh}}{e^{ikh}} p^+ \tag{1.34}$$

Substituting p^- in Eqs.1.31-1.33, and applying the definition of the impedance (Equation 1.11), the impedance $Z_{cav}/\rho c$ of the cavity is given by,

$$\frac{Z_{cav}}{\rho c} = \frac{p^+}{p^+} \frac{e^{ikh} + e^{-ikx}}{e^{ikx} - e^{-ikx}} = -i \cot(kh) = \frac{X_{cav}}{\rho c} \tag{1.35}$$

This is consistent with the impedance of the cavity already proposed in Equation 1.14. Its resonance frequency is equal to the quarter-wave resonator frequency (see Equation 1.17).

In the presence of the perforated face sheet, the impedance of the perforate plate is added to the impedance of the cavity. In the hypotheses of a normally incidence wave, and in the absence of mean flow, the resulting impedance of the Helmholtz resonator Z_H is given by,

$$\frac{Z_H}{\rho c} = i\omega m + r - i \cot(kh) \tag{1.36}$$

In Equation 1.36, m is the equivalent mass per unit area of the air in the perforate and r is its resistive component [11]. From Equation 1.36, it follows that a Helmholtz resonator works as a mass-spring-damper system. The compliance of the system is determined by the volume of air within the cavity. The volume of air is compressible, so it can be interpreted as a spring-like effect. The force exciting the system consists of the pressure of an external sound wave, which oscillates at the level of the face sheet. In a Helmholtz resonator, both the sound absorption (i.e. the dissipation of the acoustic energy), and the acoustic velocity in the holes, reach a maximum at the resonance frequency. There, the positive inertance cancels the negative reactance and the particle displacement is in quadrature (90° out-of-phase) with respect to the acoustic velocity [11].

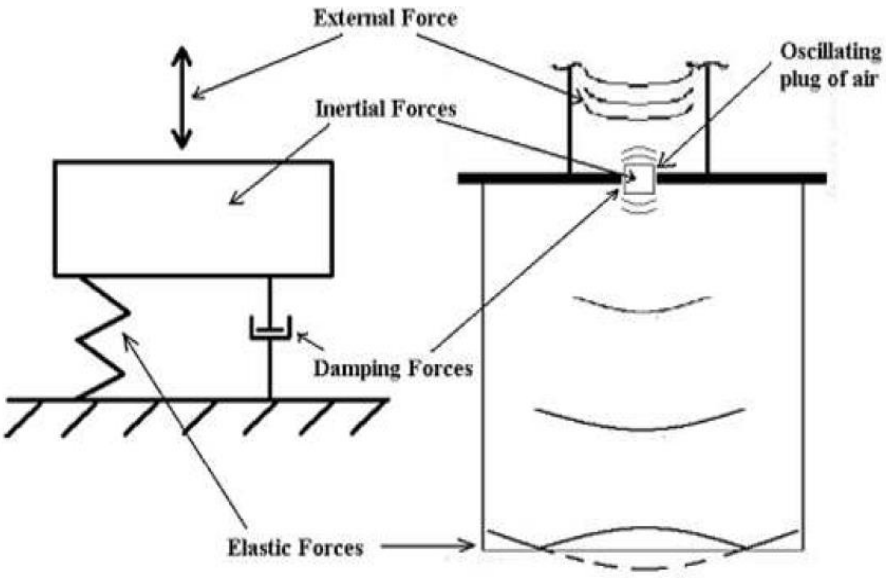

Figure 1.33. Helmholtz resonator as a mass-spring-damper system

In Equation 1.36, the inertance m of the system is related to the equivalent mass of air M in the orifice, also referred to as the neck of the resonator. The equivalent mass of air can be expressed as $M = \rho SL$, where ρ is the air density,

S is the open area of the orifice, and L is the effective length of the neck. The effective length of the neck is defined as $L = t + \epsilon d$ and it is given by the summation of the plate thickness t, plus the product of the factor ϵ and the orifice diameter d. As indicated earlier, ϵ can be firstly approximated as $\epsilon = 0.85$, but it can also be expressed as a function of the plate porosity σ or as a function of the acoustic velocity and the sound wave frequency (see 1.3.1).

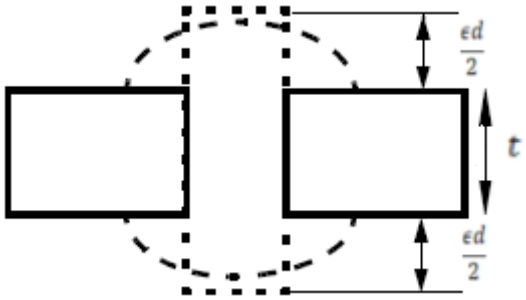

Figure 1.34. Equivalent mass of air m affected at the opening of the resonator during the oscillation [23]

In Equation 1.36, the resistance r represents the damping caused by the hole friction within the orifice and the creation of vortices from the mouth of the resonator, when the flow is excited at a high-intensity pressure level. Depending on the sound-pressure level and the source frequency [24], a Helmholtz resonator (i.e. an array of resonators) can behave either linearly or non-linearly.

In the linear regime, the flow field within the opening is assumed to be laminar. Due to the viscosity, a boundary layer is developed on the hole walls, and laminar flow propagates in the hole cross-section along the face sheet thickness. The dissipation mechanism comes about because of the viscous scrubbing losses that occur in the boundary layer.

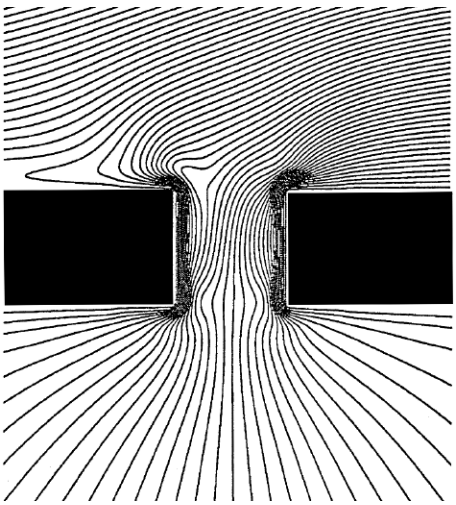

Figure 1.35. Instantaneous streamline pattern at the mouth of the resonator in linear regime. 120 dB pure tone test at 3000 Hz, in the absence of mean flow and sound incidence $\phi = 30°$ [24]

In the non-linear regime, at high sound pressure levels and near resonance, vortices are shed from the corners of the resonator mouth. Each vortex carries with it a certain amount of kinetic energy, that arises originally from the acoustic energy of the incident sound wave. The kinetic energy cannot be converted back into acoustic energy, and it is dissipated into heat through viscosity. Provided that the size of the resonator is much smaller than the acoustic wavelength, the vortex shedding is not sensitive to the direction of the sound wave and the dissipation

mechanism is weakly dependent on the angle of incidence. Vortex shedding occurs only at an incident pressure magnitude above a certain critical value (typically $\geq \sim 130\ dB$, depending on the POA) and only over a relatively narrow frequency band, centred around the resonance. In the absence of mean flow, this band depends on the geometry of the resonator. However, also far from this band, the dissipation due to the vortex shedding mechanism is more prominent than the unsteady oscillating shear mechanism of the linear regime. The shedding of the vortices is, in fact, the most significant contribution to energy dissipation at high SPLs, while the viscous scrubbing losses has a much reduced contribution [24].

The previous considerations clarify that the velocity field within and outside the resonator mouth may be separated into an irrotational and a solenoidal component [20]. It should be noted that the boundary layer and the vortex shed from the resonator opening contracts the irrotational flow field in the hole, within the so-called vena contracta. As stated above, the presence of the vena contracta is accounted for using the discharge coefficient C_D. It is recalled that the discharge coefficient is the ratio of the jet-core cross-section area S_{vena} to the area of the opening S_{hole} ($C_D = S_{vena}/S_{hole}$). In literature [16] [23], C_D is usually approximated with the constant value $C_D = 0.76$, but recent studies have shown its dependency also on the sound frequency [25] [26]. Further details are discussed in 2.1.3.

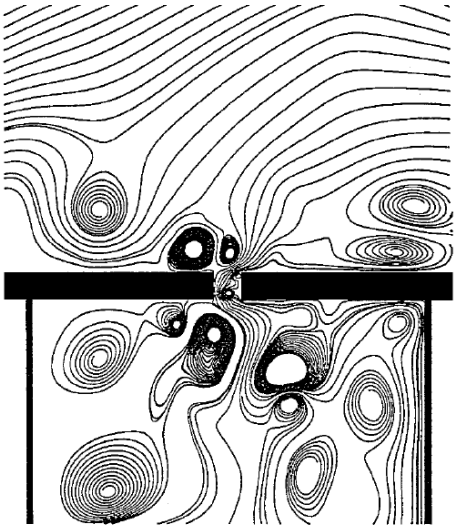

Figure 1.36. Instantaneous streamline pattern showing the shedding of vortices at the mouth of the resonator. 150 dB pure tone test at 3000 Hz, in the absence of mean flow and sound incidence $\phi = 30\,°$ [24]

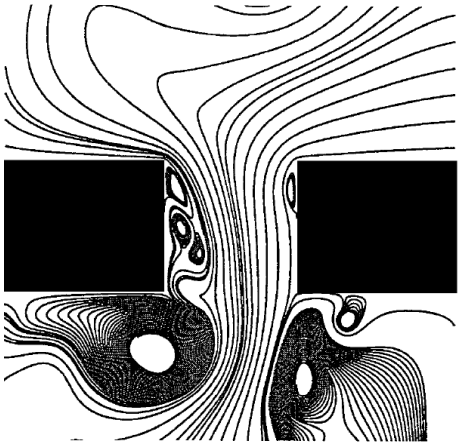

Figure 1.37. Instantaneous streamline pattern showing the shedding of vortices at the mouth of the resonator. 150 dB pure tone test at 3000 Hz, in the absence of mean flow and sound incidence $\phi = 30\,°$. Detail of the openings [24]

1.3.3 The effect of grazing flow on the liner sound absorption performance

In the presence of a mean flow, the acoustical shed vorticity at the mouth of a Helmholtz resonator is swept away by the presence of the outside flow. A vortex sheet is established from the edges of the resonator mouth outside the hole (see Figure 1.38), and some of the acoustic energy of the incident sound wave is transferred into the vortex sheet, where it is eventually dissipated into heat. The acoustic velocity in the resonator neck is greatly reduced at low SPLs, so the non-linear mechanism in the hole is not significant. The latter contribution to acoustic energy losses becomes significant at very high acoustic amplitudes near resonance (see Figure 1.39). However, in the

presence of mean flow, the sound absorption can be significant also in the case of modest levels of excitation and it occurs over a wider frequency range than in the absence of mean flow [27].

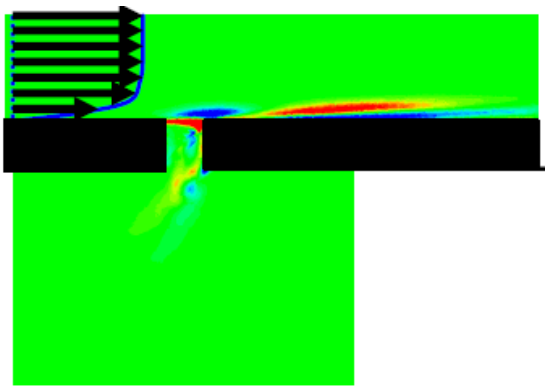

Figure 1.38. Grazing flow effect at low sound pressure level [22]

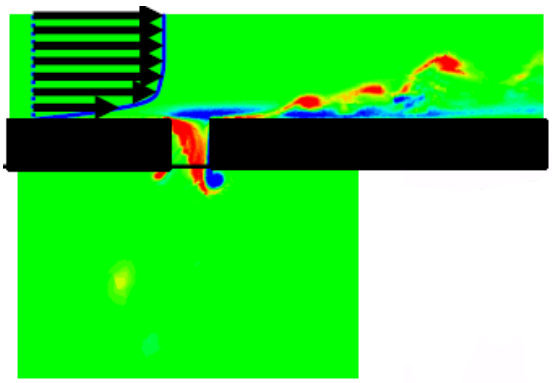

Figure 1.39. Grazing flow+non-linear effects at high sound pressure level [22]

As a result, the presence of grazing flow alters the impedance of the treatment. [28] has shown that the flow induces a change in the impedance that is mainly related to the boundary layer skin friction velocity V^*, rather than the mean flow Mach number. V^* is defined as [28],

$$V^* = \sqrt{\frac{\tau_w}{\rho_w}} = \sqrt{\frac{c_f}{2}} V_e \tag{1.37}$$

where τ_w is the local shear stress at the wall, ρ_w is the fluid density at the wall, c_f the skin friction coefficient and V_e the local velocity at the outer edge of the boundary layer. The skin friction velocity V^* provides a representation of the energy in the grazing flow in the vicinity of the perforate holes, and it accounts for the shape of the boundary layer [25]. For a given mean flow Mach number, as the skin friction velocity is reduced, the resistance of the panel decreases, while the reactance of the panel increases.

In [25], a semi-empirical model is provided for a perforate SDOF liner, accounting for the mean flow, the panel geometry, and the incident sound source features. The semi-empirical model was developed from experimental results and using the Mach number as a correlating parameter.

The normalized resistance was modelled as

$$R = R_{vis} + R_{gf} + R_{nl} \tag{1.38}$$

where R_{vis} is the resistance of the viscous losses, R_{gf} is the resistance due to the linear grazing flow, and R_{nl} is the resistance due to non-linear losses. They can be expressed as,

$$R_{vis} = \frac{k_1 \mu t}{\rho c (\sigma C_D) d^2} \tag{1.39}$$

$$R_{gf} = \frac{k_2 M \left[5 - \left(\frac{t}{d}\right)\right]}{4\sigma} - \frac{k_3 df}{\sigma c} \tag{1.40}$$

$$R_{nl} = \frac{k_4 (1 - \sigma^2)}{2c(\sigma C_D)^2} V \tag{1.41}$$

Where k_i, for $i = 1{,}4$ are empirical constants. The linear R_{vis} and non-linear R_{nl} contributions of the resistance are comparable to the terms of the resistance in the absence of mean flow (see Equation 1.27). On the contrary, R_{gf} accounts for the additional grazing flow resistance, that increases with increasing flow Mach number (or skin friction velocity if this quantity is known) and decreases with increasing frequency. As a result, the presence of grazing flow adds a resistance contribution that varies with flow velocity and frequency. The vortex shedding is strongest at or below the resonance frequency [29]. In the presence of grazing flow, R_{gf} is normally the dominant term of the resistance at the test SPL, even though the non-linear component R_{nl} remains significant at high SPL, for highly non-linear SDOF perforate panels.

As far as the normalized reactance is concerned, this was modelled as,

$$X = X_{fs} + X_{cav} \tag{1.42}$$

where X_{fs} and X_{cav} are defined as,

$$X_{fs} = k\frac{t + \epsilon d}{\sigma} \tag{1.43}$$

$$X_{cav} = -\cot(kh) \tag{1.44}$$

In Equation 1.43, the dimensionless parameter ϵ accounts for the flow Mach number dependency and is defined as,

$$\epsilon = \frac{0.85\left(1 - 0.7\sqrt{\sigma}\right)}{1 + 200M^3} \tag{1.45}$$

As in the case of the resistance, the face sheet and cavity reactance contributions do not differ greatly from the definitions provided respectively in Equation 1.14 and in Equation 1.30 in the absence of mean flow. However, ϵ includes a correction for the effect of the flow Mach number (see Equation 1.45). This correction makes the reactance decrease as the grazing flow Mach number increases, so the resonance consequently moves towards higher frequencies.

Figure 1.40 ($M = 0$) and Figure 1.41 ($M = 0.3$) show how the total panel impedance is affected by the presence of grazing flow at an incident pure tone SPL of 155dB. The resistance is most greatly affected, with a large additional linear component. However, the non-linear resistance component remains significant. Figure 1.42 shows how the liner response changes with increasing flow Mach number. The resistance increases with increasing Mach number due to the increasing skin friction velocity, while the mass reactance is progressively reduced, leading to increasing resonance frequencies.

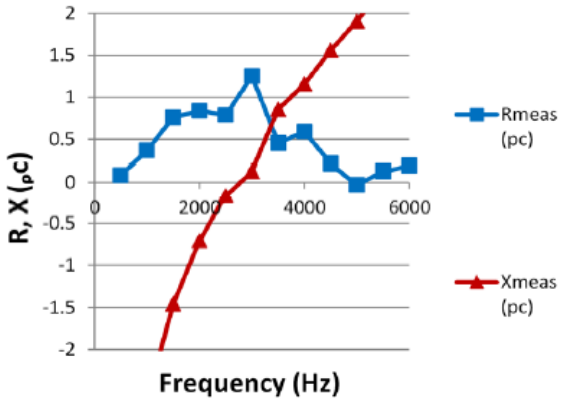

Figure 1.40. Measured in-situ impedance of a SDOF perforate liner (medium POA). 155 dB pure tone test at M=0 and grazing incidence [25].

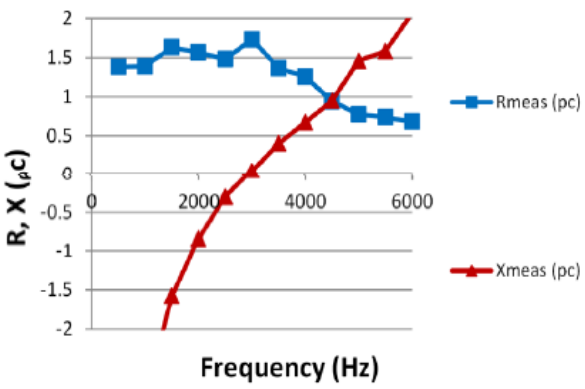

Figure 1.41. Measured in-situ impedance of a SDOF perforate liner (medium POA). 155 dB pure tone test at M=0.3 and grazing incidence [25].

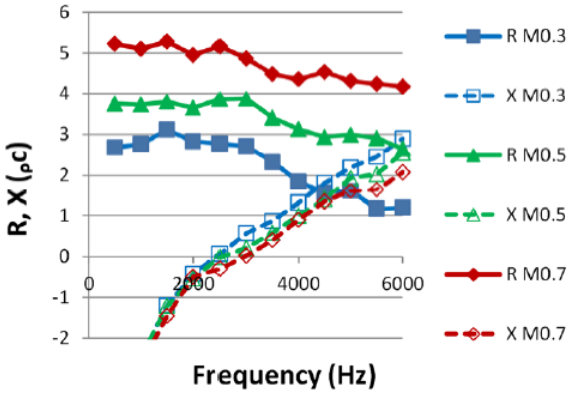

Figure 1.42. Measured in-situ impedance of a SDOF perforate liner (low POA). Pure tone tests at increasing Mach number (M=0.3, M=0.5, M=0.7) and grazing incidence [25].

Figure 1.43 shows a comparison between the predictions of the impedance model proposed in [25] with measurements at Mach 0.3, under high (non-linear) pure tone SPLs which necessarily vary with frequency for the installed speakers. The model is shown to be able to capture the rapidly changing impedance with both frequency and SPL.

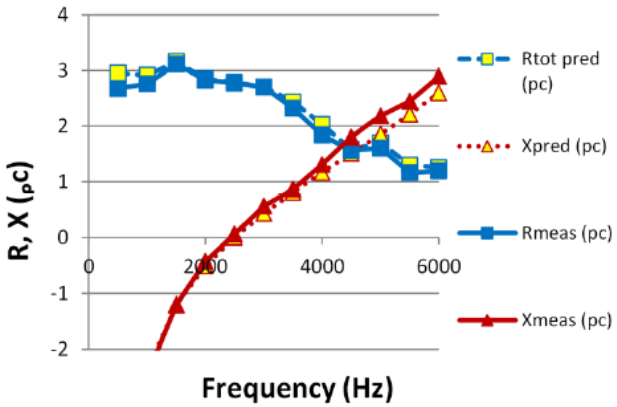

Figure 1.43. Low POA SDOF, in-situ impedance, prediction vs measurement, M = 0.3, maximum realisable Pure Tone SPL

1.3.4 The sound absorption coefficient α

The sound absorption performance of acoustic treatment is expressed conventionally using the sound absorption coefficient α. This is defined by the ratio of the sound power intensity absorbed by the panel to the sound power intensity carried by the incident wave. On the basis of the locally reactive model, a general expression of α may be derived in terms of the resistance and the reactance of the panel. As a consequence, this expression can include the dependency of α on the angle ϕ of the incident plane wave and on the flow Mach number M. As discussed in 1.3.3, in fact, the variation of the resistance and the reactance of an acoustic panel can be expressed in terms of the flow Mach number M, in addition to the sound frequency f.

Without loss of generality, α can be calculated for a given sound-absorbing panel of infinite plane surface [11].

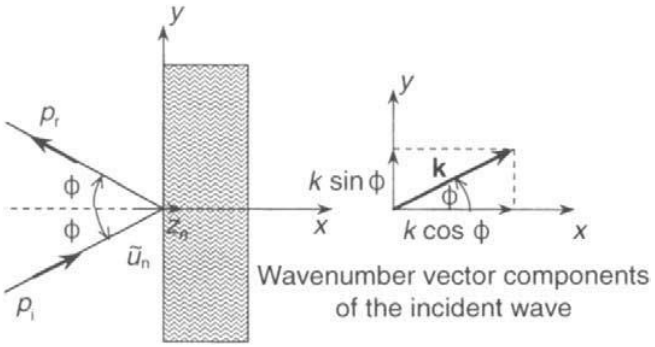

Figure 1.44. Incidence of a plane wave on an infinite plane surface of uniform impedance [11]

Referring to the figure above, the pressures in the incident p_i and reflected p_r waves are expressed as

$$p_i = p^+ e^{j(-k_x x - k_y y)} e^{j\omega t} \tag{1.46}$$

$$p_r = p^- e^{j(k_x x - k_y y)} e^{j\omega t} \tag{1.47}$$

where p^+ and p^- are the magnitude of the incident and the reflected wave, $\omega = 2\pi f$ is the circular frequency and $k_x = k\cos\phi$ and $k_y = k\sin\phi$ are the wavenumber components of the incident wave along the direction x and y. At the surface plane, $x = 0$, the total pressure p and the normal component of the acoustic velocity $\vec{v}\cdot\vec{n}$ are

$$p = (p_i + p_r)|_{x=0} = (p^+ + p^-)\, e_y^{-jk_y y} \tag{1.48}$$

$$\vec{v}\cdot\vec{n} = (\overrightarrow{v_i}\cdot\vec{n} + \overrightarrow{v_r}\cdot\vec{n})|_{x=0} = \frac{(p^+ - p^-)\cos\phi}{\rho c} e_y^{-jk_y y} \tag{1.49}$$

Substituting Eqs.1.48-1.49 into Equation 1.11 defining the impedance, Z, the ratio between the magnitude of the incident and the reflected wave is given by:

$$\frac{p^+}{p^-} = \frac{Z\cos\phi - 1}{Z\cos\phi + 1} \tag{1.50}$$

The sound power incident per unit of area I_i is given by the component of the incident intensity, normal to the wall. This is defined as [11]:

$$I_i = \frac{1}{2}|p^+|^2 \frac{\cos\phi}{\rho c} \tag{1.51}$$

The reflected power per unit of area I_r is given by [11]:

$$I_r = \frac{1}{2}|p^-|^2 \frac{\cos\phi}{\rho c} \tag{1.52}$$

Therefore, the sound absorption coefficient can be calculated as

$$\alpha = \frac{I_i - I_r}{I_i} = 1 - \left|\frac{p^-}{p^+}\right|^2 = \frac{4R(f,M)\cos\phi}{(1+R(f,M)\cos\phi)^2 + (X(f,M)\cos\phi)^2} \tag{1.53}$$

where $R = R(f,M)$ is the panel resistance and $X = X(f,M)$ is the panel reactance.

The sound absorption coefficient is an important parameter in sound-absorbing technology. It is a unique scalar value that accounts for the influence of the overall resistance and reactance, the sound-wave frequency, the mean flow, and the acoustic wave direction, on the sound absorption performance of the acoustic liner.

Equation 1.53 is valid for wave propagation in a duct, as long as ϕ is not close to 90°. When the wave is propagating parallel to the wall, in fact, a modal analysis approach is required [16]. In the case of a plane wave propagating in the duct and with no grazing incidence, α is a maximum when $R = 1/\cos\phi$ and $X = 0$; that is, to obtain maximum absorption, the angle of incidence of the sound must be taken into account. On the contrary, in the event of many propagating modes, the best choice of R and X depends on the amount of energy in each of the modes and on the relative modal attenuation rate introduced by the acoustic panel [16].

1.3.5 Measurement of the acoustic impedance: Two Microphone Method using a Normal Impedance Tube

The impedance of an acoustic liner is typically not measured directly. This would require measurements of both the acoustic pressure and the normal component of the acoustic particle velocity at the liner surface. Hence, impedance must be calculated using measures of other acoustic parameters [14].

In the current study, the impedance has been measured using the Two Microphone Method (TMM) with a Brüel and Kjaer (B&K) Normal Impedance Tube (NIT) with a flanged termination (see Figure 1.46). The tube has a 29 mm diameter, whereas the flange has a 100 mm diameter. Using the NIT, the liner impedance is measured in the absence of mean flow and for a normal incidence set-up. This is not representative of the working condition of a conventional acoustic liner (non-null mean flow and non-normally incident sound wave), but its use provides an effective way to measure the surface impedance and represent an established reference for quality control [30].

The NIT can have a closed or a flanged termination (see Figure 1.45 and Figure 1.46). The former includes a holder containing the liner sample, while the latter permits non-destructive tests directly on the liner surface, which includes tests performed on liners installed in an aircraft nacelle [30]. The 29mm diameter tube is designed for non-destructive testing, with maximum accuracy between 2KHz and 4KHz, and good accuracy between 1KHz and 5KHz, with accuracy increasing for liners with resonance frequencies within these frequency intervals. The flanged NIT typically suffers somewhat from reduced accuracy and repeatability at low frequency due to the use of a flange, especially when operated on perforated SDOF liners with low absorption at low frequencies (this aspect will be widely investigated in Chapter 2).

The use of the Two Microphone Method with a sample holder has been standardized by ISO [31] and this method is widely adopted for the characterization of acoustic liner impedance. The method applies to a normal impedance tube with an impedance termination sample cut and sealed within the dimensions of the device. An acoustic driver generates a plane wave incident upon the sample. Two microphones installed along the tube wall measure the acoustic pressure inside the tube. The distance of the microphones from the sound source and from the liner surface are dictated by [31] and they must be known to a high degree of accuracy (< 0.3mm) for varying flange geometries.

As already stated, the acoustic driver generates a plane wave sound field that propagates along the longitudinal axis $\vec{x}$ and impinges on the liner surface. The impinging pressure field is combined with the reflected wave from the liner to create a standing wave pattern. Given the incident pressure $p_i = p^+ e^{jkx}$ and the reflected incident $p_r = p^- e^{-jkx}$, the total pressure of the standing wave is defined as in Equation 1.31, $p = p^+ e^{jkx} + p^- e^{-jkx}$. It is re-called that k is the wavenumber $k = 2\pi f/c$, where f is the sound frequency and c is the air speed of sound. x is the distance from the sample surface and it is defined along the direction of the longitudinal axis of the tube.

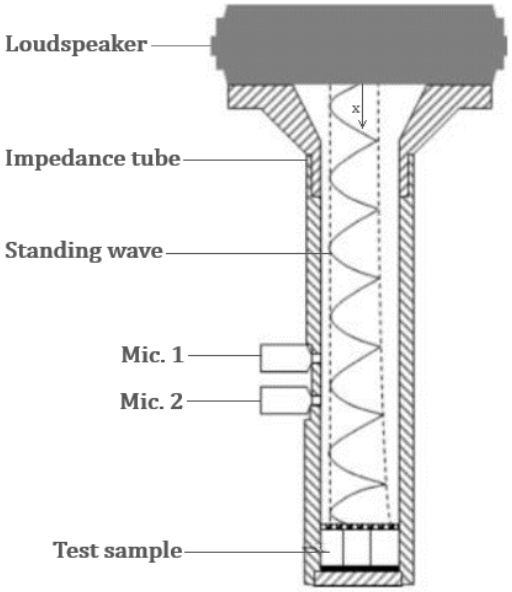

Figure 1.45. NIT with closed termination [30]

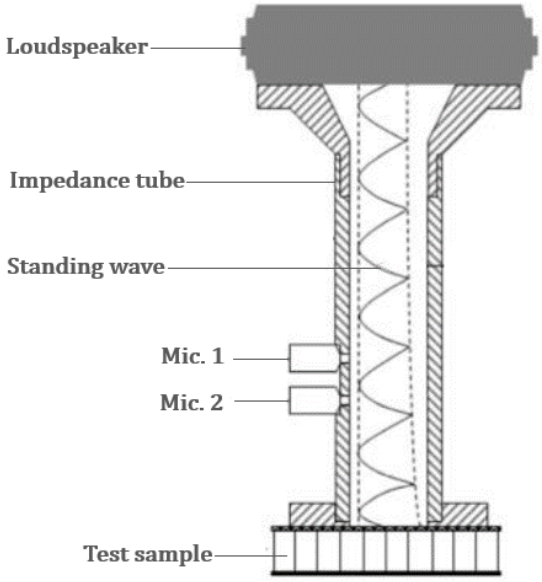

Figure 1.46. NIT with flanged termination [30]

The acoustic pressure in the tube is measured at the two microphones 1 and 2. Microphone 1 is farther than Microphone 2 from the liner surface ($x_2 > x_1$) and is distant $x_1 - x_2 = s$ from Microphone 2. The frequency transfer function H_{12} between the acoustic pressures at the Microphone 1 ($x = x_1$) and the Microphone 2 ($x = x_2$) is given by

$$H_{12} = \frac{p(x = x_2)}{p(x = x_1)} = \frac{p^+ e^{jkx_2} + p^- e^{jkx_2}}{p^+ e^{jkx_1} + p^- e^{jkx_1}} \tag{1.54}$$

The frequency transfer function H_{12} is used to calculate the complex reflection coefficient $\Gamma = \mathrm{p}^-/p^+$ on the liner surface. Solving for p^+/p^- in Equation 1.54, the complex reflection coefficient Γ is defined in terms of the transfer function between the microphones (H_{12}), the distance to the first microphone (x_1), and the distance between the microphones (s),

$$\Gamma = \frac{H_{12} - e^{-jks}}{e^{-jks} - H_{12}} e^{2jkx_1} \tag{1.55}$$

Once the complex reflection coefficient Γ is calculated, the impedance Z at the liner surface can be assessed, solving for Z in Equation 1.50 and substituting the ratio p^+/p^- with $p^+/p^- = 1/\Gamma$ (note that $\phi = 0$ in TMM using NIT):

$$Z = \frac{1 + \Gamma}{1 - \Gamma} \tag{1.56}$$

The normal sound absorption coefficient is obtained from Equation 1.53, substituting p^-/p^+ with the complex reflection coefficient Γ:

$$\alpha = 1 - |\Gamma|^2 \tag{1.57}$$

α and Γ can then be used to calculate the resistance and the reactance of the liner:

$$R = \frac{\alpha}{2\big(1 - Re(\Gamma)\big) - \alpha} \tag{1.58}$$

$$X = \frac{2\, Im(\Gamma)}{2\big(1 - Re(\Gamma)\big) - \alpha} \tag{1.59}$$

The measurements using the B&K NIT are performed by setting the Sound Pressure Level (SPL) at the liner surface. The NIT starts from an initial guess of source SPL that is then iterated until the required SPL at the liner surface is reached, therefore accounting for both the standing wave and the absorption of the test sample. The SPL is defined as,

$$SPL = 20 \log_{10}\left(\frac{p_{rms}}{p_{ref}}\right) \tag{1.60}$$

where $p_{ref} = 2 \times 10^5\ Pa$ is the reference threshold of human hearing. In Equation 1.60, p_{rms} is the root mean square of the sound pressure at a given point for a period of time T sufficiently greater than the pressure fluctuation period of the lowest frequency component of interest [26],

$$p_{rms} = \sqrt{\frac{1}{T}\int_0^T p(t)^2 dt} \tag{1.61}$$

The sound source can be tonal (i.e. pure tone), that means the frequency spectrum is set at a specific frequency, or broadband, where the source energy is spread over an extended frequency interval. If the pressure wave is composed from several frequency components, the SPL is frequently called the Overall Sound Pressure Level (OASPL). An example of the difference between results acquired using tonal and broadband sources is shown in the figures below. In this example, the impedance of a conventional perforated SDOF liner was measured with a NIT using the TMM, at the SPL at the liner surface set at 120 dB and 140 dB.

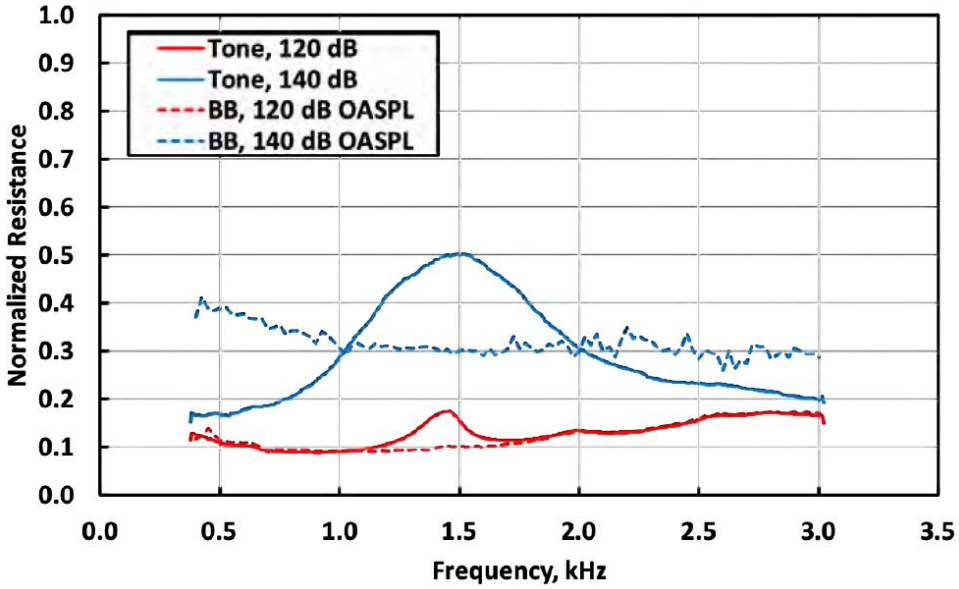

Figure 1.47. Comparison of resistance spectra for Pure Tone and Broadband (BB) sources and two SPLs [14]

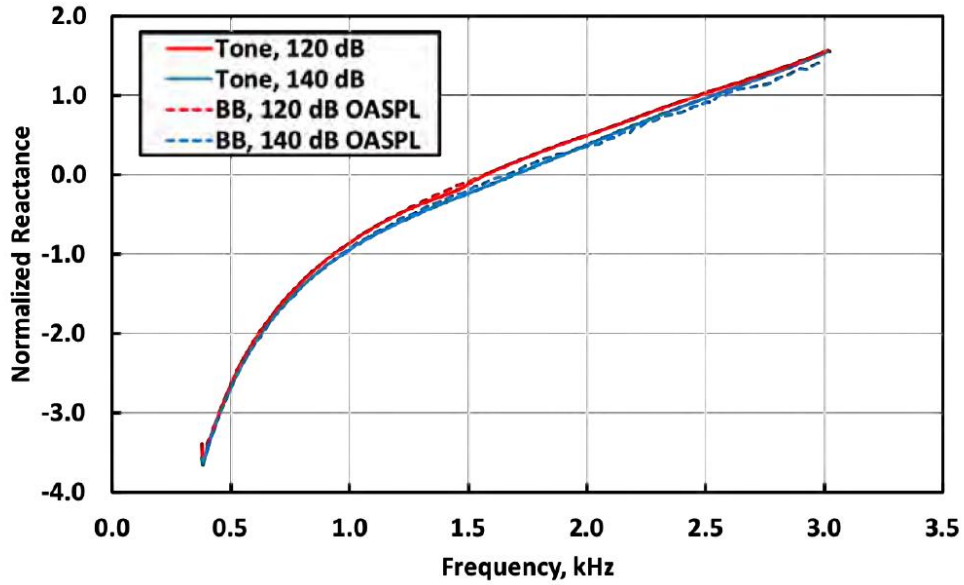

Figure 1.48. Comparison of reactance spectra for Pure Tone and Broadband (BB) sources and two SPLs [14]

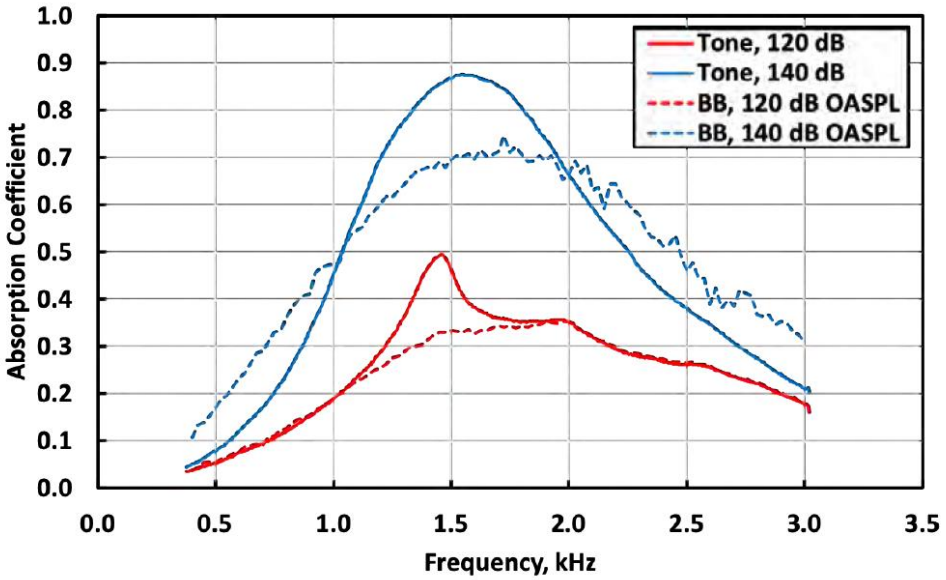

Figure 1.49. Comparison of absorption coefficient spectra for Pure Tone and Broadband (BB) sources and two SPLs [14]

The comparison of the data shows that the resistance spectra varies greatly, not only with SPL, but also with the source type. The resistance spectrum for the 120 dB tonal source compares favourably with that of the 120 dB broadband source, except near resonance. The resistance spectrum for the tonal source has a stronger peak close to resonance, with respect to the peak observed with the broadband source. On the contrary, at 140 dB, the resistance spectrum peaks at the resonance only in the case of tonal source, while it is relatively independent of frequency in the case of broadband source. In both cases, it is noted that the resistance spectrum is strongly dependent on the pressure level and the influence of the source type increases as the non-linearity of the panel arises. As far as the reactance is concerned, its frequency spectrum is only slightly affected by the source type, while it reduces with the increasing pressure level, so that it becomes slightly flatter. The increase in resistance and flattening of the reactance spectrum causes the absorption coefficient spectra to broaden with increasing source SPL [14]. It is noted that the change in non-linear response, from single pure tones, to multiple pure tones, through to a broadband source is a subject addressed in [25].

1.4 Innovative solutions of broadband acoustic liners

As widely discussed in 1.1, both fan noise and jet noise are key contributors to the propulsion noise. However, the adoption of aircraft engines with high bypass-ratios has significantly reduced the jet noise. Moreover, modifications to the fan geometry, such as the adoption of swept fan blades and the increase of the rotor-stator spacing, combined with the use of conventional narrowband acoustic liners, have significantly reduced the tonal components of fan noise radiating to the far-field [32]. As a result, broadband fan noise has become more dominant in the overall engine noise spectrum for new engine designs. Clearly, the broadband component of fan noise cannot be effectively attenuated using conventional narrowband liners. Hence, advanced liners are required, that are able to absorb sound over a wide frequency range (up to at least two but preferably more, octaves).

Furthermore, as BPR has increased, the fan diameter has become larger, and its maximum rotational speed has decreased. From an acoustic point of view, a very important consequence is that the fan noise has shifted towards lower frequencies [3]. The blade passing frequency (BPF) and its harmonics are, in fact, linearly dependent on the

fan rotation speed Ω (see Equation 1.7). In current mid-size engines (6-11 BPR), BPF is generally close to $1000\ Hz \sim 1250\ Hz$ at take-off. For the next generation of turbofan engines, with Ultra-High Bypass Ratios (15-16 BPR), it is expected that BPF at take-off will decrease well below 1KHz [3].

The future challenge is therefore to research and develop innovative configurations of acoustic liners that will improve the attenuation of broadband noise, with a particular focus on an ability to also improve sound-absorbing performance at low frequencies (< 1000 Hz). Clearly, these improvements must be developed so that they may be accommodated within the space reserved in aircraft nacelles for acoustic treatments, while limiting any possible weight penalty.

1.4.1 Broadband liners with parallel variable-depth cells and embedded mesh-caps in the honeycomb core

A preliminary study of three innovative configurations of broadband liners was performed in [32].

The first two liner concepts designed used additive manufacturing technology to create parallel-element, variable depth cells, with no face sheet bonded on the liner surface. The two liners have cavities of different widths. The first has narrow cavities (see Figure 1.50), aimed at providing significant levels of viscous losses within the cavities, potentially eliminating the requirement of a perforated face sheet. The second has wider cavities (see Figure 1.51) where the majority of the acoustic resistance is provided by a face sheet bonded on the liner surface.

Both of the two concepts have variable-depth cavities to help achieve broadband noise attenuation. Each chamber works as a quarter-wave resonator and it is tuned at a unique resonant frequency. It should be recalled that the maximum sound absorption of a liner occurs around the resonant frequency, whose definition is directly related to the depth of the cavity (see Equation 1.16 and Equation 1.17). Hence, cavities of variable depth drive the liner impedance to have different resonant frequencies. As a result, the spectral shape of the reactance is closer to zero across a broad frequency range, and the sound absorption can be enhanced over a wide frequency interval.

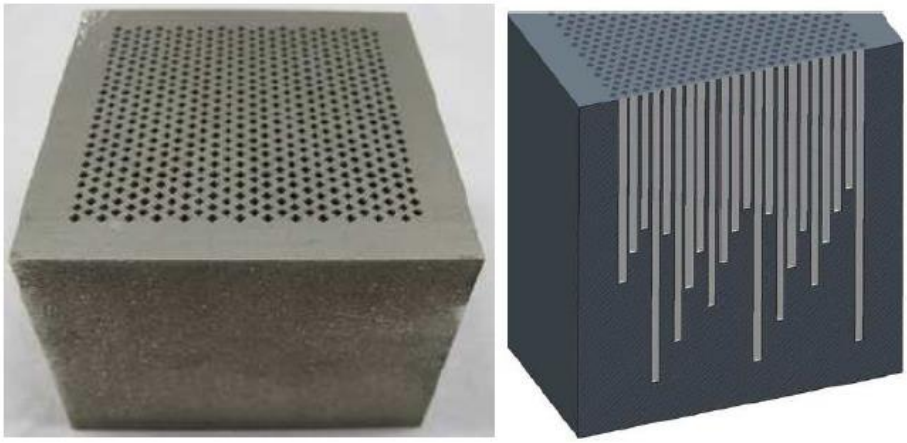

Figure 1.50. Cutaway view of variable-depth, narrow open chamber liner [32]

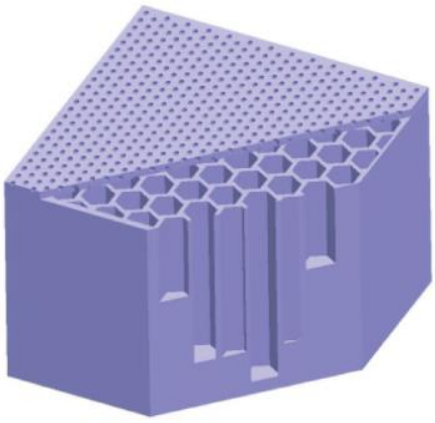

Figure 1.51. Cutaway view of variable-depth, wide-chamber liner with perforated face sheet [32]

The third liner concept developed in [32] increased the sound absorption over a wider frequency range by replacing the uniform embedded septum of the classical DDOF configuration with distinct mesh caps (resistive sheets) that can be mounted at selected heights and with prescribed resistances in each individual core chamber (see Figure 1.52).

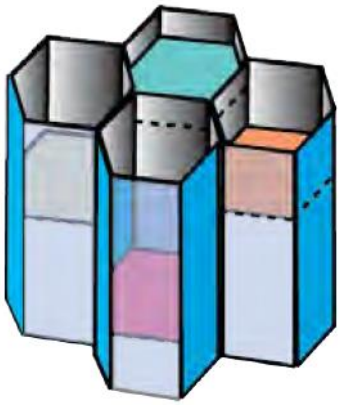

Figure 1.52. Four chambers of a liner core with embedded mesh-caps [32]

In [32], each of the three liner concepts were designed and tested in the absence of mean flow and with a normal incidence set-up. Follow-on studies investigated and optimized their features, considering grazing incidence and mean flow [33] [34] [35]. In all of these studies, the designed and the measured impedances were favourably correlated. The three configurations developed in [32] provided excellent sound absorption performance over an extended frequency range, but they are still not effective in providing sound absorption at low frequencies. In the case of the variable-depth, parallel-element liners, with core layouts designed within the adopted maximum depth of the cavities ($h_{max} \leq 80\ mm$), they were unable to realise zero reactance at frequencies lower than 1000 Hz ($f_{res} \geq c/4h_{max} \approx 1000\ Hz$). These liner concepts do not exploit the maximum space available in the core as the core volume is partially unused.

1.4.2 Skewed cells of extended depth to improve sound absorption at low frequency

As shown in 1.4.1, the main obstacle to achieve low frequency performance is the requirement for a reduced overall liner depth in order to satisfy space and weight constraints. In [36], the effective depth of a resonator

absorber was increased by skewing the resonator channel away from the usual orientation, normal to the local absorber surface (see Figure 1.53). The implementation of an appropriate bend arrangement, in addition to the skewed one, will further increase the resonator length and maximize the utilisation of available space.

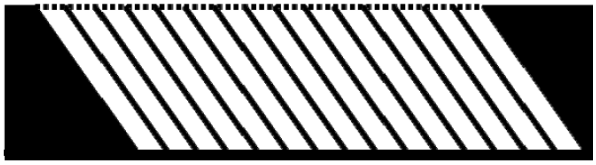

Figure 1.53. Skewed resonators packaged as a conventional liner [36]

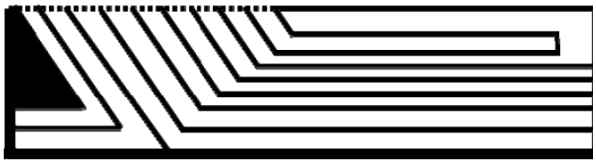

Figure 1.54. Resonator combining skew and bends [36]

The study [36] demonstrated favourable agreement between measured and the predicted impedance values. The presence of skew and sharp bends does not significantly alter the impedance of the resonator, with respect to its straight counterpart of the same depth. This liner concept drives the first resonance frequency lower than 1000 Hz ($\sim 500\ Hz$) and makes the liner have at least four resonances in the frequency range up to 3500 Hz (see Figure 1.56). It is noted that the skewed and bent resonators have an effective centreline length of $h_{cell} = 171.5\ mm$, while the overall height of the liner is about $h_{liner} = 120\ mm$. However, the liner concepts do not avoid anti-resonances (i.e. frequencies where the impedance has peaks and troughs and $R, X \to +\infty$, where the sound absorption tends to zero).

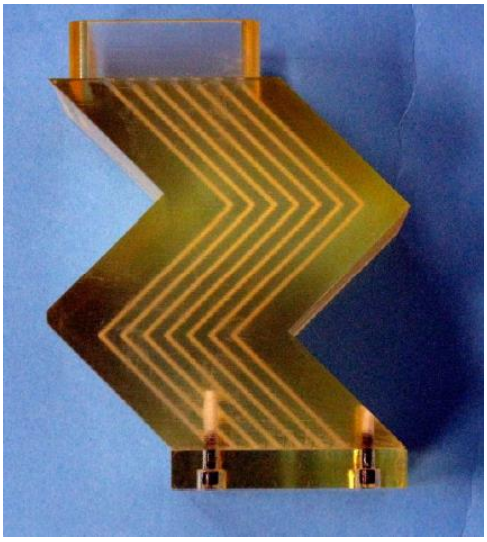

Figure 1.55. Example of liner sample designed and tested in [36], with double 90° channel bend

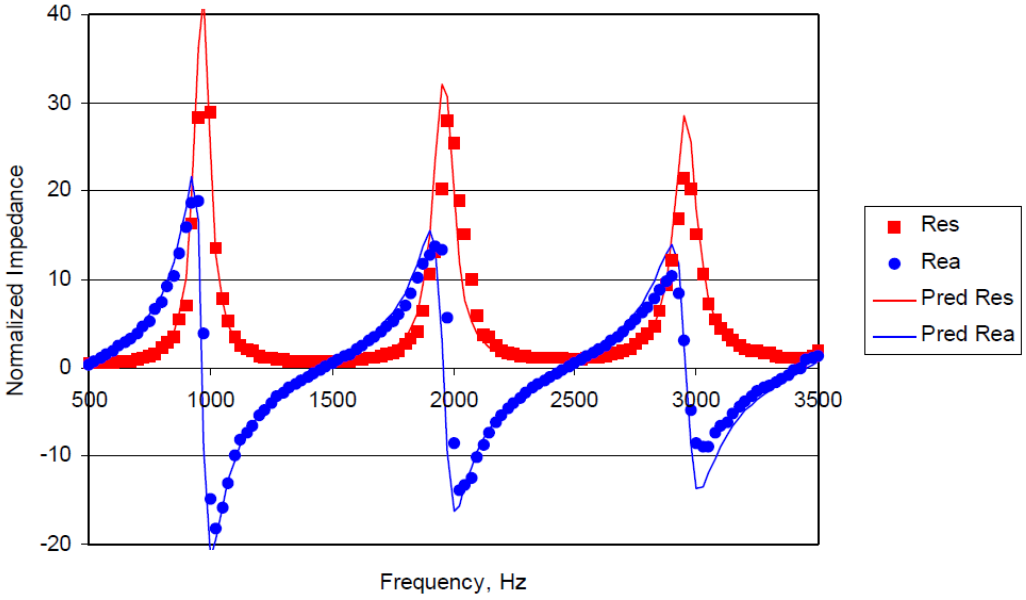

Figure 1.56. Comparison between measured and predicted impedance of the liner sample in Figure 1.55 [36].

As a consequence, the liner concept developed in [36] is effective in driving the maximum sound absorption to frequencies lower than that seen for conventional liners of the same overall depth ($h_{cell} = 171.5\ mm > h_{liner} = 120\ mm$). However, each cell has the same effective centreline length and their depths are not combined to flatten the reactance spectrum (close to zero) over a wide frequency bandwidth. Therefore, the acoustic performance of the liner concept developed in [36] does not differ greatly from that of a conventional liner with a depth $h_{liner} = 171.5\ mm$. However, this liner concept suggests that angling cavities in a liner of limited depth can drive good sound absorption at low frequencies (< 1000 Hz).

1.4.3 Folded cavities to enhance sound absorption on a wide frequency band and at low frequencies

Sugimoto et al. [6] demonstrated that an effective reduction of both the mid-high and low-frequency noise can be achieved via liners that included folded cavities. For a given overall height, folding cavities can extend the effective centreline length of the cavities with respect to conventional straight cavities. In this way, the liners can effectively reduce the low-frequency component of fan noise, while respecting space and weight constraints.

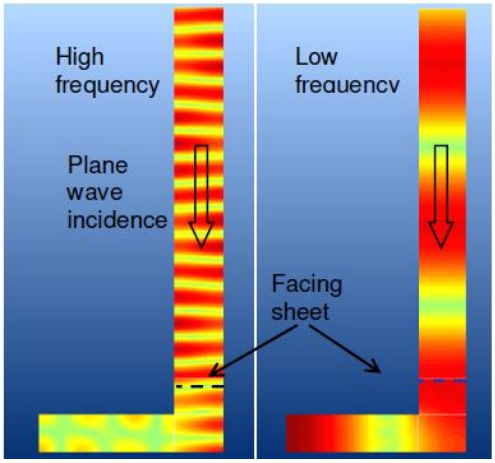

Figure 1.57. Concept of folded cavity, total pressure field for an incident sound plane wave [6]

Folding cavities makes them deeper than the overall liner depth and able to fit in a shallow space. These cavities behave like a mixture of deep and shallow cavities, with complex frequency characteristics [6]. An example of folded cavity is provided in Figure 1.57. A face sheet is bonded onto the cavity surface and the cavity is subject to an impinging plane wave. At low frequencies, the acoustic wave propagating through the face sheet turns the corner and propagates, as it does not "see" the fold. At high frequencies, the wave is mostly reflected from the fold, and it is hardly transmitted beyond the corner. Therefore, this folded cavity behaves as a deeper cavity at low frequencies, and as a shallow cavity for high frequencies. The combination of these behaviours makes the folded cavity effective in abating noise over a wide frequency range.

In [6], the favourable agreement between the predicted and the measured data confirmed the broadband sound absorption performance of this concept. Moreover, it was found that the impedance oscillations can be damped by introducing a septum of high resistance parallel to the face sheet, before the fold.

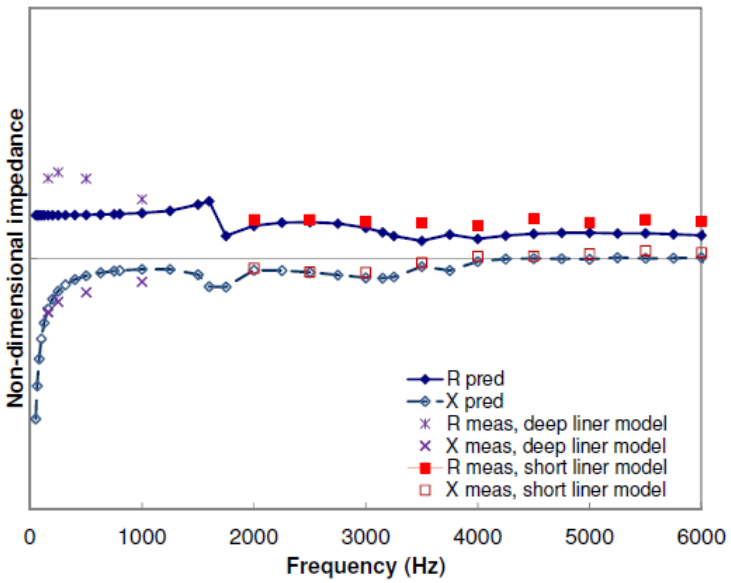

Figure 1.58. Comparison between measured and predicted impedance of the folded cavity liner in Figure 1.58 [6]

In Figure 1.58, the results of the measured and the predicted impedance of the folded-cavity liner sample are provided. The sound absorption is maximized over a wide frequency interval and at low frequency, as the reactance

is close to zero for frequencies above 400 Hz. The tested liner sample (see Figure 1.59) had an overall depth of 65 mm, and the effective centreline length was 115 mm. In the neck, it had a honeycomb core to ensure plane wave propagation in the upper layer. The results shown in Figure 1.58 were obtained for the face sheet resistance $R_{fs} = 1.0\ [\rho c] + i\ k \left[\frac{1}{m}\right] \cdot (0.002\ [m])\ \rho c$ and a septum resistance of $R_{septum} = 2.0\ \rho c$.

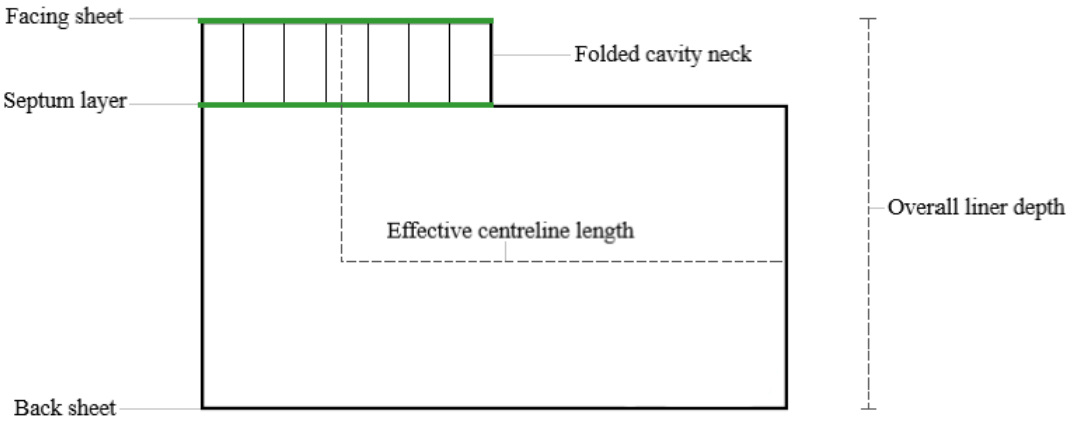

Figure 1.59. Scheme of folded cavity liner, arranged from [6]

1.4.4 Packaged folded cavity and spiral-shaped liners to abate low-frequency and broadband noise

In [37], the possibility of improving broadband low-frequency acoustic absorption performance was demonstrated by packing tuned combinations of folded cavities within a prescribed volume (see Figure 1.60). A liner of 38.1 mm overall height was used to attenuate sound below 500 Hz and the design of the core was optimized to maximise the sound absorption in the vicinity of 350 Hz.

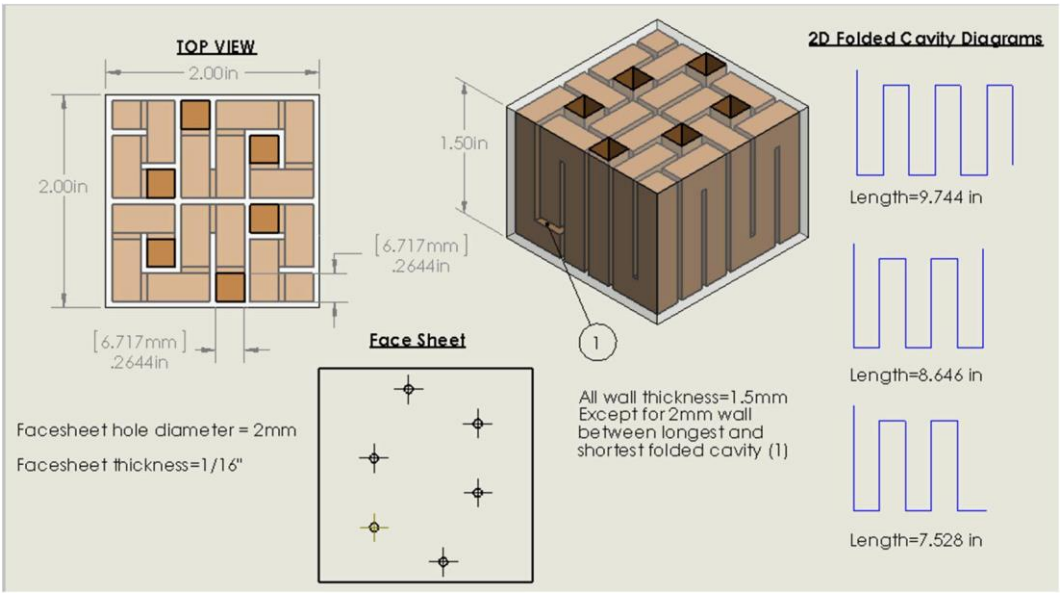

Figure 1.60. CAD drawing for the optimized 3D folded cavity liner design [37].

The optimized configuration had the folded cavities packaged to avoid the presence of unused, dead volume. The good agreement displayed between the measurements and the predictions confirmed the excellent sound absorption performance around 350 Hz, but the sound absorption is limited outside the frequency interval centred around 350 Hz (see Figure 1.61).

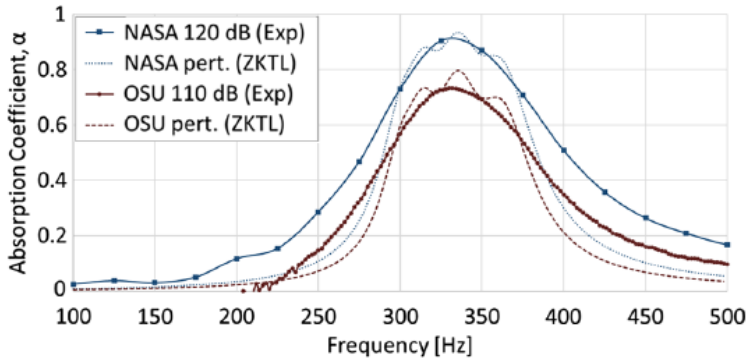

Figure 1.61. Comparison between measured and predicted sound absorption coefficient α for the optimized 3D folded cavity liner design in Figure 1.60 [37]

Apart from the liner concept in Figure 1.60, [37] also demonstrated that good absorption of broadband sound can be effectively obtained with the insertion of 3D spiral-shaped cavities of different lengths in the aluminium honeycomb core of the liner. The concept of spiral-shaped cavities derives from [3], where they were first designed. These cavities were created from a helicoidal profile, whose rotation axis is centred on the cavity cross-section and is perpendicular to the skin. In [37], five different spiral cavity lengths were placed in repeating arrays within the liner, as shown in Figure 1.62. The specific cavity lengths were chosen to distribute their resonances within the frequency band below 1000 Hz. The favourable correlation between the measured and predicted absorption demonstrated good sound absorption over a wide frequency range below 2600 Hz (see Figure 1.63). However, in this case, the overall liner depth is not used completely, so some dead volume is present. Moreover, the fabrication process of spiral-shaped cavities may create non-uniform internal wall surfaces that can deteriorate the overall sound absorption.

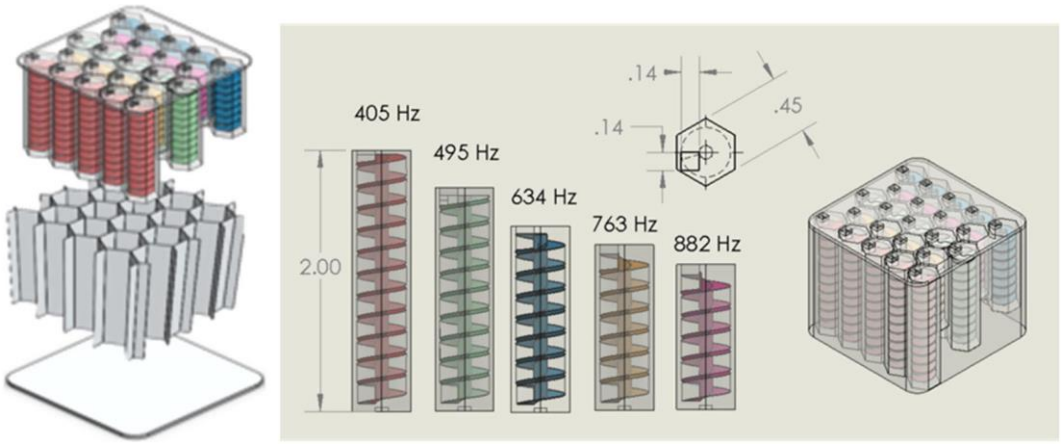

Figure 1.62. CAD drawing for the broadband spiral insert liner design [37]

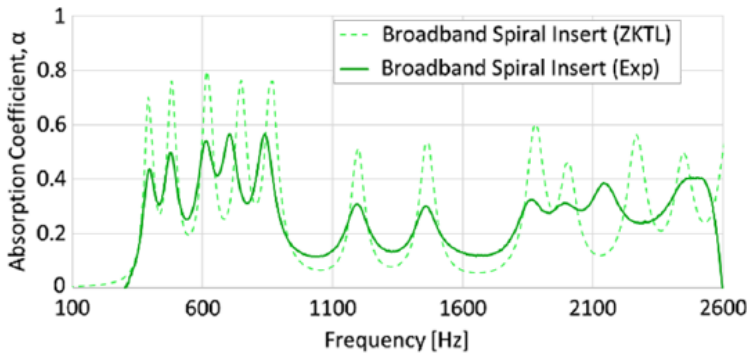

Figure 1.63. Predicted and measured sound absorption coefficient α for the broadband spiral insert liner design in Figure 1.62 [37]

1.4.5 Purpose and outline of the current thesis work

The purpose of the current thesis work is to research and develop an innovative configuration of broadband acoustic liner that can be effective in abating low-frequency noise while also respecting the conventional space and weight constraints of an aircraft nacelle. This liner concept derives from those presented in 1.4.1-1.4.4, but overcomes their main drawbacks. In 1.4.1, the liner designs drives the reactance close to zero across an extended frequency range, but the sound absorption at lower frequencies is limited. Then, in the case of liner concepts with parallel, variable-depth cavities, the core volume is not used completely. In 1.4.2, the cavities are assembled to elongate their effective centreline length, exceeding the given overall liner depth. However, their depths are not combined to improve the sound absorption over a wide frequency bandwidth. The liner design enhances the reduction of noise at lower frequencies, but does not flatten the reactance curve close to zero over a wide frequency range. In 1.4.4, the first liner design is effective in sound absorption around 350 Hz, but the acoustic performance degrades outside that frequency interval. On the contrary, the second liner design has good broadband sound absorption performance, but the cavities are not arranged to avoid dead, unused volume.

The liner concept proposed in this thesis employs both folded and straight cavities of variable depths to achieve broadband sound absorption. The cavities are packaged to avoid dead volume and maximize the space available. Moreover, the configuration is optimised to enhance sound absorption between 500 Hz and 4000 Hz, so that the liner concept can be effective in abating noise also at low frequencies. Two optimal liner configurations are proposed. The first has a typical overall depth (50 mm) adopted in current aircraft nacelle; the second has an extended overall depth (100 mm) in order to evaluate the theoretical gain in sound absorption at lower frequencies that may be obtained with deeper liners.

The acoustic proprieties of the designed broadband liners are studied using COMSOL 5.4 and their configuration is optimized in MATLAB R2019a using the Genetic Algorithm. The optimal liner configurations are then fabricated using stereolithography using the 3D printers of Leonardo Aircraft.

In Chapter 2, the ability of COMSOL to predict the measured impedance is verified through the analysis of three conventional liners, manufactured in Leonardo. Thereafter, some relevant considerations are outlined which must be accounted for in the simulation of the conventional acoustic treatments. Chapter 3 reports on the test and analysis of a preliminary sample of a broadband liner designed and 3D printed in Leonardo. Extensive numerical analysis is performed to identify the most relevant numerical techniques to adopt in the simulation of broadband

liners with complex configurations. In Chapter 4, an innovative broadband liner concept is developed, and its acoustic properties are investigated in detail, both numerically and analytically. The liner design is optimised for two liner depths, and the impedance of their scaled samples is measured and compared with predictions. Furthermore, an analytical routine is validated which may be used to study the acoustic performance of the liners with complex configurations.

2. Evaluation of the acoustic performance of conventional perforate SDOF and DDOF liners with COMSOL 5.4

The purpose of the current work is to research and develop acoustic liners with innovative configurations. These liners are designed to reduce the broadband and tonal noise generated by an aeronautical engine fan over a wide frequency bandwidth. During the last few decades, many innovative solutions have been proposed (see Chapter I) and the physics behind their acoustic properties has been studied with either commercially available software (ACTRAN-TM [6] [3], COMSOL [33] [38] [39] [40]), or in-house acoustic propagation codes (NASA CHE [33] [40], NASA CDL [33] [40] [41] [42] [34], ZKTL-based code [37] [36]). In the current work, the acoustic characteristics of broadband liners are predicted using COMSOL 5.4 (see Chapter III and Chapter IV). The COMSOL predictions are expected to compare favourably with the measured data, as previous studies [39] [40] have demonstrated. However, before developing any innovative configuration of acoustic liner, the ability of COMSOL to predict the measured impedance of a liner was verified. The COMSOL modelling has been validated through the analyses of three conventional acoustic liners, currently manufactured in Leonardo; a perforated single-degree-of-freedom liner, and two perforated double-degree-of-freedom liners. The current chapter illustrates the two-dimensional numerical models used to simulate the liners and discusses the possible sources of mismatch between the predicted and measured data in detail. The chapter finishes with a summary of the most important points to consider when conventional acoustic treatments are numerically simulated in COMSOL.

2.1 COMSOL numerical simulation of a punched aluminium SDOF liner

The two-dimensional numerical model of the SDOF liner is labelled “SDOF-PP” and is illustrated in Figure 2.1. SDOF-PP simulates a punched aluminium liner sample of $POA = 5.20$ %, plus the normal impedance tube with a closed termination. The liner impedance is measured using a normal incidence set-up following the Two Microphone Method (TMM) [31], introduced in Chapter I. Due to the proprietary nature of the study, the measurements of the liner and the NIT are not presented; however, in the progression of this paragraph, the main features of SDOF-PP are duly discussed.

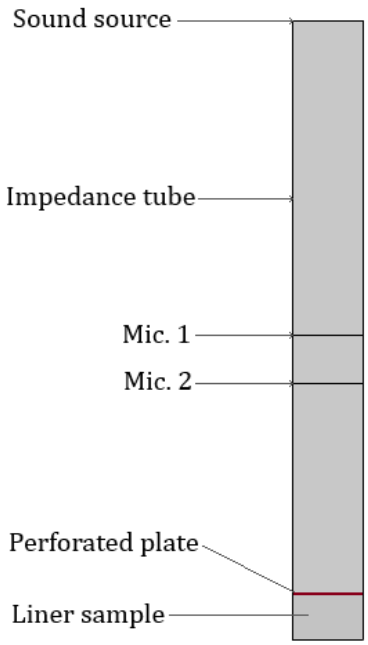

Figure 2.1. SDOF-PP

In two-dimensions, the liner sample and the NIT are modelled as rectangles, whose width coincides with the tube diameter of 29 mm. The grey regions are where the pressure acoustic field in the frequency domain is set. COMSOL solves the homogeneous Helmholtz equation, given by [23]:

$$\nabla \cdot \left(-\frac{1}{\rho}\nabla p\right) - \frac{k^2}{\rho}p = 0 \tag{2.1}$$

where ρ is the air density, p the total pressure, and k the wave number. p is given by the summation of the incident acoustic pressure p_i and reflected pressure p_r, while k is the wave number, given by $k = 2\pi f/c$, with f the source frequency, and c the speed of sound in air.

In the model, the sound source is set at the top of the tube with an amplitude of 1 Pa, simulating the acoustic drivers that produce a plane wave sound field propagating inside the NIT. In SDOF-PP, the incident plane wave travels normally along the axial tube direction and is of the type:

$$p_i(x) = p_0 e^{-ikx} \tag{2.2}$$

with p_0 the wave amplitude, and x the location on the axial direction. In the Equation 2.2, p_0 is given by

$$p_0 = p_{ref} 10^{\frac{SPL}{20}} \tag{2.3}$$

where SPL is the Sound Pressure Level and p_{ref}, equal to $2 \times 10^{-5} Pa$, is the reference threshold of human hearing. No flow is included in the simulation of the normal impedance tube.

Along the boundaries of the tube and the liner, hard wall boundary conditions are imposed. In COMSOL this boundary condition is defined from the condition of zero acoustic velocity,

$$-\vec{n} \cdot \left(-\frac{1}{\rho}\nabla p\right) = 0 \tag{2.4}$$

Finally, on the boundary between the tube and the liner, the COMSOL embedded impedance model for a thin perforate plate is introduced. This is defined as,

$$\frac{Z}{\rho c} = -Re\left(\frac{i\omega}{c\sigma C_D^{lin}}\frac{t_p + 2\delta f_{int}}{\Psi_V}\right) - i\,Im\left(\frac{i\omega}{c\sigma C_D^{lin}}\frac{t_p + 2\delta f_{int}}{\Psi_V}\right) + \frac{(1-\sigma^2)}{(\sigma C_D^{nl})^2}\frac{f_{nl}}{2c}|u_n| + \theta^{user} + i\chi^{user} \qquad (2.5)$$

In Equation 2.5, the face sheet impedance Z is normalized by the air impedance ρc. The first and the second terms are linked to the linear response of the perforated plate, the third to the nonlinear response of the resistance at high SPL. The fourth and the fifth terms are optional user-defined resistance and reactance components that can be included in the model. In SDOF-PP, θ^{user} and χ^{user} are set equal to zero.

The COMSOL model of the perforated plate impedance resembles that introduced in Chapter I and is defined by the following parameters:

- $\omega = 2\pi f$ is the circular frequency.
- c, the speed of sound.
- t_p, the thickness of the plate.
- d_h, the hole diameter.
- σ, the liner porosity, that corresponds to the hole fraction of the boundary surface area, and ranges from 0 to 1 ($\sigma = POA/100$). For a square pattern, it is defined as $\sigma = \pi d_h^2/4a^2$, with a the radius of the circular hole.
- C_D, the discharge coefficient set equal to $C_D^{lin} = 1$ for the linear part and $C_D^{nl} = 0.76$ for the nonlinear part. As introduced in Chapter I, it accounts for the ratio of actual rate of the flow through a hole to the theoretical flow.
- δ, the end correction to the resistance δ_{resist} and to the reactance δ_{react}, labelled as ϵ in previous chapter. The default built-in sets $\delta_{resist} = \delta_{react} = 4d_h/3\pi$.
- f_{int}, a dimensionless function that accounts for the influence of the porosity on the end correction. It coincides with the Fok function with eight terms and it is defined as $f_{int} = \sum_{n=0}^{8} a_n\left(\sqrt{\sigma}\right)^n$.
- Ψ_v is a geometry and material-dependent viscous function, that is linked to the acoustic impedance of a narrow waveguide, and for a circular duct of radius a is given by [23]

$$\Psi_v = -\frac{J_2(ka/2)}{J_0(ka/2)} \qquad (2.6)$$

  In Equation 2.6, J_2 and J_0 are Bessel functions of the first kind of second and zero order.

In SDOF-PP, the internal partitions are not modelled because the cavity width of conventional liners does not have a direct influence on the calculation of the liner impedance [16]. It should be noted that this hypothesis is valid while the cavity width is large enough to minimise viscous losses (as in case considered, with about 9 mm cavity width), and the honeycomb is covered by the face sheet to make the cells locally reacting.

It is noted that the normal impedance tube should ideally have a closed termination, and not a flanged termination, where, as the tube covers an uneven number of cells, there is a mismatch between the tube area and the area available for sound propagation within the liner. Hence, as shown later in 2.1.5, in a flanged normal incidence set-up, the internal partitions must be modelled to best capture the measured impedance. Although the internal partitions are not simulated in SDOF-PP, the hypothesis of a normally incident plane wave propagating across the liner

extent still holds, as the tube is narrow enough to ensure zero phase difference between cells. The maximum frequency considered in the following numerical analyses, in fact, is just above the first cut-on frequency [11] ($f_{I\,cut-on} = c/2d_{tube} \approx 6000\ Hz$, where $d_{tube} = 29\ mm$ is the tube diameter).

SDOF-PP is meshed using free quadrilateral plane elements, whose maximum element size is at least ten times smaller than the acoustic wavelength at the highest frequency of interest ($\lambda_{min} = \frac{c}{f_{max}} = \frac{345\,\frac{m}{s}}{6400\ Hz} \approx 54\ mm$). This mesh density criterion is suggested in [26] to ensure high confidence in the numerical results. It is more refined than the mesh density criterion adopted in [39], where the maximum element size is at least eight times smaller than the minimum acoustic wavelength λ_{min}.

In the current study, all of the measurements are performed with a lightweight portable NIT with a flanged termination, whose inner tube diameter is 29 mm and the flange diameter is 100 mm. As a side note, the pure tone tests are henceforth simulated numerically by iterating the SPL at the sound source until the required SPL at the liner surface is achieved. On the contrary, the "broadband" tests in COMSOL are actually a series of pure tones, simulated by setting the source pressure magnitude at a specific SPL, without any iteration to get the required SPL at the liner surface. This last procedure does not reflect how the overall SPL of the broadband source is commonly set [26] [14], but no significant error is expected in the liner response, and the results are considered valid. In the figures provided later, the tonal measurements are referred to as "PT", while the broadband measurements are referred to as "BB".

For the sake of brevity, in following paragraphs, the normalized resistance and reactance will be simply quoted as resistance and reactance, although they are normalized by the air impedance ρc.

2.1.1 SDOF liner: comparison between predicted and measured data

Figure 2.2 and Figure 2.3 provide a preliminary comparison between the predicted and the measured impedance of SDOF- PP. The numerical results are obtained by setting the source SPL at 130 dB and 150 dB, while the experimental results are measured using a 130 dB and a 150 dB OASPL broadband signal. In the numerical analysis, the impedance is calculated with the pure tone frequency source ranging between 100 Hz and 6400 Hz with a 100 Hz step, while in the broadband test the frequency source ranges from 8 Hz to 6400 Hz with 8 Hz step. It is noted that for an OASPL of, say, 130dB, the individual levels in each band are significantly lower than the COMSOL simulations.

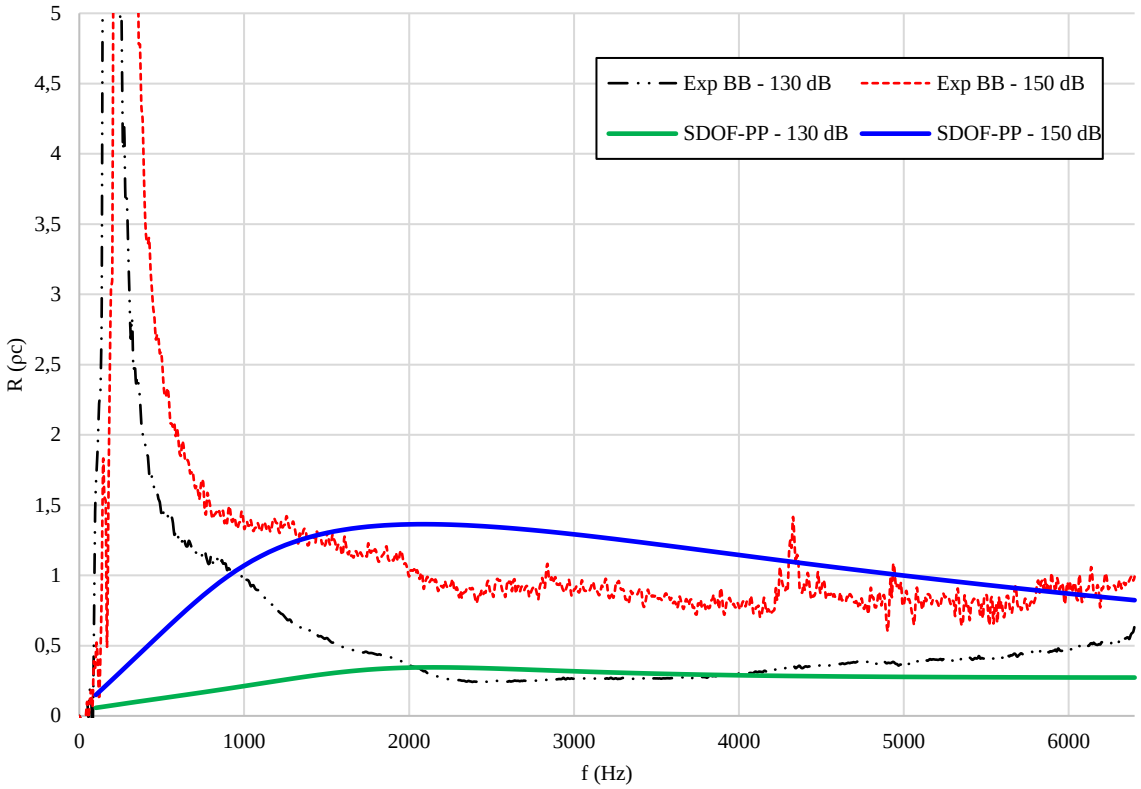

Figure 2.2. Normalized Resistance, R

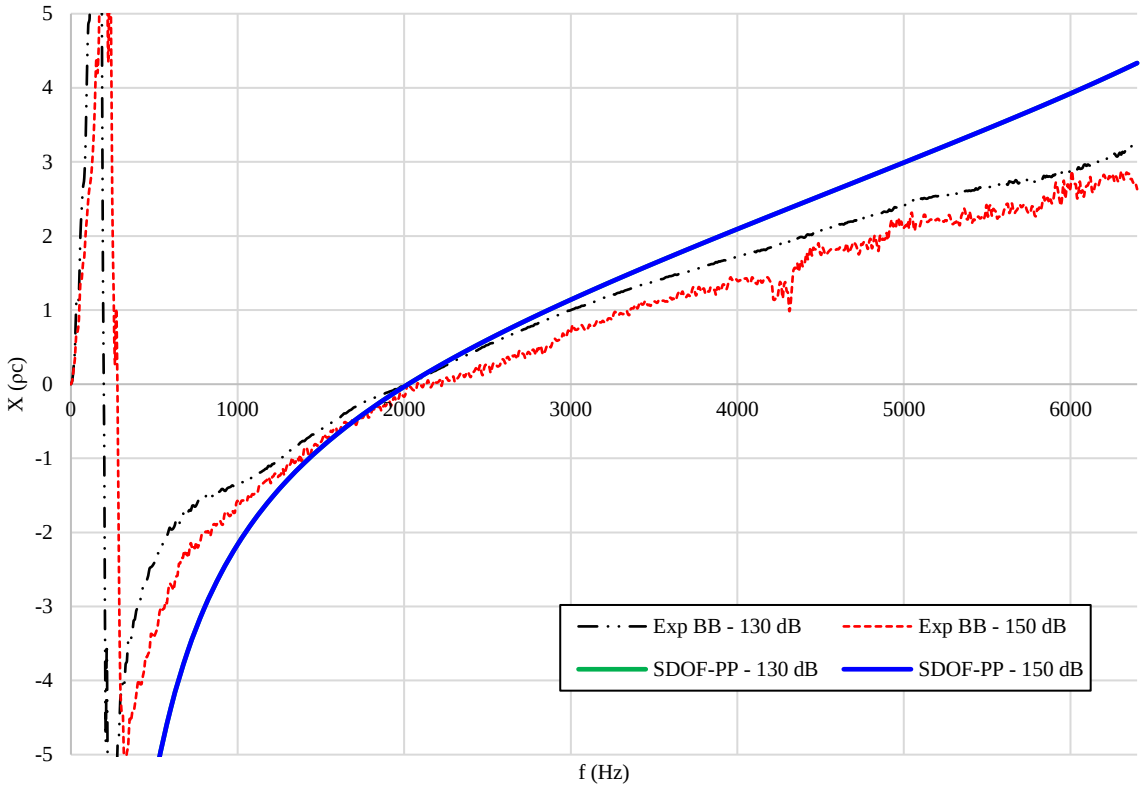

Figure 2.3. Normalized Reactance, X

The above figures show relatively poor agreement between the numerical and the experimental results.

As far as the resistance is concerned, the numerical data achieved with the source SPL set at 130 dB are similar to the experimental data in the frequency range between 2000 Hz and 5000 Hz. However, they significantly differ over the remaining frequency bandwidth. Below 2000 Hz and above 5000 Hz, the numerical model does not capture the increase of the resistance measured in the test with the flanged NIT. Regarding the resistance at 150 dB, while the numerical data displays the expected increase of resistance with SPL, it overestimates the measured increase. However, it is noted that the numerical simulations were performed with a tonal signal, so all of the energy is concentrated at the frequency in consideration, while the broadband measurements have significantly lower energy levels in each 8Hz band (~30dB lower). The broadband measurements also have significant interactions between the responses of the panel to each input frequency.

As far as the reactance is concerned, the predictions achieved at 130 dB and 150 dB follow the expected $-\cot(kh)$ type relationship and show no variation with level. However, they differ significantly from the corresponding experimental curve over the entire frequency bandwidth. The measured resonant frequency is successfully captured by the predicted reactance at 130 dB, while the predicted reactance at 150 dB fails to capture the measured resonant frequency. Also, the predicted reactance at 150 dB does not catch the expected reduction of the liner reactance with increasing SPL.

Previous works [16] [43] [44] [26] [14] suggest that the poor agreement between the numerical and the experimental results can stem from:

- An incomplete simulation of the physics of the liner (e.g. SPL differences).
- A mismatch between the nominal and the real liner geometry, caused by the manufacturing process.
- The sensitivity of the experimental results to the measurement set-up, due to the mismatch between the honeycomb cell volume exposed to the incident sound and the tube. Edge effects occur and they greatly influence the measured data, driving the increase of the low-frequency resistance (and the high-frequency resistance to a lesser degree) [45].

In the current study, these aspects are investigated in detail, and, in the end, the COMSOL SDOF-PP model is corrected to take account of their effects on the numerical simulation.

2.1.2 Sensitivity of the perforate liner impedance to the manufacturing process

The sensitivity of the panel impedance to the manufacturing process was examined extensively in [26] and [43].

The nominal geometry of a face sheet can be altered by the adhesive bonding process of the face sheet to the honeycomb core. Bonding the core to the face sheet through the application of the adhesive onto the core can block the holes, in some cases greatly reducing the effective open area. On the contrary, the application of the adhesive to the face sheet helps leave the holes open. In both cases, the final form of the adhesive around each hole will affect the acoustic losses through variations in vortex shedding, and variations in the effective discharge coefficient.

Alongside the bonding process, the drilling process can realize holes in the panel that are not perfectly straight. The resultant hole shapes can be conical, have rounded edges, or have small chamfers. Moreover, the location of the holes above the honeycomb can lead to some of them being obstructed by the partition walls (see Figure 2.4).

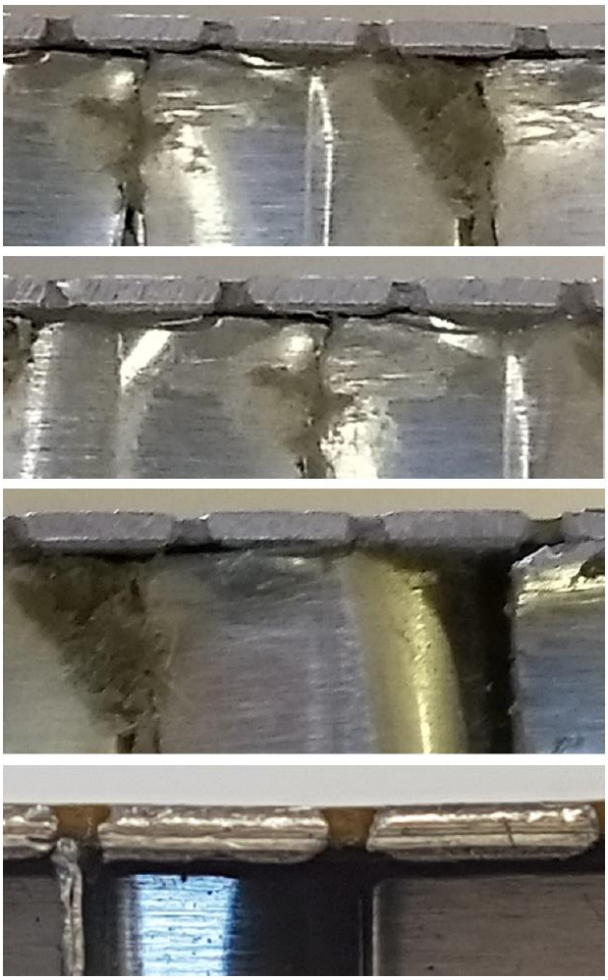

Figure 2.4. [26] Cross section of a punched aluminium perforate liner. Details on the panel holes.

Therefore, the manufacturing processes can greatly affect the effective porosity of the perforated plate. To best capture it, the nominal percentage open area POA must be replaced by the effective open area, $POAeff$.

In [43], alongside the DC flow rig, $POAeff$ is calculated from the face sheet resistance measured in a series of pure tone tests with increasing levels, performed at the resonant frequency with a normal impedance tube. As provided in [16], and discussed in Chapter I, in absence of grazing flow, the face sheet resistance of a perforated plate may be approximated by a linear function dependent on the acoustic velocity V, of the form:

$$R_{fs} = A + B \cdot V \tag{2.7}$$

In Equation 2.7, the constant A and B are determined by linearly fitting the measured resistance as a function of the acoustic velocity. Once the constant B is determined, the $POAeff$ is calculated through the following relation

$$POAeff = \sqrt{\frac{\rho}{2BC_D^2}} \tag{2.8}$$

where ρ is the air density and C_D is the discharge coefficient.

With the purpose of evaluating $POAeff$, a series of pure tone tests at increasing SPLs (from 130 dB to 150 dB with a 5dB step) was performed experimentally with the flanged NIT. The measurement was performed by setting the tonal source slightly above the resonance (at 2500 Hz) and not at the resonance (~2000 Hz). As illustrated in

Figure 2.2 and Figure 2.3, near $f = 2000\ Hz$ the measured data are still affected by the edge effects while at $f = 2500\ Hz$ the edge effects disappear. However, no significant differences are expected in the non-linear resistance, and the resultant $POAeff$ is considered valid.

Together with the pure tone tests at 2500 Hz, additional pure tone tests were performed at frequencies ranging between 3000 Hz and 5000 Hz, with a resolution of 500 Hz. In this frequency bandwidth, the edge effects are minimal, and there is confidence in the results achieved with the flanged set-up. The measurements were performed with the SPL increasing from 130 dB to 150 dB, with a 5 dB step. Figure 2.5 provides the measured data plus the additional values of resistance automatically extracted by the impedance meter at $V = 20\ cm/s$, $V = 105\ cm/s$ and $V = 200\ cm/s$.

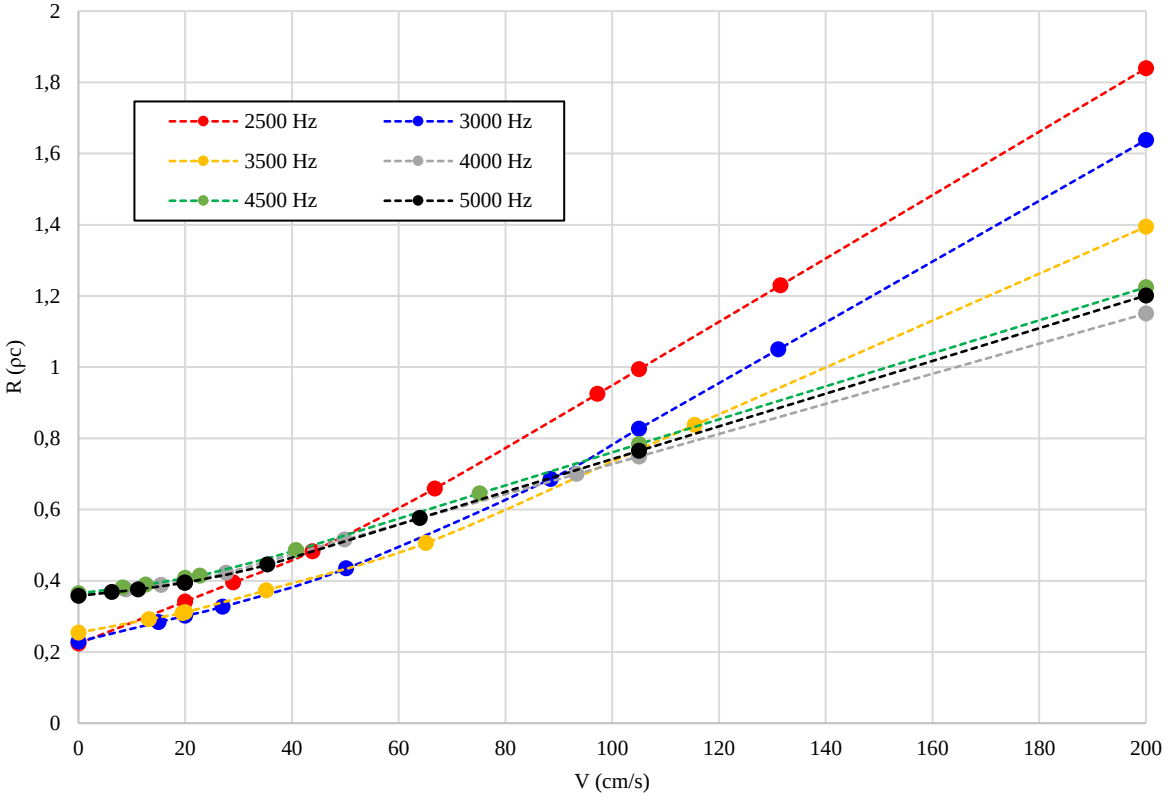

Figure 2.5. Measured liner resistance R versus acoustic velocity V, for different pure tone tests at increasing SPL

The resultant curves can be approximated as the union of a parabolic part [22] below $\sim 60\ cm/s$ and a linear part above $\sim 60\ cm/s$. For each tonal source, the intercept A is firstly approximated with the value of the interpolating curve at $V = 0\ cm/s$, while B is approximated with the extracted slope of the interpolating curve above $V = 60\ cm/s$. Once B is found at 2500 Hz, the $POAeff$ of the tested panel is calculated:

$$POAeff = 5.31\ \%$$

The resultant $POAeff$ is higher than the nominal $POA = 5.20\%$ using equation 2.8 This result is consistent with that obtained in [43] for a panel of a comparable POA (5.70%), whose $POAeff$ is slightly higher ($POAeff = 6.05\ \%$) than the nominal. Hereinafter, the POA of SDOF-PP is substituted by $POAeff$, and the porosity σ of the COMSOL perforate plate impedance model is set equal to $\sigma = POAeff/100$.

In Figure 2.5, the behaviour of the resistance as function of the acoustic velocity provides an interesting overview on the acoustic behaviour of the perforated SDOF liner. At 2500 Hz (near the resonance) and at 3000 Hz, the slope of the curves is significantly greater than that seen at higher frequencies. As the tonal source increases, the slope of the curves decreases to a minimum, measured at 4000 Hz, 4500 Hz and 5000 Hz. On the contrary, the intercepts of the curves are relatively small at 2500 Hz, 3000 Hz and 3500 Hz and they increase to a maximum value, measured at 4000 Hz, 4500 Hz and 5000 Hz. As discussed in Chapter I, the intercept A of the $R - V$ curve is related to the losses caused by the viscous friction in the holes, while the slope B is related to the non-linear losses caused by the vortex shedding at the entrance and exit of the holes. At high SPL, the term $B \cdot V$ is the major component of the resistance, while the term A is relatively small. However, the vortices are shed from the hole edges more at frequencies close to the resonance [24] (2500 Hz and 3000 Hz), where the acoustic velocity is highest for a given SPL, while their shedding is reduced far from the resonance. Hence, despite the high SPL, far from resonance, the contribution of the non-linear losses to the dissipation of the acoustic energy reduces [25], while the linear losses increase. The measured data in Figure 2.5 capture this trend: the slopes are maximum near resonance (at 2500 Hz and 3000 Hz), while they are lower at higher frequencies (at 4000 Hz, 4500 Hz and 5000 Hz); on the contrary, the intercepts are minimum near resonance (at 2500 Hz and 3000 Hz), while they increase at higher frequencies (at 4000 Hz, 4500 Hz and 5000 Hz).

Finally, it is recalled that the observations about the face sheet resistance are valid in case of a tonal source. In case of a broadband source, the presence of a multitude of lower level sources, at different frequencies, impinging onto the liner complicates the description of the physics and, at high SPLs, the panel acoustic response to a broadband source differs greatly from its response to a tonal source [26] [14].

2.1.3 Mass inertance end correction

Alongside the effective panel porosity, an additional source of poor agreement between the measured and the predicted data in Figure 2.2 and Figure 2.3 may be an incomplete simulation of the physics of the liner. The perforate plate impedance model embedded in COMSOL (see Equation 2.5), in fact, does not include any non-linear term of the face sheet reactance.

As discussed in Chapter I, the reactance term of a SDOF liner is defined as:

$$X = X_{fs} + X_{cav} \tag{2.9}$$

with X the liner reactance, X_{fs} the face sheet reactance, and X_{cav} the cavity reactance.

The cavity reactance is defined as a function of the cavity height h, given by

$$X_{cav} = -\cot(kh) \tag{2.10}$$

The face sheet mass reactance X_{fs} is usually defined as the product of the wavenumber k and the face sheet inertance m_{fs}, given by

$$X_{fs} = k \cdot m_{fs} \tag{2.11}$$

The face sheet inertance is commonly expressed as,

$$m_{fs} = \frac{t + \epsilon d}{\sigma} \tag{2.12}$$

where t is the thickness of the face sheet, ϵ the dimensionless end correction, d the hole diameter, and σ the face sheet porosity. m_{fs} accounts for the mass of air oscillating in and near the holes, and it is defined as the ratio between the effective thickness of the plate L ($L = t + \epsilon d$), and its porosity σ. Early literature suggests that the dimensionless end correction can be approximated by $\epsilon = 0.85$ or by a function dependent on the plate porosity σ, $\epsilon = 0.85\left(1 - 0.7\sqrt{\sigma}\right)$. However, those definitions miss the dependency of ϵ on the SPL [16], and on the sound wave frequency [25] [26], omitting the non-linearity of the face sheet reactance. If ϵ is expressed by a dimensionless function dependent on SPL and the wave frequency f, the face sheet reactance is defined as

$$X_{fs} = k\frac{t + \epsilon(SPL, f)d}{\sigma} \tag{2.13}$$

As provided in [16], the dependency of ϵ on SPL can be expressed in terms of acoustic velocity through a logarithmic function of the type:

$$\epsilon(V, f) = \epsilon_0(f) - \epsilon_V(f)\, logV \tag{2.14}$$

This can be firstly approximated as,

$$\epsilon(V, f) \approx \epsilon_0(f) - \epsilon_V(f)\, V \tag{2.15}$$

Substituting this into Equation 2.13, X_{fs} can be finally rewritten as,

$$X_{fs} \approx k\frac{t + \epsilon_0(f)d}{\sigma} - k\frac{\epsilon_V(f)}{\sigma}V \tag{2.16}$$

In Equation 2.16, the face sheet reactance is composed of a linear term $X_{fs_{lin}}$ and a non-linear term $X_{fs_{nl}}$.

$$X_{fs} = X_{fs_{lin}} + X_{fs_{nl}} \tag{2.17}$$

The expression in Equation 2.16 reveals the effective dependency of the face sheet reactance to the acoustic velocity. As seen in [20], the volume of the air oscillating in and near the holes depends on the acoustic velocity field within and on each side of the holes. At low SPL, the flow is mainly irrotational, and the volume of air oscillating in the hole region is a maximum; on the contrary, as the flow separates at the walls, the turbulence increases, vortices are shed at the outlet of the orifice and the volume of oscillating air reduces. In addition, these phenomena are strictly correlated to the sound wave frequency: at high SPL and near resonance, the vortex shedding dominates, while away from resonance, or at lower SPL, the acoustic velocity field is mainly irrotational, and the non-linear losses diminish. As a consequence, if the non-linear term of the face sheet impedance is not included in the numerical simulation, the physics of the acoustic liner is only partially represented, and the comparison between the predicted with the measured impedance can be unfavourable.

This is what happens with SDOF-PP, because COMSOL does not account for the non-linear term of the reactance. In Equation 2.5, in fact, the end correction δ is set equal to the value proposed by Helmholtz for an orifice in an infinite plate $\left(\delta = \frac{4d}{3\pi}\right)$ and is multiplied by the factor $f_{int} = \sum_{n=0}^{8} a_n\left(\sqrt{\sigma}\right)^n$ to account for the mutual interaction between adjacent holes. However, the sensitivity of the end correction to SPL and to the sound wave frequency is

not considered, and this contributes to the poor agreement between the numerical and the measured results shown in Figure 2.2 and Figure 2.3.

In the current study, the sensitivity of the face sheet reactance to SPL and source frequency was demonstrated through a series of pure tone tests, with the tonal source ranging from 2500 Hz to 5000 Hz (500 Hz step), and with the liner surface SPL varying from 130 dB to 150 dB (5 dB step). The measurements were performed using the flanged normal impedance tube. The measured liner reactance is provided in Figure 2.6 as a function of the acoustic velocity. As for the previous case, the pure tone tests were performed in the frequency range where the measured data are not influenced by edge effects.

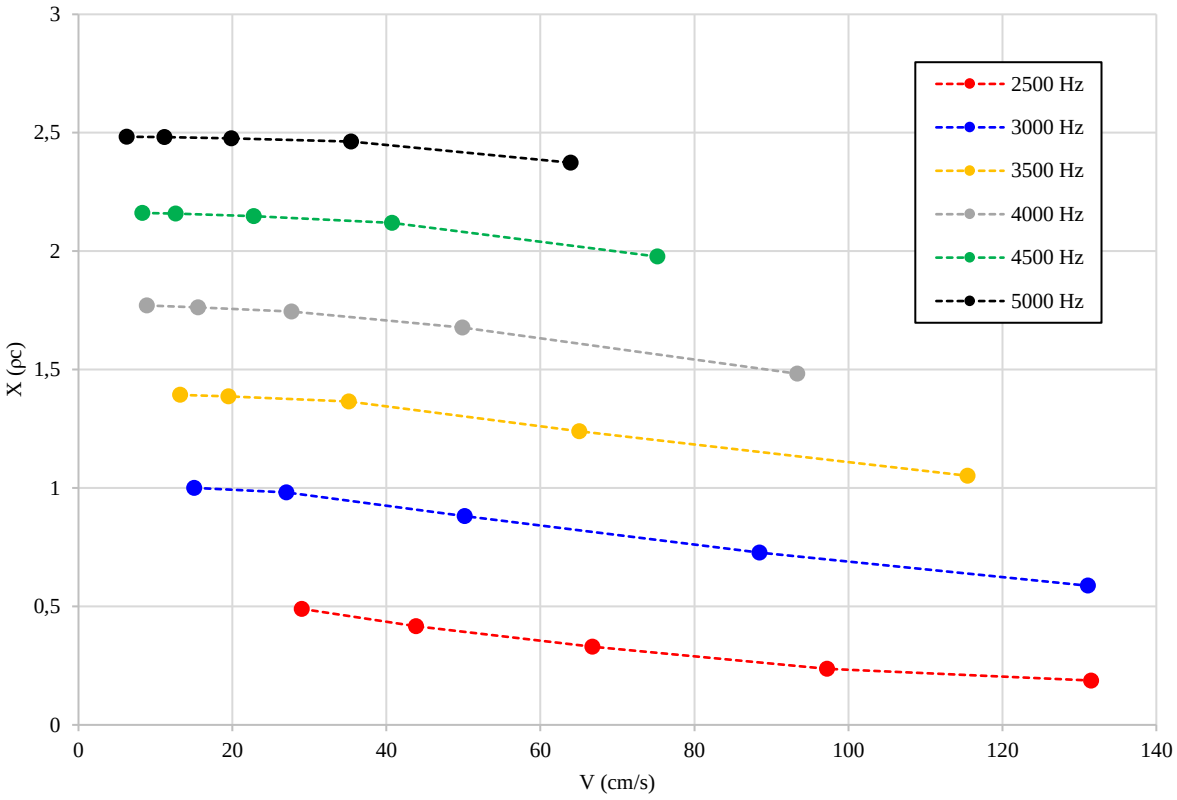

Figure 2.6. Measured liner reactance X versus acoustic velocity V, for different pure tone tests at increasing SPL

In Figure 2.6, the liner reactance follows the expected reduction with increasing acoustic velocity and it also shows the expected increase with increasing sound wave frequency. In order to isolate the variation of the face sheet reactance as function of the acoustic velocity, the cavity reactance contribution X_{cav} is removed from the measured reactance data and the results are divided by the wavenumber k.

$$m_{fs} = \frac{X_{fs}}{k} = \frac{X - X_{cav}}{k} \tag{2.18}$$

Substituting Equation 2.16 into Equation 2.18, the face sheet inertance is given by

$$m_{fs} = m_{fs_0}(f) - m_{fs_V}(f)\, V \tag{2.19}$$

Figure 2.7 provides the extracted values of m_{fs} as a function of the acoustic velocity V, for the different pure tone tests.

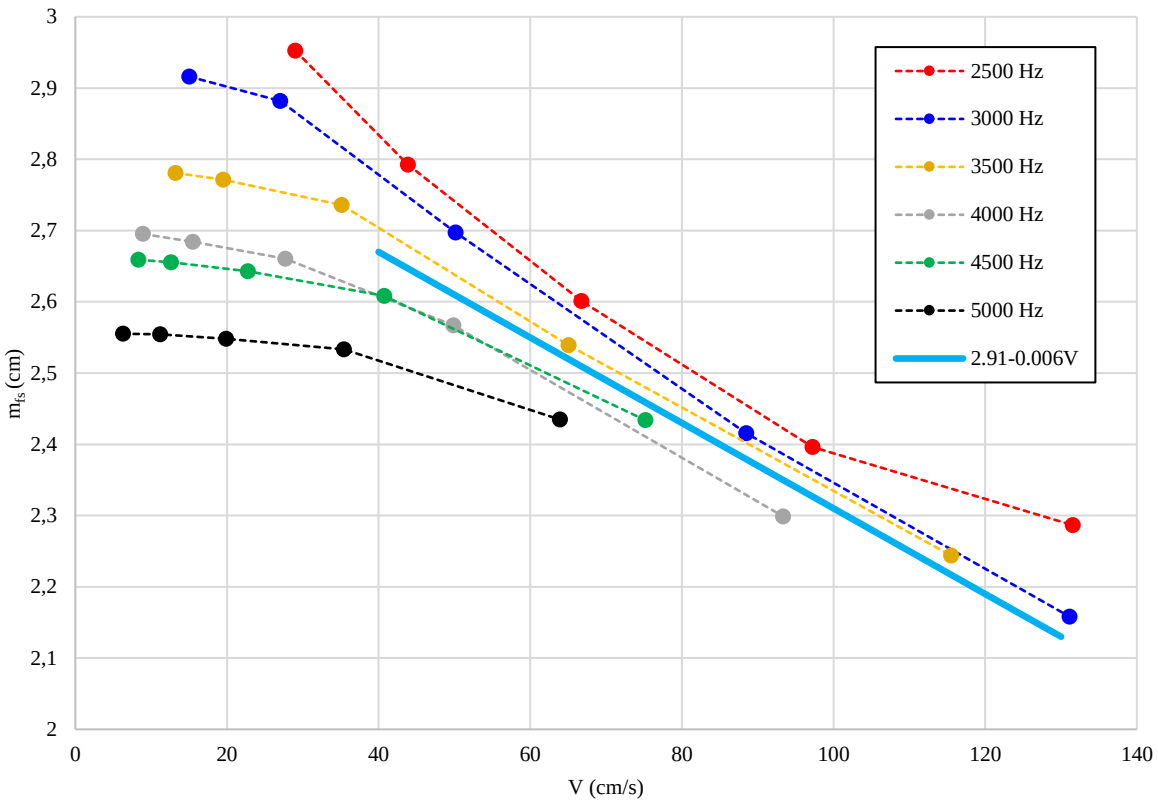

Figure 2.7. Measured face sheet inertance m_{fs} versus acoustic velocity V, for different pure tone tests at increasing SPL

The data provided in Figure 2.7 reflects the expected trend of the face sheet inertance expressed in Equation 2.19. In addition, Figure 2.7 confirms the explanation of the physical behaviour of the reactance as a function of SPL and source frequency. At lower SPLs, or far from resonance, the viscous scrubbing losses dominate and the face sheet inertance can be approximated by the linear term $m_{fs_0}(f)$. There, the acoustic flow is mainly irrotational, and the volume of oscillating air within and near the holes is maximized. In contrast, at higher SPLs near the resonance frequency, m_{fs} decreases to smaller values because the vortex shedding dominates, the region of irrotational acoustic flow reduces, and, as a result, the volume of oscillating air diminishes. At low SPLs, the value of m_{fs_0} is seen to reduce with increasing frequency. The variation of the volume of oscillating air with increasing frequency, and therefore the variation of the face sheet inertance with frequency, can be reflected via a varying discharge coefficient C_D [26]. C_D indeed, accounts for the rate of the real flow through a hole to the theoretical flow. A varying discharge coefficient is discussed in [26] and [25], but it is not generally included in most semi-empirical impedance models in the literature (and in COMSOL [23]). An approximation of a fixed $C_D = 0.76$ is generally adopted. This approximation holds for low frequencies (usually $f <= 3000\,Hz$) while at higher frequencies, away from the resonance, the discharge coefficient commonly tends to the unity [26] [25] because the non-linear effects decay as the particle velocity reduces with increasing frequency ($v \propto p/|Z|$ and $|Z|$ increases as the cavity reactance increases). The influence of $C_D(f)$ on the face sheet inertance can be assessed by making the dependency of σ_{eff} on frequency explicit. From Equation 2.8,

$$\sigma_{eff} = \frac{1}{100}\sqrt{\frac{\rho}{2BC_D(f)^2}} \tag{2.20}$$

where ρ is in g/cm^3, and the slope is in cgs $Rayl/(cm/s)$.

Substituting σ in Equation 2.12, the expression of the face sheet inertance in function of the frequency is achieved.

$$m_{fs}(f) = 100 \cdot (t + \epsilon d)\sqrt{\frac{2B}{\rho}}C_D(f) \tag{2.21}$$

In order to assess the sensitivity of the face sheet inertance to the source frequency properly, an empirical function of $C_D(f)$ must be extracted from a series of experimental pure tone tests, fixing the $POAeff$ and using the measured slope B of the $R - V$ curve [25] [26]. However, the limited number of pure tone tests performed in the current study is not sufficient to attain a reliable function of $C_D(f)$ and the discharge coefficient is hereinafter set at $C_D = 0.76$. Hence, for the liner studied, the dependency of the face sheet reactance on the source frequency is not considered, and only its sensitivity to the acoustic velocity is accounted for.

As a side note, Equation 2.21 provides an interesting overview on the relation between the panel resistance and the face sheet reactance. According to the Equation 2.21, m_{fs} is directly proportional to the square root of the slope B of the resistance-velocity curve and the results provided in Figure 2.7 reflect this trend. The face sheet inertance reaches the highest values near resonance, where the slope B is a maximum, while far from resonance, the face sheet inertance reduces.

In SDOF-PP, the perforate plate impedance model (see Equation 2.5) partially takes account of the constant contribution of face sheet inertance, while the non-linear term is omitted. Neglecting the sensitivity of the face sheet inertance to the sound wave frequency, the data provided in Figure 2.7 can be effectively approximated by a linear function fitting the data above $V = 40\ cm/s$ (above $V = 40\ cm/s$, the non-linear contribution dominates). On the contrary, at low velocities ($V < 40\ cm/s$) the face sheet inertance can be approximated by a constant term because the face sheet reactance is dominated by the linear term m_{fs_0}.

The linear curve fitting the data above $v = 40\ cm/s$ is given by the following function

$$m_{fs} = m_{fs_0} + \frac{\partial m_{fs}}{\partial V}V \tag{2.22}$$

where m_{fs_0} is the intercept and $\frac{\partial m_{fs}}{\partial V}$ is the slope of the curve. In the current study, $\frac{\partial m_{fs}}{\partial V}$ equals

$$\frac{\partial m_{fs}}{\partial V} = -0.006\ [s]$$

while m_{fs_0} equals

$$m_{fs_0} = 2.91\ cm$$

Therefore, the final linear curve fitting the data is

$$m_{fs} = 2.91\ [cm] - 0.006[s] \cdot V\ \left[\frac{cm}{s}\right] \tag{2.23}$$

The linear estimate of m_{fs_0} included in COMSOL is calculated by evaluating Equation 2.9 at the resonance ($f \approx 2000\ Hz$) and equals,

$$m_{fs_0-COMSOL} = 2.54\ cm$$

This estimate is fixed for all hole shapes, and it should be corrected for the hole shape of the test panel. Hence, the linear approximation of the $m_{fs} - V$ curve that should be introduced in COMSOL is

$$m_{fs} - m_{fs_{0-COMSOL}} = 0.37\ [cm] - 0.006\ [s] \cdot V\ \left[\frac{cm}{s}\right] \tag{2.24}$$

However, a preliminary numerical analysis showed that any significant difference is not predicted by setting $m_{fs_0} = 0\ cm/s$ or $m_{fs_0} = 0.37\ cm/s$. The baseline value of $m_{fs_{0-COMSOL}}$ is sufficient in order to provide a reliable estimate of the variation of m_{fs} in function of the acoustic velocity.

With these observation in mind, the sensitivity of the face sheet reactance to the acoustic velocity is introduced in SDOF-PP by adding an additional user-defined reactance $\chi^{(user)}$ at

$$\chi^{(user)} = k\left(-0.006[s] \cdot V\left[\frac{m}{s}\right]\right) \tag{2.25}$$

2.1.4 Effects of high acoustic velocity inertance correction in the numerical simulation

The inclusion of $POAeff$ and the $m_{fs} - V$ curve in SDOF-PP is expected to enhance the simulation of the SDOF liner acoustic characteristics. The validity of the corrections introduced must be verified.

To this purpose, two versions of SDOF-PP are developed: one accounts for the effective percentage open area $POAeff$, and the other accounts for $POAeff$ and the inertance non-linearity. The former is labelled "SDOF-PP-σ", while the latter is labelled "SDOF-PP-σ+χ_v". Figure 2.8 recaps the features of the SDOF-PP-type models.

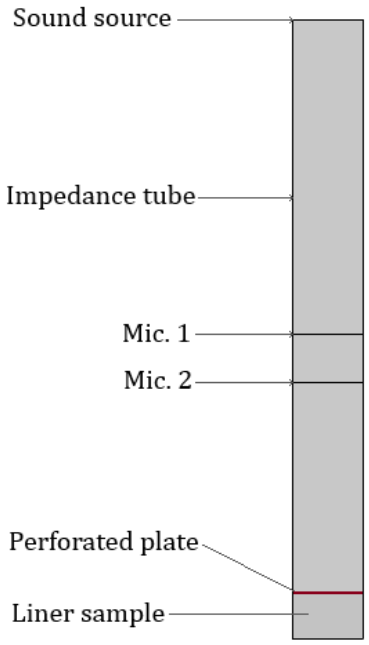

Figure 2.8. SDOF-PP-type model

The following figures provide the predicted data of SDOF-PP-σ and SDOF-PP-σ+χ_v achieved from a series of pure tone tests. The results were obtained by setting the pure tone source frequency from 2500 Hz to 5000 Hz, with a

500 Hz step. They were measured as a function of the liner surface SPL (130 dB, 140 dB, 145 dB and 150 dB). The predictions are compared to the measured data below.

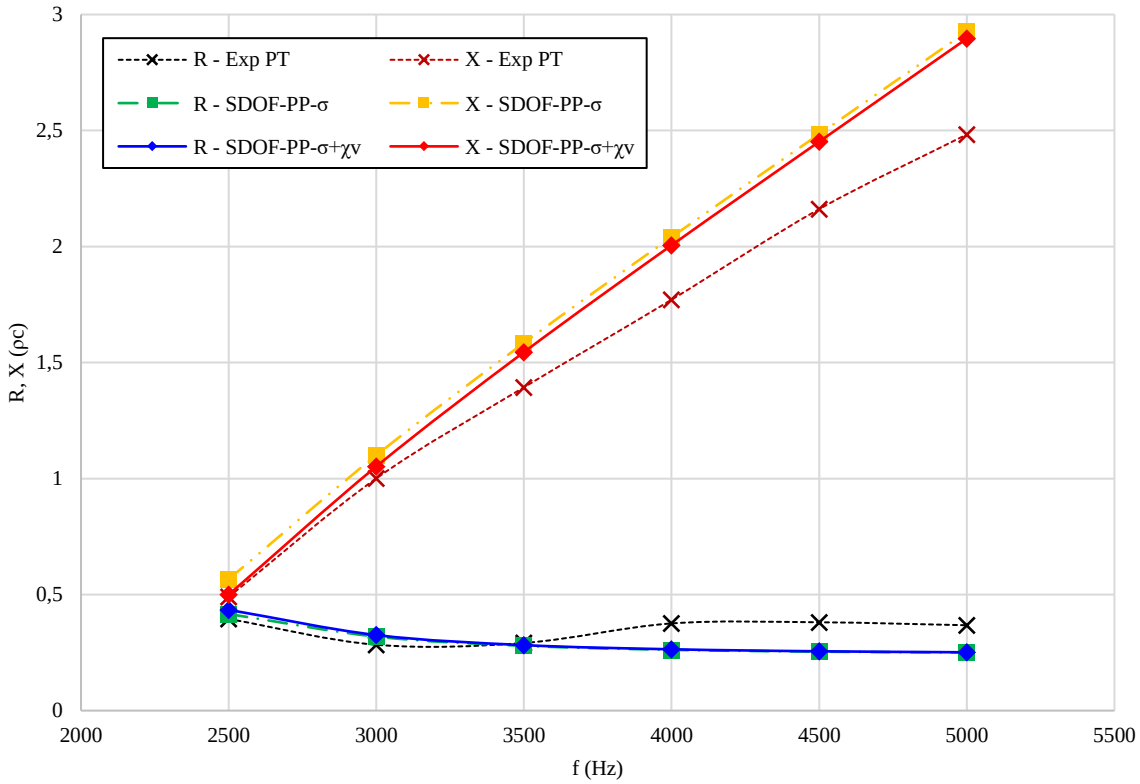

Figure 2.9. SDOF liner: predicted and measured impedance in pure tone tests at 130 dB

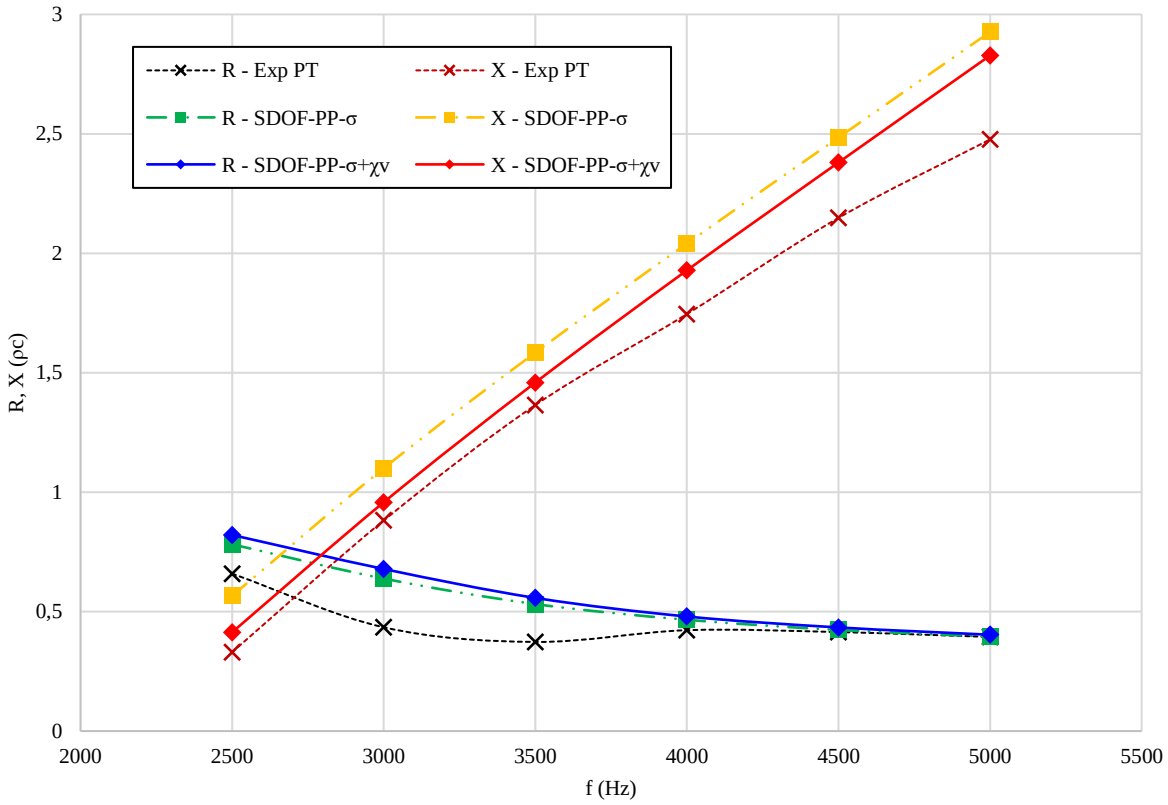

Figure 2.10. SDOF liner: predicted and measured impedance in pure tone tests at 140 dB

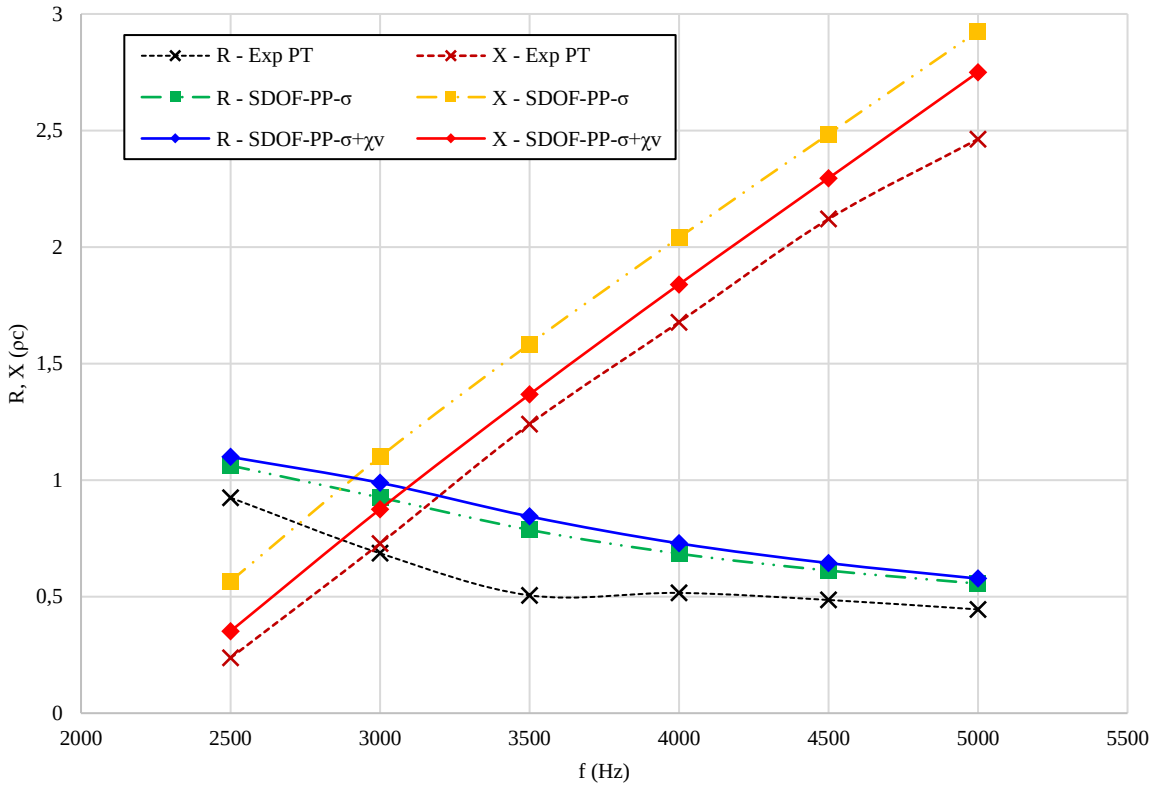

Figure 2.11. SDOF liner: predicted and measured impedance in pure tone tests at 145 dB

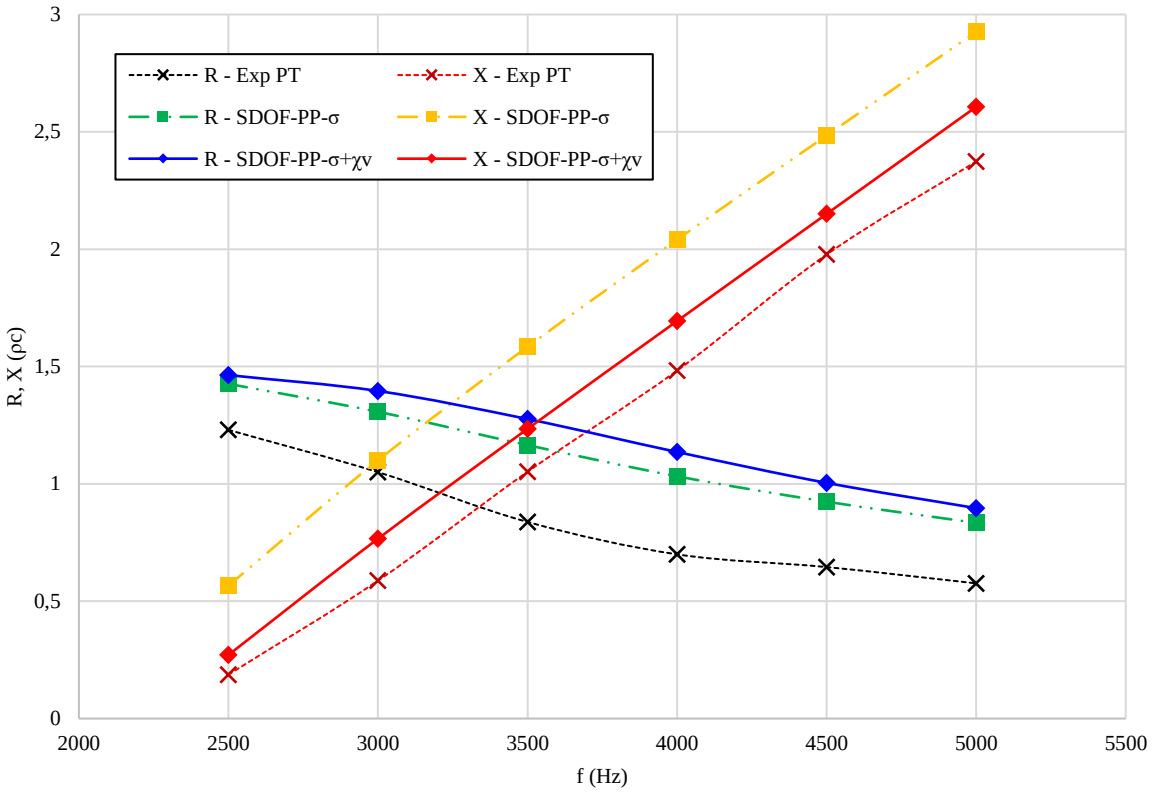

Figure 2.12. SDOF liner: predicted and measured impedance in pure tone tests at 150 dB

Figure 2.9 shows quite good agreement between the measured and the data predicted by SDOF-PP-σ+χ_v, while the agreement degrades somewhat with increasing SPL (see Figure 2.10, Figure 2.11 and Figure 2.12). On the contrary, except for Figure 2.9 (130 dB), the comparison between the measurements and the predictions of SDOF-PP-σ is poor for each SPL. This is unsurprising as the effects of the acoustic velocity on the face sheet reactance become significant with increasing acoustic velocity and SDOF-PP-σ neglects these effects. The above figures confirm that the simulation of the impedance without a non-linear correction does not completely describe the physics of a low open area perforate liner and the simulation of the non-linear face sheet reactance must be included in the numerical model. Hence, the SDOF-PP-σ predictions will be henceforth neglected and the discussion of the results will focus on the predictions of SDOF-PP-σ+χ_v.

Although SDOF-PP-σ+χ_v provides an improved prediction of the liner impedance, the predictions do not match the experimental reactance data for each tonal source. In Figure 2.9 and Figure 2.10, the SDOF-PP-σ+χ_v data successfully captures the measured data at the frequencies near resonance, while far from the resonance the agreement degrades. It is recalled that, as discussed in 2.1.4, the sensitivity of the face sheet inertance to frequency has been neglected, so the included correction provided in Equation 2.25 does not account for the variation of the discharge coefficient with frequency. The embedded COMSOL $C_D = 0.76$ predicts the expected discharge coefficient near resonance well, but it is less accurate at higher frequencies, where $C_D \to 1$ [25]. On the contrary, in Figure 2.11 and Figure 2.12, the distance between the SDOF-PP-σ+χ_v predicted and measured reactance is approximately constant for each tonal source though it suffers somewhat from the absence of the sensitivity of the inertance to frequency. The latter results suggests that the reactance may reach a minimum value for very high

SPLs, and that the remaining mismatch in reactance may be due to the difference in the actual hole shape of the sample versus the square-edged assumption in the COMSOL model.

Apart from Figure 2.9, the predicted SDOF-PP-$\sigma+\chi_v$ resistance and reactance are higher than the measured data and the overestimation increases with increasing SPL. Similar overestimations have been obtained also in Serrano's thesis [26], where the experimental results of a series of pure tone tests on a SDOF liner have been compared to the numerical results of the corresponding COMSOL model. In [26], the measured and the predicted data were obtained with the tonal source ranging from 600 Hz to 5100 Hz and at 130 dB, 140 dB, and 150 dB. The panel tested in [26] has a similar geometry to the panel considered in the current study, but it has a lower porosity. The main difference from SDOF-PP-$\sigma+\chi_v$ and Serrano's model is the hole shapes of the perforate plate. In [26] they were simulated with the plausible shapes that the holes of a punched aluminium panel can have (see Figure 2.4 - straight, chamfer, conical and convergent-divergent) while in SDOF-PP-$\sigma+\chi_v$ they are considered straight. Neglecting the differences among the different simulation techniques, in [26] the measured resistance is underestimated at lower SPL, while is overestimated at higher SPL for each hole shape modelled (as is the case for the measurements in this study). The predicted and the measured reactance show better agreement in the case of a straight and a chamfered hole, but in the case of conical and convergent-divergent holes, the agreement degrades. Serrano suggests that the significant difference between the experimental and the predicted results at higher SPL may be due to the actual hole shape, that can be different from the nominal considered in the formulation of the COMSOL perforate plate impedance model (straight hole, Equation 2.5). A similar consideration can effectively be adopted also in the current study and the source of mismatch between the predicted and the measured results at higher SPL (see Figure 2.11 and Figure 2.12) may well be due to the effective shape of the panel holes, different from the nominal.

The assessment of the actual hole shape might help in clarifying the source of mismatch between the predicted and measured data, but it would require further investigations (e.g. time domain simulations) that go beyond the scope of this study. In the current study, the SDOF liner has been tested in a normal acoustic incidence set-up with no flow, but these conditions differ from the typical operating conditions with grazing flow and non-normal incident sound. As shown in [43] and [25], the presence of the flow significantly alters the acoustic impedance characteristics, and the flow must be accounted for in the design of an acoustic liner. Hence, the numerical simulation of the SDOF liner herein provided cannot be used to design the installed liner impedance. Nonetheless, the model can be exploited to preliminarily design the frequency spectrum of the liner impedance. In particular, the reactive part is key for these complex cavities, and this will exhibit a much-reduced sensitivity to grazing flow, unlike the facing sheet.

The figures above show that numerical predictions capture the trend of the reactance near resonance at each SPL considered. The good agreement between the predicted and measured reactance near resonance is considered sufficient for validating the use of COMSOL. The panel is tuned to absorb around the resonance frequency, and the acoustic performance is less efficient far from the resonant frequency. COMSOL is indeed able to model impedance at the frequency range where the sound absorption of the liner is maximised. The remaining differences between the measurements and the predictions are not considered critical at this stage, and they are neglected.

In conclusion, the comparison between the measured and predicted data with SDOF-PP-σ+χ_v is considered sufficiently good, COMSOL is considered validated, and it is able to preliminary describe the acoustic properties of SDOF liners.

2.1.5 Edge effects at low frequencies and the effect of flange leakage

Alongside the $POAeff$ and the omitted sensitivity of the face sheet reactance to SPL, a dominant source of poor agreement between the measured and the predicted low-frequency data in Figure 2.2 and Figure 2.3 is the mismatch between the honeycomb cell volume exposed to the incident sound and the tube area.

In the flanged NIT, the holes covered by the flange give access to honeycomb cavities that are extended over a wider area compared to the inner tube area. This is because the cavity width of the traditional perforate sample is nominally 9mm. Hence, when the plane wave impinges on the face sheet, the wave is scattered at the edges of the sample, and the sound propagates in the adjacent cavities (see Figure 2.13 and Figure 2.14). Consequently, the face sheet area on which the plane wave impinges mismatches the back-sheet area where the sound propagates and the volume of air perturbed is higher than expected. The influence of the edge effects on the normal impedance tube set-up are particularly evident at low frequencies and, up to a certain extent, even at higher frequencies (see Figure 2.2, resistance at 130 dB). [30] observes that the edge effects significantly influence the accuracy of the measured impedance when the liner tested has a low porosity (3-6/7%), the orifices have a diameter of approximately 1 mm, and the honeycomb cells have a width of approximately 9 mm. The SDOF liner tested in the current study has similar dimensions, so the sensitivity of the measurements to the edge effects is expected to be significant at low frequencies. However, the results remain good around the resonance frequency and the flanged design allow non-destructive measurements to be made on final parts of any curvature. Finally, while it may be obvious, it is noted that these impedance edge effects are solely due to the flanged set-up, and will not be seen for destructive sample holder tests, or for panels installed in a duct.

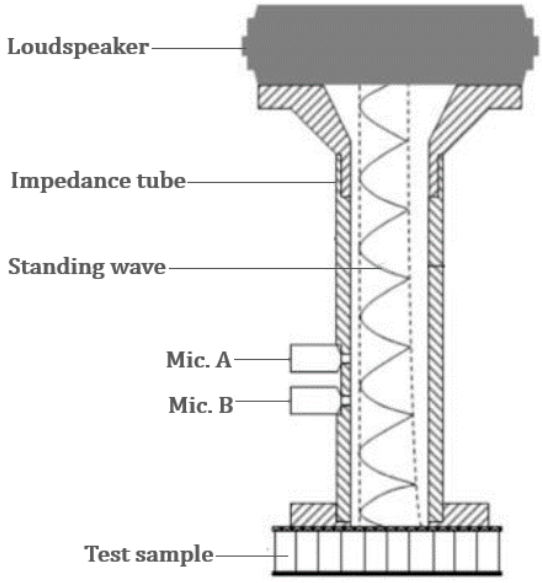

Figure 2.13. Normal incidence set-up with flanged NIT [26].

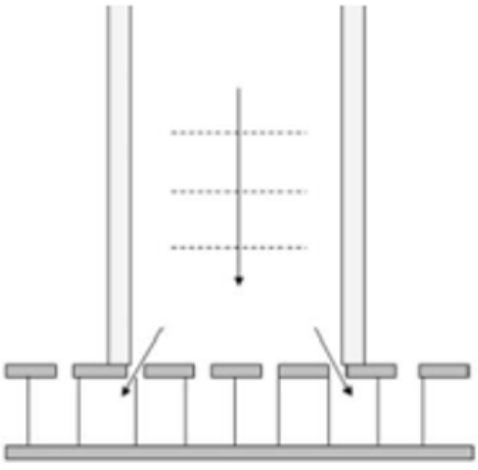

Figure 2.14. Low frequency sound scattering produced in an impedance tube equipped with flanged termination [30]

An additional source of poor agreement between the measured and the predicted low-frequency data can be driven by the sound leakage that may occur at low frequencies through the flange and the liner surface [30]. The flange

is usually covered by a rubber closure designed to limit possible sound leakage. However, wear and ageing of the rubber closure, or the presence of dust of considerable particle-size, can be detrimental to the adherence of the flange to the liner surface, and hence sound leakage can occur.

Furthermore, the measured impedance can suffer from the variability of the liner geometry across the liner surface and, as a result, the measured impedance can vary with the position of the impedance tube over the liner surface. Nonetheless, this issue is of secondary order in the case of a conventional POHC liner, due to the regularity of the honeycomb configuration along its extent. On the contrary, as will be seen in Chapter III, this issue becomes significant in case of broadband liners with a variable configuration of the core in the axial and spanwise direction.

In the current study, a numerical model has been developed to simulate the edge effects and flange leakage and to investigate their impact on impedance measurements. The numerical model is derived from SDOF-PP-σ+χ_v and it is labelled as "SDOF-PP-σ+χ_v-EE"; its main features are shown in Figure 2.15 and Figure 2.16.

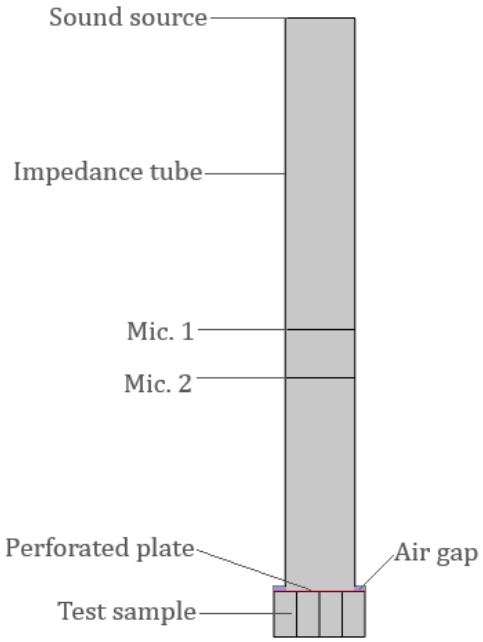

Figure 2.15. SDOF-PP-σ+χ_v-EE

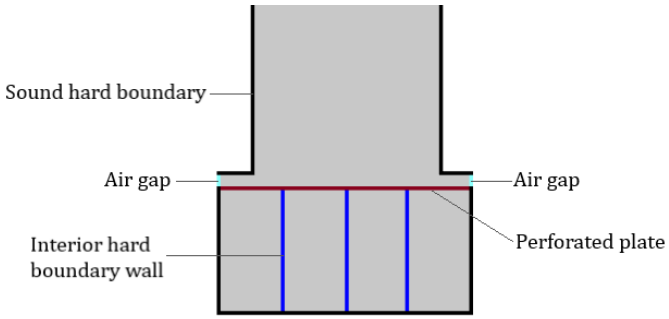

Figure 2.16. SDOF-PP-σ+χ_v-EE. Detail on the flanged tube termination and the liner sample

Figure 2.16 illustrates the distinctive features of SDOF-PP-σ+χ_v-EE with respect to SDOF-PP-σ+χ_v. The two models share the same simulation of the normal impedance tube, but the tube termination is modelled differently. SDOF-PP-σ+χ_v-EE replicates the flange termination and it covers a liner sample of increased extent compared to the inner tube area. The liner model consists of the two cavities theoretically covered by the impedance tube plus the two adjacent cavities. The cavities are separated by the internal partitions to capture the edge effects and the walls are modelled as rigid and reflective. The choice of cavity width reflects that typically employed in nacelle liners.

In SDOF-PP-σ+χ_v-EE, the impedance of the perforated plate is simulated with the embedded COMSOL model plus the non-linear reactance correction, whose characteristics are identical to those adopted in SDOF-PP-σ+χ_v. The perforate plate is separated from the flange by a tiny space, at whose terminations the air impedance $Z = \rho c$ is modelled. The tiny space is meant at simulating a possible air gap between the liner surface and the flange rubber closure through which the sound can leak. In order to investigate the most effective way to simulate the air gap,

five versions of SDOF-PP-σ+χ_v-EE are realized, each of them with a different air gap size. The models are labelled as "SDOF-PP-σ+χ_v-EE", "SDOF-PP-σ+χ_v-EE-0.1", "SDOF-PP-σ+χ_v-EE-0.2", "SDOF-PP-σ+χ_v-EE-0.5" and "SDOF-PP-σ+χ_v-EE-1.0" where the air gap size is respectively 0.0 mm, 0.1 mm, 0.2 mm, 0.5 mm and 1.0 mm. The models are meshed with free quadrilateral plane elements, whose maximum size is set to have at least ten elements at the minimum wavelength considered $\left(\lambda_{min} = \frac{c}{f_{max}} \approx \frac{345\frac{m}{s}}{6400\ Hz} \approx 54\ mm\right)$.

Figure 2.17, Figure 2.18, Figure 2.19 and Figure 2.20 provide the impedances predicted by setting the source pure tone SPL at 130 dB and the frequency source ranging between 100 Hz and 6400 Hz, with a resolution of 100 Hz. Predictions were made without any edge effect ("in tube predictions"), with then edge effect, and finally with the edge effect and a specified gap height. The figures also provide the experimental results obtained in a broadband test at 130 dB, with the frequency ranging between 8 Hz and 6400 Hz, with 8 Hz step. While the latter data was measured with a broadband source, it is included for comparative reasons.

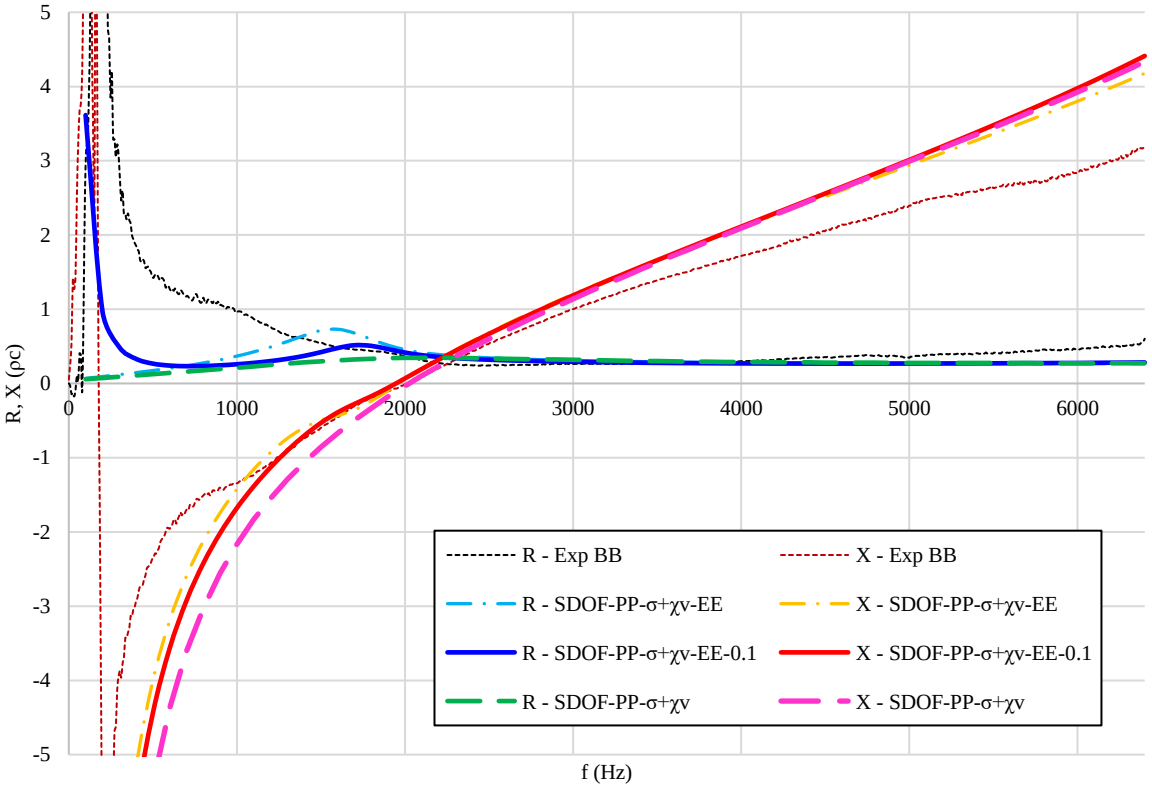

Figure 2.17. Perforated SDOF liner. Measurements vs Predictions, air gap size = 0.1 mm (Pure Tone predictions 130dB, measured broadband OASPL 130 dB)

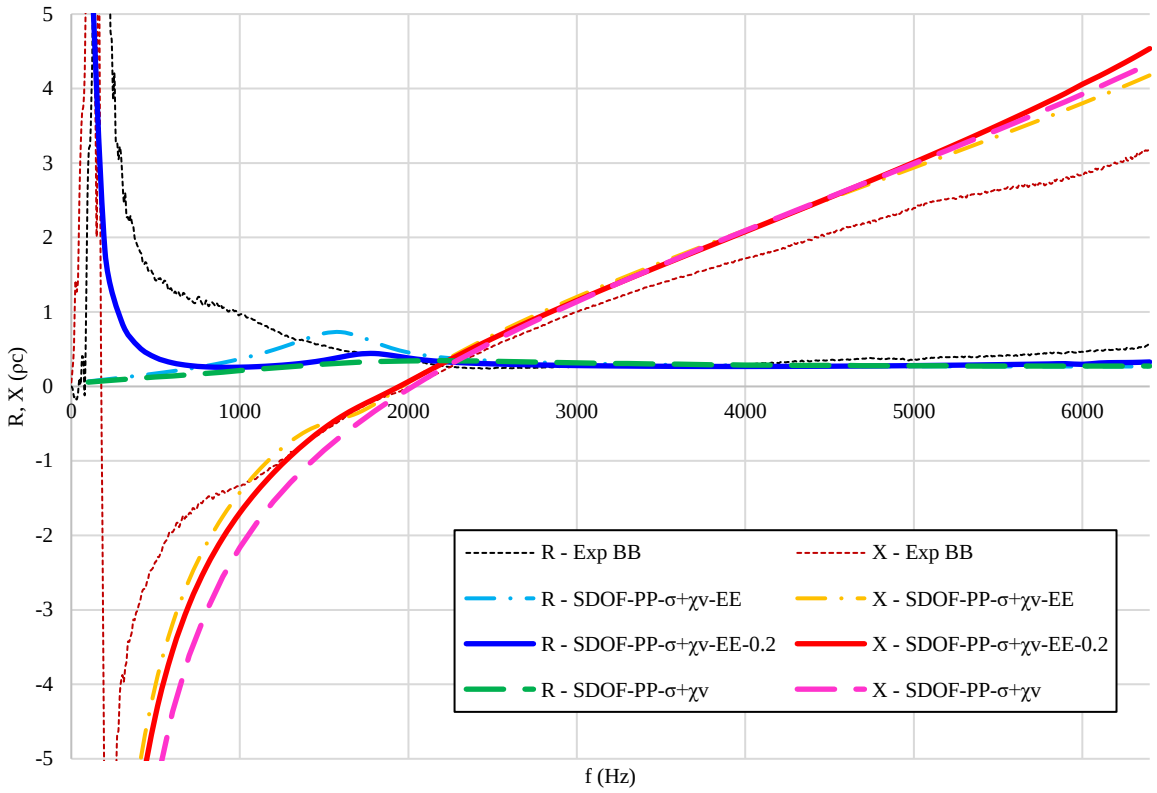

Figure 2.18. Perforated SDOF liner. Measurements vs Predictions, air gap size = 0.2 mm (Pure Tone predictions 130dB, measured broadband OASPL 130 dB)

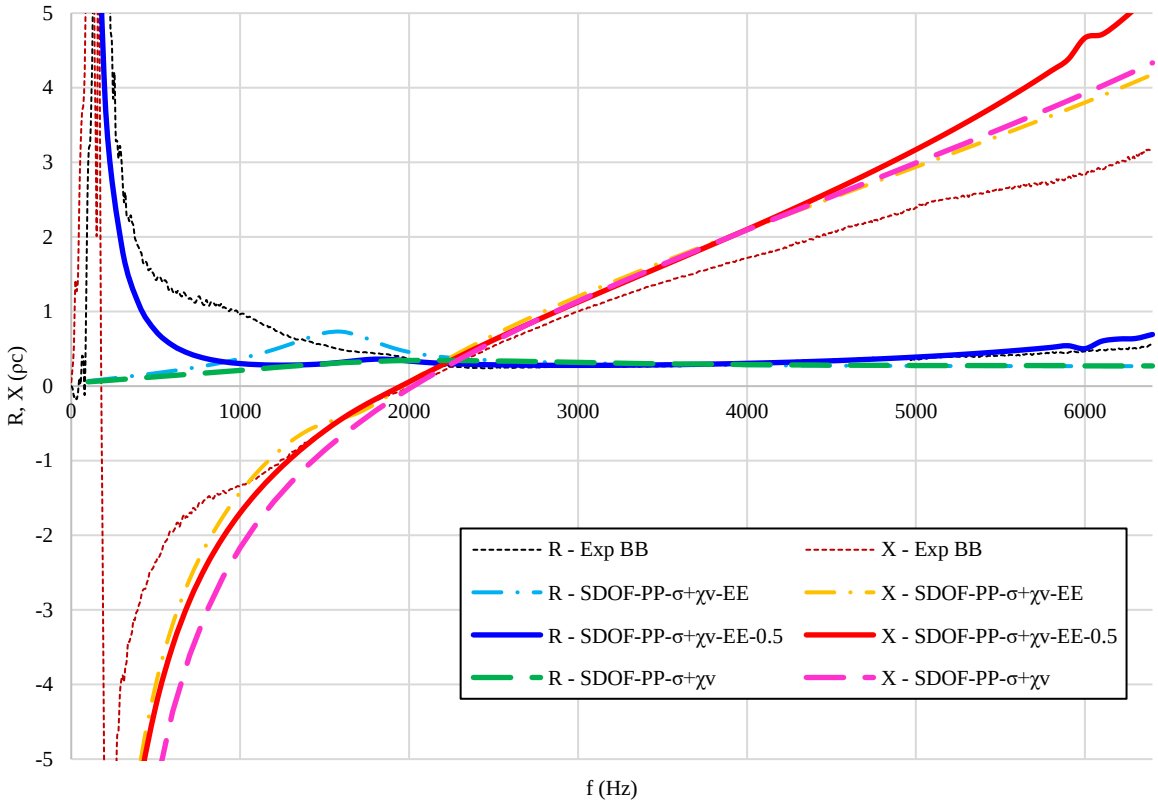

Figure 2.19. Perforated SDOF liner. Measurements vs Predictions, air gap size = 0.5 mm (Pure Tone predictions 130dB, measured broadband OASPL 130 dB)

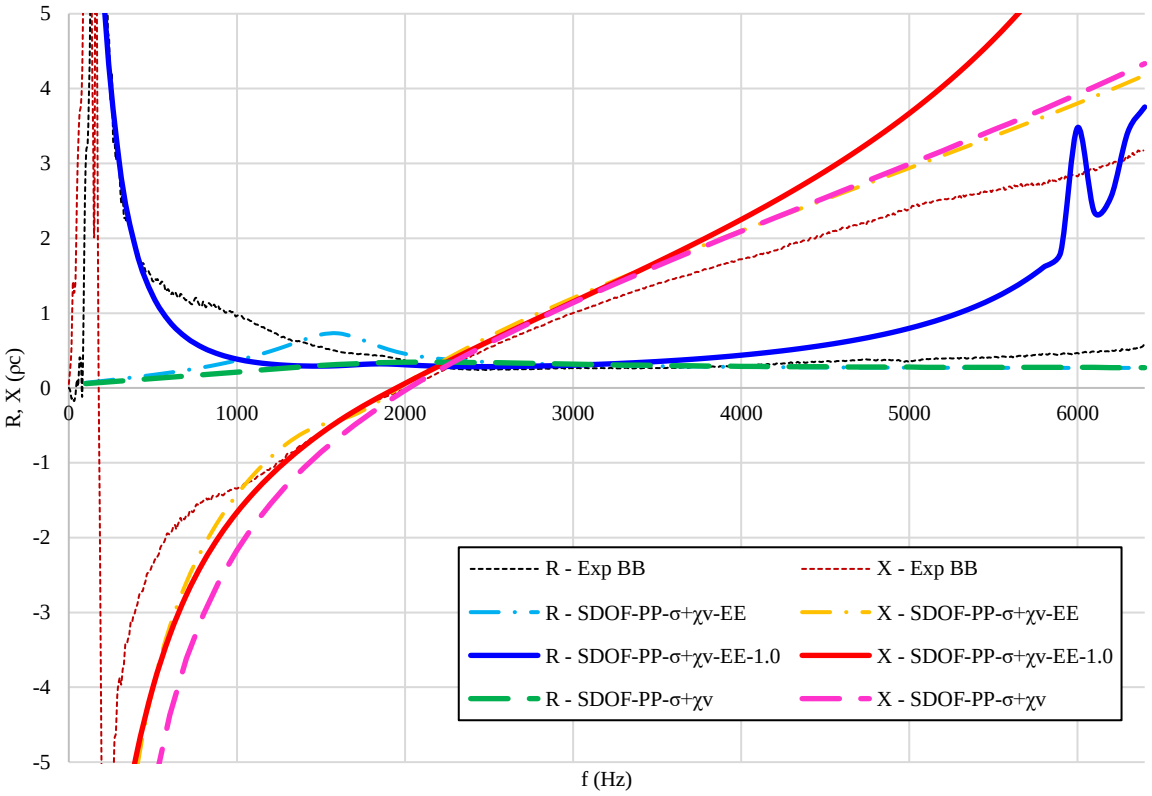

Figure 2.20. Perforated SDOF liner. Measurements vs Predictions, air gap size = 1.0 mm (Pure Tone predictions 130dB, measured broadband OASPL 130 dB)

Regardless of the size of the air gap, all of the SDOF-PP-σ+χ_v-EE-type models do a good job of capturing the increase of the resistance at lower and higher frequencies. However, SDOF-PP-σ+χ-EE-0.5 provides the best match to the measured resistance. For the air gap size smaller than 0.5 mm, the measure resistance is under-predicted, while for higher air gap size, the measured resistance is over-predicted. It should be noted that each model over-predicts the measured high-frequency reactance because the SDOF-PP-σ+χ_v-EE-type models do not simulate the variation of the discharge coefficient with frequency. The measured low-frequency reactance is captured between 1000 Hz and the resonant frequency, while it is under-predicted below 1000 Hz.

The numerical results highlight the need to model both the edge effects and potential sound leakage in order to capture the sensitivity of the impedance to the flanged tube set-up. In the propagation through the adjacent cavities and through the air gap, the sound perturbs a higher volume of air that makes the honeycomb core be perceived with a deeper height, so the reactance registered is less negative [44]. The increase of the perceived honeycomb height h (at low frequencies) increases the effective cavity reactance ($-\cot(kh)$) and this effect has a major influence at low frequencies. Moreover, the sound wave sees the air gap as a narrow-folded cavity in which viscous scrubbing losses occur [32] and the effective liner resistance increases. Nonetheless, the increase in effective resistance can be perceived only at low frequencies, because the longer acoustic wavelengths do not "feel" the fold [6] and the sound wave can propagate from the tube to the far-field through the air gap. At higher frequencies the sound beams, so the sound wave is mainly reflected from the panel back into the impedance tube and it barely propagates in the air gap.

This part of the numerical study investigated the sensitivity of the measured liner impedance to the edge effect and air gap for a flanged normal impedance tube. As noted in [30], the flanged termination does not yield physical results at low frequencies where it globally provides a higher resistance value in comparison to the measurements with a closed tube termination. The latter destructive tests enhance the accuracy of the impedance measurements conducted at low frequencies. The results obtained are generally repeatable and almost insensitive to the local variation of the liner geometry across the surface. Nonetheless, the closed termination requires a sample to be cut from an existing panel, and the cut sample must be sealed to fit the tube dimensions. The flanged tube, on the contrary, allows non-destructive tests to be performed on installed acoustic liners. However, when the flanged tube is used, some considerations must be made:

- The resistance and the reactance data are reliable where the resistance curve is flat, namely above the resonance.
- A perfect sealing rubber between the flange and the liner surface is needed to prevent sound leakage.

In the current study, the influence of the edge effects was also investigated for the case of a SDOF liner covered by a wire-mesh (a linear liner). To this purpose, the impedance of a SDOF linear liner was measured with a flanged NIT and three corresponding numerical models of the linear SDOF liner were developed. The first replicates the tube with closed termination and is labelled as "LIN-PP". The second replicates the tube with a flanged termination and is labelled as "LIN-PP-EE". The last replicates the tube with a flanged termination and an air gap of 0.1 mm size and is labelled as "LIN-PP-EE-0.1". The models derive respectively from SDOF-PP-σ+χ_v, SDOF-PP-σ+χ_v-EE and SDOF-PP-σ+χ_v-0.1, but the perforate plate impedance model is substituted by an impedance model that simulates the features of the wire-mesh plate. This is given by:

$$Z_{fs} = R_{fs} + iX_{fs} \tag{2.26}$$

In Equation 2.26, R_{fs} is the face sheet resistance and X_{fs} is the face sheet reactance and they are set equal to those of the linear panel tested, $R_{fs} = 2\,\rho c$ and $X_{fs} = 0.002\,m$. Preliminary analyses revealed that an air gap size different from 0.1 mm did not capture the sensitivity of the liner impedance to the measurements with the flanged NIT.

The predicted data are achieved by setting the sound source at 130 dB and with the source frequency ranging between 100 Hz and 6400 Hz, with a 100 Hz resolution. In Figure 2.21, the predicted data are compared to experimental results achieved with the flanged NIT, in a broadband test with the OASPL at 130 dB and the frequency ranging between 8 Hz and 6400 Hz, with a 8 Hz step.

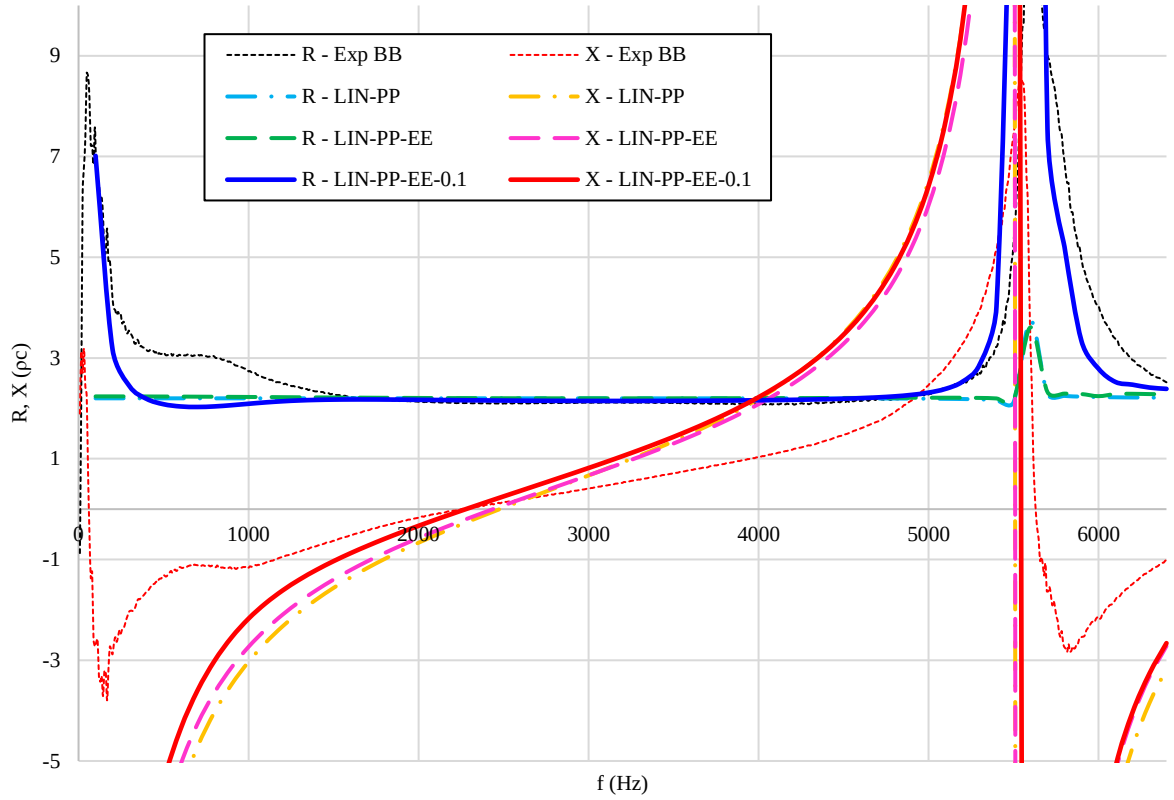

Figure 2.21. Linear SDOF liner. Measurements vs Predictions, air gap size = 0.1 mm (OASPL 130 dB)

The above figure shows that also in case of a linear SDOF liner, the flanged tube termination affects the measured impedance at low frequencies but, as suggested in [30], the linear SDOF liner is less sensitive to the edge effects. This is likely due to the increased damping from the facing sheet. The resultant increased resistance is, in fact, confined to lower frequencies (<1500 Hz).

2.2 COMSOL numerical simulation of two punched aluminium DDOF liners

The numerical study heretofore conducted validates the use of COMSOL for predicting the acoustic properties of a perforate single-layer liner. Provided that the nonlinearity of the face sheet reactance and the effective porosity are introduced in the numerical model, the COMSOL predicted impedance compares well with the measurements and the software can be used to preliminary design the frequency spectrum of a conventional perforated SDOF liner.

In the course of the work, COMSOL has also been used to predict the acoustic properties of two double-layer perforate liners. The predictions have been later compared to the measurements.

Figure 2.22 shows the numerical model used for the simulation of the double-layer perforate liners. The model replicates the liner sample plus the NIT with a closed termination. The width of the liner sample is equal to the tube diameter, so there is no edge effect in the predictions. Two versions of this model were developed, one labelled "DDOF-PP-6" and the other "DDOF-PP-14". The former has a facing sheet $POA = 6\%$, while the latter has a facing sheet $POA = 14\%$. Due to the proprietary nature of the study, the proper measures of DDOF-PP-6 and DDOF-PP-14 are not presented, but their main features are extensively discussed.

In DDOF-PP-6 and DDOF-PP-14, the adopted physics is nearly identical to the physics adopted in SDOF-PP. In Figure 2.22, the grey regions indicate the application of pressure acoustics in the frequency domain. Along the external boundaries of the sample and the tube, the sound hard boundary conditions are imposed, while at the top of the tube the source of sound plane-wave is set. The face sheet is simulated with a perforated plate while the internal porous layer, commonly called septum, is characterized by the following impedance features:

$$Z_{septum} = R_{septum} + iX_{septum} \tag{2.27}$$

R_{septum} is the septum resistance and is defined by a linear function dependent on the acoustic velocity through the parameters A_{septum} and B_{septum}, given by

$$R_{septum} = A_{septum} + B_{septum}V \tag{2.28}$$

The definition of the septum resistance resembles the definition of the resistance proposed for the perforate plate in Equation 2.7, except that the intercept is much greater for a porous layer and the slope is reduced. A_{septum} and B_{septum} are obtained through the following relations:

$$\begin{cases} A = R_{septum_{105\ cm/s}} - 105 \cdot B \\ B = \dfrac{R_{septum_{105\frac{cm}{s}}}}{\dfrac{20 \cdot NLF - 200}{1 - NLF} + 105} \end{cases} \tag{2.29}$$

In Equation 2.29, $R_{septum_{105\ cm/s}}$ is the septum resistance measured at $V = 105\ cm/s$ and NLF is the nonlinearity factor, given by

$$NLF = \frac{R_{septum_{200\frac{cm}{s}}}}{R_{septum_{20\frac{cm}{s}}}} \tag{2.30}$$

with $R_{septum_{200\ cm/s}}$ and $R_{septum_{20\ cm/s}}$ being the septum resistance measured respectively at $V = 200\ cm/s$ and $V = 20\ cm/s$. The data $R_{septum_{105\ cm/s}}$ and NLF were obtained in a series of pure tone tests near resonance performed with increasing SPL, from 130 dB to 150 dB, with a step of 5 dB, in a normal acoustic incidence set-up.

In Equation 2.27, X_{septum} corresponds to the septum reactance and in both the models is set to $X_{septum} = 0.0002\ m$, as Leonardo experience suggests.

Figure 2.23 shows the numerical model that simulates the double-layer liner plus the NIT tube with a flanged termination. Two versions of the model were developed and are respectively labelled as “DDOF-PP-6-EE” and “DDOF-PP-14-EE”. Both have identical characteristics to the corresponding model with closed tube termination, if not for the extended width of the liner sample. In DDOF-PP-6-EE and in DDOF-PP-14-EE the liner width is four times the width of the cavity. The previous analysis (see 2.1.5), in fact, shows that the use of a liner model with four cavities do a good job in predicting the sensitivity of the measured impedance to the tube with flanged termination.

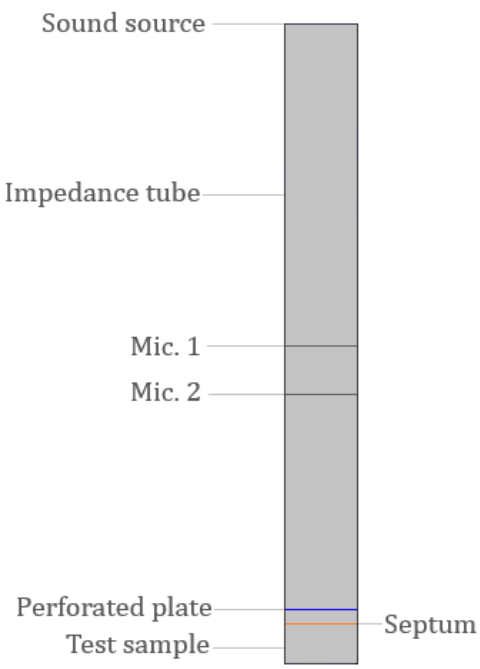

Figure 2.22. DDOF-PP-type model

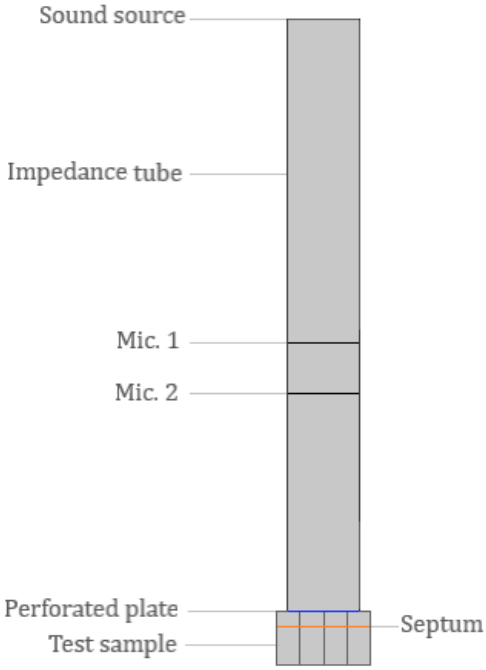

Figure 2.23. DDOF-PP-EE-type model

The two models were numerically analysed by setting the source SPL at 130 dB and 150 dB, with the frequency source ranging from 1000 Hz to 6000 Hz, with a 100 Hz step. In Figure 2.24, Figure 2.25, Figure 2.26 and Figure 2.27, the predictions are compared to the measurements.. The measurements were carried out in a normal impedance set-up with a flanged tube at 130dB and 150dB OASPL.

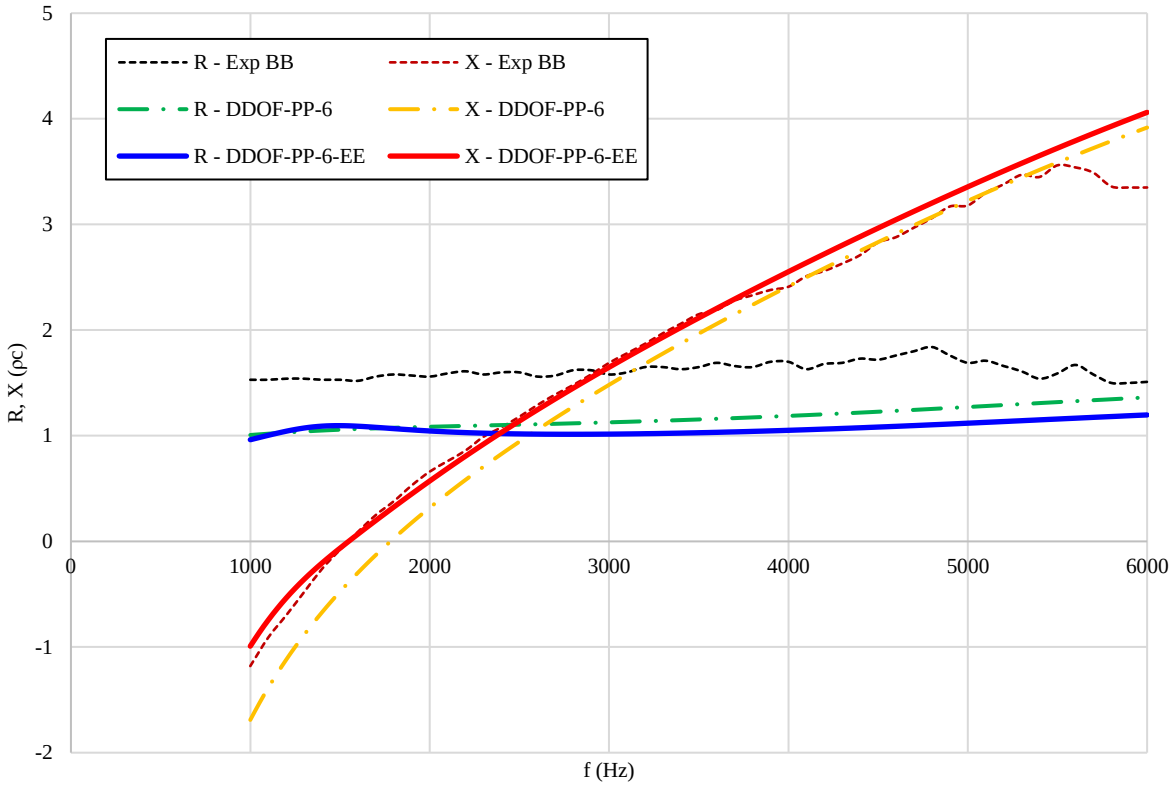

Figure 2.24. Perforated DDOF liner, POA=6%. Measurements vs Predictions (OASPL 130 dB)

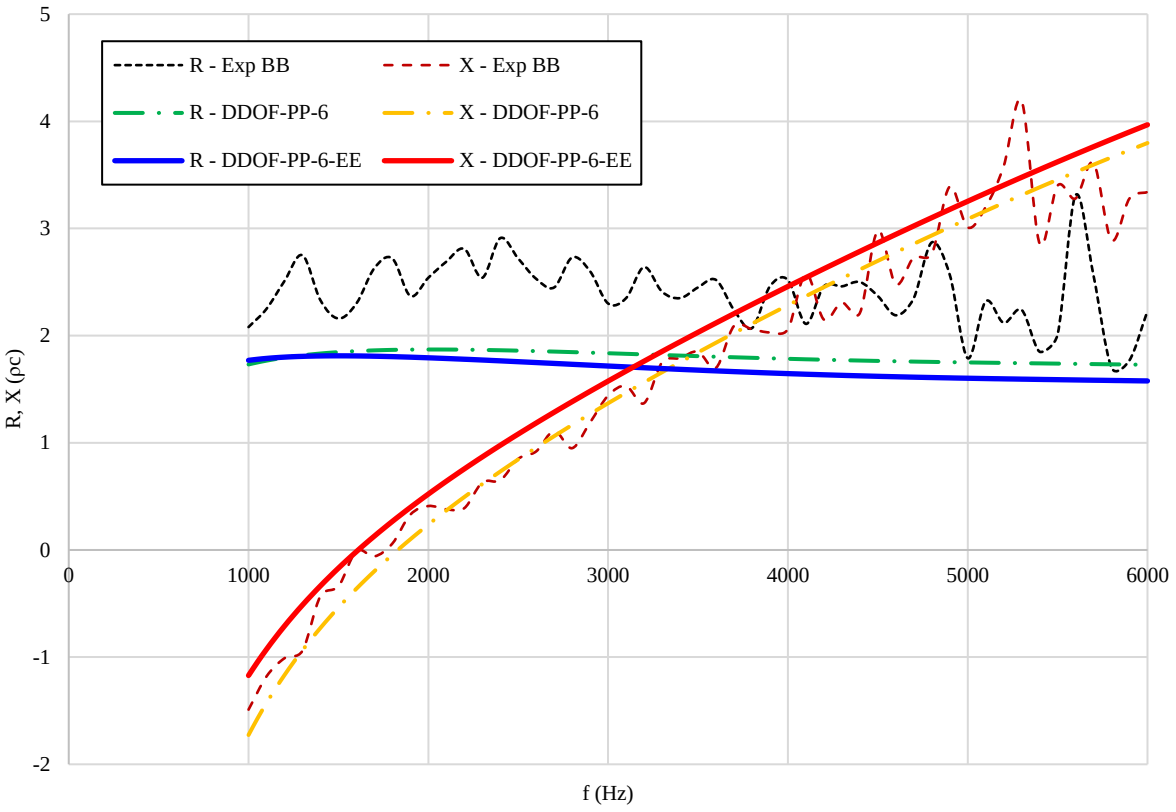

Figure 2.25. Perforated DDOF liner, POA=6%. Measurements vs Predictions (OASPL 150 dB)

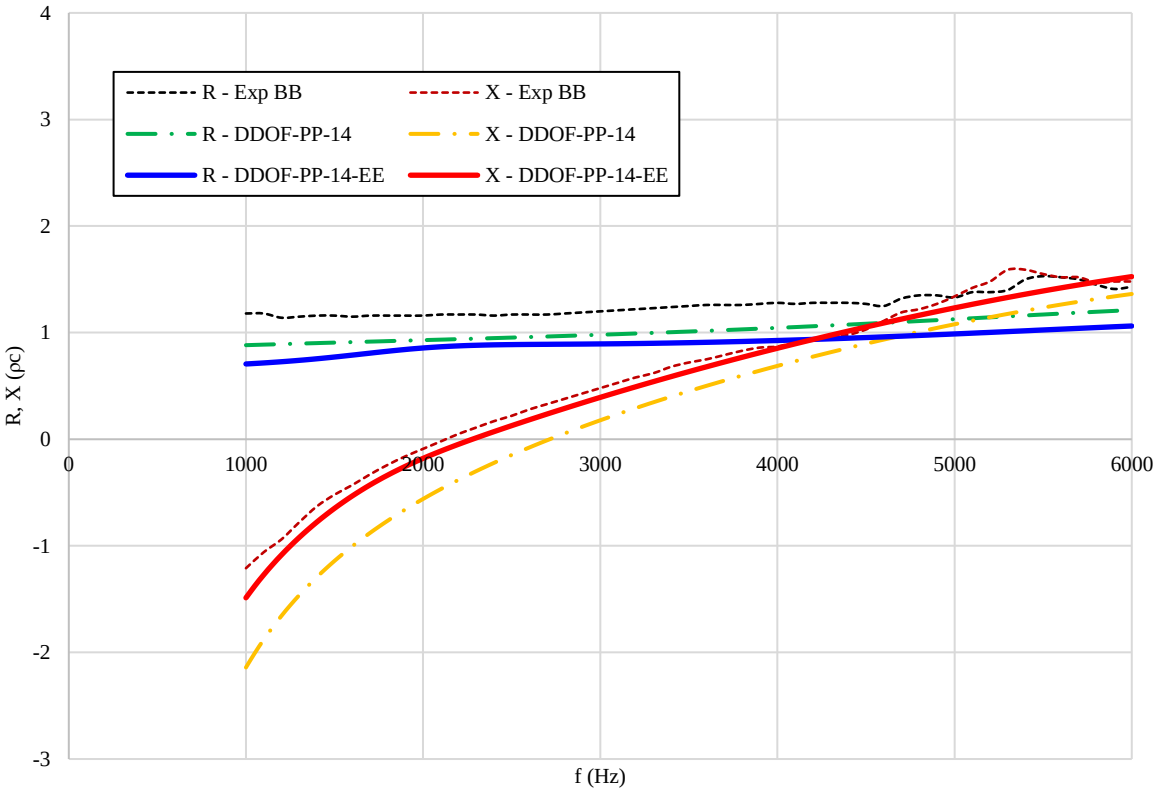

Figure 2.26. Perforated DDOF liner, POA=14%. Measurements vs Predictions (OASPL 130 dB)

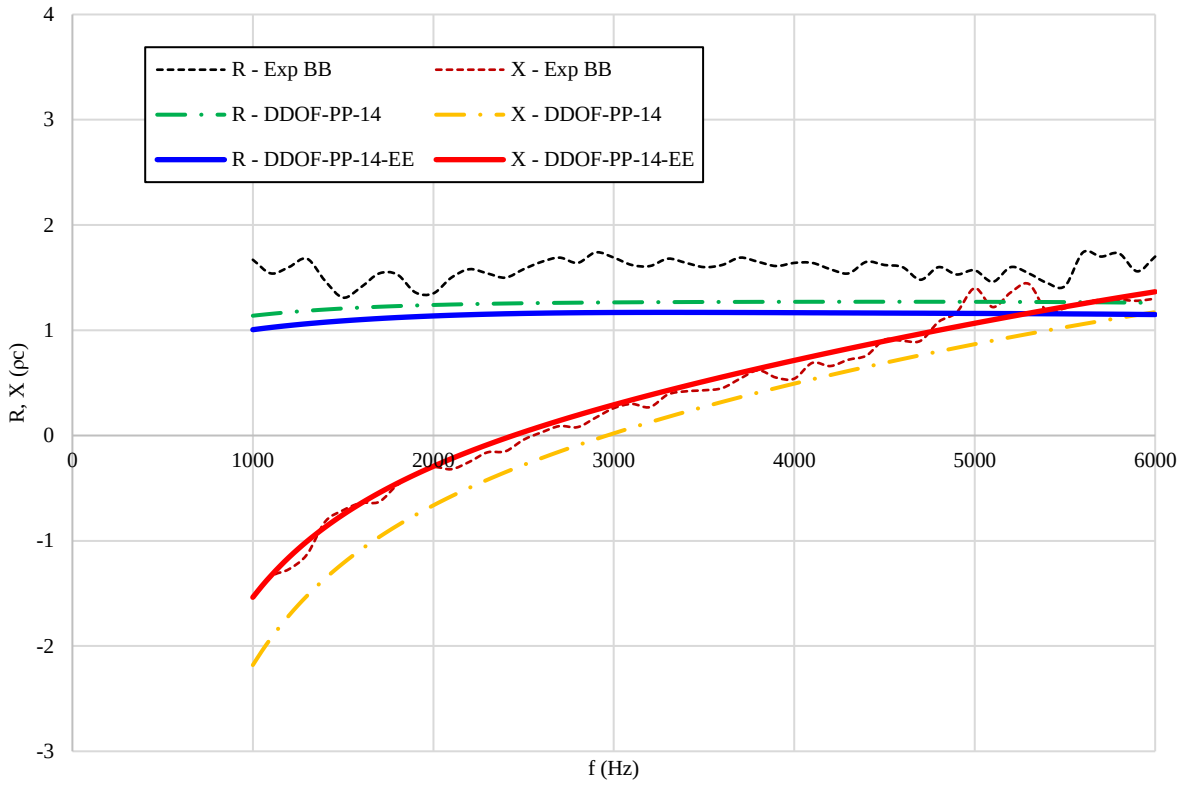

Figure 2.27. Perforated DDOF liner, POA=14%. Measurements vs Predictions (OASPL 150 dB)

The figures above show good first order agreement between the measured and predicted reactance with a flanged tube. On the contrary, the reactance predicted by the models with the closed termination underestimates the measured reactance. In DDOF-PP-6-EE at 130dB, the agreement degrades at higher frequencies (>5500 Hz), because the sensitivity of the face sheet reactance to the source frequency has not been included. On the contrary, the comparison between the DDOF-PP-14-EE and the measured reactance is successful over the entire frequency range considered. After all, as given in Equation 2.12, the inertance is inversely proportional to the panel porosity, so the influence of frequency on m_{fs} is reduced for $POA = 14\%$ rather than for a $POA = 6\%$. Both in DDOF-PP-6-EE and in DDOF-PP-14-EE, the reactance reduces with increasing SPL, and no face sheet reactance correction is required. As observed in [16], the impedance of a DDOF panel is predominantly controlled by the septum rather than by the face sheet, so the sensitivity of the face sheet inertance to the SPL is of second order.

As far as the resistance is concerned, in all the models the predicted resistance significantly under-predicts the measured resistance with the mismatch increasing for the lower porosity. The data may differ due to a lower face sheet effective open area or even because the hypothesis of plane wave propagation in the space comprised between the perforate panel and the septum is wrong. Once the sound wave passes through the face sheet, the plane wave is perturbed and the local perturbations decay exponentially going further from the face sheet. However, as the space between the perforate panel and the septum is very limited, the local perturbations to the plane wave could not have still decayed and the hypothesis of plane wave could not be representative of the sound wave. Further investigations are required in order to identify the reason(s) for the mismatch between the predicted and the measured resistance. Nonetheless, further investigations on the difference between the measured and the predicted resistance go beyond the scope of this work. The various DDOF-PP-EE-type models adequately capture the

frequency spectrum of the measured impedance and the agreement is considered satisfactory for the purpose of this study. The comparisons confirm that COMSOL can be effectively used also to preliminary design the impedance spectrum of double-layers liners.

It should be noted that the measured impedance is affected by the edge effects below the resonance frequency in the above figures. Clearly, further measurements are required below 1000 Hz to assess how the influence of the edge effects on the measured results at lower frequencies. However, as suggested in [30], with panel of high porosity (>6-7%), the sensitivity of the measurements to the presence of a flanged termination is limited and the accuracy of the results at lower frequencies increases. Finally, the superimposed impedance oscillation registered in Figure 2.25 and Figure 2.27 is likely due to a varying SPL of the sound wave impinging on the liner surface, that varies with frequency [44] and dominates at higher source SPLs.

As a side note, the predicted acoustic characteristics of SDOF and DDOF liners are compared to briefly overview the main differences between the two conventional acoustic treatments. Figure 2.28 provides a comparison between the normal incidence sound absorption coefficient bandwidth of the single-layer liner and the double-layer liner, respectively achieved with SDOF-PP-$\sigma+\chi_v$ and DDOF-PP-6. Both the models simulate a normal impedance tube set-up with a closed termination.

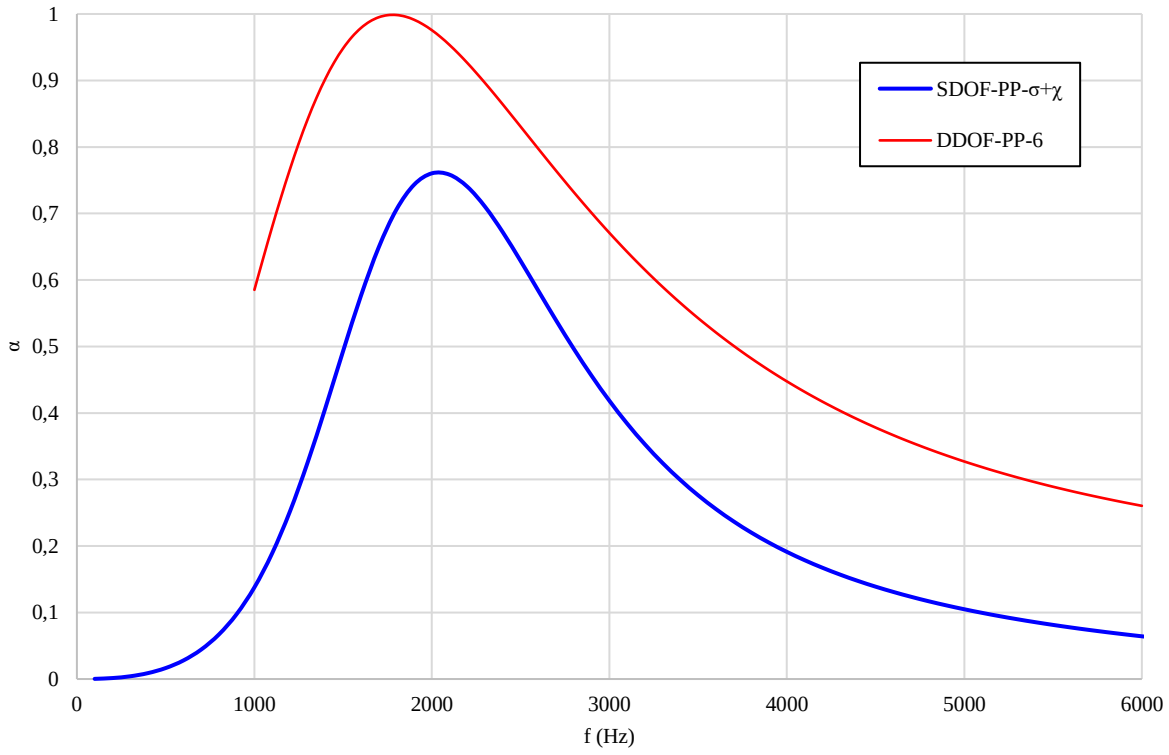

Figure 2.28. Normal incidence sound absorption coefficient α

Despite the different frequency for peak normal incidence absorption, which is due to the differing geometries, the main difference between the single-layer and the double-layer liner is the extension of the frequency bandwidth in which the noise is suppressed. The SDOF liner is effective in a narrow bandwidth, which is usually about an octave of the resonant frequency [16]. The SDOF liner is designed to tune for maximum sound absorption in the frequency band containing the single fan tone of greatest concern [16]. The principal design variables are the honeycomb

core height h and the face sheet geometry, that control the definition of the resonant frequency through the following relation (extracted from Equation 2.9):

$$X_{fs} - \cot(kh) = 0 \tag{2.22}$$

On the contrary, the DDOF is an effective noise absorber within about two octaves of the resonant frequencies [16], and it can be carefully designed to extend the useful bandwidth to cover the BPF and its next two harmonics. The main design variables are the face sheet geometry, the septum characteristics, the honeycomb core height, and the distance of the septum from the face sheet. The design of the double-layer liner is more complex than the SDOF design, but it increases sound absorption over a wider frequency bandwidth.

For the sake of clarity, it should be noted that both SDOF and DDOF liners are principally meant at working with grazing flow in non-normal acoustic incidence conditions [43] [25]. Their sound absorption performance in their usual working conditions will differ from those depicted in Figure 2.28. However, the figure clarifies that the single and double-layer liners are narrowband acoustic treatments and they can abate noise only over a limited frequency range, centred around the resonant frequency. They are not expected to successfully absorb broadband noise, and they may be ineffective in reducing noise of high BPR engines, where broadband acoustic treatments are required.

2.3 Chapter II: Final remarks

The purpose of the study was to confirm the ability of COMSOL 5.4 to predict the acoustic properties of conventional acoustic liners, currently used in the nacelles for the abatement of the engine fan noise. The validity was verified in previous studies [39] [40]. However, it has been demonstrated (and improved) also in the current work, along with providing an assessment of measurement sensitivities, before developing broadband liners with innovative configurations (see Chapter III and Chapter IV). Different numerical models of three conventional liners manufactured in Leonardo have been developed and the numerical results have been compared to the corresponding measurements. The analysis led to some interesting outcomes, that are recapped below:

- The embedded COMSOL model of the perforate plate impedance does not account for the non-linearity of the face sheet reactance. Pure tone tests must be performed on the panel to define a linear curve $X_{fs} - V$ fitting the experimental data. This curve can describe the sensitivity of the face sheet reactance to the acoustic velocity.
- The embedded COMSOL model of the perforate plate impedance must be used with the effective percentage open area $POAeff$. $POAeff$ can be extracted from pure tone tests performed at resonance with increasing SPL, or, alternatively, with broadband measurements.
- The measurements performed using a NIT with a flanged termination affects the measured impedance at lower frequencies (and sometimes even at higher frequencies). The influence on the results is caused by edge effects and potential sound leakage that may occur between the flange termination and the liner surface. Some numerical models were developed to account for the flanged tube and they were shown to capture the sensitivity of the measurements to the use of the flanged NIT.

- A numerical model that simulates a normal acoustic incidence set-up with no flow can be successfully used to design acoustic panels, using a sample holder set-up. It may also be used to model flanged measurements.

The considerations related to the edge effects will be very useful in Chapter III in the analysis of the results achieved with a three-dimensional numerical model. A numerical model simulating a normal incidence acoustic set-up with no flow is then used in Chapter IV to design an innovative broadband liner.

3. Simulation techniques for broadband liners with a complex configuration

In October 2019, at the Acoustic Division of Leonardo Aircraft, a sample of a broadband liner was designed and manufactured to determine whether the innovative concepts and the additive manufacturing processes proposed in previous studies [32] [33] [34] [37] [6] can be successfully used for achieving promising sound absorption performance over a wide frequency bandwidth.

The broadband liner was submitted to a series of experimental tests to verify the liner absorption and its properties were numerically investigated with COMSOL 5.4. The numerical study reported here has identified some relevant modelling techniques to adopt for a simplified simulation of broadband liners with a complex configuration. Relatively little detail of the COMSOL modelling of these types of configuration has been provided in the literature. The validity of these modelling techniques has therefore been evaluated and described in this chapter. This chapter finishes with a summary of the main outcomes of the numerical study.

3.1 Principal characteristics of the 3D printed liner and measured impedance

The original broadband liner sample was 3-D printed using stereolithography. It has a core containing complex cavities, without any face sheet bonded on the surface, as the focus of the design was to investigate the reactive performance of these types of cavity. The square sample configuration was designed by repeating a 4x4 cavity cluster twenty-five times within the liner extent. The 4x4-cavity cluster is formed by repeating four times along its surface a cluster composed by a 3x1-cavity cluster plus a straight cavity at its side. Hereinafter, the sample is labelled as “3D-LS”, the 4x4 cavity cluster is labelled as “3D-4CC”, and the 3x1-cavities cluster with the side cavity added as “3D-3+1CC”. Among the four cavities composing the 3D-3+1CC, one is folded and other three are straight. The cavities are square, of variable effective centreline length, and are arranged to avoid the presence of dead volume. All the sample cavities have the same width and are separated by axial and spanwise partitions whose thickness is a tenth of the cavity width. Due to the proprietary nature of the study, the actual geometry of the sample is not provided here; however, in the following figures, detailed drawings of the sample and of its basic clusters are provided.

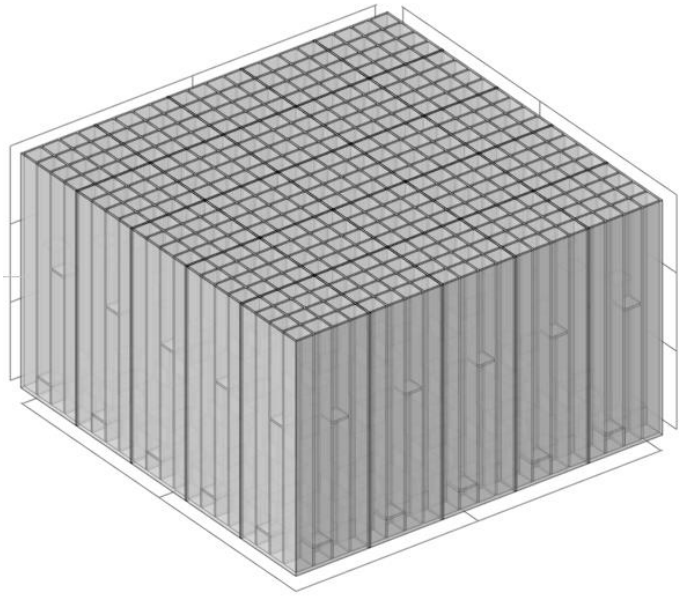

Figure 3.1. 3D-LS

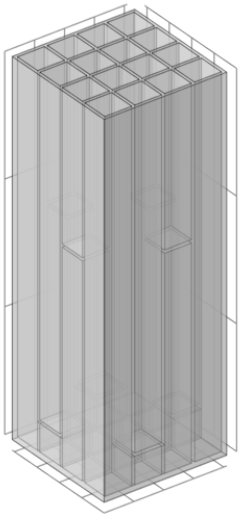

Figure 3.2. 3D-4CC

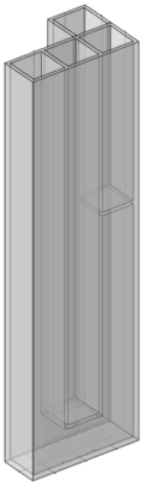

Figure 3.3. 3D-3+1CC

The impedance of the sample was measured in a series of tests using a flanged Normal Impedance Tube (NIT), following the Two-Microphone Method [14] (TMM). During the test, the 3D-LS impedance was measured in three different positions across the liner surface to monitor how the liner acoustic characteristics change as a function of test location. Measurements were made using a 130dB OASPL broadband signal ranging from 8 Hz to 6400 Hz with output at a resolution of 8Hz. The measured resistance and reactance of 3D-LS are provided in Figure 3.4.

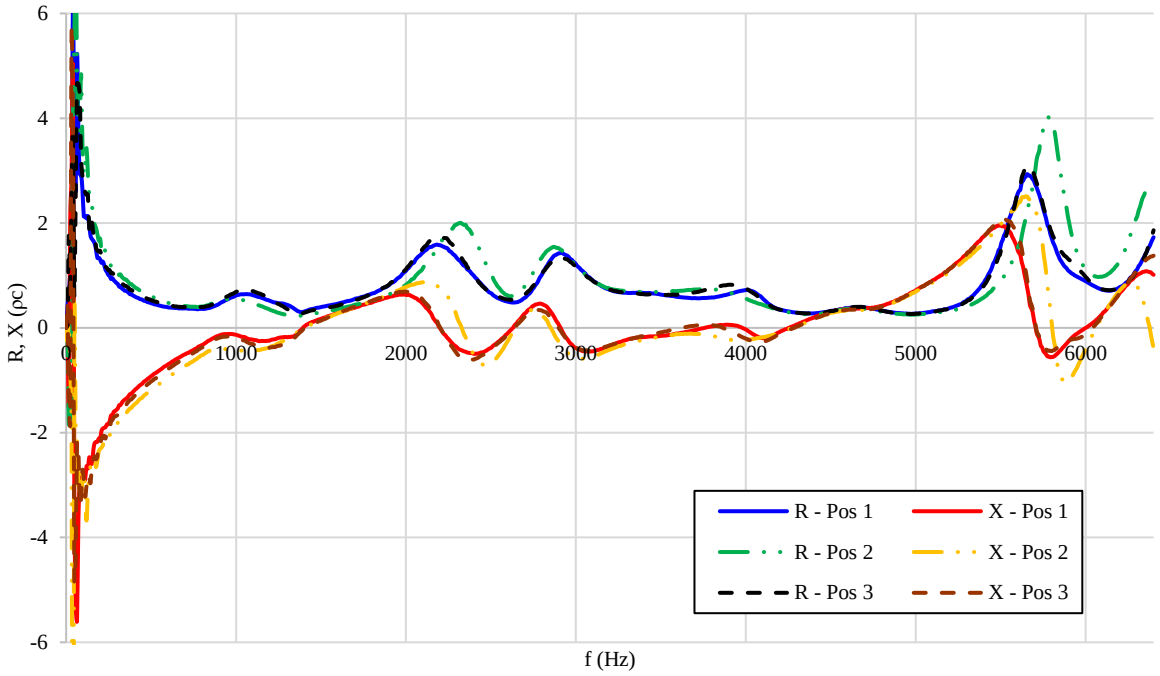

Figure 3.4. R, X of 3D-LS, OASPL 130 dB – Experimental results

Figure 3.4 shows a favourable comparison between the data measured at the three different test locations and the results are similar. The main differences are observed at low frequencies and in the region of the impedance peaks and troughs, but the variations are reasonably limited. At low frequencies (below 1KHz), the differences are mainly due to edge effects, while at other frequencies the mismatches between the results are linked to the variation of the liner geometry across the surface covered by the 29mm diameter NIT. Therefore, despite the complexity of the sample configuration, its impedance does not significantly vary with test location, and its acoustic properties are quite uniform across the surface.

3.2 Main physical features of the numerical models

In the course of the study, numerical models of varying complexity have been developed to investigate the acoustic characteristics of the liner core. The models have been realized in COMSOL 5.4, whose efficiency in predicting the impedance of narrowband and broadband liners was previously verified respectively in Chapter 2 and in [40]. In the numerical models, the liner impedance is calculated according to the Two-Microphone Method in a simulation of the normal impedance tube set-up used in the experimental phase. All the numerical models developed share a common formulation of the physics, which accounts the main acoustic features of the liner sample and the NIT. Figure 3.5 and Figure 3.6 provide an example of a numerical model and the domains and boundaries where the physics is defined.

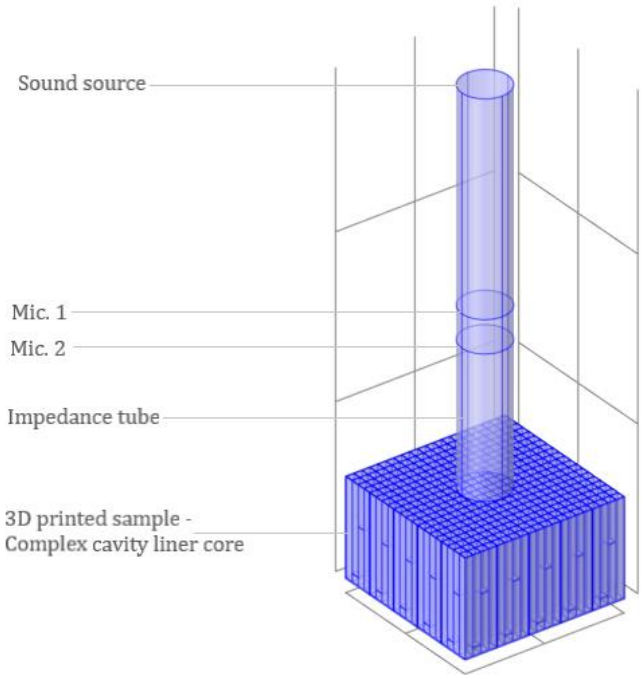

Figure 3.5. 3D-LS-C and main physical features/1

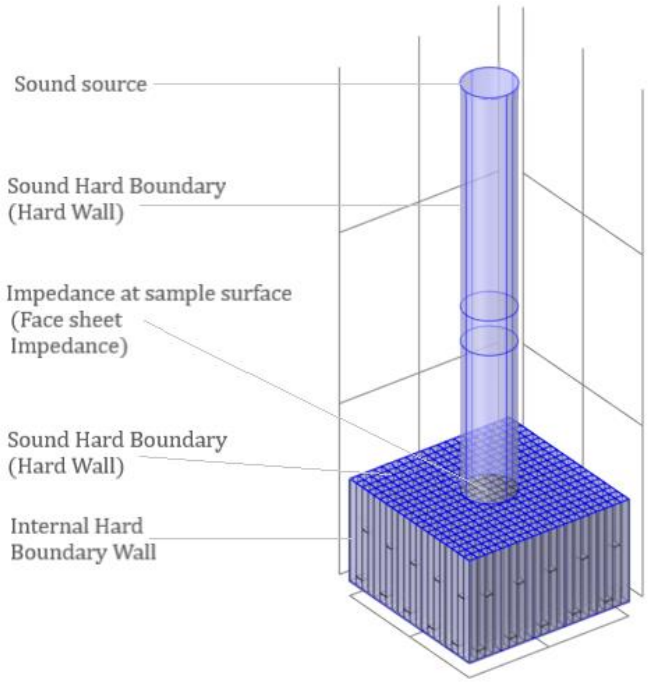

Figure 3.6. 3D-LS-C and main physical features/2

The TMM numerical procedure for the measurement of the liner impedance is extensively explained in Chapter 1, but it is herein briefly recapped, referring to the numerical model provided in the figures above. The plane wave sound field is generated by the acoustic drivers located at the top of the impedance tube ("Sound source" in Figure 3.5). It travels along the tube and impinges on the liner surface ("Face sheet Impedance" in Figure 3.6) where it is partially absorbed and partially reflected. The combination of the incoming and the reflected wave creates a standing wave pattern in the tube, whose complex acoustic pressure is measured by two microphones ("Mic. 1" and "Mic.2" in Figure 3.5). These microphones are located along the tube wall, at two calibrated distances from the

liner surface. The measures of the complex acoustic pressure are used for assessing the frequency-dependent quantities of the normal sound absorption coefficient and normalized resistance and reactance of the liner in absence of mean flow [31].

Figure 3.5 and Figure 3.6 highlight the model domains where the pressure acoustics field in the frequency domain and the initial conditions are set. Figure 3.6 shows the surfaces where the boundary conditions are imposed. Hard wall conditions are imposed along the boundaries of the impedance tube and along the external boundaries of the sample; the hard wall conditions are set also along the boundaries of internal partitions of the sample. The manufactured walls are considered sufficiently rigid to maintain the acoustic isolation between adjacent cavities. Finally, at the sample surface covered by the tube, the physical characteristics of a porous sheet are introduced through the impedance Z_{fs}

$$Z_{fs} = R_{fs} + i\mathrm{X}_{fs} \tag{3.1}$$

with R_{fs} indicating the face sheet resistance and X_{fs} the face sheet reactance. Both Z_{fs}, R_{fs}, and X_{fs} are quantities normalized by ρc, where ρ is the air density and c is the speed of sound.

As indicated earlier, a facing sheet is not bonded over the 3D-LS sample and the liner consists of only the complex core. Recent studies [32] demonstrated that 3D printed liners with narrow cavities damp the acoustic energy even without any face sheet because of the viscous losses that arise in narrow cavities; on the contrary, liners with wide cavities lowers the damping of the acoustic energy because the viscous losses are largely eliminated. In the current study, there are no thermo-viscous losses on the cavity walls, and the possible damping of acoustic energy in relatively narrow cavities is modelled through the inclusion of a surface impedance over the liner. In this way, the problem is solved uniquely in the acoustic domains and no other physical domain, as thermo-viscous acoustics must be introduced for capturing possible viscous losses. The resistance term R_{fs} is adjusted to match the measured level of the panel, while the inertance term X_{fs} is set to zero. In fact, preliminary analyses verified that the numerical results are barely sensitive to the presence of the inertance term and X_{fs} is set to zero for simplicity. Hence, the impedance Z_{fs} at the sample surface will be quoted simply with its resistance term R_{fs}.

In the following sections, the various numerical models developed for the calculation of the sample impedance are presented and their main features are exhaustively discussed.

3.3 Assessment of the simulation techniques

3.3.1 Effect of cavity wall thickness

The first numerical models developed in the study are labelled as “3D-LS-C”, “3D-LS-TH0-C” and “3D-LS-TH0-C.a” and they are aimed at verifying the effect of the cavity wall thickness in the prediction of the overall liner impedance. The internal partitions are considered as sufficiently rigid and reflective so that they do not transmit the sound wave between adjacent cavities. The wave propagation inside the liner core is not expected to change if the internal partitions are modelled with two-dimensional or with three-dimensional reflective elements. However, the internal partitions actively contribute to the definition of the liner impedance and, when their thickness th_w is

set to zero in a model, the width of the cavities must be changed to correctly capture their impact on the liner impedance. The following points summarise the main features of the three models developed:

- The model 3D-LS-C replicates the 3D-LS liner sample and the normal impedance tube set-up in detail. All the cavities have the same width w_i, and are separated by axial and spanwise partitions whose thickness th_w is a tenth of the cavity width. The internal partitions are modelled with three-dimensional reflective elements.
- The model 3D-LS-TH0-C is a variant of 3D-LS-C with the thickness of the internal partitions th_w set to zero, and the width of the cavities increased from w_i in 3D-LS-C to w_j to ensure almost the same impedance of 3D-LS-C; in 3D-LS-TH0-C, the internal partitions are modelled with two-dimensional reflective elements.
- 3D-LS-TH0-C.a retains the zero wall thickness of 3D-LS-TH0-C and adjusts the width of its cavities w_k equal to the width of the 3D-LS-C cavities w_i. Also in 3D-LS-TH0-C.a, the internal partitions are modelled with two-dimensional reflective elements.

In each of the three models, the resistance at the sample surface is initially set equal to $R_{fs} = 0\ \rho c$: at this stage of the study, the models are mainly developed to validate the best practices of numerical simulation to adopt in the progression of the studies, instead of accurately describing the 3D-LS impedance.

The predicted impedance of each model is obtained with the SPL of the sound source set to 130 dB and the signal frequency ranging between 500 Hz and 6000 Hz, at a wide step (500Hz) to reduce the computational time. Due to the different configurations, the models are meshed differently in the analysis. In 3D-LS-C, the acoustic domains and the internal wall partitions are meshed using free tetrahedral elements. In 3D-LS-TH0-C and 3D-LS-TH0-C.a the acoustic domains are meshed using free tetrahedral elements, while the internal wall partitions are meshed using free quadrilateral elements. The various models are extremely finely discretized to be confident in the numerical results and the maximum element size is twenty-five time smaller than the minimum acoustic wavelength of interest. This is more refined than the maximum element size adopted in [39] for a similar analysis, which is eight time smaller than the minimum acoustic wavelength.

A comparison of the predicted reactance for each model assumption with the broadband impedance measurements is shown in Figure 3.7. Only the reactance data are presented because the face sheet resistance R_{fs} in the models is null.

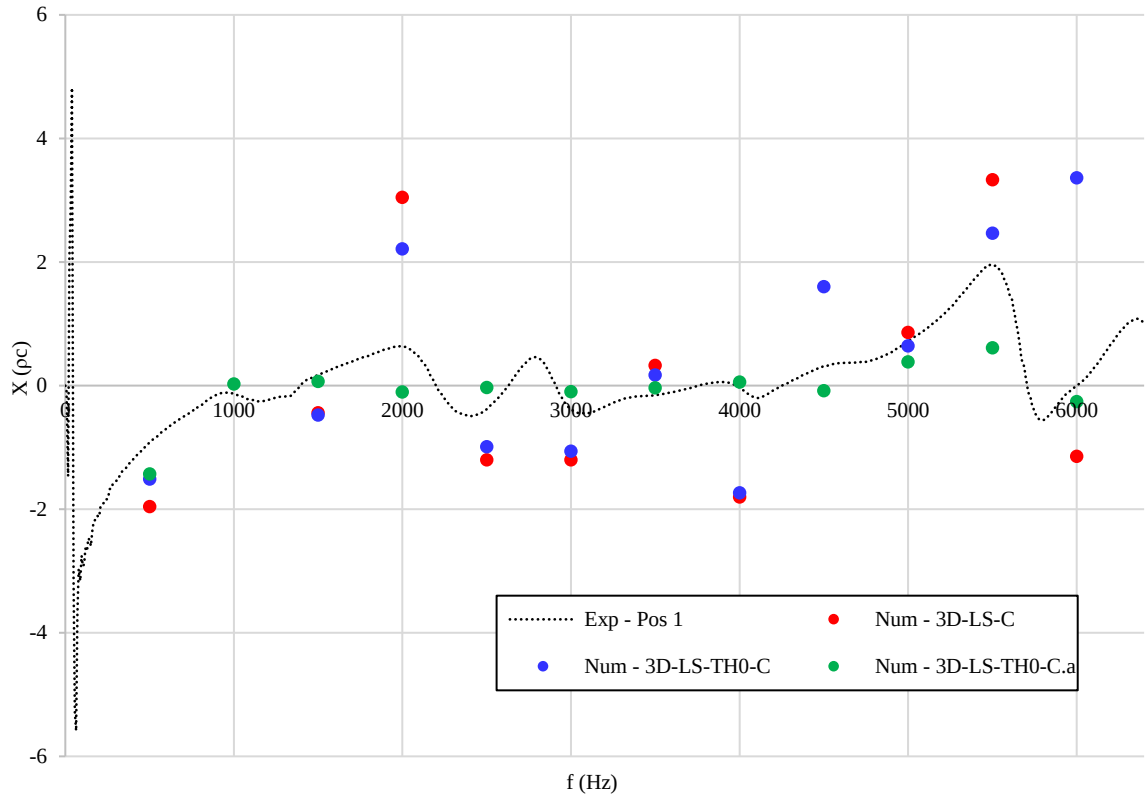

Figure 3.7. Normalized reactance, X

The comparison between prediction and measurement show that the predictions confirm the panel has a desirable broadband reactance characteristic (close to zero), but that the measured reactance is more damped than the predicted reactance, in that it generally remains closer to zero than the predictions. After all, in 3D-LS-C, 3D-LS-TH0-C and 3D-LS-TH0-C.a any source of damping has not been included, as the resistance at the sample surface is set equal to zero.

Figure 3.7 provides a favourable comparison between the predicted data of 3D-LS-C and 3D-LS-TH0-C. They capture the reactance peaks and troughs of the measured data. Apart from below 1000 Hz, where the results are affected by edge effects, and at frequencies close to the reactance peaks and troughs, the difference between 3D-LS-C and 3D-LS-TH0-C are limited and can be neglected. On the contrary, both the 3D-LS and the 3D-LS-TH0-C results differ more greatly from those of 3D-LS-TH0-C.a and the difference is more significant at the frequencies of the reactance peaks and troughs.

The poor agreement between the predictions of 3D-LS-C and 3D-LS-TH0-C.a highlights the sensitivity of the liner impedance to the internal partitions. In 3D-LS-TH0-C.a, the sole reduction of the internal walls without changing the width of the cavities misses the significant contribution of the internal walls to the definition of the liner reactance and the liner impedance of the 3D-LS-C is not preserved. On the contrary, the good agreement between the predictions of 3D-LS-C and 3D-LS-TH0-C confirms that the reduction of the internal walls with the simultaneous increase of the width of the cavities ensure almost the same impedance of 3D-LS-C. The comparison validates the measure of the width w_j used for modelling the width w_j of the 3D-LS-TH0-C cavities (see Equation 3.10). The following procedure shows how w_j has been calculated.

The predicted surface reactance Z_{3D-LS} of the 3D-LS sample represents a good preliminary estimation of the liner reactance that the 3D-LS-TH0-C must provide, despite the approximation introduced (internal walls discretized by two-dimensional elements instead of three-dimensional elements). The impedance Z_{3D-LS} is calculated from the reciprocal of the liner admittance A_{3D-LS}, obtained by combining the weighted admittance A_i of the individual cavities, and the weighted admittance of the internal partitions A_{hw} [39]. The admittances are dimensionless quantities, multiplied by ρc, where ρ is the air density and c is the speed of sound.

$$A_{3D-LS} = \sum_{i=1}^{n} [\sigma_i A_i + (1 - \sigma_i) A_{hw}] \tag{3.2}$$

$$Z_{3D-LS} = \frac{1}{A_{3D-LS}} \tag{3.3}$$

In A_{3D-LS}, the admittance of the internal partitions is estimated around $A_{hw} \approx 1e-7$, while σ_i stands for the ratio of the inlet area of the i-th cavity to the total surface area of the sample. In 3D-LS, with square cavities of width w_i and the width of the sample w, σ_i equals

$$\sigma_i = \frac{w_i^2}{w^2} \tag{3.4}$$

and the estimated A_{3D-LS} becomes,

$$A_{3D-LS} = \sum_{i=1}^{n} \left[\frac{w_i^2}{w^2} A_i + \left(1 - \frac{w_i^2}{w^2}\right) A_{hw} \right] \tag{3.5}$$

A_{3D-LS} is expected to be well simulated with the 3D-LS-C model, that replicates 3D-LS and the NIT features in detail.

In order to maintain the acoustic characteristics of 3D-LS in 3D-LS-TH0-C, its admittance $A_{3D-LS-TH0-C}$ must be equal to the admittance A_{3D-LS}, even though the contribution of the internal partition to $A_{3D-LS-TH0-C}$ is null because of $\sum_{j=1}^{n}\left[(1 - \sigma_j) A_{hw}\right] = 0$.

$$A_{3D-LS-TH0-C} = \sum_{j=1}^{n} \sigma_j A_j = \sum_{i=1}^{n} [\sigma_i A_i + (1 - \sigma_i) A_{hw}] \tag{3.6}$$

In Equation 3.6, the subscript j indicates the characteristic dimensions of 3D-LS-TH0-C, the subscript i the characteristic dimensions of the 3D-LS sample, and σ_j is the ratio of the inlet area w_j^2 of the j-th cavity in 3D-LS-TH0-C to the total surface area w^2 of the sample. In the supposition that all the cavities of 3D-LS-TH0-C and 3D-LS have the same σ_j and the same σ_i, and that the effective centreline length of the individual cavity is preserved passing from 3D-LS-C to 3D-LS-TH0-C, σ_j is derived from Equation 3.6,

$$\sigma_j = \sigma_i \frac{\sum_{i=1}^{n} A_i}{\sum_{j=1}^{n} A_j} + \frac{A_{hw} \sum_{i=1}^{n} (1 - \sigma_i)}{\sum_{j=1}^{n} A_j} \tag{3.7}$$

$$\sigma_j = \sigma_i + \frac{A_{hw} \sum_{i=1}^{n} (1 - \sigma_i)}{\sum_{j=1}^{n} A_j} \tag{3.8}$$

Writing $\sigma_i = \frac{w_i^2}{w^2}$ and $\sigma_j = \frac{w_j^2}{w^2}$ and multiplying both the left and the right-hand side by w^2, the following expression is obtained

$$w_j = \sqrt{w_i^2 + \frac{A_{hw} \sum_{i=1}^{n} (w^2 - w_i^2)}{\sum_{j=1}^{n} A_j}} \tag{3.9}$$

Equation 3.9 defines the width w_j that the cavities must have to preserve the 3D-LS impedance in 3D-LS-TH0-C. w_j depends non-linearly on the width w_i of the cavities in 3D-LS and on the quantity $\sum_{i=1}^{n} (w^2 - w_i^2)$, which is almost equal to the area originally covered by the internal partitions along the 3D-LS surface.

In the 3D-LS-TH0-C, the cavity width w_j is approximated with

$$w_j = w_i + \frac{21}{20} th_w \tag{3.10}$$

This represents the summation of the individual cavity width w_i in 3D-LS with the internal wall thickness th_w amplified by the factor $\frac{m+1}{m} = \frac{21}{20}$, where m is the number of cavities along one side of the sample.

In Figure 3.7, the limited amount of numerical data points cannot completely verify the real effectivity of the 3D-LS-TH0-C in predicting the measured liner impedance. However, it confirms the expected favourable comparison between the results of a detailed model and the results of an approximated one. The time taken to perform the calculation of the liner impedance differs from 3D-LS-C and 3D-LS-TH0-C: the first took 40min while the second took 21min. Hence, the approximated model predicts nearly identical data to those of the detailed model, but it gains in computational time.

Considering the quality of the results and the gain in computational time, the approximation of the internal walls in surfaces is hereinafter adopted and the modelling techniques used in 3D-LS-C and 3D-LS-TH0-C.a are no longer pursued.

3.3.2 Sensitivity of the numerical results to the impedance tube position

In the wake of the tests performed in the experimental phase, the 3D-LS-TH0-C impedance is assessed while shifting the tube position across the liner surface from the original to other two randomly chosen locations. These positions are shown in Figure 3.9 and Figure 3.10 and are respectively labelled as “Pos B” and “Pos C”; Instead, the original position of the tube is provided in Figure 3.8 and is labelled as “Pos A”.

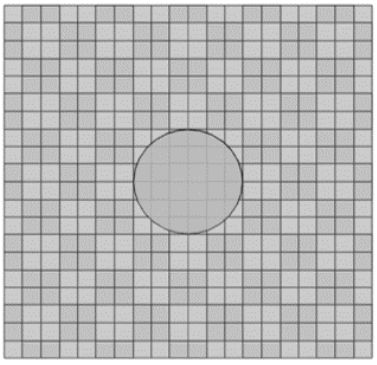

Figure 3.8. POS A, top view

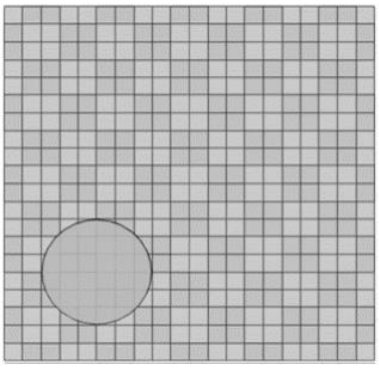

Figure 3.9. POS B, top view

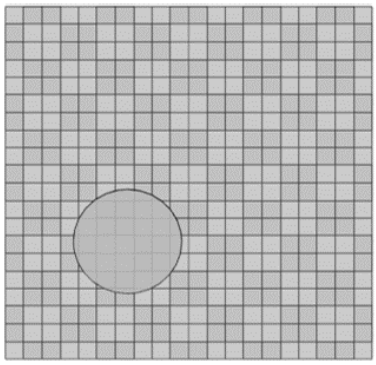

Figure 3.10. POS C, top view

The 3D-LS-TH0-C impedance for the different tube positions is obtained with the SPL of the sound source at 130 dB and by varying the frequency spectrum from 100 Hz to 6400 Hz, with a 100 Hz step. Due to the absence of a facing sheet resistance ($R_{fs} = 0\ \rho c$) in 3D-LS-TH0-C, the numerical results concerning the liner resistance are zero, so they are not represented. The numerical reactance results achieved in the three cases are presented in Figure 3.11.

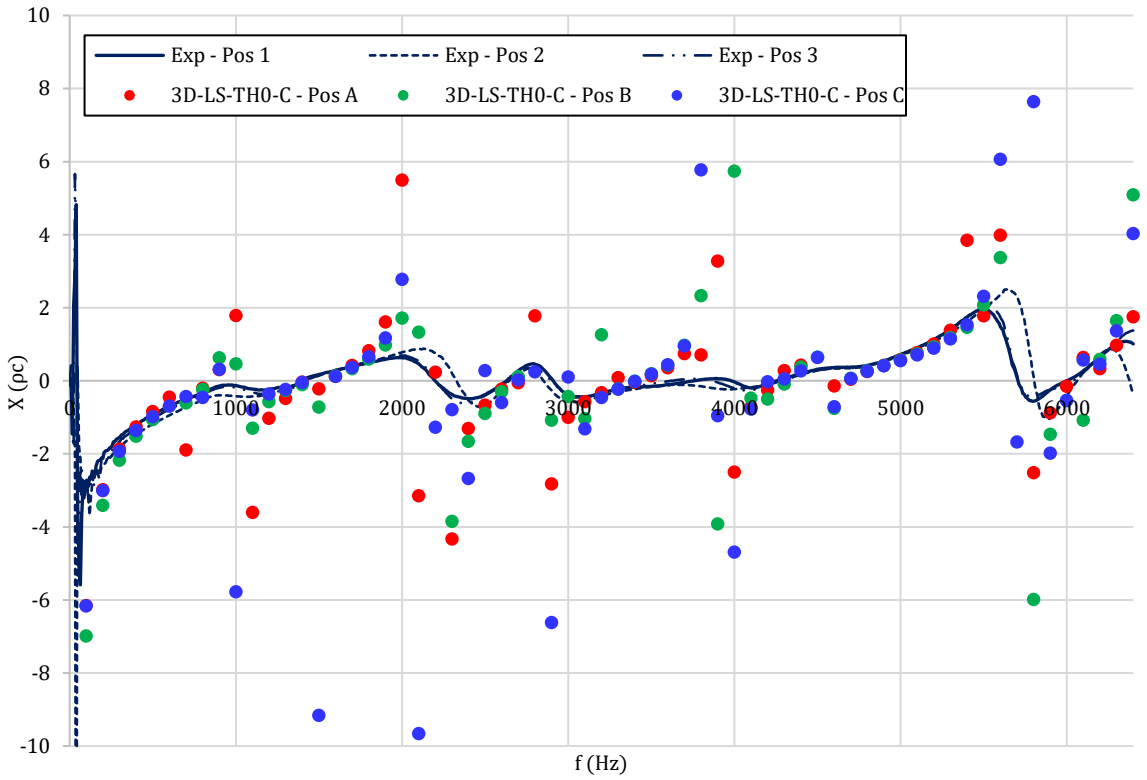

Figure 3.11. Normalized reactance, X

Figure 3.11 shows a favourable comparison between the numerical data of the three different tube positions. The main differences occur at the reactance peaks and troughs and at a few other points. These differences can be neglected and, except at the peaks and troughs of the reactance, they are caused mainly by the variation of the liner geometry across the surface covered by the tube. Hence, the prediction of the liner impedance with the 3D-LS-TH0-C model is generally not greatly affected by the position of the impedance tube and setting the impedance tube in "Pos A" is sufficient for obtaining reliable results. In addition, Figure 3.11 shows a favourable comparison

between the predicted and the experimental data, if not at the frequencies of the reactance peaks and troughs, where the experimental reactance is damped out with respect to that predicted. This observation suggests that the 3D-LS-TH0-C model successfully predicts the frequency content of the liner reactance but, at the same time, misses the simulation of acoustic energy damping that occurs in the liner. In 3.3.4, the simulation of the energy damping is accounted for by adding a face sheet resistance R_{fs}, that is changed from zero to a value that best fits the measured data.

3.3.3 Alternative simulation of the impedance tube

Along with the previous models, an additional simulation of the impedance test condition is realized with the numerical model labelled as "3D-LS-TH0-SQ". This is developed for validating a different way of simulating the impedance tube and its configuration is depicted in Figure 3.12.

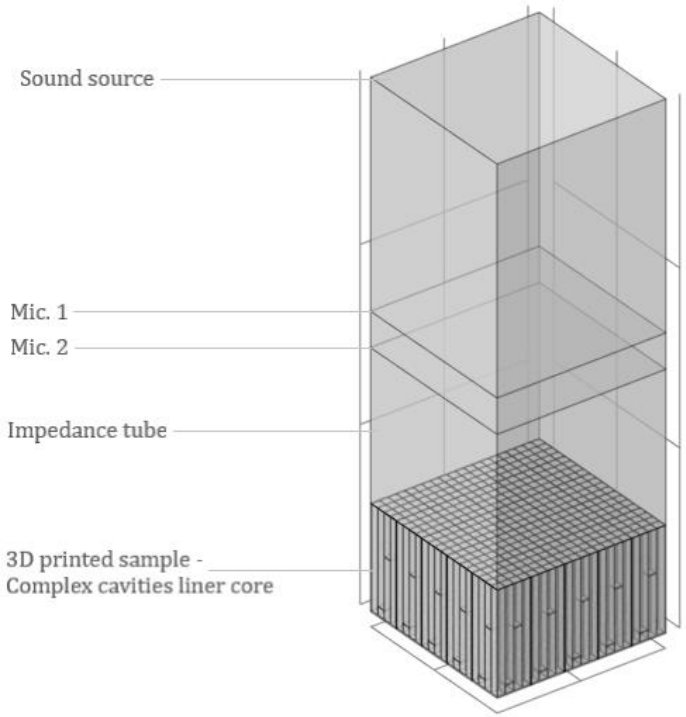

Figure 3.12. 3D-LS-TH0-SQ

The 3D-LS-TH0-SQ features derive from those of 3D-LS-TH0-C, but the impedance tube of circular cross-section is substituted with an impedance tube of square cross-section, with the side equal to the width *w* of the liner sample.

Figure 3.13 provides a comparison between the reactance predicted with 3D-LS-TH0-C and 3D-LS-TH0-SQ and the measured reactance. The numerical results are obtained by setting the SPL of the source at 130 dB and varying the frequency content of the source between 100 Hz and 6400 Hz, at 100 Hz step.

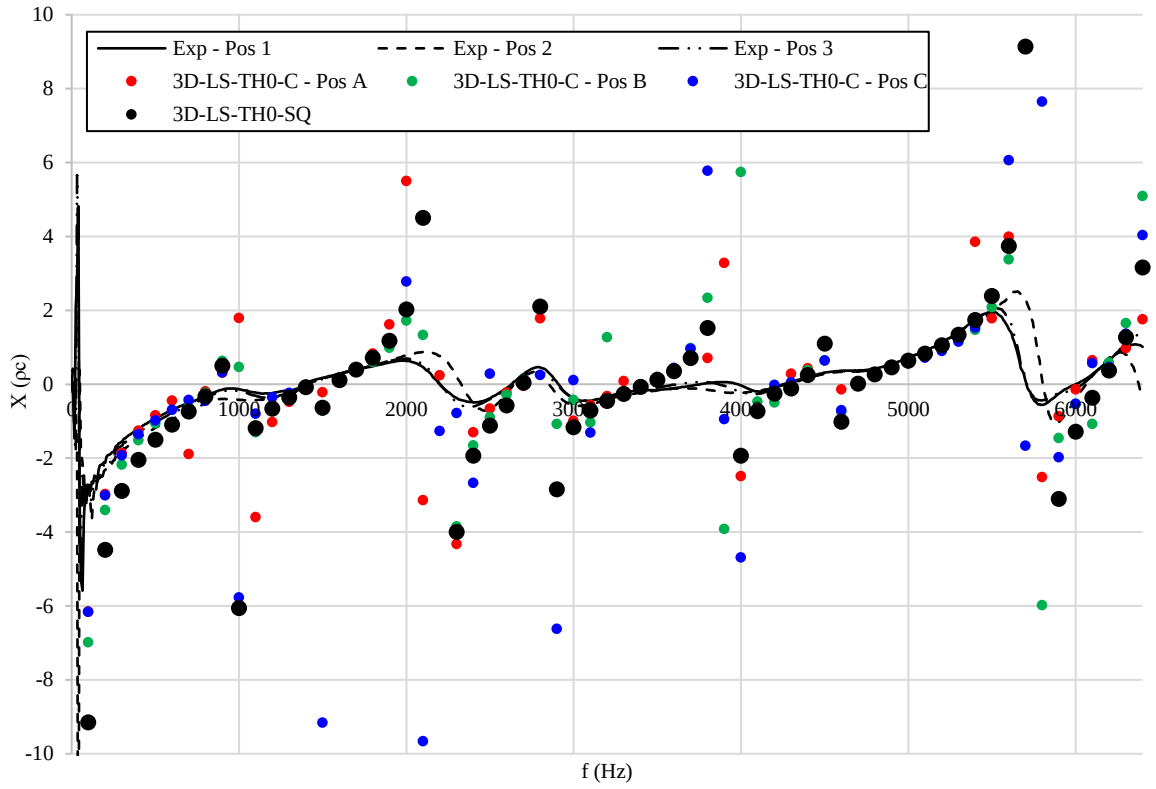

Figure 3.13. Normalized reactance, X

The comparison of the results shows that 3D-LS-TH0-SQ eliminates the variability of the 3D-LS-TH0-C data caused by the different position of the tube. In 3D-LS-TH0-SQ, the liner impedance is indeed averaged over the entire liner surface and not over a smaller local surface as it occurs in 3D-LS-TH0-C. The adoption of a tube that covers the overall liner surface allows the 3D-LS-TH0-SQ model to avoid the edge effects below 1000 Hz, that are predicted by 3D-LS-TH0-C. In fact, as Figure 3.13 shows, below 1000 Hz, 3D-LS-TH0-C better predicts the measured sample reactance. This is not surprising as this circular model reflects the circular geometry of the impedance tube. Nevertheless, the true behaviour of this sample will be reflected in the square model that captures a full, rather than a partial, set of cavities. Hence, the impedance tube is hereinafter modelled with a cross-sectional area that has the same shape and size of the overall liner surface.

3.3.4 Simulation of the energy damping within the liner numerical model

As suggested above, as long as the resistance within the cavities is not simulated, the numerical models cannot predict the energy damping that has been measured in the liner. In order to investigate the most effective way to simulate the energy damping, five versions of 3D-LS-TH0-SQ are developed and in each of them the resistance of the face sheet R_{fs} is set to different values. The values adopted in this study are $R_{fs} = 0\ \rho c$, $R_{fs} = 0.05\ \rho c$, $R_{fs} = 0.1\ \rho c$, $R_{fs} = 0.2\ \rho c$ and $R_{fs} = 0.5\ \rho c$ and the correspondent models are respectively labelled as "3D-LS-TH0-SQ", "3D-LS-TH0-SQ.05", "3D-LS-TH0-SQ.1", "3D-LS-TH0-SQ.2" and "3D-LS-TH0-SQ.5".

The liner impedance is predicted with the SPL of the sound source at 130 dB and for frequencies varying from 100 Hz to 6400 Hz, at a 100 Hz step. The results are provided in Figure 3.14 and Figure 3.15.

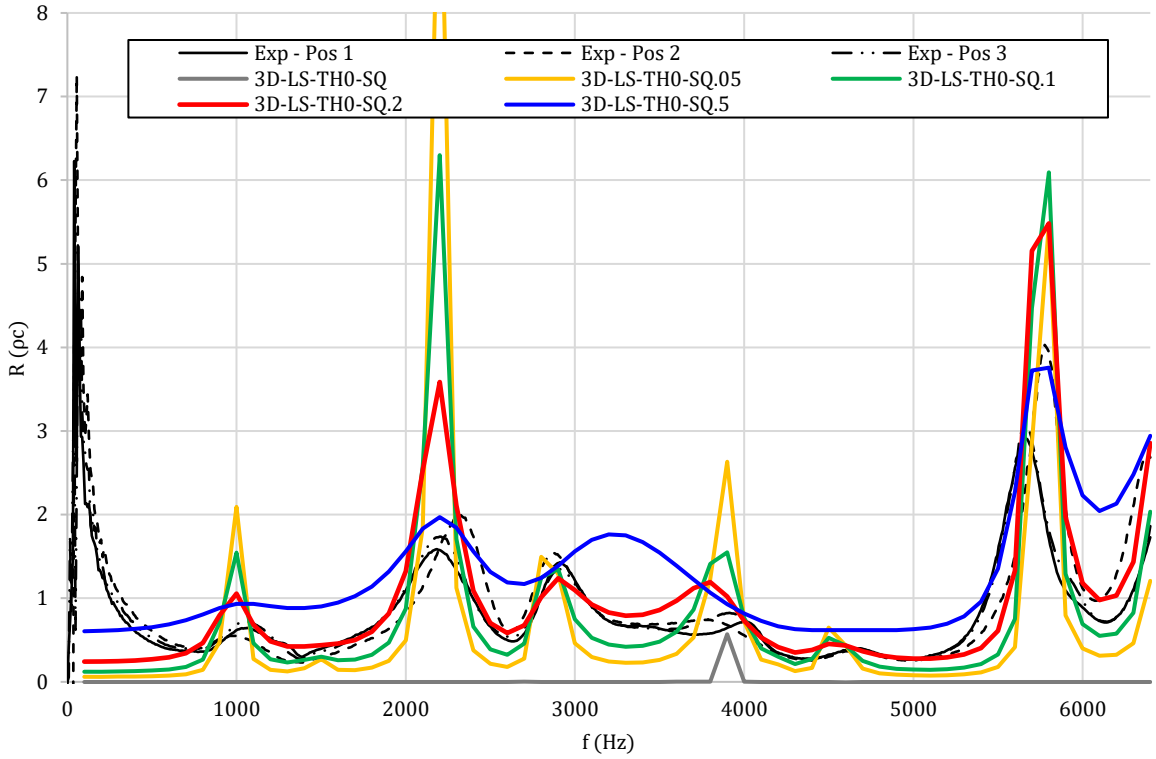

Figure 3.14. Normalized resistance, R

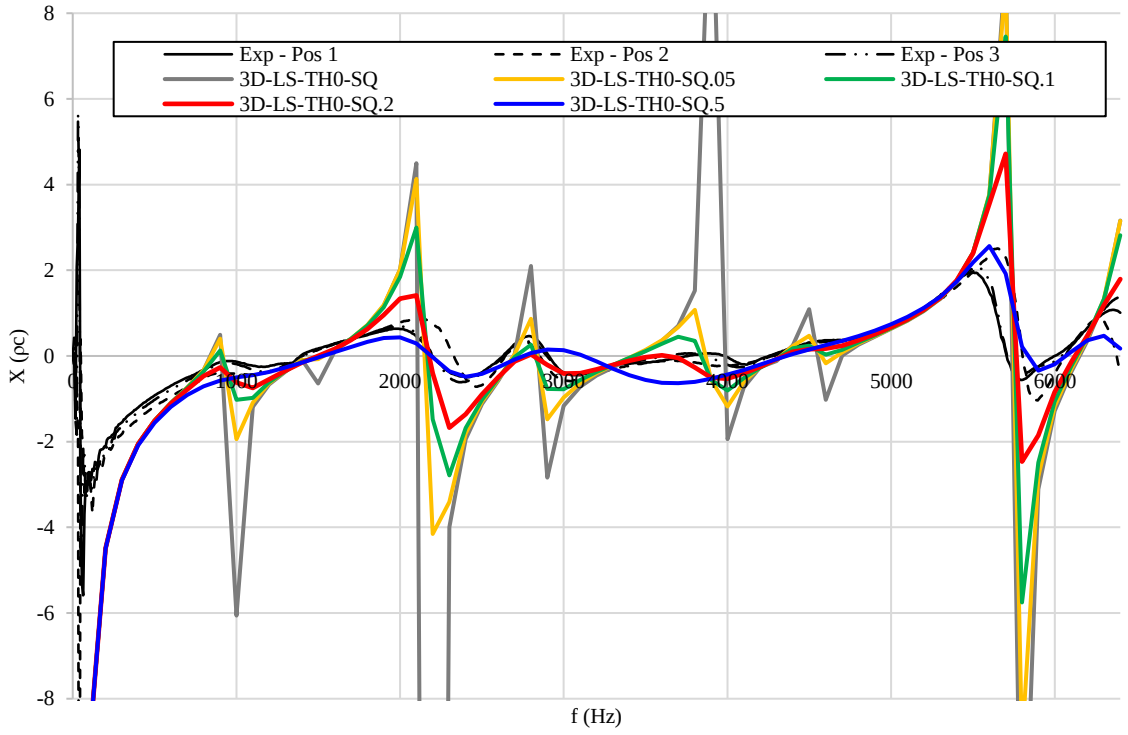

Figure 3.15. Normalized reactance, X

As shown in Figure 3.14 and Figure 3.15, regardless of the value of the face sheet resistance R_{fs}, the 3D-LS-TH0-SQ-type models do a good job of capturing the frequency spectrum of the complex cavity liner. However, 3D-LS-TH0-SQ.2 provides the best match to both the measured resistance and the measured reactance.

Aside from 3D-LS-TH0-SQ.2, the other numerical models are not able to correctly predict the resistance offered by the 3D printed liner. Lower values of R_{fs} do not provide enough acoustic energy damping as the liner, while higher values of R_{fs}, as $R_{fs} = 0.5\ \rho c$, introduce too much resistance with respect to the measured values.

The inclusion of a uniform face sheet resistance across the liner surface just approximates the resistance of the cavities. Clearly, further investigations are required in order to provide improved understanding of the physics behind the predicted energy damping. In recent studies [32], the source of the resistance in broadband liners with variable-depth, narrow straight cavities has been attributed to viscous losses. However, the validity of this hypothesis must be proved for liners with more complex configurations. Notwithstanding this, whatever is the source of damping, the results in Figure 3.14 and Figure 3.15 highlight that the resistance of the liner sample can be effectively modelled by simply introducing a uniform face sheet resistance over the liner surface. A constant value of R_{fs} is sufficient to model the energy damping and no advanced simulation techniques are required. This outcome is significant as it permits the use of reduced complexity modelling of these types of liner. Reliable results are, in fact, obtained by the sole solution of the Helmholtz equation subject to appropriate boundary conditions and no further physical characteristics, for instance the introduction of thermal-viscous acoustics need be introduced.

In the optimization process of an innovative liner configuration in Chapter 4, the face sheet resistance R_{fs} is considered as a design variable. There, R_{fs} accounts both for the viscous losses within the cavity (even there they are not captured directly in the model) and for the resistance of a face sheet that may be bonded on the liner surface. In the optimization process, R_{fs} is used to search for the optimal value of resistance that maximizes the sound absorption and it is not aimed solely at modelling the damping of the liner, as in the current study.

Figure 3.16 and Figure 3.17 provide impedance predictions which summarise the impact of modelling square versus circular impedance tubes and the introduction of a non-zero face sheet resistance. The figures provide a comparison between the measured data, the square impedance tube 3D-LS-TH0-SQ.2 ($R_{fs} = 0.2\ \rho c$) model, and the 3D-LS-TH0-C.2 circular impedance tube ($R_{fs} = 0.2\ \rho c$, measured at position A). The numerical results are obtained with the SPL of the sound source at 130 dB and varying the source frequency between 100 Hz and 6400 Hz, at a 100 Hz step.

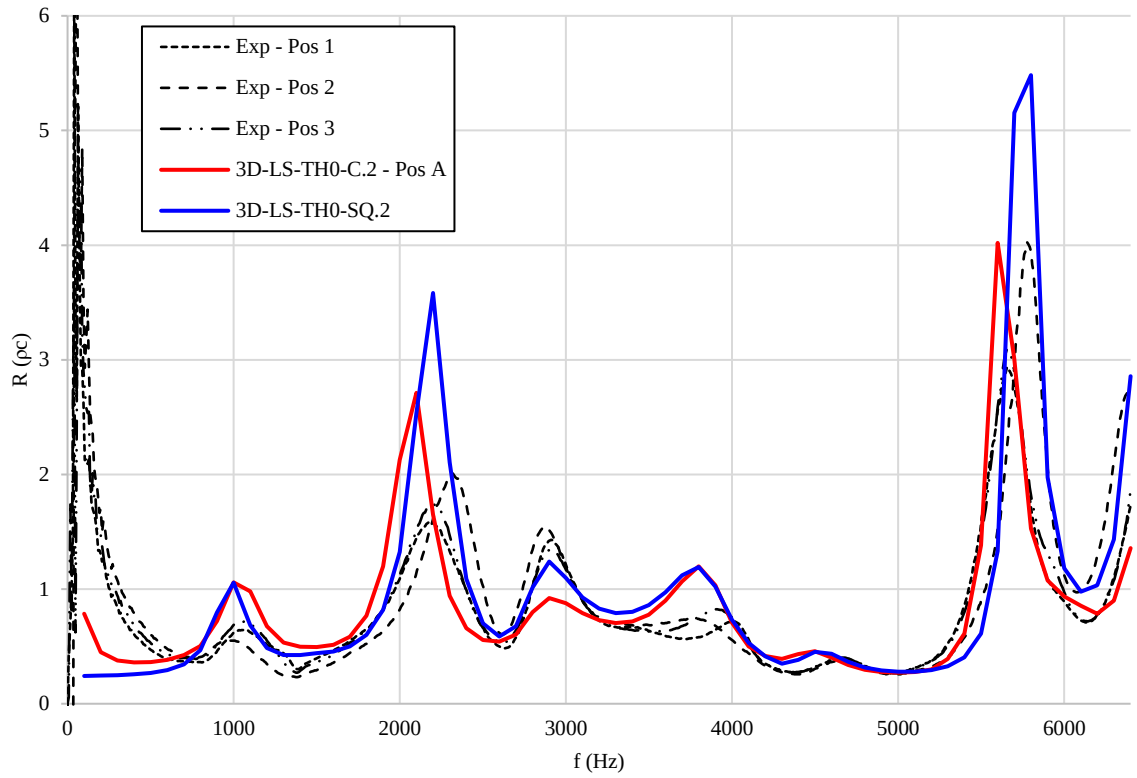

Figure 3.16. Normalized resistance, R

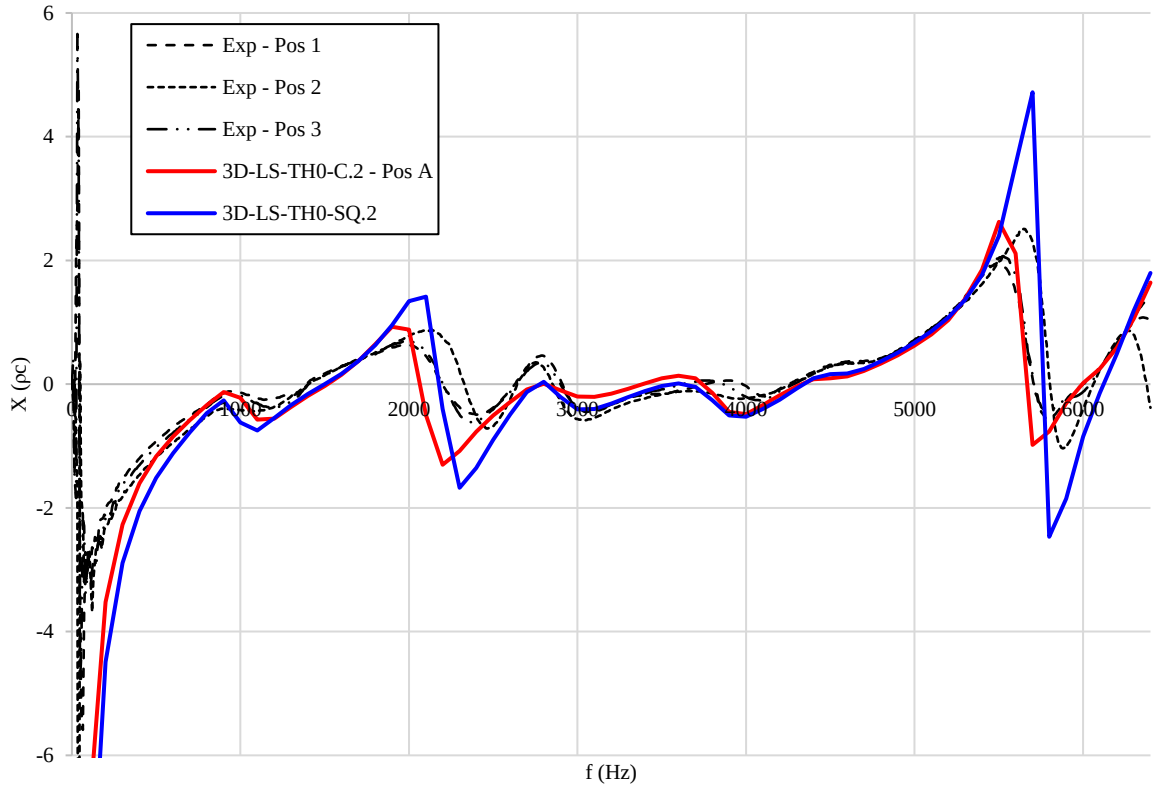

Figure 3.17. Normalized reactance, X

The figures confirm the considerations previously stated concerning the use of a cylindrical tube and of a non-null face sheet resistance. As expected, the 3D-LS-TH0-C.2 data best capture the edge effects below 1000 Hz, both in terms of reactance and in terms of resistance when $R_{fs} = 0.2\ \rho c$. Agreement is poorer at very low frequencies and at the reactance peaks and troughs. The 3D-LS-TH0-SQ.2 and 3D-LS-TH0-C.2 data are quite similar. The 3D-LS-TH0-SQ.2 predictions are preferred as the square tube captures the true response of the liner. Finally, setting $R_{fs} = 0.2\ \rho c$, the damping of the reactance peaks and troughs is indeed caught both in 3D-LS-TH0-SQ.2 and in 3D-LS-TH0-C.2.

3.3.5 Reduced three-dimensional model for the prediction of the liner impedance

Figure 3.2 shows the 4x4-cavity clusters (3D-4CC) which form the building blocks of the complex cavity sample, while Figure 3.3 shows the fundamental four-cavity component (3D-3+1CC) which drives the acoustic response of this sample. Each of the modelling techniques discussed in the preceding analyses is adopted in the development of the numerical models that simulate the 3D-4CC and the 3D-3+1CC clusters. The internal partitions are modelled as reflective and rigid surfaces, and the impedance tube is chosen as square in order to capture the complete surface area of each of these configurations, hence avoiding any edge effect. Finally, the facing sheet resistance, R_{fs}, is set to $0.2\ \rho c$.

The numerical model used for the analysis of the 3D-4CC acoustic properties is labelled as "3D-4CC-TH0.2" and it is shown in Figure 3.18.

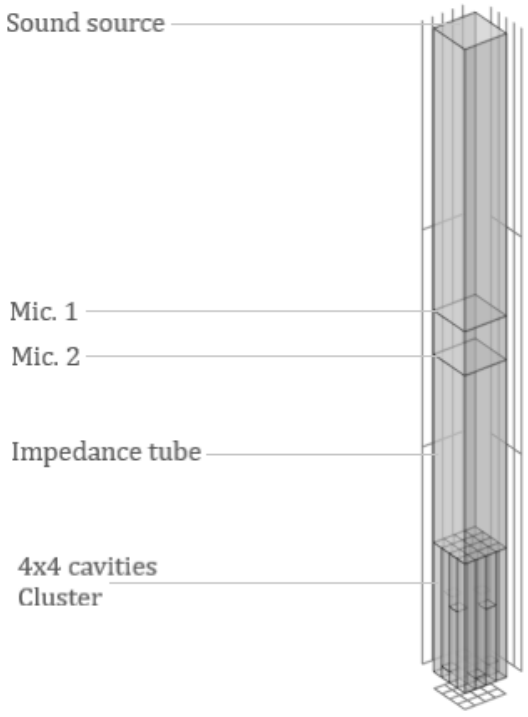

Figure 3.18. 3D-4CC-TH0.2

The 3D-3+1CC impedance is analysed using three models that differ through the number of cavities and their arrangement. In each of these models, the straight cavity, that is marked with yellow lines in Figure 3.20 and Figure 3.21, is hereinafter labelled as "cavity S". The first model is labelled as "3D-3+1CC-TH0.2-I" and has the

same configuration of the 3D-3+1CC cluster shown in Figure 3.3. The second model is labelled as “3D-3+1CC-TH0.2-II” and has the same cavities of the 3D-3+1CC cluster, but they are arranged in a different way to assess the sensitivity of the cluster impedance to the position of the cavities: in 3D-3+1CC-TH0.2-II, in fact, the cavity S is shifted back alongside the longest folded cavity. Finally, the third model is labelled “3D-3CC-TH0.2” and models the 3x1-cavities cluster that composes the 3D-3+1CC cluster, but it does not include the cavity S.

A detailed representation of the models hitherto introduced is given in the following figures, where blue lines surround the 3x1-cavity cluster and yellow lines surrounds the cavity S. Figure 3.19 shows the 4x4-cavity cluster modelled in 3D-4CC-TH0.2, Figure 3.20 the 3x1-cavity cluster plus the cavity S modelled in 3D-3+1CC-TH0.2-I, Figure 3.21 the 3x1-cavity cluster plus the cavity S modelled in 3D-3+1CC-TH0.2-II. Finally, Figure 3.22 shows the 3x1-cavity cluster modelled in 3D-3CC-TH0.2 and Figure 3.23 the overall complex cavity liner sample modelled in 3D-LS-TH0-SQ.2.

The predicted resistance and reactance of these models are shown respectively in Figure 3.24 and Figure 3.25. They are obtained with the SPL at the sound source set to 130 dB and by varying the source frequency between 100 Hz and 6400 Hz, with a 100 Hz step.

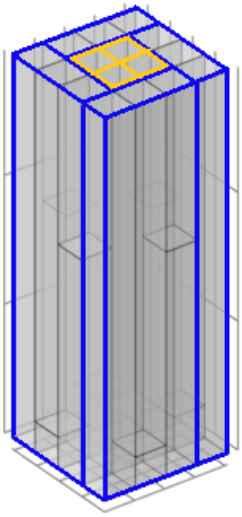

Figure 3.19. 3D-4CC-TH0.2 core

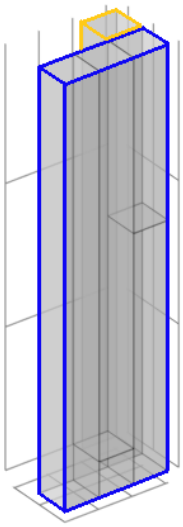

Figure 3.20. 3D-3+1CC-TH0.2-I core

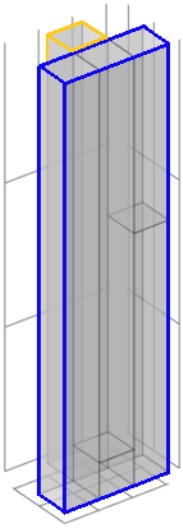

Figure 3.21. 3D-3+1CC-TH0.2-II core

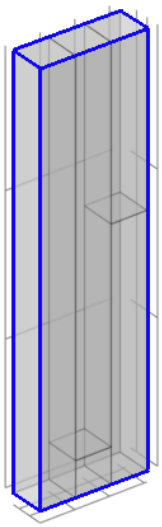

Figure 3.22. 3D-3CC-TH0.2 core

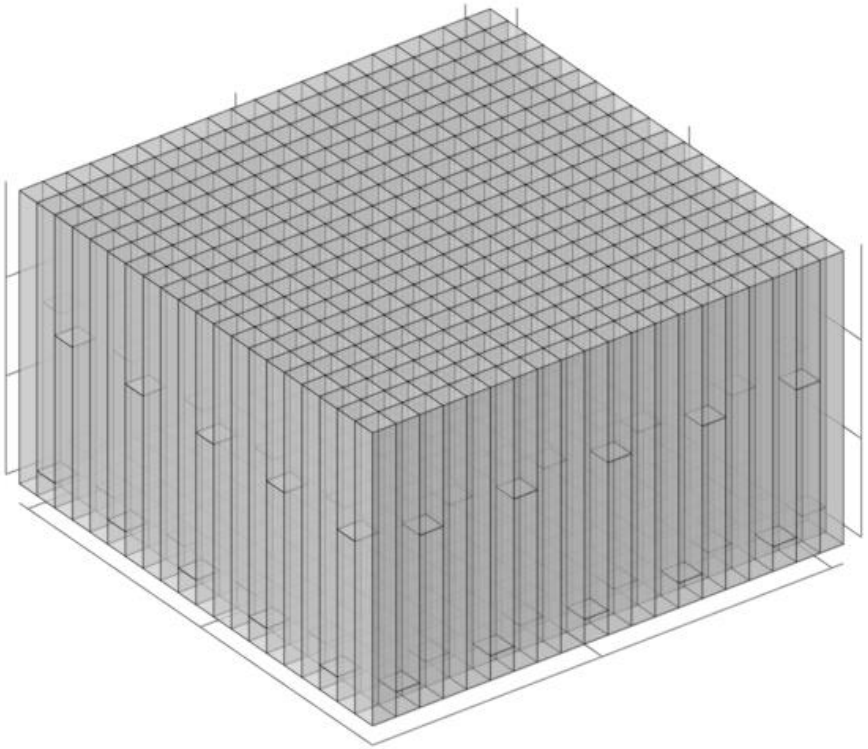

Figure 3.23. 3D-LS-TH0-SQ.2 core

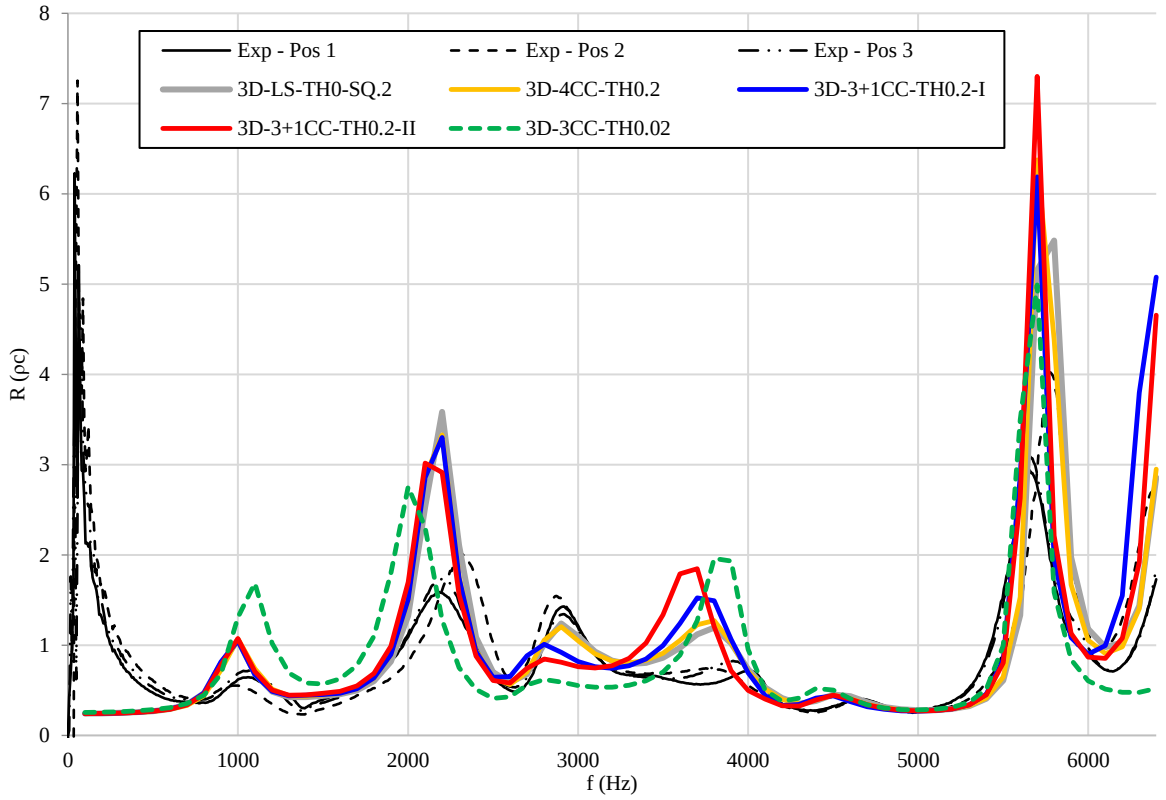

Figure 3.24. Normalized resistance, R

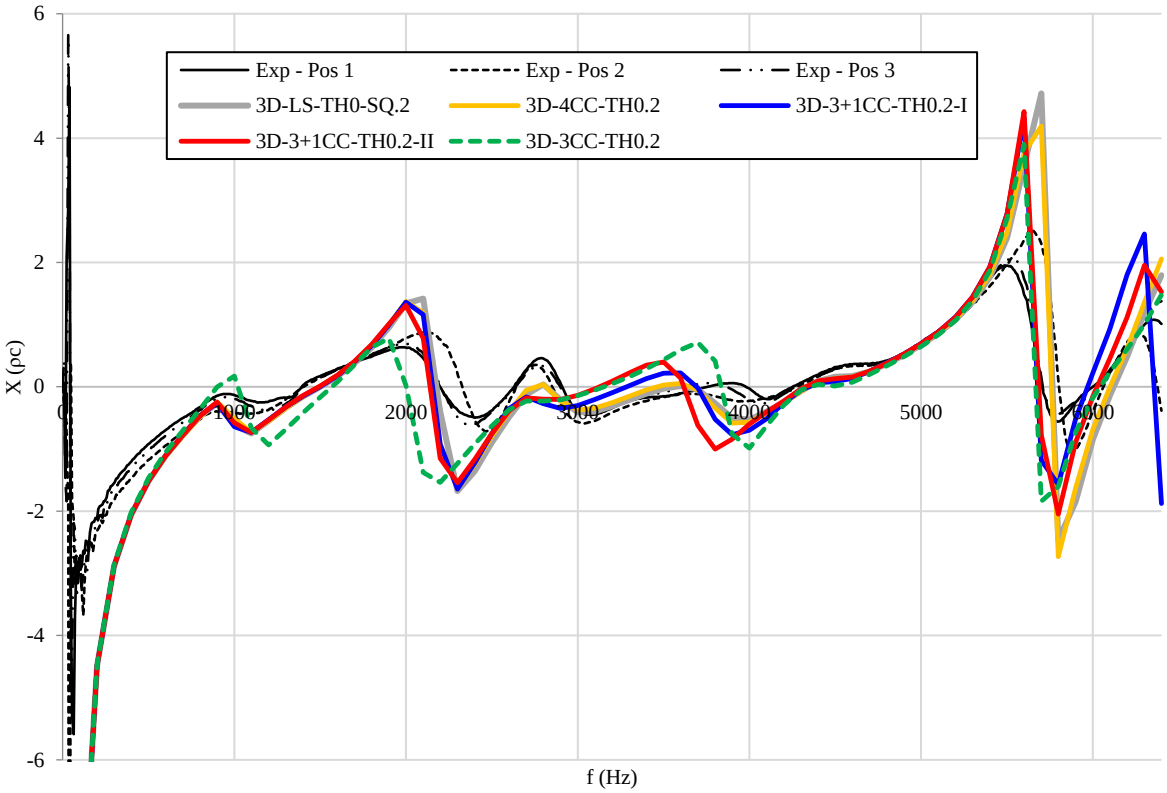

Figure 3.25. Normalized reactance, X

In Figure 3.24 and Figure 3.25, the numerical results achieved with the models 3D-LS-TH0-SQ.2, 3D-4CC-TH0.2, 3D-3+1CC-TH0.2-I and 3D-3+1CC-TH0.2-II are successfully compared. They are nearly similar and differ only in correspondence of the peaks and troughs of the reactance.

The predicted data of the 3D-4CC-TH0.2 model are nearly identical to those of the 3D-LS-TH0-SQ.2 and no noticeable difference emerges. Therefore, at least in the frequency bandwidth analysed, 3D-4CC-TH0.2 can effectively substitute 3D-LS-TH0-SQ.2 for predicting the liner impedance and this key finding results in a considerable reduction of the computational time. The level of agreement seen between the data of 3D-4CC-TH0.2 and 3D-LS-TH0-SQ.2 demonstrates that both models accurately capture the physics of the four-cavity design.

Previous studies [32] [33] determined that the impedance variability of a liner can be ignored if the geometry variability is confined within a small portion of the full liner and it is repeated periodically over its full extent. For grazing incidence, as long as the extension of the small portion is less than a third of the minimum wavelength of the source frequency, it was shown that the liner impedance can be assumed uniform over its entire area and the impedance of the small portion can be smeared over the entire liner extent. In the case of 3D-LS, modelled in 3D-LS-TH0-SQ.2, the overall configuration is obtained by repeating the configuration of 3D-4CC twenty-five times. The fundamental component is modelled in 3D-4CC-TH0.2 and its maximum size is about a third of the minimum acoustic wavelength considered $\left(\lambda_{min} = \frac{c}{f_{max}} = \frac{345\,\frac{m}{s}}{6400\ Hz} \approx 18\ mm\right)$. Hence, the 3D-4CC impedance can be appropriately smeared over the extent of 3D-LS and the liner impedance can be modelled as a lumped element with the same impedance of the 3D-4CC cluster. It should be noted that in [33], the assumption of the smeared response of the liner is obtained with plane waves at grazing incidence, so the frequency limit must also be evaluated for normal incidence. However, the favourable comparison shown in Figure 3.24 and Figure 3.25 suggests that the assumption can be relaxed for normal incidence, without losing confidence on the results obtained albeit for a different set-up.

In the wake of these considerations, in Figure 3.24 and Figure 3.25 it is found that the numerical results of 3D-4CC cluster are well predicted by those of the 3x1+1-cavities cluster, that is the smallest portion of the 4x4-cavities cluster in which the geometry varies. In fact, both the numerical results of the 3D-3+1CC-TH0.2-I and 3D-3+1CC-TH0.2-II match the numerical results of the 3D-4CC-TH0.2, except for few points where the differences are negligible (e.g. frequencies with large moduli of reactance, which result in reduced absorption). Therefore, the 3x1+1-cavity cluster impedance can be used to represent the acoustic response of the full panel.

It is noted that the results of 3D-3+1CC-TH0.2-I and 3D-3+1CC-TH0.2-II are not identical over the entire frequency bandwidth and some differences occur in correspondence with the reactance peaks and troughs. These differences arise due to the different position of the cavity S in the 3x1-cavity clusters because, above a certain frequency, the cavity S and the folded cavity can mutually interact driving a change of the impedance predicted by the two models. It may be seen that the two impedances in question show nearly perfect agreement up to approximately 2600 Hz. This equates to a wavelength of 133mm, which is just below eight times the maximum width of the clusters. It was shown [32] that for normal incidence, the impedance can be assumed uniform as long as the geometry variability is confined within an eighth of the minimum wavelength. The impedance becomes sensitive to the position of the cavity S above 2600 Hz and the two impedances are similar, but not identical, up to the highest frequency considered (6400 Hz). Although it is not perfect, the comparison between the impedances

is favourable and supports the grazing incidence conclusion, [5], of a smeared response up to one-third of the incident wavelength, applying also for normal incidence.

The effects of the variation in the phase and amplitude of the sound wave for the differing cavities of a liner can be accounted in the radiation impedance Z_i, defined as [39],

$$Z_i = Z_{ii} + \sum_{j=1}^{n} \left[Z_{ij} \left(\frac{v_j}{v_i} \right) \right] \tag{3.11}$$

In Equation 3.11, Z_i is the individual cavity impedance, Z_{ii} is the self-radiation impedance, Z_{ij} the mutual radiation impedance of the j-th cavity on the i-th cavity and v_j/v_i is the ratio of the inlet velocities in the i-th and j-th cavities. Z_{ii} considers the radiation impedance of the cavity in isolation, while Z_{ij} accounts for the induced pressure on the inlet of the i-th cavity due to the radiation from the j-th cavity, weighted by the ratio of the acoustic velocities v_j/v_i at the inlet of the cavities. The mutual impedance is mainly significant when both the i-th and j-th cavities are in resonance because, at the resonance, the ratio v_j/v_i weighting Z_{ij} is not negligible; on the contrary, far from the resonance, the mutual interaction between cavities is negligible. Therefore, the interactions between cavities that are tuned for different resonant frequencies can be neglected and only the cavities with a similar height can effectively interact. The mutual interaction between similar cavities is stronger when the cavities are close while, as the separation distance between cavities increases, the mutual radiation impedance term decays. A preliminary approximation [39] of mutual radiation impedance indeed shows this dependency of Z_{ij} on the separation distance d between cavities.

$$Z_{ij} \approx \rho c \left(\frac{\sin(kd)}{kd} + i \frac{\cos(kd)}{kd} \right) \tag{3.12}$$

It should be noted that the approximation in Equation 3.12 considers the inlet of the i-th and j-th cavities set in an infinite plate and it is not consistent with the tested liner sample; nonetheless, it is helpful to clarify when the mutual interaction between cavities can be properly neglected.

[39] shows that the self-radiation impedance may be approximated by,

$$Z_{ii} = \rho c \frac{(kr)^2}{2} + j \rho c \frac{8kr}{3\pi} \tag{3.13}$$

where $k = 2\pi f/c$ is the wave number, and $r = \sqrt{A/\pi}$ is the equivalent radius of the cavity (A is its cross-sectional area). Clearly, this component becomes more significant as frequency and cell equivalent radius increase, but the 3D-LS cavities are sufficiently narrow to avoid this effect. Nonetheless, the COMSOL model captures the impact of cell-to-cell interactions, but the radiation impedance is not explicitly modelled. It is noted that the COMSOL and the semi-empirical models should ideally include this effect, but the comparison between prediction and measurement will identify its importance.

In case of the 3x1+1-cavities cluster, all of the cavities have different resonant frequencies and they are not expected to mutually interact. However, as demonstrated in [6], at high frequencies the sound wave in the folded cavity is largely reflected back by the backing sheet and it barely propagates beyond the corner, so the folded cavity tends to behave as a shallow cavity and its effective centreline length gets smaller. A similar result is found in the 3x1+1-cavities cluster, where in the folded cavity, at high frequencies, the sound waves barely propagates

beyond the corner and the folded cavity acoustically behaves as if it was the cavity S. As the source frequency rises, the impact of the radiation impedance of each cell increases, and it becomes stronger especially in the 3D-3+1CC-TH0.2-II model, where the cavity S acoustically resembles the folded cavity. Nevertheless, despite these considerations, the differences between the 3D-3+1CC-TH0.2-I and the 3D-3+1CC-TH0.2-II data is mainly located at the reactance peaks and troughs and is the importance of the location of the straight cavity is considered to have a second order influence. It is deduced that the acoustic properties of the 3x1+1-cavities cluster are greatly not affected by the position of the cavity S and both 3D-3+1CC-TH0.2-I and 3D-3+1CC-TH0.2-II can effectively predict the 3D-LS impedance.

Finally, in Figure 3.24 and Figure 3.25, the 3D-3CC-TH0.2 (i.e. missing the cavity S) predicted data does not match the numerical results of the other numerical models and at the same time does not predict the impedance of the liner sample with sufficient accuracy. After all, 3D-3CC-TH0.2 simulates only the 3x1-cavity cluster, omitting the contribution of the cavity S to the overall impedance. For sure, the 3D-3CC-TH0.2 reactance peaks and troughs are not so far from those of the other models and highlight how extensively the 3D-LS acoustic characteristics are dominated by the acoustic characteristics of the 3x1-cavity cluster. The counter argument is that the three-cavity cluster performed almost as well as the four-cavity cluster, opening up the possibility for further simplification of this particular design.

3.3.6 Simplified two-dimensional model for the prediction of the liner impedance

In addition to the models presented above, two two-dimensional models of the 3x1+1-cavity cluster and the impedance tube are realized. They are presented in Figure 3.26 and Figure 3.27.

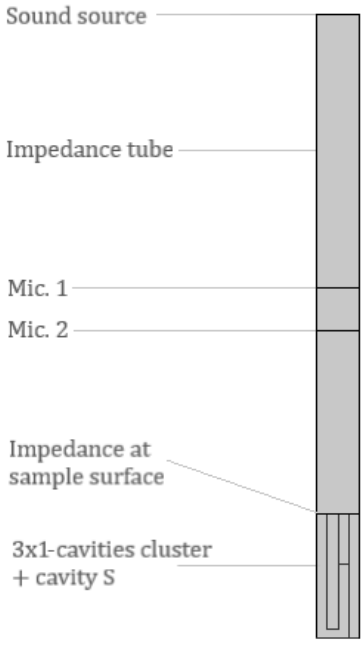

Figure 3.26. 2D-4CC-TH0.2-I

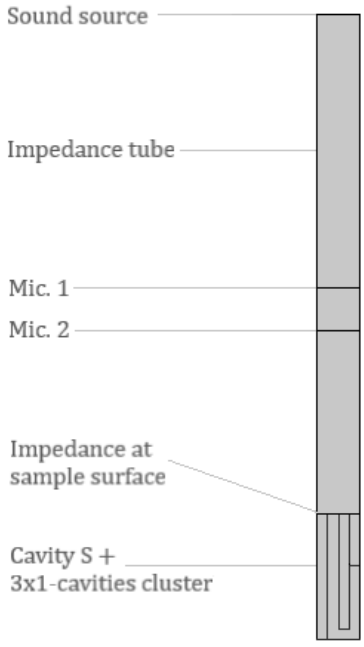

Figure 3.27. 2D-4CC-TH0.2-II

The model in Figure 3.26 is labelled as 2D-4CC-TH0.2-I. It simulates the 3x1-cavity cluster plus the cavity S, at the right side of the cluster. The model in Figure 3.27 is instead labelled as "2D-4CC-TH0.2-II" and differs from 2D-4CC-TH0.2-I only for the position of the cavity S, set at the left side of the 3x1-cavities cluster. In both the

models, the cavities have the same effective centreline length of the cavities in 3D-3+1CC-TH0.2-I but they are placed on the same plane, differently from 3D-3+1CC-TH0.2-I/II, where the cavity S is out of the plane of the 3x1-cavity cluster. The different positions of the cavity S is selected in order to assess where the cavity S should be placed in a two-dimensional model in order to adequately simulate the response of liner configuration 3D-3+1CC-TH0.2-I/II.

The two models are discretized with free quadrilateral elements. Their maximum size is chosen to have at least 10 nodes for the minimum wavelength. The impedance of the two models is calculated between 100 Hz and 6400 Hz at a 100 Hz step, with the SPL of the sound source set at 130 dB. The 2D-4CC-TH0.2-I and 2D-4CC-TH0.2-II numerical results are provided in Figure 3.28 and Figure 3.29, where they are both compared to the 3D-LS-TH0-SQ.2 numerical results, and to the measured liner impedance.

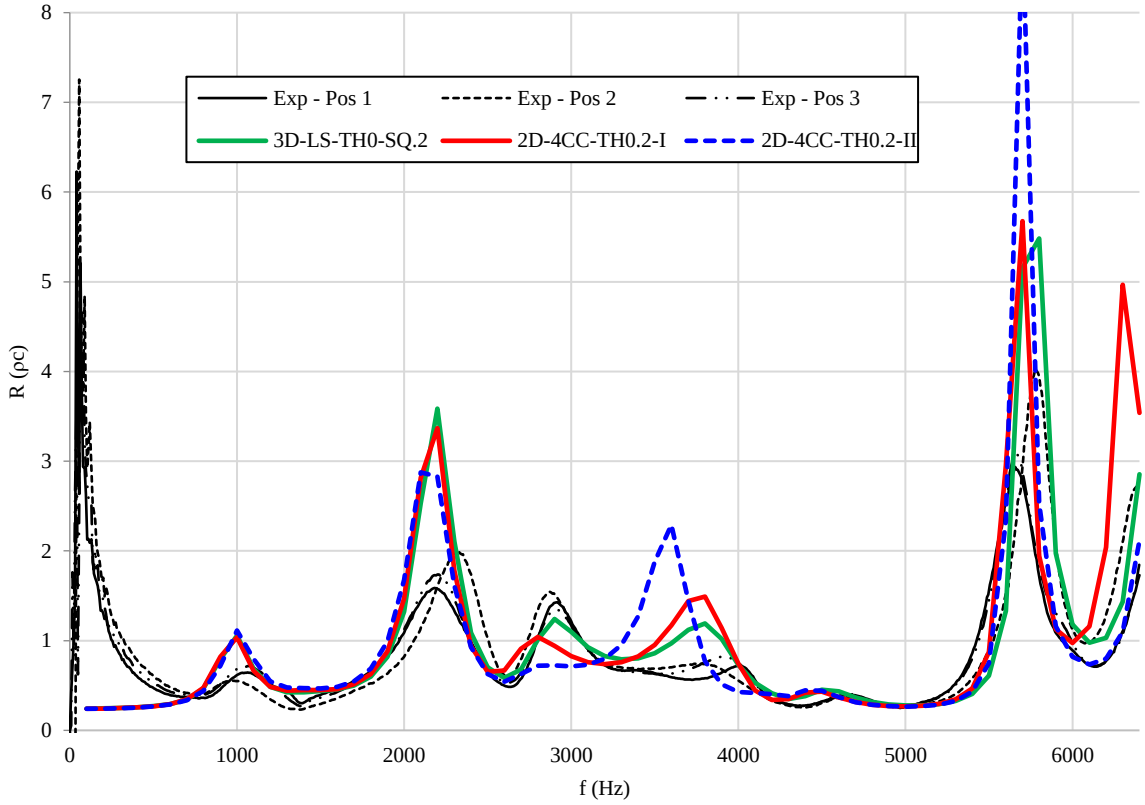

Figure 3.28. Normalized resistance, R

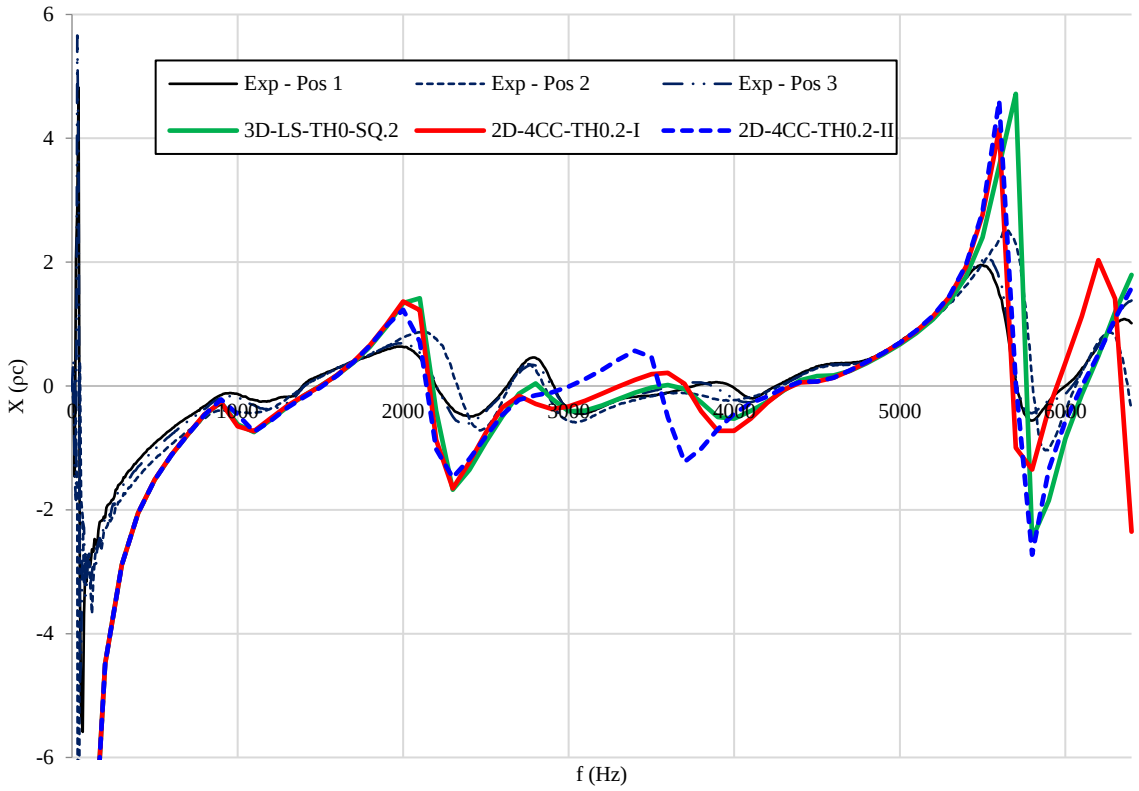

Figure 3.29. Normalized reactance, X

The comparison of the results shows that the 2D-4CC-TH0.2-I data and the 2D-4CC-TH0.2-II data are nearly identical and the main differences are likely due to the relative position of the cavity S with respect to the folded cavity. In fact, as with the three-dimensional cases, the mutual interaction between the folded cavity and the cavity S occurs above approximately 2600 Hz, whereupon it begins to have a greater influence on the impedance. However, the differences are relatively limited and may be considered negligible, confirming that the position of the cavity S does not greatly influence the evaluation of the acoustic properties.

Figure 3.28 and Figure 3.29 show good agreement between the predictions of the two-dimensional models and the data of 3D-LS-TH0-SQ.2. The main divergences at the reactance peaks and troughs are not of significant interest. The comparison demonstrates that the 2D models of the 3x1+1-cavity cluster can effectively simulate the 3D-LS-TH0-SQ.2 impedance. This dramatically reduces the computational time of the calculation of the 3D-LS impedance: 3D-LS-TH0-SQ.2 took 10min, while the 2D models took only 5s. Therefore, provided that the smallest cell cluster in which the liner geometry varies is lower than a third of the minimum wavelength, the liner impedance can be effectively simulated with a two-dimensional model of this cluster. This outcome is demonstrated in Figure 3.28 and Figure 3.29 by the good agreement between the 2D model and the measured data. The main differences between those results mainly occur at the reactance peaks and troughs, and at low frequencies. They are herein neglected as the low frequency effect is a measurement effect, and the liner is less efficient around the impedance peaks and troughs

Clearly, the validity of this hypothesis is restricted to the specific case considered and further tests are needed in order to verify its applicability to different configurations. However, it is an excellent starting point for future research and it can considerably simplify the numerical simulation of the liners with complex configurations.

3.4 Chapter III: Final remarks

The purpose of the current study was to numerically investigate the acoustic properties of the liner sample designed and printed in Leonardo and to find an effective way to numerically simulate its impedance. To this aim, the liner sample has been subjected to a series of experimental and numerical analyses where the liner impedance has been measured in the absence of grazing mean flow and in the frequency range between 100 Hz and 6400 Hz, with the source SPL set at 130 dB. In the study, the models and the numerical analyses were performed with COMSOL 5.4. The analyses led to some interesting outcomes. The conclusions are recapped below.

- If the internal partitions of the 3D printed liner are sufficiently rigid to acoustically isolate adjacent cavities, the internal partitions can be simulated as reflective and rigid surfaces along which the hard wall boundary conditions are imposed. The reduction of the internal partitions to surfaces must be compensated with a modification of the width of the cavities, in order to reflect the response of the liner, i.e. the effect of the finite wall thickness is then accounted for.
- A tube with the cross-section of the same shape and size of the liner surface is preferred to the circular cross-section tube, as this captures the true response of the liner. However, in this way, the prediction of the edge effects seen with a circular impedance tube are missed at low frequencies.
- The energy damping experimentally registered in the liner can be effectively simulated by introducing a fictitious face sheet over the liner surface. A successful simulation requires a sole constant quantity of face sheet resistance, whose value must be determined through a parametric analysis.
- The liner impedance can be effectively simulated with a two-dimensional model of the smallest portion in which the liner geometry varies, provided that the size of the smallest portion is lower or comparable to a third of the minimum wavelength considered. This assumption holds for a normal incidence set-up.

The adoption of these considerations in the numerical models led to a dramatic reduction of the computational time. They identify a simplified means of modelling a liner with a complex configuration. The validity of these considerations is limited at present to the case considered and further investigations are required for the simulation of other liners. However, these considerations represent a starting point for future numerical analyses, and, in the next chapter, a preliminary optimal liner configuration is sought using a two-dimensional model derived from the two-dimensional modelling procedure introduced in this chapter.

4. Design and optimization of a broadband liner

The previous chapter introduced a simplified numerical model for studying the acoustic properties of a complex liner. This numerical model reduced the complexity of the detailed three-dimensional model initially used for studying the liner sample, and focused solely on the four-cavity cluster that represents the smallest portion in which the liner geometry varies.

The favourable comparison between the measured and the predicted results provided confidence about the possibility of designing a liner with a complex configuration focusing simply on a small portion of its geometry. In addition, the sound absorption of the liner can be improved through an optimization process that targets the fundamental cell cluster of the liner and does not need to model the complete liner configuration.

With these observations in mind, in this chapter, a four-cavity cluster is developed for designing an innovative configuration of broadband liner. The acoustic properties of the liner are designed using a numerical model in which the most important remarks of the previous numerical study are adopted. Besides the numerical model, the liner properties are also studied using an analytical model that considers the liner impedance as 'smeared' over its extent. The good correlation between the numerical and the analytical results validate the use of the analytical model for designing and optimizing the liner configuration and, in the end, two optimal liner configurations are designed with different maximum overall heights. The two optimal liner configurations envision promising sound absorption performances over a wide frequency bandwidth. These are verified experimentally in the final stage of the study. Three scaled samples of the optimal liners are manufactured, and their acoustic properties are tested. The measured impedances confirm the expected sound absorption performances over a broad frequency band.

The numerical models are designed in COMSOL 5.4, while the analytical model and the two optimal configurations are respectively developed in Microsoft Excel and MATLAB R2019a.

4.1 Baseline liner model and three different methods for evaluating its impedance

Figure 4.1 shows the baseline liner model adopted to search for the optimal configurations. Due to the proprietary nature of the study, the liner dimensions cannot be presented; however, a general understanding of the baseline model and its main characteristics are duly discussed.

In Figure 4.1, the different colours introduce the individual cavities of the liner whose effective centreline lengths are indicated by the dashed lines. Blue stands for first cavity, red for second cavity, yellow for third cavity and green for fourth cavity.

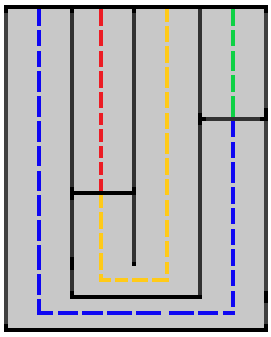

Figure 4.1. Baseline liner model and effective centreline lengths of its cavities.

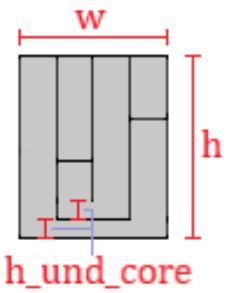

Figure 4.2. Baseline liner model and overall principal dimensions.

The baseline liner model derives from the 3x1+1-cavity cluster of the 3D printed liner analysed in Chapter 3. It is a cluster composed by four cavities both folded and straight, that are packaged to minimize the overall height and to exploit the maximum space available. This concept avoids the presence of dead volume and enables cavities to be designed with a long effective centreline length, crucially significantly exceeding the maximum overall height. Thus, the compact liner is expected to be efficient in abating noise at lower frequencies.

The liner geometry is defined by its maximum width w and height h, while each cavity is defined by its width w_i and its effective centreline length h_i. The maximum overall height h is based on the presumed space available in the inner walls of the nacelle, while the maximum overall width w is below a third of the minimum sound wavelength λ_{min} up to approximately 2900Hz. As emerged in previous chapter, if the variability of the liner geometry is confined within this limit, the impedance of the baseline liner model behaves as if it is averaged over its extent and the liner impedance can be effectively described by the analytical model introduced later.

In addition to the quoted dimensions, the folded cavities are defined also by the height of the underlying passage $h_{und_{core}}$, that is set a tenth of the overall height h to reduce acoustic wave reflections from impedance changes due to area changes and to limit viscous losses that occur in narrow cavities [37]. The baseline liner partitions between the cavities are considered infinitesimally thin and both rigid and reflective from an acoustic point of view.

The constraints on the liner geometry are enforced through the relations in Eqs.4.1-4.3, where the subscripts $i = 1,4$ stand for the correspondent cavity to which the dimension refers to.

$$w_1 + w_2 + w_3 + w_4 = w \tag{4.1}$$

$$h_1 + h_4 = 2h + \frac{1}{2}(w_1 + w_4) + w_2 + w_3 - h_{und_{core}} \tag{4.2}$$

$$h_2 + h_3 = 2h + \frac{1}{2}(w_2 + w_3) - 3h_{und_{core}} \tag{4.3}$$

As far as the physics of the baseline liner is concerned, the physics already introduced in the previous chapter is adopted. The only difference is represented by the inclusion of a surface impedance, that will be used in the current liner to capture either any facing sheet impedance that may be added to optimise a given geometry (Z = 1 + 0j is sought at all frequencies). It also will account for radiation impedance, and viscous losses in the liner core, as these effects, though second order, are not captured in the modelling. The facing sheet impedance Z_{fs} is defined as,

$$Z_{fs} = R_{fs} + i\mathrm{X}_{fs} \tag{4.4}$$

with the assumption of constant resistant R_{fs} and null inertance X_{fs}, following on from the previous chapter. Z_{fs}, R_{fs} and X_{fs} are normalized by ρc, where ρ is the air density and c is the speed of sound.

A complete characterization of the resistance term R_{fs} of the following models can be obtained only through experimental tests that quantify the amount of the facing sheet resistance (if present), along with the radiation impedance (greatly reduced if a facing sheet is present), and cavity wall losses.

Alongside the baseline model with folded cavities, a corresponding numerical model is developed with straight cavities. This straight cavity model has the same width and physics of the folded-cavities liner, except for the maximum overall height h and the constraints on the individual cavity heights, that are not enforced. Each straight cavity has the width and the effective centreline length of the equivalent folded cavity, and the impedance at the liner surface is kept unaltered at low frequencies where sound easily diffracts around corners. As with the folded-cavities model, the straight-cavities model is developed in COMSOL 5.4 (see Figure 4.3 and Figure 4.4).

The straight-cavities numerical model will be assessed against the folded-cavities baseline model, to see if it can be successfully used for predicting the liner acoustic properties. Recent studies [34] have shown that the overall noise attenuation of a liner with folded cavities is predicted well at low frequencies by the correspondent liner with straight cavities, for grazing incidence and a no-flow condition (Mach 0.0). However, it is noted that [6] [3] do not demonstrate good agreement at higher frequencies, where the additional reflections from folds in the cavities alter the acoustic performance. The straight-cavity model can significantly reduce the efforts of finding the optimal solution: first, the complexity of the model decreases due to the reduction of the model variables ($h_{und_{core}}$ disappears) and due to the simplification of the acoustic domain geometry; secondly, a proven irrelevance of the folds in the cavities at low frequencies in the liner impedance calculations permits the use of an analytical routine to model the liner impedance. This can be implemented easily in spreadsheets and in different coding languages. Earlier studies [42] used an analytical routine for optimizing liners and a good correlation between the measured and the analytically predicted impedance was demonstrated. The results confirmed the validity of the use of the analytical model for assessment of liner impedance of complex configurations.

The analytical routine considers the liner impedance as uniform and smeared across the width of the liner for normal incidence impedance measurements. The smallest portion in which the variability of the liner geometry is confined is lower than a third of the minimum wavelength up to approximately 2900 Hz (here, the design maximum $w = 40mm < \lambda_{min}/3$), so the impedance can be considered as averaged across the liner extent [33]. The numerical study performed in Chapter 3 indicates that the frequency limit assumption can be relaxed in a normal incidence set-up. Ultimately, the frequency limit of the assumption of a smeared response must be confirmed for this type of configuration in a grazing incidence set-up.

The normalized liner impedance Z is obtained by assembling the normalized impedance of the individual cavities Z_i and inverting the overall liner admittance A, as shown in the following procedure.

The i-th individual impedance Z_i is defined as,

$$Z_i = R_{fs} + i\mathrm{X}_i \tag{4.6}$$

where R_{fs} the liner resistance and X_i the reactance of the i-th cavity. The resistance term R_{fs} is kept constant, as in the numerical baseline model, while the reactance X_i is defined as $\mathrm{X}_i = -\cot(kh_i)$ and corresponds to the quarter-wave resonator reactance, whose height equals the effective centreline cavity height h_i.

The liner admittance is calculated by summing all the individual cavity admittances $\frac{1}{Z_i}$ weighted for their width w_i and dividing the summation for the overall liner width w.

$$A = \frac{1}{w}\sum_{i=1}^{4}\frac{w_i}{Z_i} \tag{4.7}$$

Then, the liner impedance is given as

$$Z = \frac{1}{A} \tag{4.8}$$

It is noted that the liner admittance A does not consider the admittance of the internal partitions (c.f. Equation 3.2) because in the current baseline liner model the internal walls are considered as being infinitesimally thin, and therefore they do not contribute to the definition of the overall admittance A. Moreover, in Equation 4.7, A does not account for any radiation impedance or wall friction of the cavities because the numerical studies in Chapter 3 showed that their contribution to A is of second order.

It is noted for completeness that the influence and interactions of the radiation impedance of the cavities may become more significant for larger cavities at higher frequencies [39]. However, if these designs are to be integrated into an aircraft engine duct, they will require a facing skin for structural and drag purposes, in addition to providing the additional resistance to match the optimum for a given duct. In this case, the radiation impedance will be negligible [32]. Also, if cavity widths increase above the levels used to date, the wall friction losses will also reduce to negligible levels [46].

4.2 Validation of the numerical and analytical routines

The hypothesized correlation between the numerical folded-cavity model and the straight-cavity model is tested in COMSOL 5.4. The numerical results are then compared with the results predicted using the analytical model.

Three case studies are deployed. A folded-cavity numerical model, labelled CS1–F, the correspondent straight-cavities model labelled CS1–S, and an analytical model with the same characteristics of the CS1-S model, labelled CS1-A. Each of the three case study models are analysed for frequencies ranging between 100 and 4000 Hz (with a 100Hz step), that is comfortably below the first cut-on frequency of the cross modes propagating in the 29mm diameter impedance tube. The current study is conducted with a normally incident plane-wave source and a no-flow condition.

The CS1-F core is developed using an iterative procedure. First, the resonant frequency f_{res_i} of the individual cavities is set, and the correspondent effective centreline length h_i is calculated as if the cavity was a quarter-wave resonator.

$$h_i = \frac{c}{4 \cdot f_{res_i}} \tag{4.9}$$

Then, the individual cavity widths w_i are chosen. Following the definition of the individual h_i and w_i, a check is made to see if the chosen geometry violates the constraints and, if necessary, the individual cavity dimensions are modified to ensure the constraints are respected. In the CS1-F model, the liner has a maximum overall height and width that depend respectively on the maximum space available in the inner walls of the nacelle and the maximum wavelength considered in the study. The minimum width of an individual cell is set at 5 mm.

Finally, the normalized resistance at the liner surface was iterated to a value, R, that made the average normalized resistance over the frequency range close to unity, given that a panel with a resistance of 1 ρc and reactance of 0 ρc will provide 100% absorption at normal incidence. In the current study case CS1-F, $R = 0.34\ \rho c$.

The CS1-F model characteristics are then replicated in the corresponding CS1-S model: this has the same maximum overall width of the CS1-F model, while no limitation is set for the maximum overall height. The CS1-S geometry and its dimensions are then adopted in the deployment of the CS1-A model.

Figure 4.3 and Figure 4.4 show CF1-F and CS1-S. In addition to the corresponding liner core, each of them replicates the normal impedance tube, whose width is set equal to the liner width w. In the numerical models, the liner impedance is calculated according to the Two-Microphone Method in a simulation of the normal impedance tube set-up. The models are meshed with free quadrilateral elements and the maximum size is set to a tenth of the minimum acoustic wavelength considered $\left(\frac{\lambda_{min}}{10} = \frac{c}{10 \cdot f_{max}} = \frac{345\frac{m}{s}}{10 \times 4000\ Hz} \approx 8.5\ mm\right)$. In the grey regions, the pressure acoustics, frequency domain are selected, and the initial conditions are defined. The sound hard boundary conditions are imposed along the external boundaries of the tube and the liner core. The internal partitions are modelled as rigid and reflective one-dimensional elements.

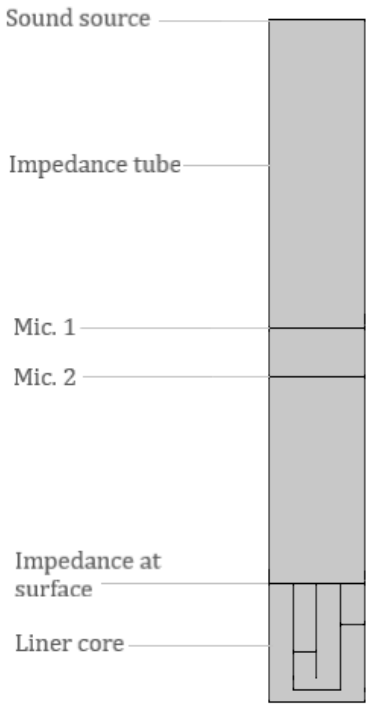

Figure 4.3. CS1-F: Folded-cavity liner and impedance tube COMSOL model

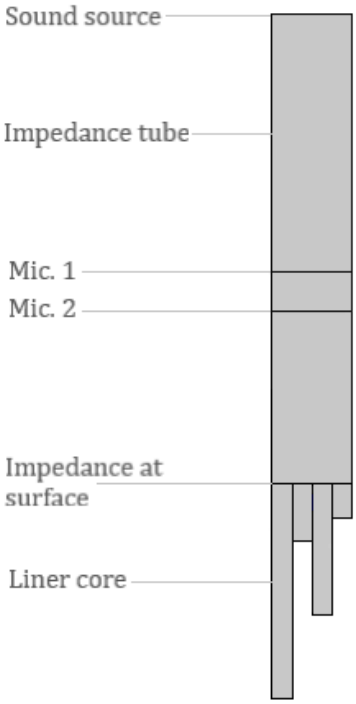

Figure 4.4. CS1-S: Straight-cavity liner and impedance tube COMSOL model

The numerical results of the CS1-F and CS1-S models obtained with the source SPL set to 130 dB and the analytical results of the CS1-A are compared in Figure 4.5 and Figure 4.6. Figure 4.5 provides the impedance of the three models, while Figure 4.6 provides their normal incidence sound absorption coefficient.

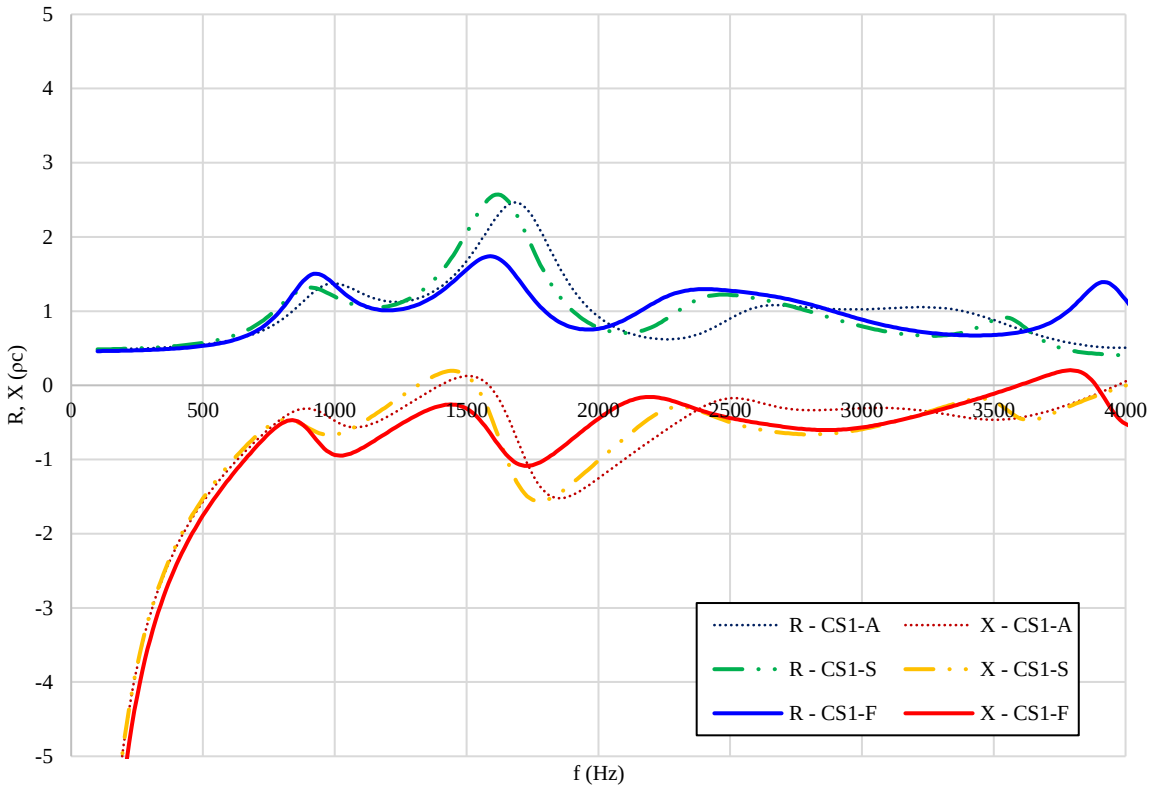

Figure 4.5. CS1-F, CS1-S and CS1-A impedance, OASPL 130 dB

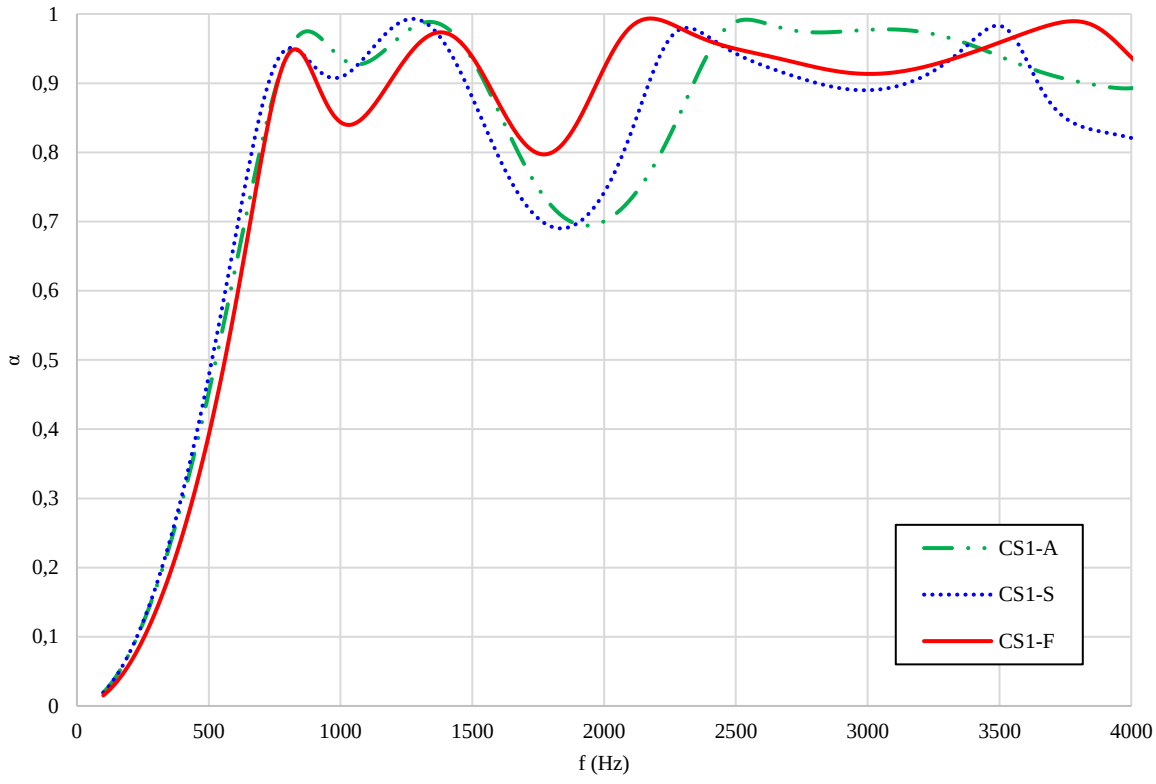

Figure 4.6. CS1-F, CS1-S and CS1-A normal sound absorption coefficient, OASPL 130 B

Figure 4.5 and Figure 4.6 illustrate a favourable comparison between the numerical results of CS1-F and CS1-S. This confirms the hypothesis suggested in [6] [34] that, to a first order, the liner sound absorption is not influenced by the presence of folded cavities. The acoustic characteristics of the CS1-F model are successfully predicted by the CS1-S model, if not in the region of the reactance peaks and troughs and for few points at high frequencies.

It is noted that agreement between CS1-F and CS1-S begins to degrade above approximately 800Hz. The divergence arises from the variation in acoustic performance of straight cavities and the folded cavities when the sound wave pressure impinges on the liner at high frequencies. Figure 4.7, Figure 4.8, Figure 4.9 and Figure 4.10 provide examples of the total acoustic pressure propagating and reflecting in the impedance tube and inside the liner core of CS1-F and CS1-S models. The selected frequencies of 1900Hz and 3800Hz are chosen in order to highlight the regions of maximum divergence in the folded and straight cavity performance.

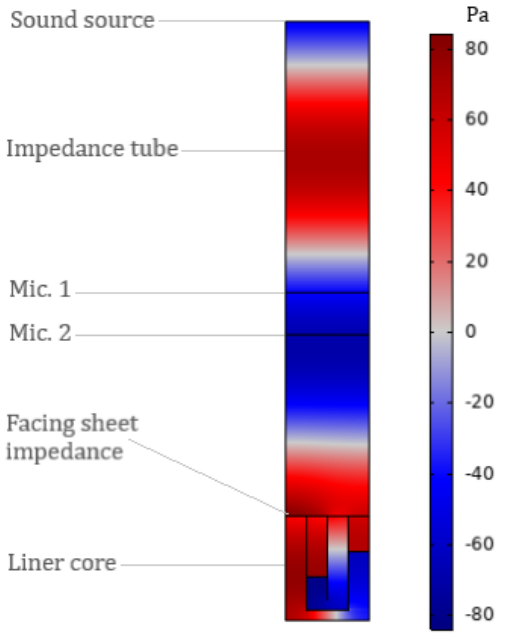

Figure 4.7. CS1-F, total acoustic pressure at 1900 Hz

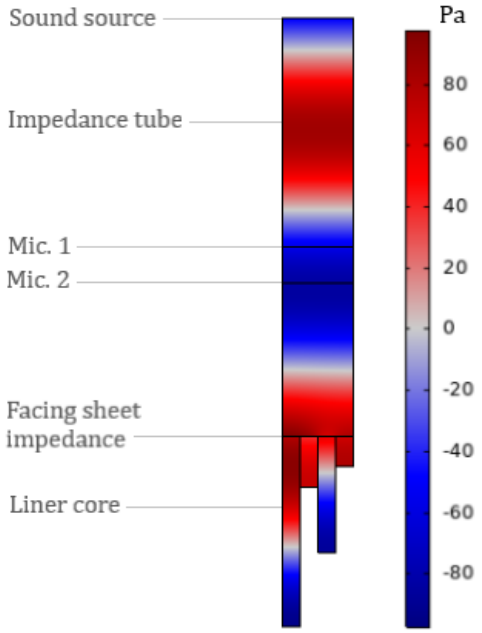

Figure 4.8. CS1-S, total acoustic pressure at 1900 Hz

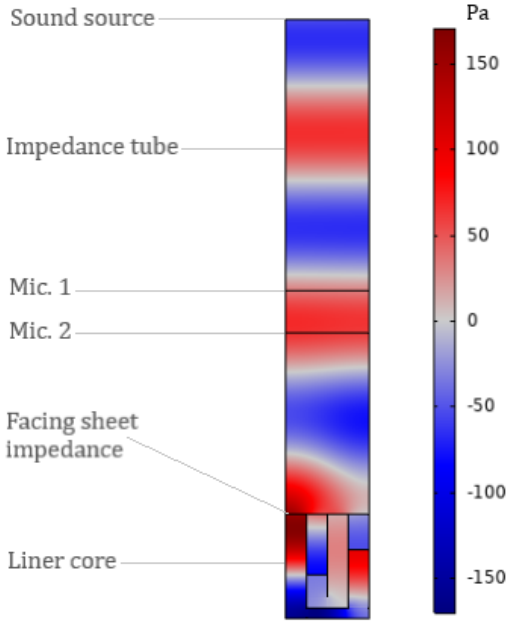

Figure 4.9. CS1-F, total acoustic pressure at 3800 Hz

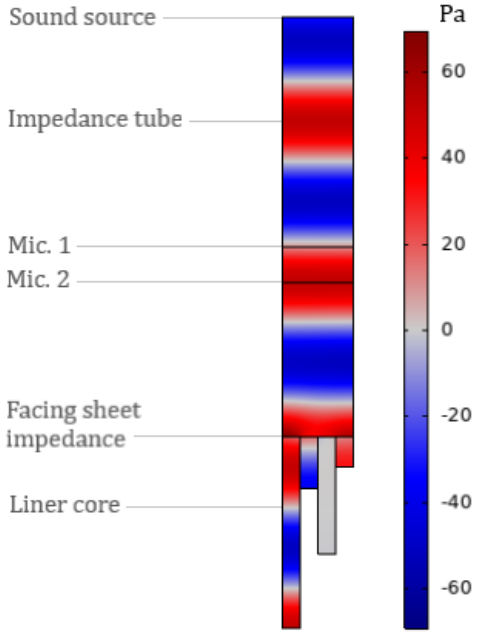

Figure 4.10. CS1-F, total acoustic pressure at 3800 Hz

Reference [6] highlighted the change in the response in folded cavities at high frequencies, when the sound begins to beam, and is partly reflected from the first fold. At 1900 Hz, there is a slight difference between the total acoustic pressure field in CS1-F and the total acoustic pressure field in CS1-S. This seems to be attributed to changes in the response of cavity 1. At 3800 Hz the incident pressure wave in the CS1-F impedance tube is clearly reflected differently when compared to the pressure wave in CS1-S impedance tube. This is particularly evident in the contribution from the first and third cavities. This is due to increased reflection at the fold that arises from increasing beaming at higher frequencies. On the contrary, as the noticeable correlation between the CS1-F and the CS1-S reactance curves clarifies, the differences are subdued at low frequencies, because the pressure wave propagates

in the folded cavities for their entire effective centreline lengths, with their longer wavelengths not “seeing” the fold. Their acoustic performance therefore resembles those of their straight counterparts [6].

Figure 4.5 and Figure 4.6 also show good agreement between the numerical results of the CS1-S and the analytical results of the CS1-A, with agreement reducing somewhat for higher frequencies. The divergences are due to the missed considerations in the analytical model concerning the individual wave reflections for each cell, which locally alter the pressure wave in the impedance tube and hence also alter the calculation of the liner impedance in CS1-S. However, the relatively small differences between the results are more than acceptable and the good correlation suggests that the liner impedance can be well predicted by the analytical model.

In general, from Figure 4.5 and Figure 4.6, it may be concluded that there is good agreement between the results of the three models and it confirms the previously hypothesised validity about the use of the analytical model for representing the liner impedance, even when folded cavities are present in the baseline model.

The correlation between the three different models is now shown for variations in cavity order across the liner. Previous studies [34] demonstrated that, under a normally incident plane-wave source and for a grazing incidence no flow condition, a variation in the order of the cavities affects the acoustic pressure profile along a duct, but the effects on the overall noise attenuation is reasonably limited and can be neglected. To prove this hypothesis in a normal impedance tube set-up, the order of the cavities in the CS1-F model was arranged in three different ways, and their correspondent straight-cavity models were built. These models are respectively labelled as CS1-F-a, CS1-F-b, CS1-F-c and CS1-S-a, CS1-S-b, CS1-S-c and their configurations are shown in Figure 4.11 to Figure 4.18. In the CS1-F-type models, the arrangement of the cavities in the prescribed orders conflicts with the imposed maximum overall height h, and the effective centreline length of the longest cavities are slightly changed to respect this constraint (maximum change is 5 mm). On the contrary, in the CS1-S type models, the effective centreline lengths of the individual cavity are preserved, and the CS1-S-a, CS1-S-b and CS1-S-c are distinguished only by the order of the cavities.

It should be noted that the reordering of the liner cavities is irrelevant in the CS1-A modelling, because the analytical model considers the liner impedance as smeared over its length; hence, no additional analytical models are deployed in addition to CS1-A.

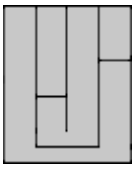

Figure 4.11. CS1-F

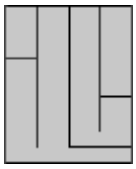

Figure 4.12. CS1-F-a

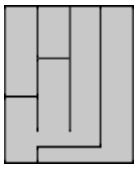

Figure 4.13. CS1-F-b

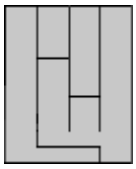

Figure 4.14. CS1-F.c

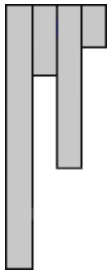

Figure 4.15. CS1-S

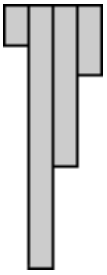

Figure 4.16. CS1-S-a

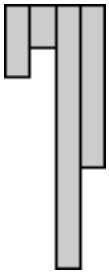

Figure 4.17. CS1-S-b

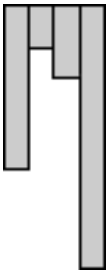

Figure 4.18.CS1-S-c

The following figures provide the liner impedance of the models introduced and their respective sound absorption coefficients, achieved with the source SPL set at 130 dB, in absence of mean flow and for a normally incident plane wave.

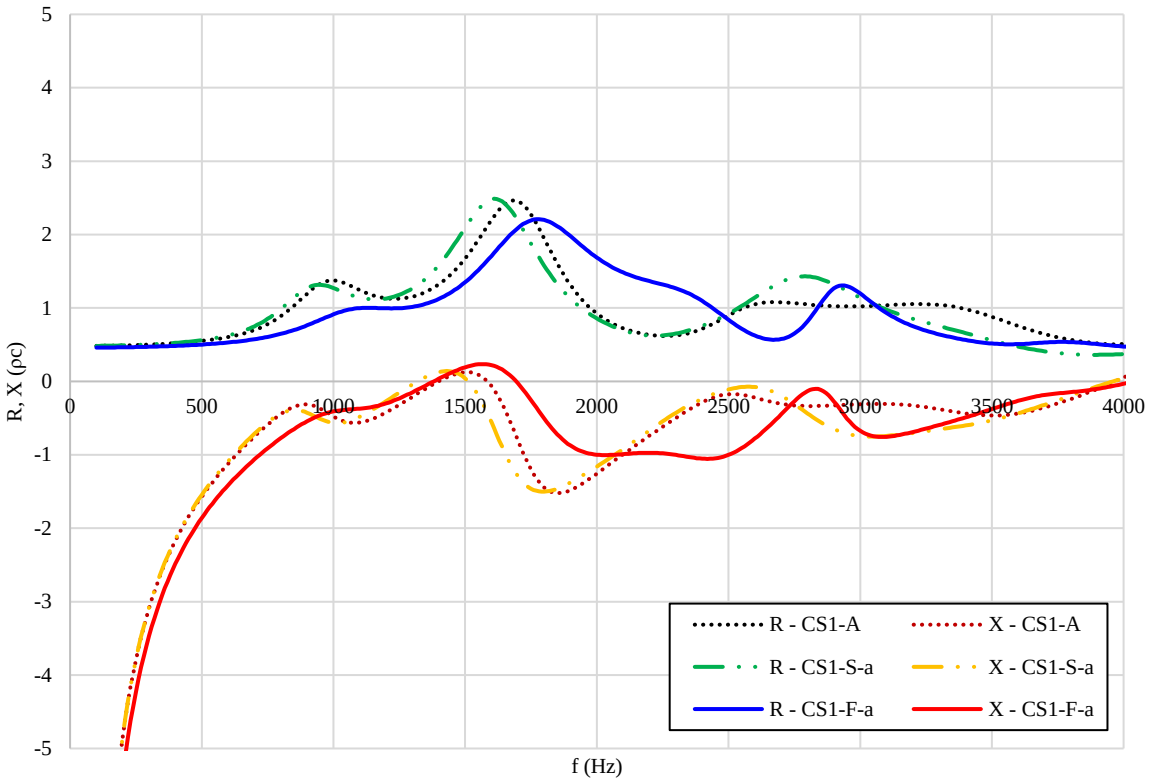

Figure 4.19. CS1-F-a, CS1-S-a and CS1-A impedance, OASPL 130 dB

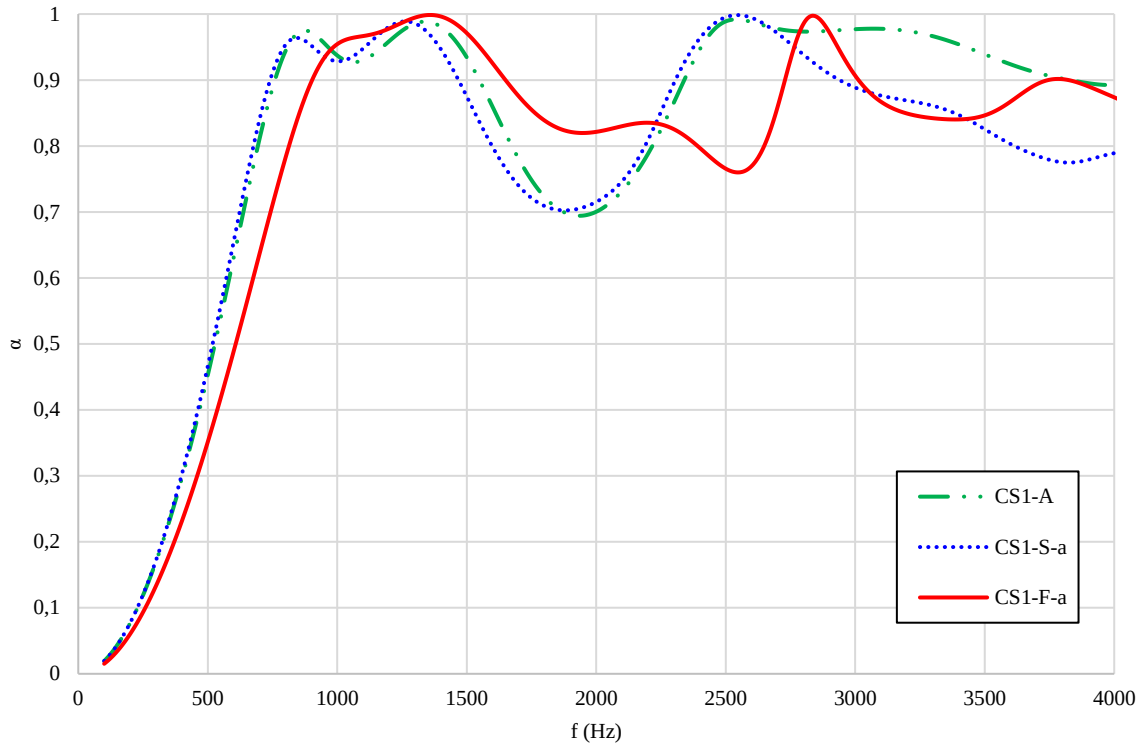

Figure 4.20. CS1-F-a, CS1-S-a and CS1-A normal sound absorption coefficient, OASPL 130 B

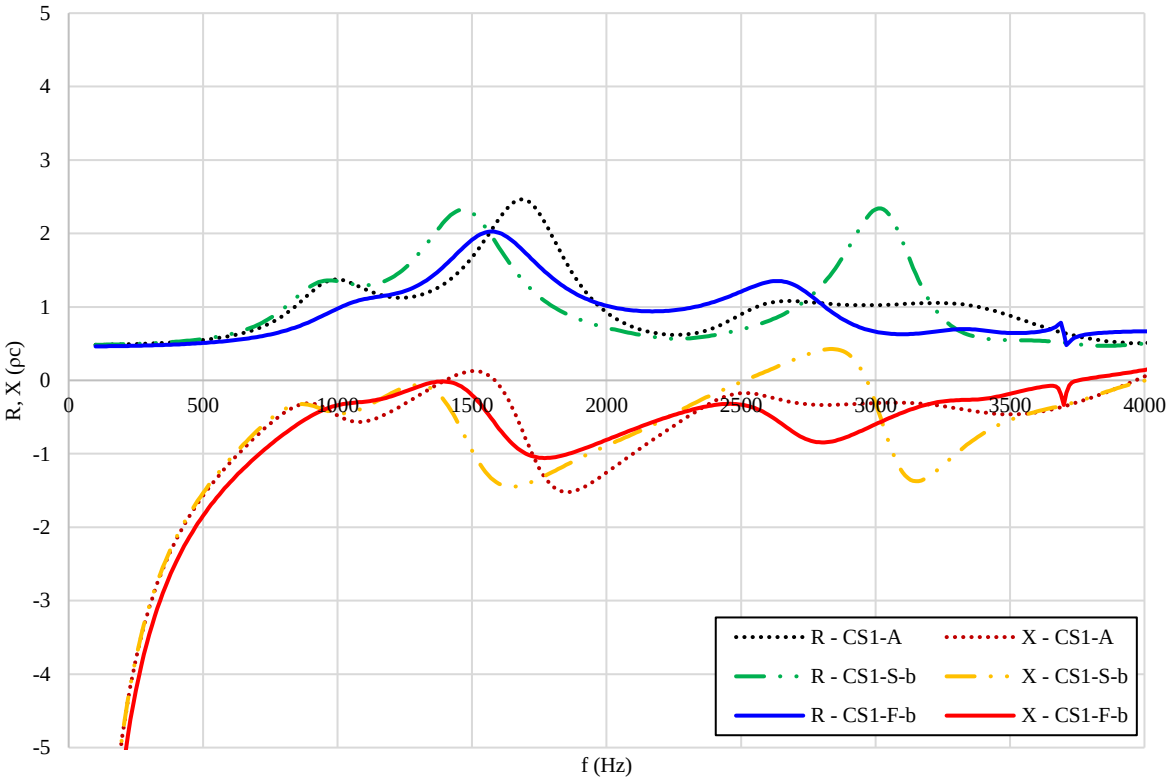

Figure 4.21. CS1-F-b, CS1-S-b and CS1-A impedance, OASPL 130 dB

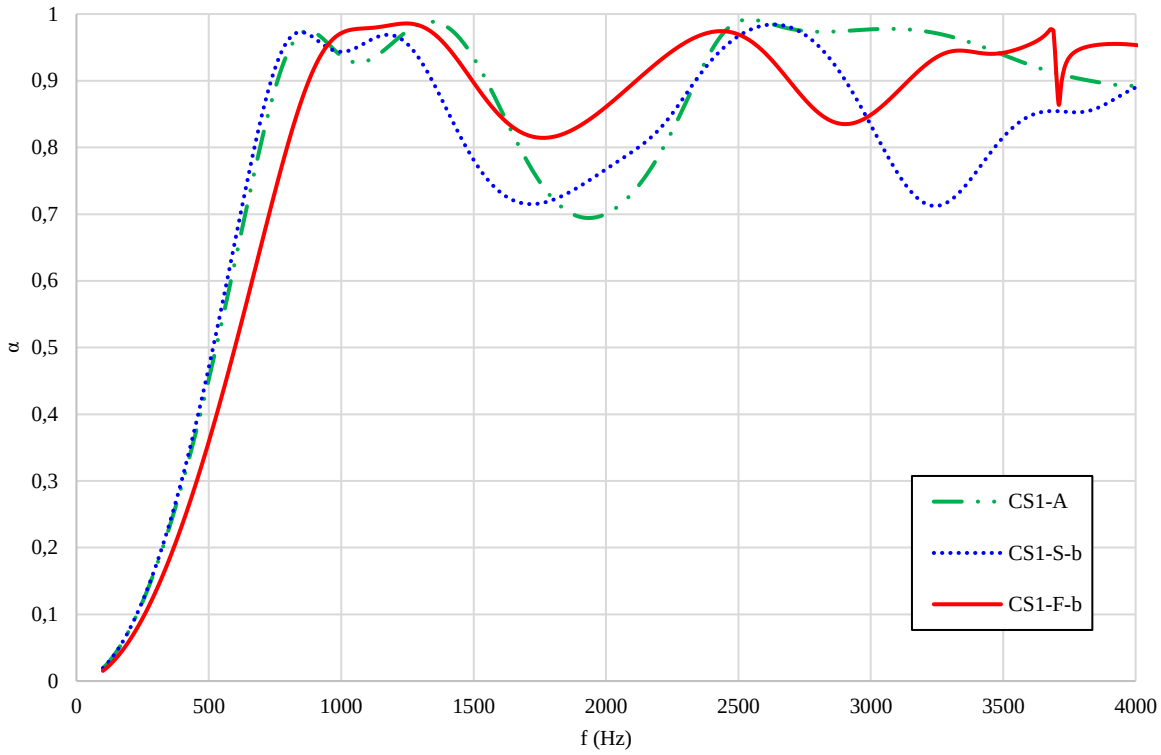

Figure 4.22. CS1-F-b, CS1-S-b and CS1-A normal sound absorption coefficient, OASPL 130 B

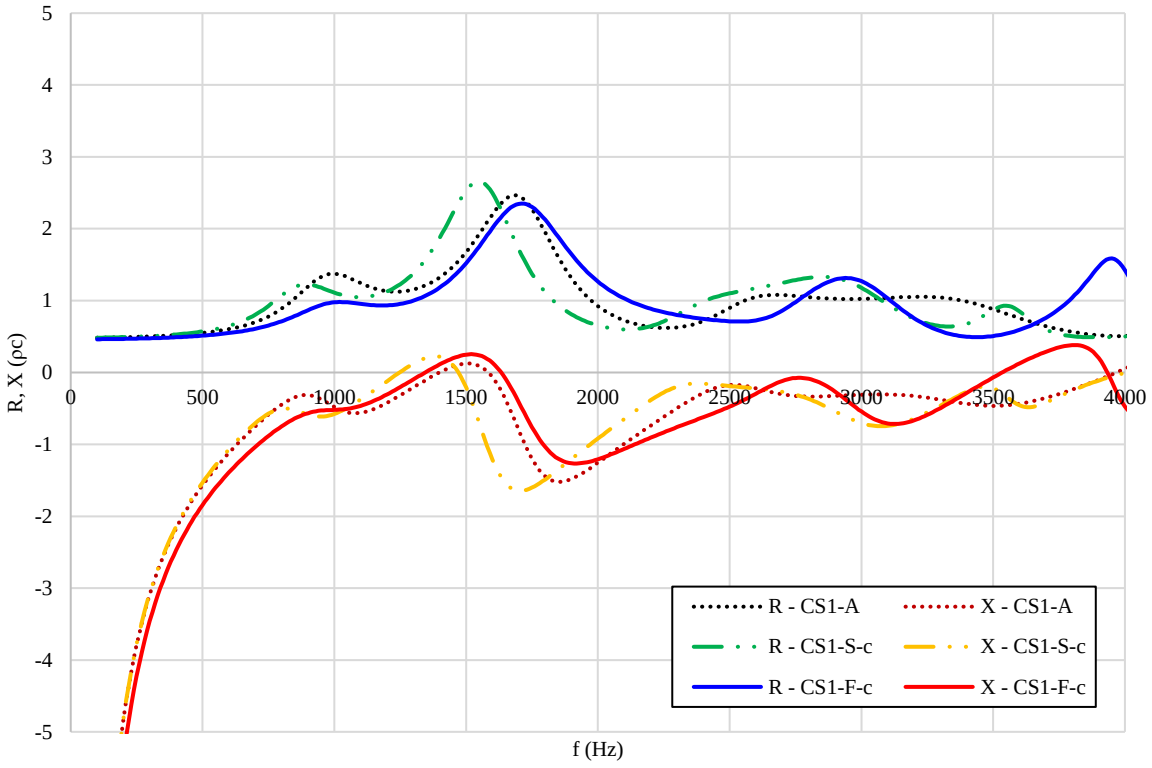

Figure 4.23. CS1-F, CS1-S and CS1-A impedance, OASPL 130 dB

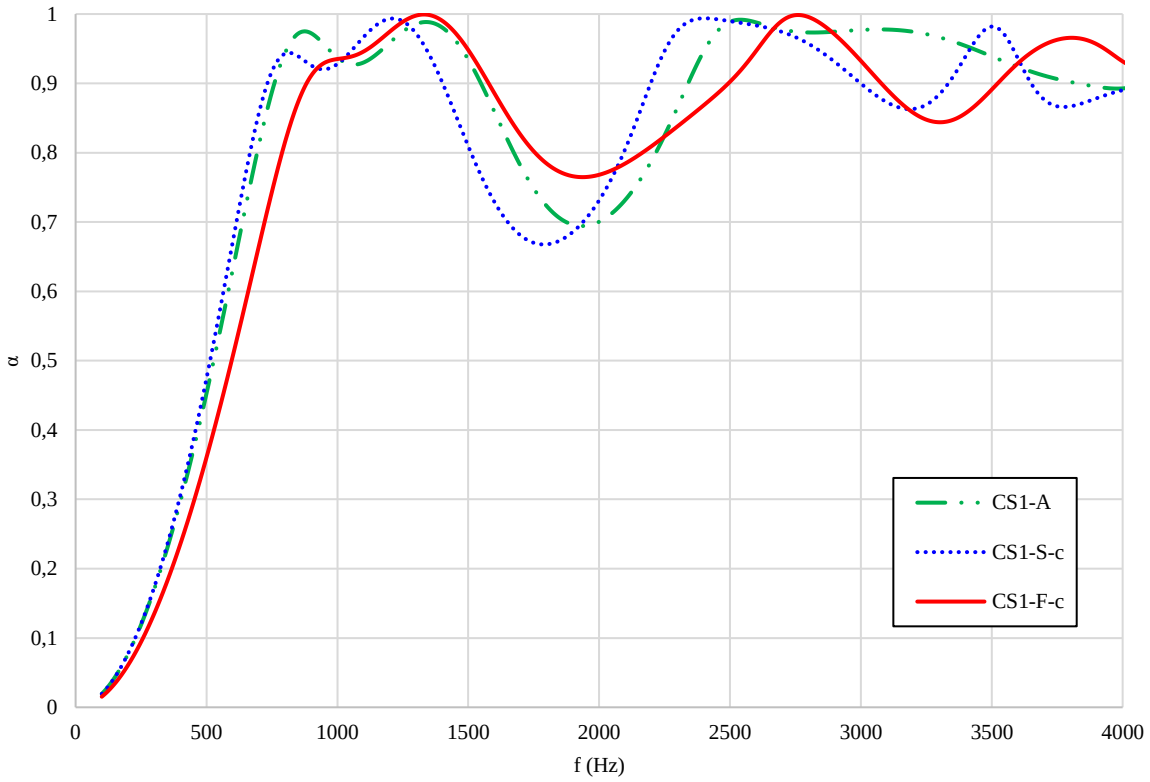

Figure 4.24. CS1-F-c, CS1-S-c and CS1-A normal sound absorption coefficient, OASPL 130 B

The above figures clarify that the CS1-A model generally well predicts the numerical results of both the CS1-F-type and the CS1-S-type models, whatever the cavity order. The main differences between the numerical and the analytical results occur at lower frequencies and close to the peaks and troughs of the reactance. They occur primarily as a result of the above-mentioned change in the effective centreline length of the longest cavities, that varies the acoustic properties of the liners slightly, particularly at low frequencies. However, the limited differences between the numerical and the analytical results are not considered critical at this stage and the analytical model confirms its capability of successfully predicting the sound absorption performances of the liners, in the case of both folded and straight cavities.

With these observations in mind, the analytical model is later used for studying the sensitivity of the liner acoustic properties to the individual cavity width and to the number of cavities. Then, the analytical model is adopted as the baseline model for the optimization process of the liner configurations.

4.3 Influence of the individual cavity width on the baseline liner impedance

Before conducting the liner optimization, a sensitivity analysis is performed in order to assess the influence of the individual cavity width and the number of the cavities on the liner acoustic properties. This investigation completes the general understanding on how the liner geometry affects its acoustic properties and highlights which geometry parameters are worth considering in the optimization process.

The first part of the study focuses on the effects of the individual cavity width on the liner impedance and, to this goal, four analytical models were deployed (CS1-A.1, CS1-A.2, CS1-A.3 and CS1-A.4, see Figure 4.26 to Figure

4.29). Each of them has the width of a single cavity doubled with respect the width of the correspondent cavity in CS1-A, while the width of the remaining cavities is kept unaltered. CS1-A.1 doubles the first cavity width of the CS1-A model, CS1-A.2 the second, CS1-A.3 the third and CS1-A.4 the fourth, while their facing sheet impedance and individual cavity heights equals those of CS1-A. Clearly, changing an individual cavity width while preserving the widths of the remaining cavities infringes the constraint on the maximum overall width *w* and reduces the maximum frequency where the response may be considered smeared. However, this concept provides improved understanding of the liner impedance sensitivity to the width of a single cavity, whereas respecting the constraint on the maximum overall width *w* would require altering the widths of the remaining cavities and this would make the effect of the individual cavity widths unclear. Notwithstanding the increased width, the liner impedance is still considered as smeared over its length, as the analytical model is not used for designing the liner impedance, but only to conduct the sensitivity analysis.

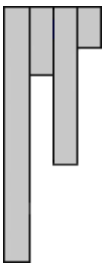

Figure 4.25. CS1-A

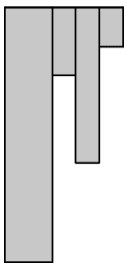

Figure 4.26. CS1-A.1

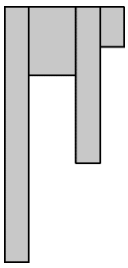

Figure 4.27. CS1-A.2

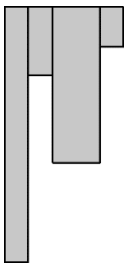

Figure 4.28. CS1-A.3

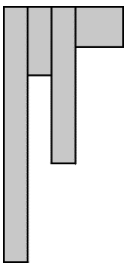

Figure 4.29. CS1-A.4

The figures below provide the impedance and the normal sound absorption coefficient of the models CS1-A.1, CS1-A.2, CS1-A.3 and CS1-A.4, in the frequency range between 100 Hz and 4000 Hz, with a resolution of 100 Hz.

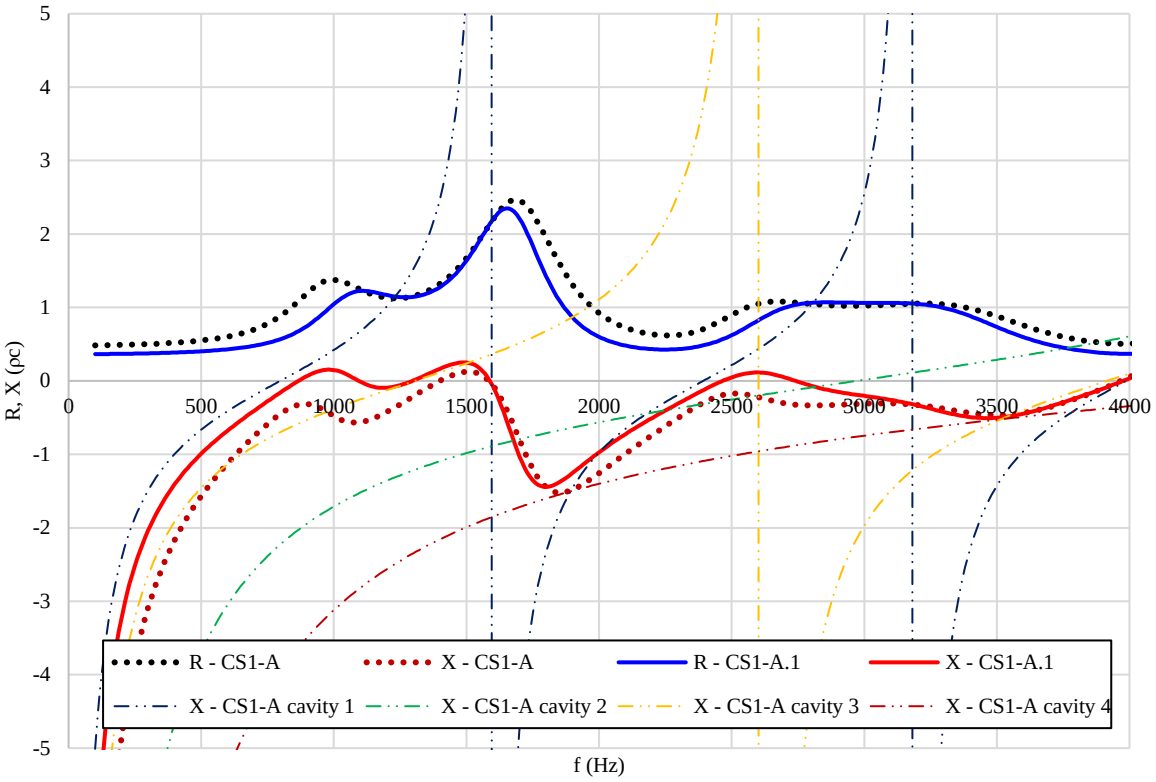

Figure 4.30. CS1-A and CS1-A.1 impedance

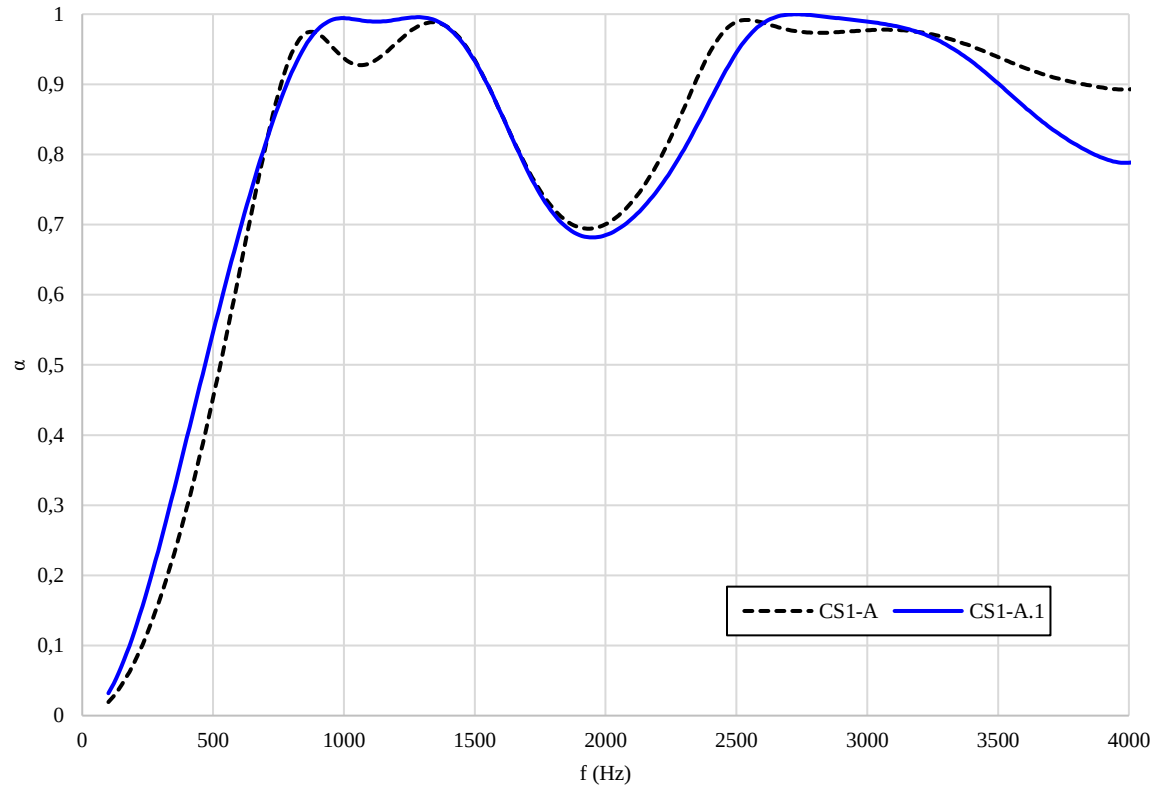

Figure 4.31. CS1-A and CS1-A.1 normal sound absorption coefficient

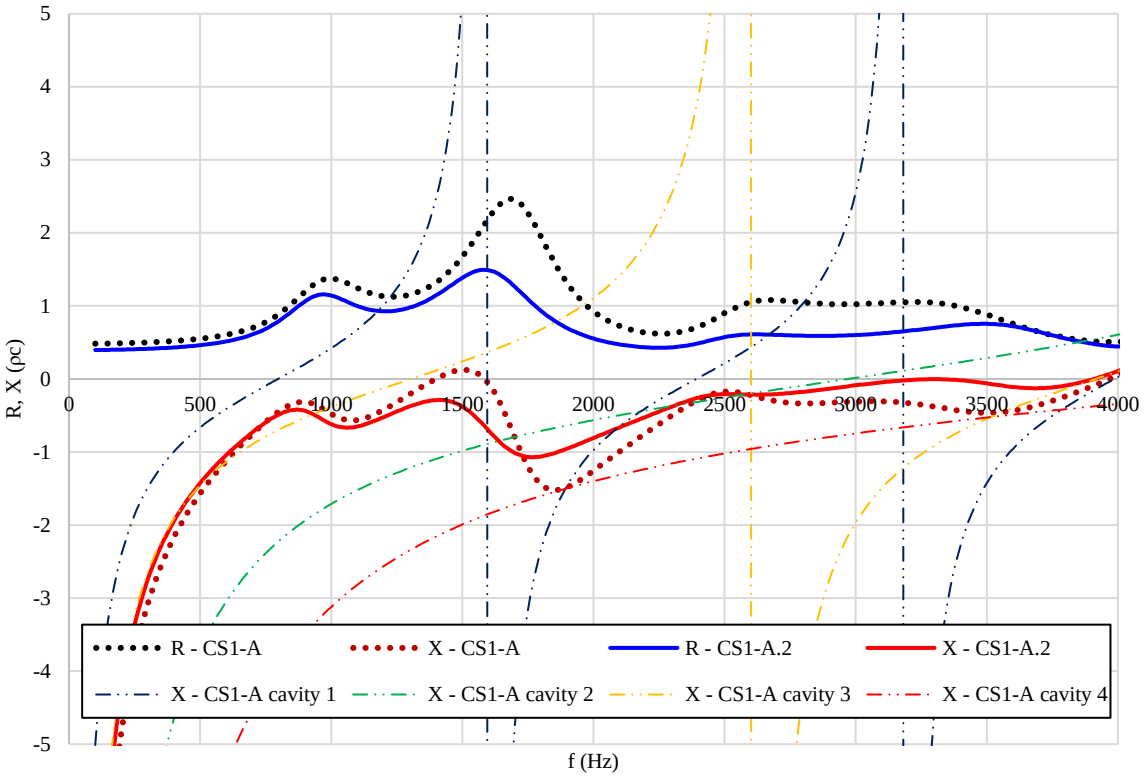

Figure 4.32. CS1-A and CS1-A.2 impedance

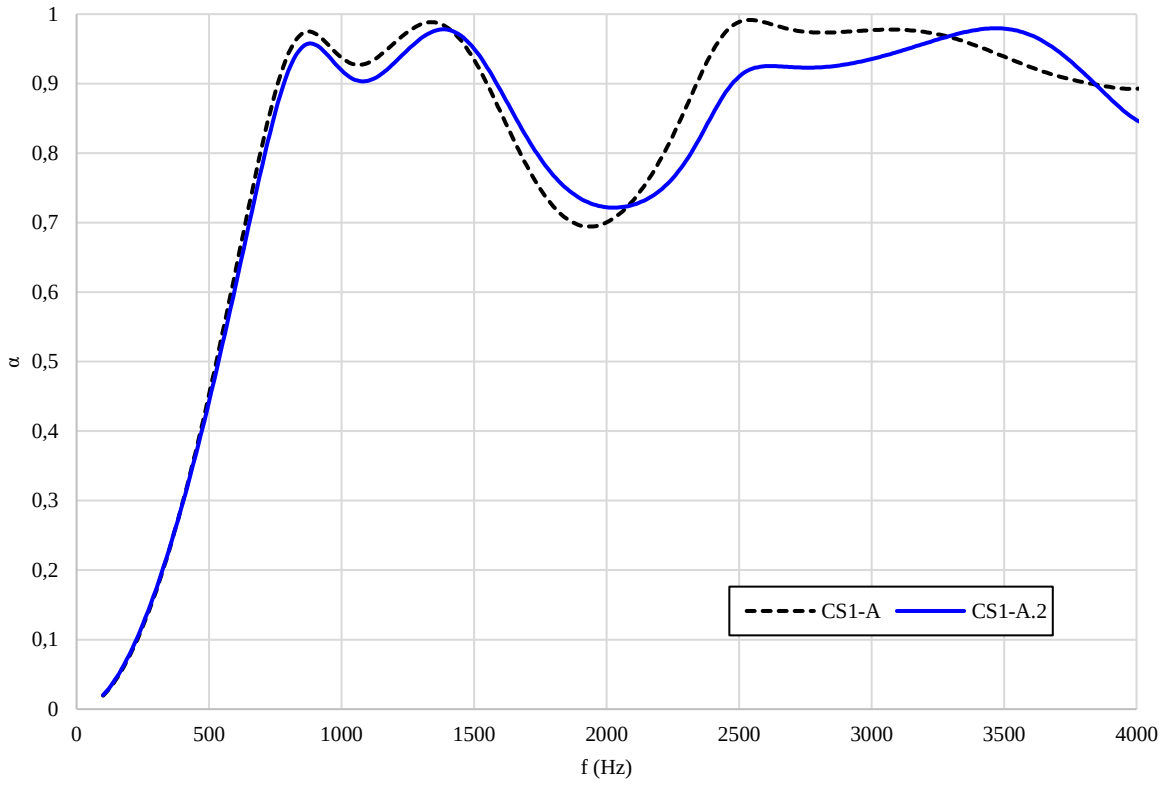

Figure 4.33. CS1-A and CS1-A.2 normal sound absorption coefficient

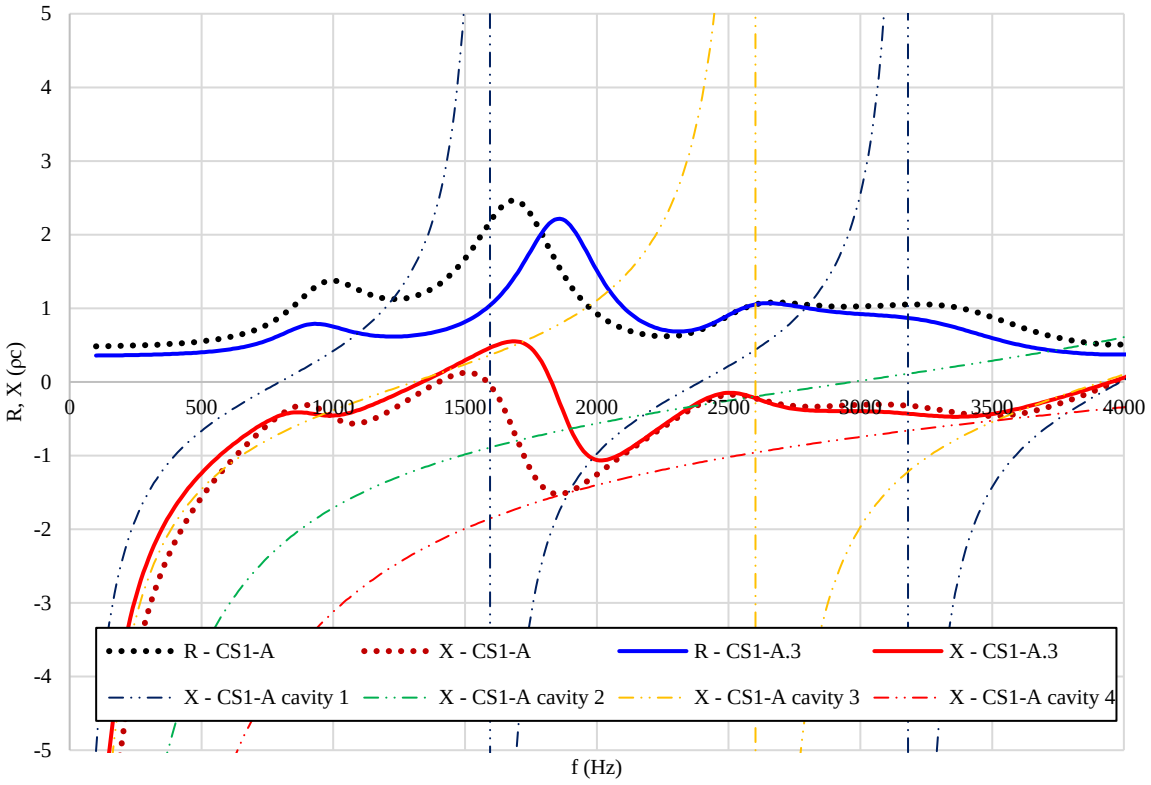

Figure 4.34. CS1-A and CS1-A.3 impedance

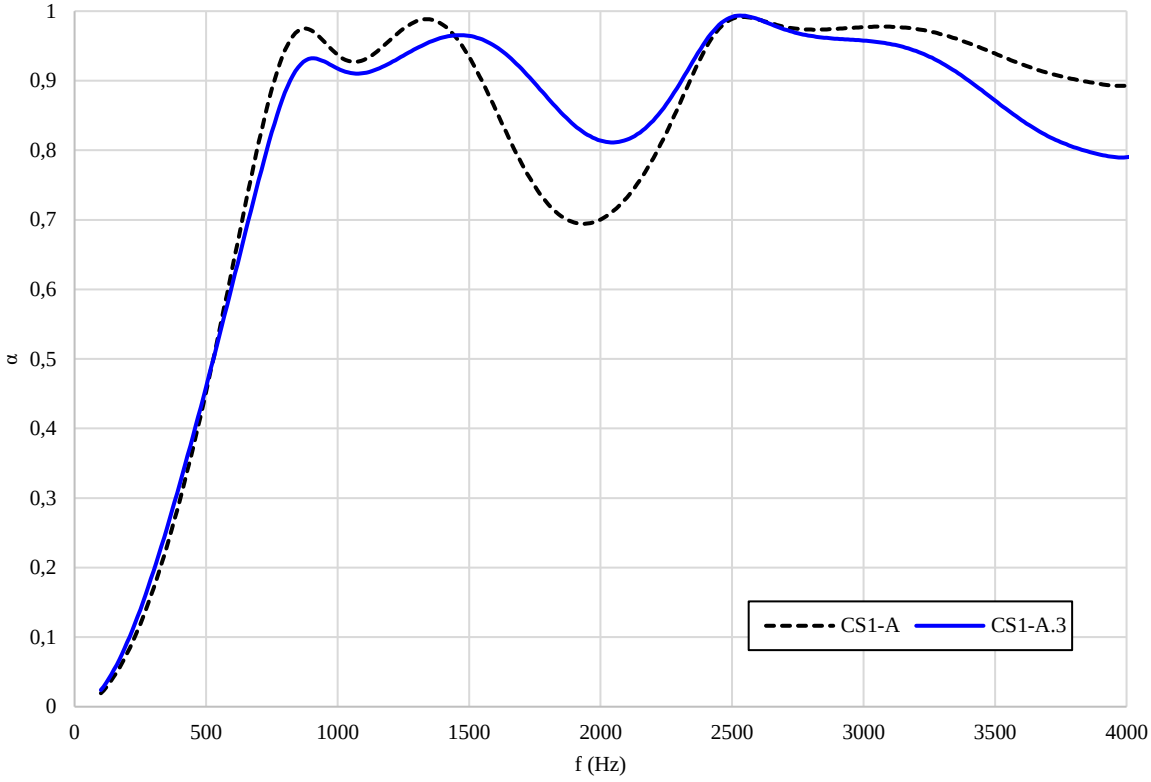

Figure 4.35. CS1-A and CS1-A.3 normal sound absorption coefficient

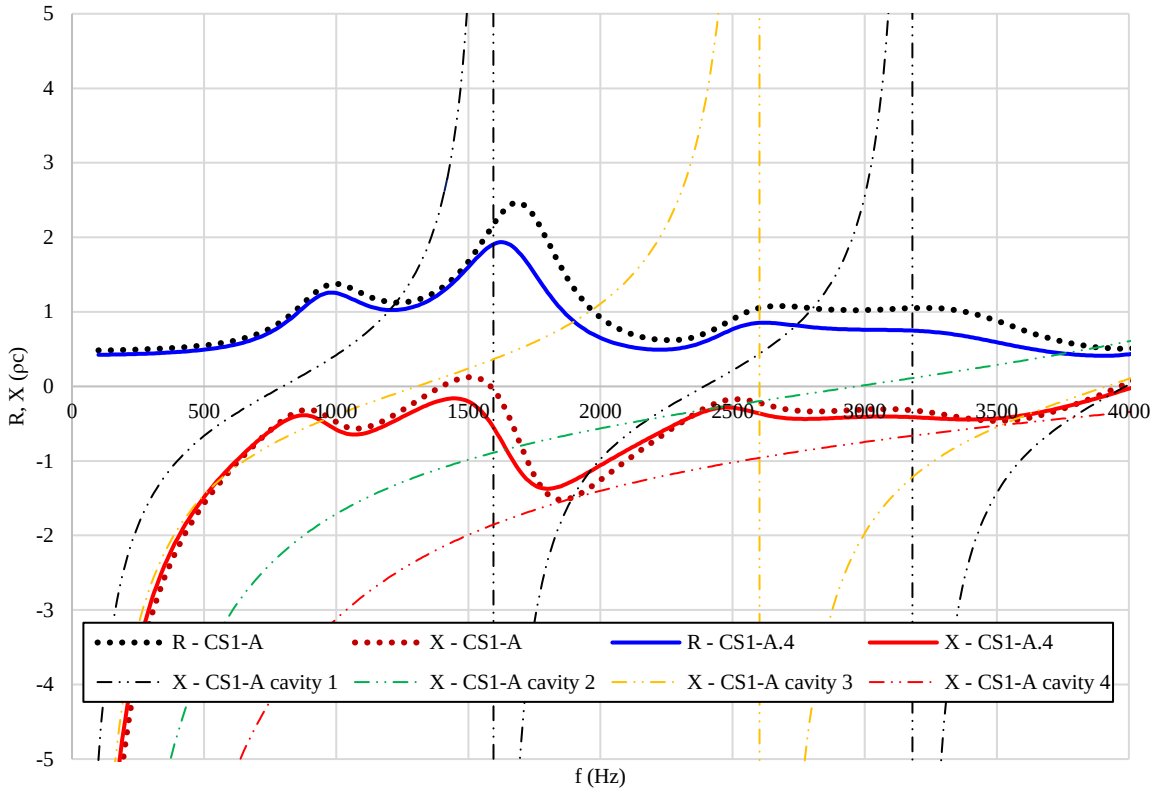

Figure 4.36. CS1-A and CS1-A.4 impedance

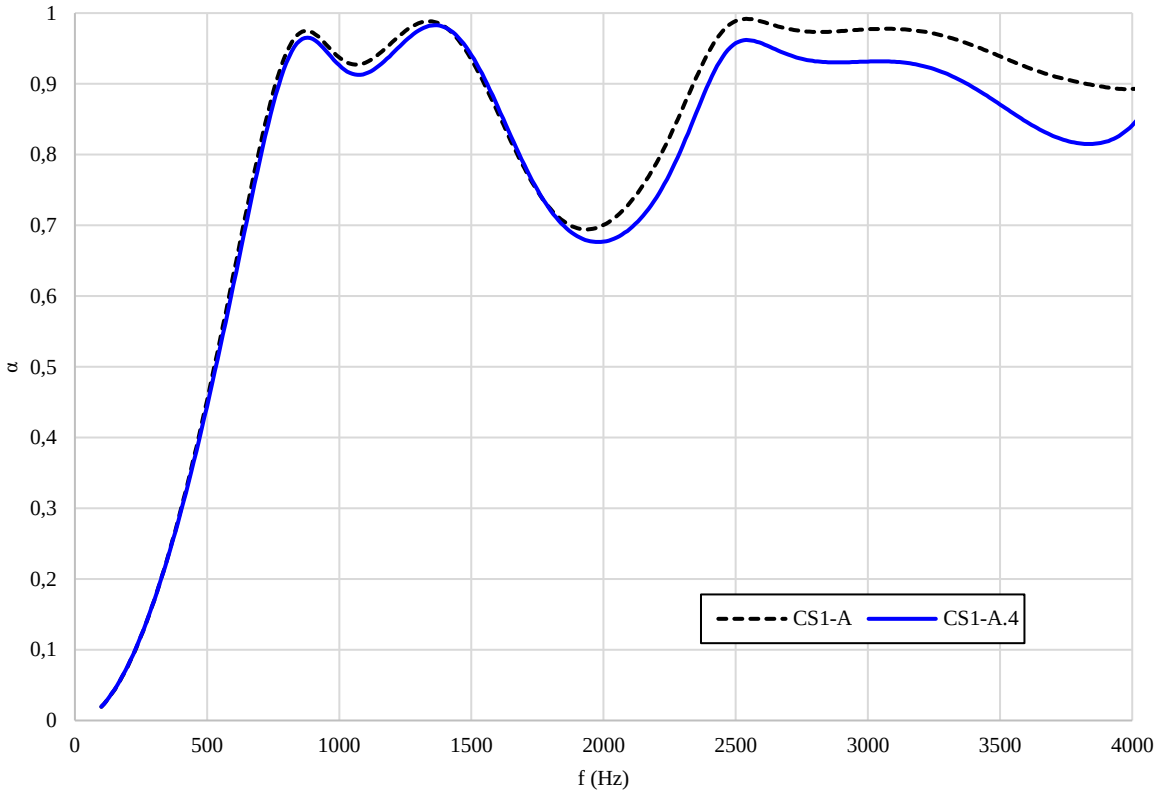

Figure 4.37. CS1-A and CS1-A.4 normal sound absorption coefficient

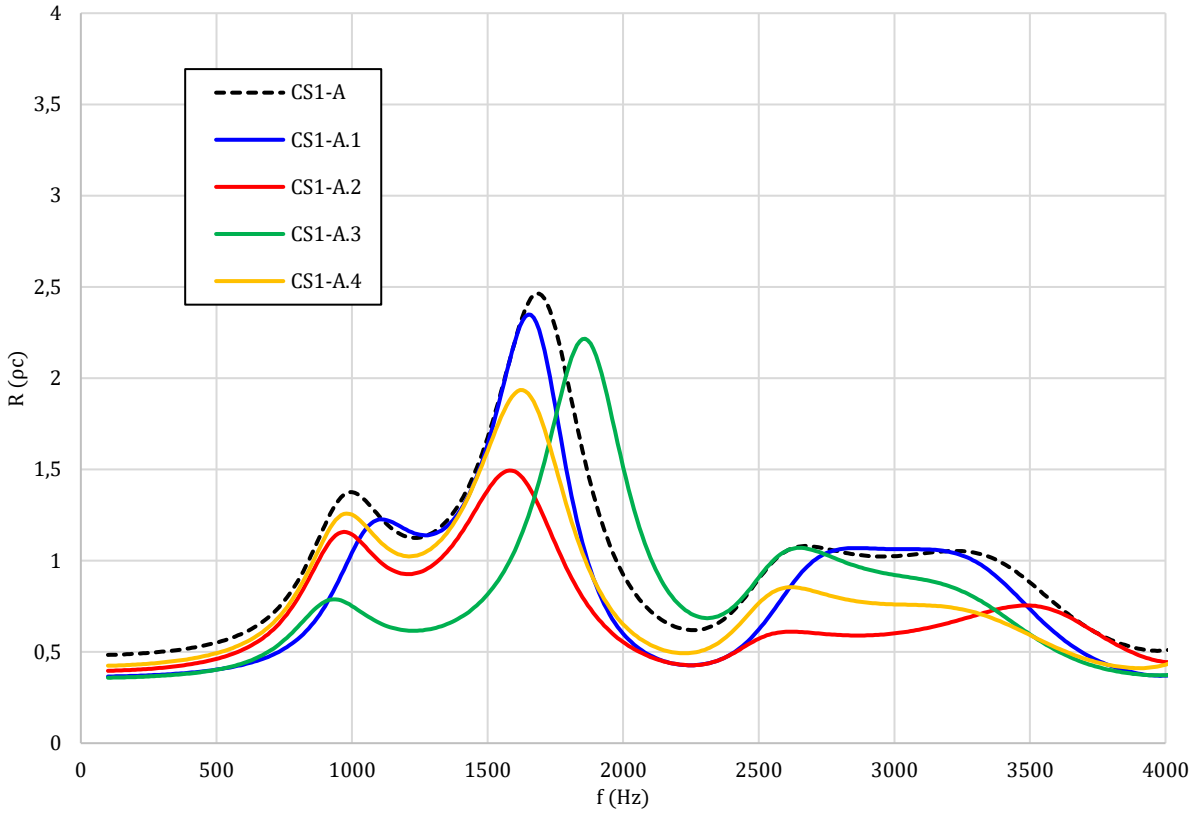

Figure 4.38. CS1-A, S1-A.1, CS1-A.2, CS1-A.3 and CS1-A.4 normalized resistance, R

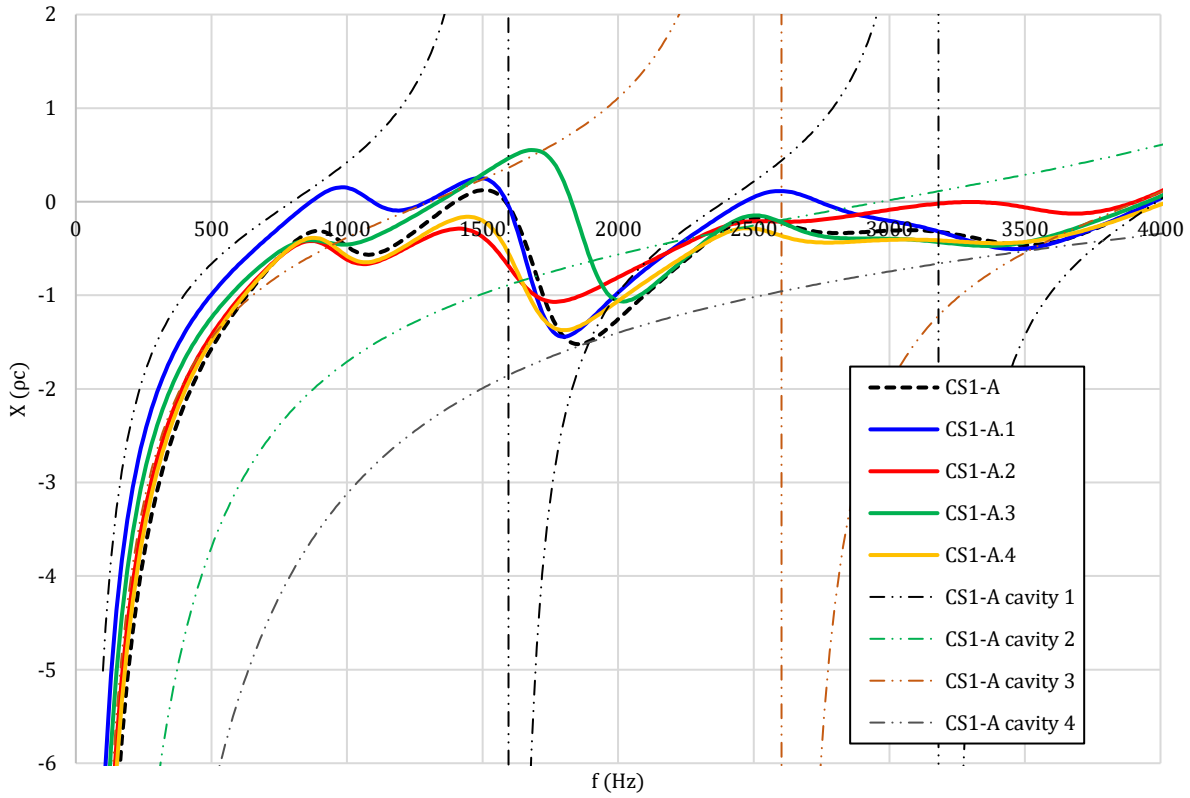

Figure 4.39. CS1-A, S1-A.1, CS1-A.2, CS1-A.3 and CS1-A.4 normalized reactance, X

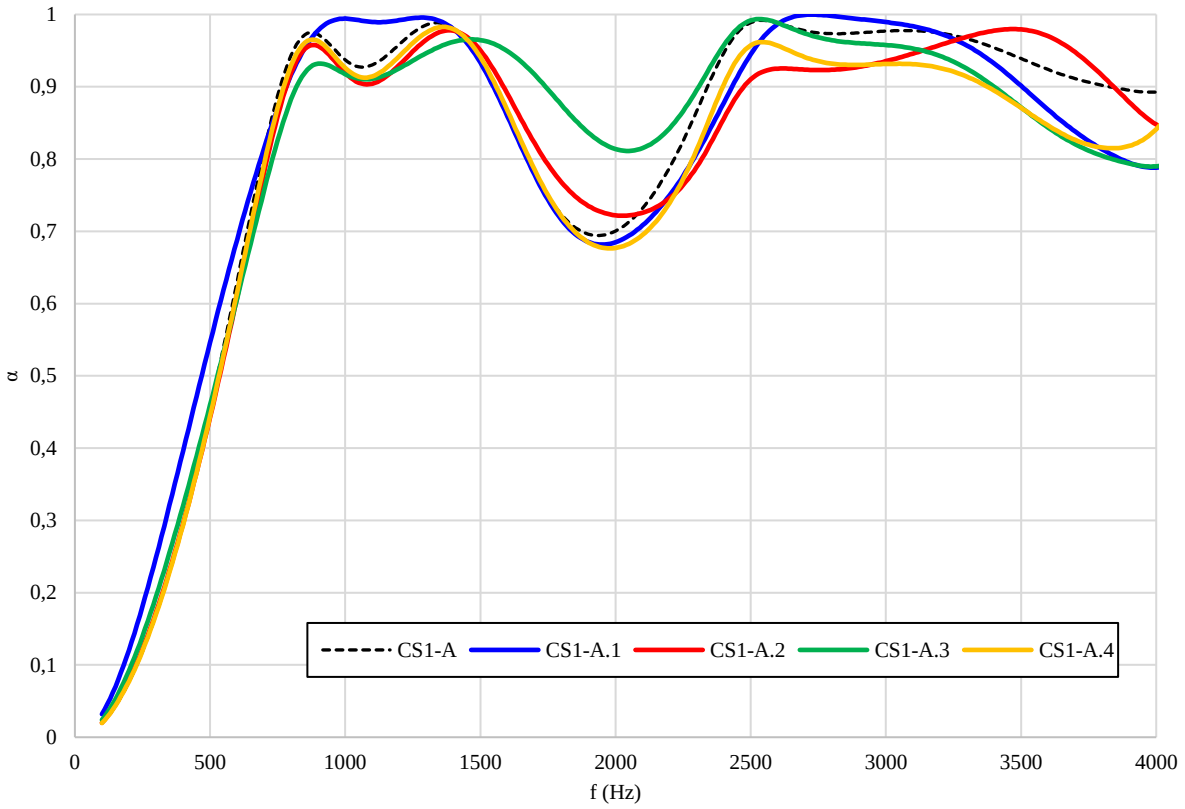

Figure 4.40. CS1-A, S1-A.1, CS1-A.2, CS1-A.3 and CS1-A.4 normal sound absorption coefficient α

From Figure 4.31, Figure 4.33, Figure 4.35 and Figure 4.37 (and overall from Figure 4.40), it emerges that increasing the width of a deep cavity with a low resonance frequency improves the liner sound absorption at lower frequencies; on the contrary, increasing the width of a cavity with a high resonant frequency greatly affects the impedance at high frequencies, while the effects at the low frequencies are subdued. In general, the cavity width influences the sound absorbing performance mainly close to the individual cavity resonant frequency, while in the remaining frequency range the performance differs only slightly from the original.

The influence of the cavity width on the liner acoustic characteristics is investigated further in the following example. A liner composed by two cavities, with an overall width w and face sheet impedance $Z_{fs} = R_{fs} = 0\ \rho c$ is assessed and its impedance is modelled analytically. The individual cavity widths are indicated by w_1 and w_2, while the individual cavity heights are indicated by h_1 and h_2. In the supposition of increasing the width of the first cavity by Δw_1, the total reactance X changes as follows

$$\mathrm{X} = \frac{(w_1 + w_2 + \Delta w_1) \cdot \mathrm{X}_1 \mathrm{X}_2}{(w_1 + \Delta w_1) \cdot \mathrm{X}_2 + w_2 \mathrm{X}_1} \tag{4.10}$$

In the hypothetical limit for which the first cavity width is enlarged up to w, with $w_1 < w$, then $(w_1 + \Delta w_1) \cdot \mathrm{X}_2$ in the denominator dominates and the overall reactance tends to the reactance of the first cavity

$$\lim_{w_1 + \Delta w_1 \to w} \mathrm{X} \to \mathrm{X}_1 \tag{4.11}$$

Hence, when the width of a cavity is increased, the liner acoustic characteristics are dominated by those of the enlarged cavity. This observation highlights the importance of the individual cavity width in the definition of the overall liner impedance.

4.4 Influence of the number of cavities on the baseline model impedance

Alongside the individual cavity width influence on the liner impedance, a sensitivity analysis is conducted to analyse the importance of the number of cavities in the definition of the liner impedance. To this aim, an analytical liner model is created enforcing the same constraints of the CS1-A liner, but with a doubled number of cavities (8 instead of 4) and the individual cavities widths halved. The model dimensions are chosen to respect the following constraints (Equations 4.12-4.16), equivalent to those of the CS1-A model, but extended to the increased number of cavities. This model is labelled CS2-A.

$$w_1 + w_2 + w_3 + w_4 + w_5 + w_6 + w_7 + w_8 = w \tag{4.12}$$

$$h_1 + h_4 = 2h + \frac{1}{2}(w_1 + w_4) + w_2 + w_3 - h_{und_{core}} \tag{4.13}$$

$$h_2 + h_3 = 2h + \frac{1}{2}(w_2 + w_3) - 3h_{und_{core}} \tag{4.14}$$

$$h_5 + h_8 = 2h + \frac{1}{2}(w_5 + w_8) + w_6 + w_7 - h_{und_{core}} \tag{4.15}$$

$$h_6 + h_7 = 2h + \frac{1}{2}(w_6 + w_7) - 3h_{und_{core}} \tag{4.16}$$

The following figures provide the impedance and the normal sound absorption coefficient of the CS2-A model, which are then compared with the corresponding sound absorbing performance of the CS1-A model. It is noted, once more, that the optimum normal impedance will be Z = (1,0).

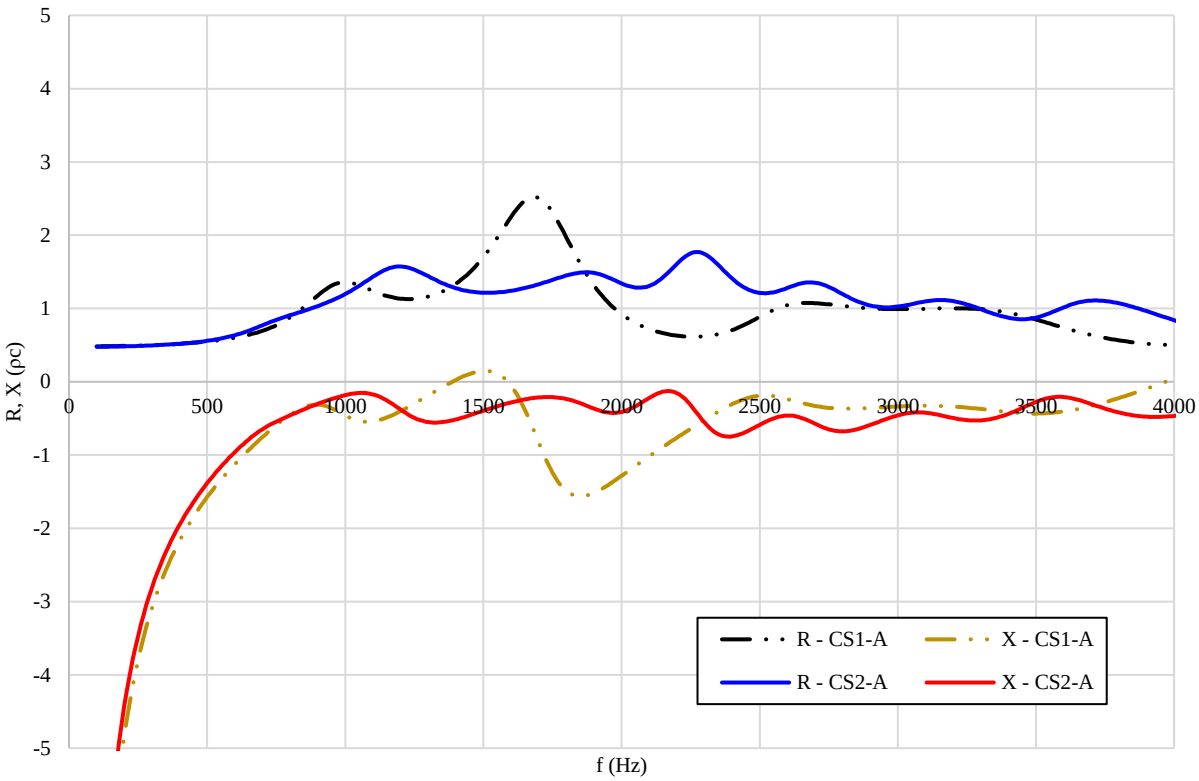

Figure 4.41. CS1-A and CS2-A impedance

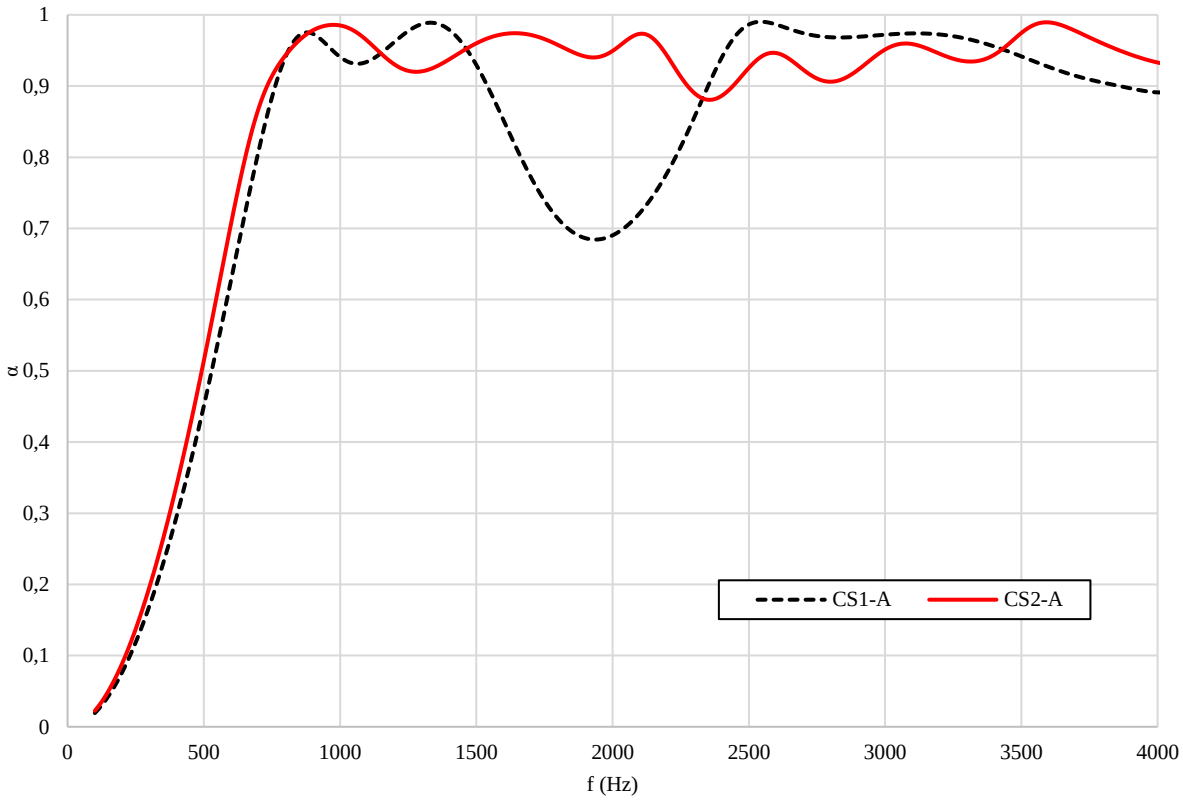

Figure 4.42. CS1-A and CS2-A normal sound absorption coefficient

The comparison of the results shows that the sound absorbing performance of the CS2-A model is generally similar to that of the CS1-A model, if not at frequencies around the CS1-A anti-resonance near 1700 Hz, where the CS2-A absorption capabilities exceed those of the CS1-A model. The enhancement of the sound absorbing performance is obtained thanks to the increased number of variables in the CS2-A model, that allows more control during the liner design phase. The individual cavity resonant frequencies, in fact, are selected to attenuate the anti-resonance peaks from other cavities, and to flatten the overall liner reactance over the widest possible frequency range. However, the difference between the results of the CS1-A model and the results of the CS2-A model, while significant at some frequencies, is reasonably limited. The increased number of cavities presents a trade between increased model complexity and increased performance.

Comparing the effects of cavity width and number of cavities, it may be concluded that varying the cavity width provides relatively greater control on the liner optimisation. Hence, in forthcoming studies in the optimization process of the liner configuration, a four-cavity model is considered, and the enhancement of the liner sound absorption performances is obtained by properly selecting the individual cavity width and height of the four-cavity model rather than increasing the number of cavities.

The four cavity liner absorption is also optimized through the choice of the appropriate facing sheet resistance R_{fs}, which has a limited effect on the spectral shape of the impedance, but affects the overall sound absorption, shifting the overall resistance up and down, and flattening the overall reactance. Therefore, the individual cavity widths and heights and the facing sheet resistance become the design variables to act on for designing the optimal liner configuration.

4.5 Two optimal liner configurations designed to abate noise over a wide frequency bandwidth

The previous studies demonstrated that, under certain conditions, the acoustic properties of a folded-cavity liner are well predicted by an analytical routine. The sensitivity of the liner absorption to its geometrical parameters was also investigated. The four-cavity model was shown to be effective in designing a liner able to absorb normally incident sound over a wide bandwidth, and the primary variables which may be used to tune the liner absorption were highlighted. It is noted that the optimum impedance for an engine inlet or bypass duct will have a different optimum resistance and reactance due to the change in incidence angle of the impinging sound waves.

With these considerations in mind, the four-cavity analytical model is implemented in MATLAB and the Genetic Algorithm (GA) of the Global Optimization toolbox is used to search for two optimum liner configurations that maximize the average sound absorption coefficient α over the frequency range between 500 Hz and 4000 Hz. In the first case, the maximum overall liner height is set equal to $h = 50\ mm$, that is a typical maximum dimension of current aircraft liners. In the second case, the maximum overall height is set equal to $h = 100\ mm$ to explore the theoretical gains in absorption at lower frequencies which may be realised from an increased liner core height.

4.5.1 Impedance of the two optimal liners and comparison between their acoustic performance

The facing sheet resistance R, the individual cavity width w_i and the individual cavity height h_i are considered the design variables of the optimization process, and these dimensions are constrained by the limitations given above.

The two optimal configurations are searched for the no-grazing flow condition $M = 0$ and for a normally incident pressure wave $\phi = 0°$.

The sound absorption coefficient α

$$\alpha(f,\, M,\, \phi) = \frac{4\, R(f,\, M)cos(\phi)}{(1 + R(f,\, M)cos(\phi))^2 + (\mathrm{X}(f,\, M)cos(\phi))^2} \tag{4.17}$$

is chosen as the fitness function because it includes in a unique scalar value the influence of the overall resistance and reactance, the sound-wave frequency, the grazing flow and the acoustic wave direction have on the liner absorptivity. The liners are sized for maximum absorption coefficient averaged over the frequency interval between 500Hz and 4000Hz.

Previous studies [47] investigated the optimum liner impedance variation as a function of flow Mach number and direction and the sound-source characteristics, for a duct with dimensions of 300mm height x 150mm width x 850mm length. Figure 4.43 shows how the optimum resistance and reactance for this duct geometry vary with frequency, Mach number, and direction of flow. The optimum liners of this study may be tuned to adapt to the optimum impedance targets of a given duct by altering the resistive facing sheet geometry and/or type.

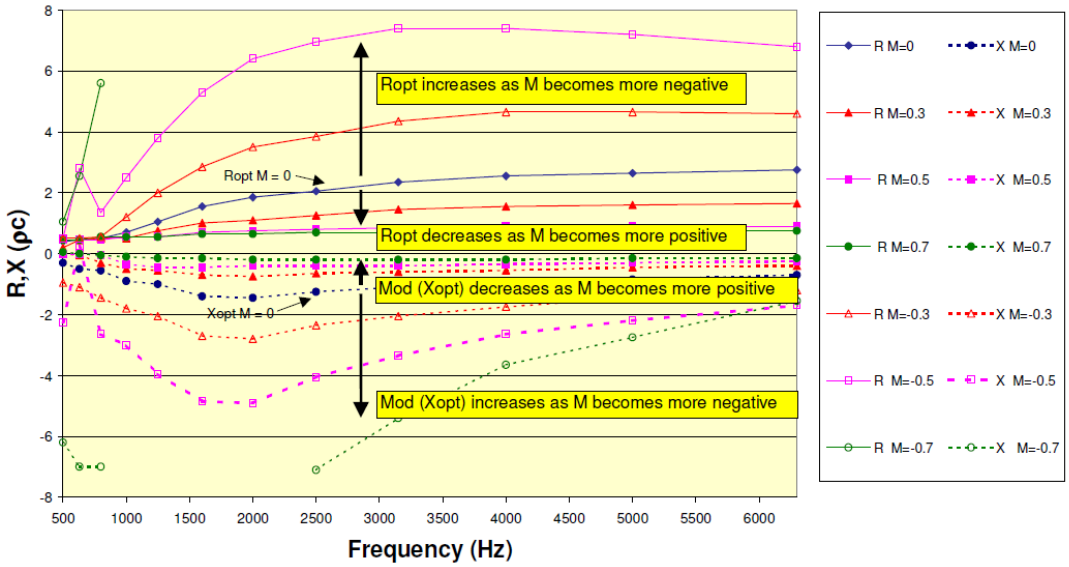

Figure 4.43. [47] Optimum liner impedance for different grazing flow conditions (duct geometry 300mm x 150mm x 850mm)

The search of the optimum configurations is pursued using the GA algorithm to explore the maximum field range of solutions and to overcome the presence of possible local optima. Figure 4.44 exemplifies how the sound absorption coefficient α averaged over a set of frequencies, for a normally incident plane wave, and in the absence of mean flow, varies as a function of the facing sheet resistance and the individual cavity height. The set of frequencies over which α is averaged in Figure 4.44 is given by $f = \{900\ Hz, 1500\ Hz, 2500\ Hz, 3500\ Hz\}$. These frequencies are randomly chosen in the frequency range of the optimization (between 500 Hz and 4000 Hz) to preliminarily understand the trend of the average sound absorption coefficient α (i.e. the fitness function). Figure 4.44 shows that the optimum solution is not unique and the adoption of a gradient-based method to search for the best solution may make the algorithm tend to a local optimum depending on the initial guess provided.

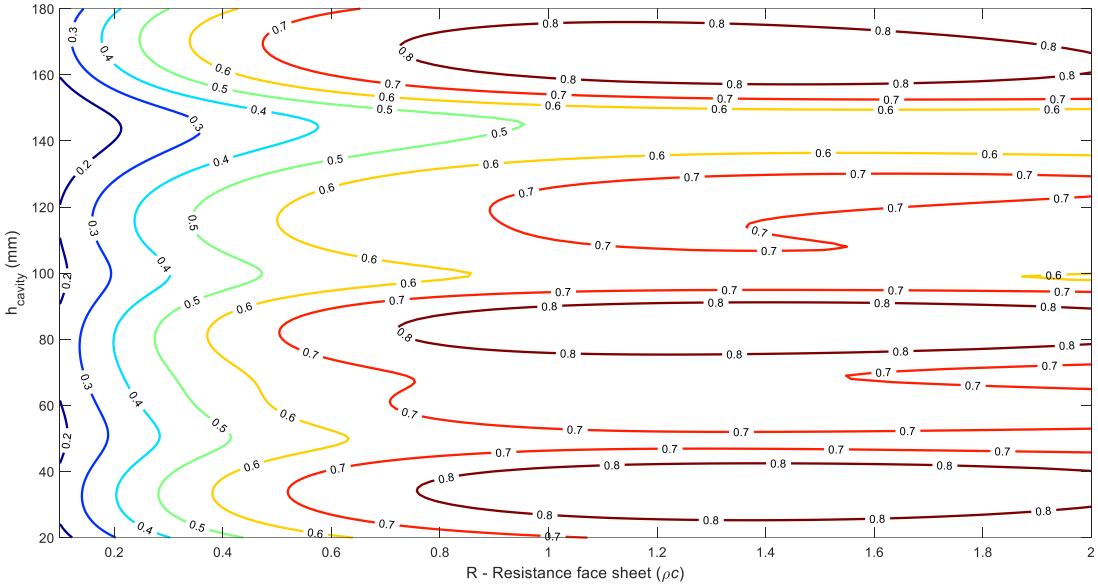

Figure 4.44. Contour plots of α averaged over 900 Hz, 1500 Hz, 2500 Hz, 3500 Hz, as a function of the individual cavity height h_{cavity} and facing sheet resistance R.

Figure 4.45 and Figure 4.46 provide the geometries of the optimal configurations found. The optimum liner configuration with the overall maximum height $h = 50\ mm$ is labelled as OPT-1, while the optimum liner configuration with the overall maximum height $h = 100\ mm$ is labelled as OPT-2. The normal incidence impedance and sound absorption coefficient of the optimal liner configurations are provided in Figure 4.47-Figure 4.50 and are compared to the CS1-A counterparts.

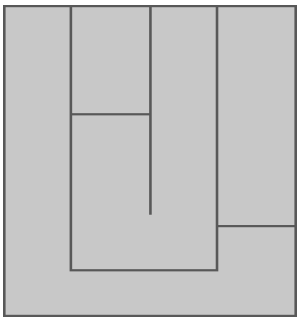

Figure 4.45. OPT-1 model (drawing not in scale)

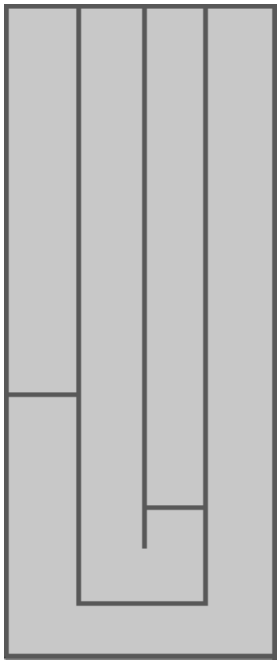

Figure 4.46. OPT-2 model (drawing not in scale)

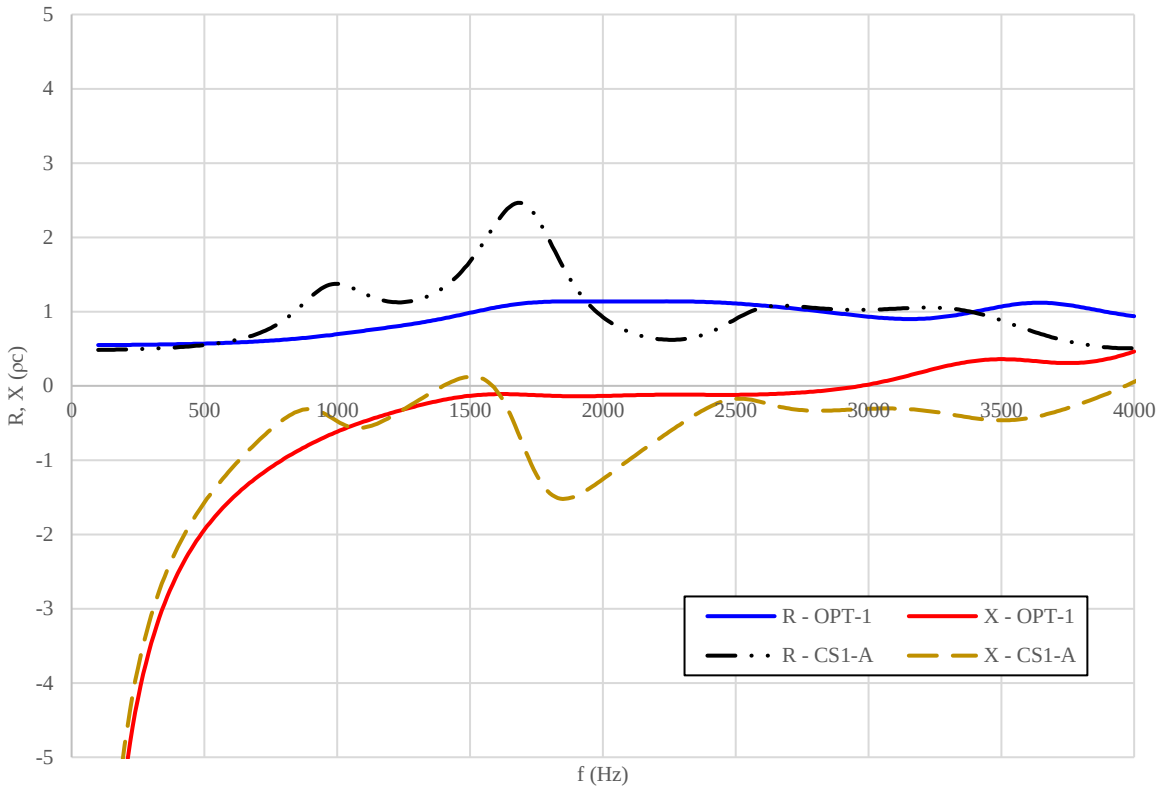

Figure 4.47. OPT-1 and CS1-A normalized impedance

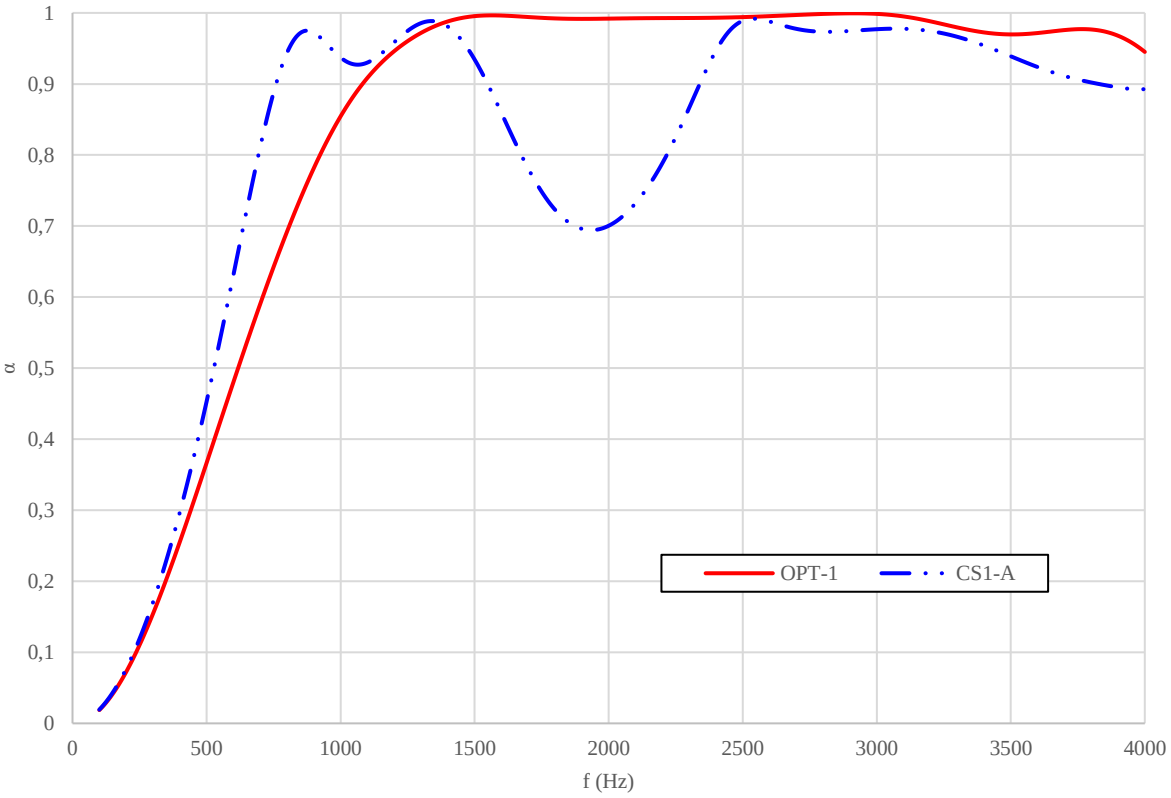

Figure 4.48. OPT-1 and CS1-A normal sound absorption coefficient α

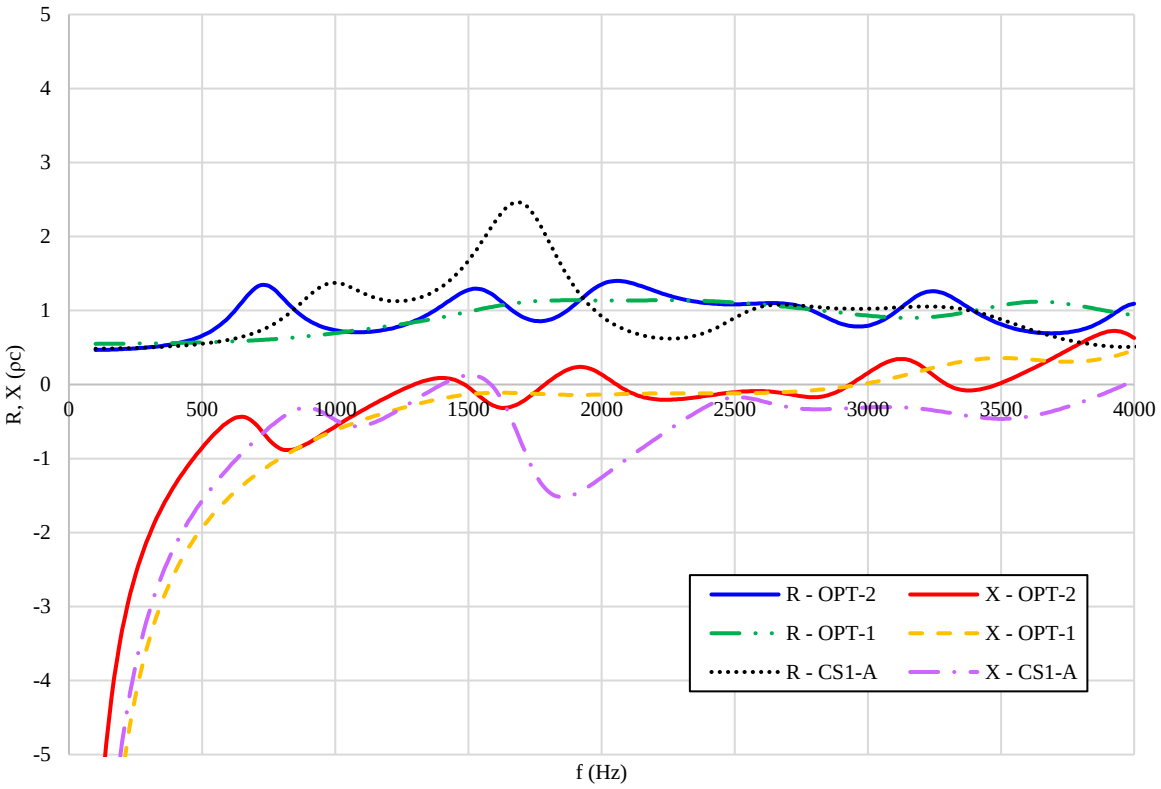

Figure 4.49. OPT-2 and CS1-A normalized impedance

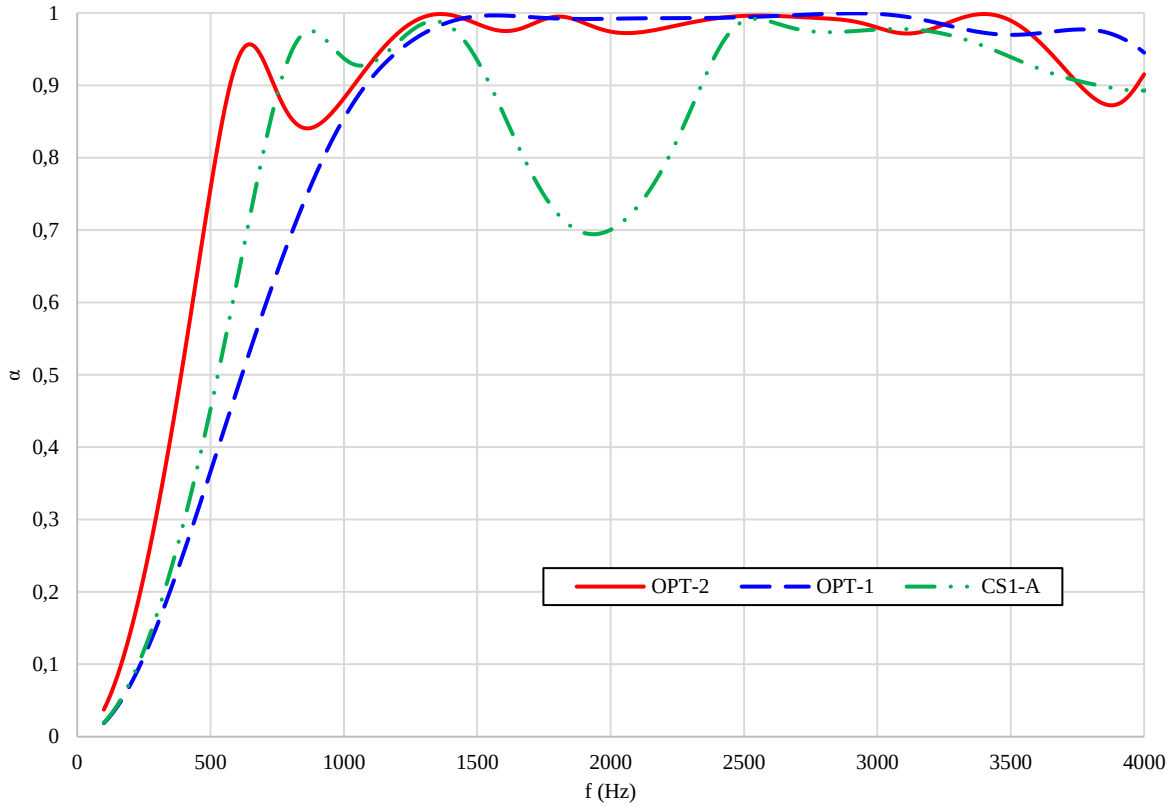

Figure 4.50. OPT-1, OPT-2 and CS1-A normal sound absorption coefficient α

The comparison between the sound absorption coefficients of OPT-1 and CS1-A shows the overall improvement offered by the optimum liner configuration with respect to the previous case analysed. The OPT-1 liner is expected to absorb the sound of the impinging sound waves almost completely over a wide frequency bandwidth, except at lower frequencies, where the OPT-1 model has poorer performance with respect to CS1-A because of the reduced effective centreline length of its longest cavity.

An improvement of the sound absorption at lower frequencies can be obtained with OPT-2, thanks to the increased maximum overall height of the liner that permits longer effective centreline lengths. From Figure 4.50, it emerges that the OPT-2 model has nominally the same sound absorbing performance of OPT-1 above 1300 Hz bandwidth but, in addition, it provides higher sound absorption at lower frequencies.

The promising results offered by the OPT-2 model suggests that an efficient abatement of the broadband engine fan noise can be gained by changing the current design philosophy of the nacelle and reserving a larger space for the acoustic liners. The adoption of this solution is currently prevented by the limited space available in the nacelle, in addition to weight constraints. Hence, only the liner cavity solution proposed by the OPT-1 model can be successfully installed unless some of these constraints are relaxed.

4.5.2 3D printed samples of the two optimal liners and measured impedance

After the two optimal liners were found, three scaled models of OPT-1 and OPT-2 were 3D printed using stereolithography. The liner samples were designed to repeat the respective baseline cluster three times in the axial direction and twelve times in the spanwise direction. No facing sheet was bonded on the surface, in order to focus on the reactive performance of these optimal liners. Before manufacturing full-scale liners, it should be tested if the stereolithography can effectively realize liner cores with the designed complex cavities.

In the manufacturing process, the axial dimensions of the liners were scaled down to 60% to improve the chances of getting good data in the measurements with the 29 mm diameter impedance tube. As shown in Figure 4.51 and Figure 4.52, the tube would not capture enough cells if their width was not downscaled. The height of the liners was not changed. Scaling the width of the cells down of the 60% forced some small adjustments of the effective centreline lengths, but the differences from the original length are not significant. On the contrary, the cells of all the samples have the same dimensions in the spanwise direction. The cells are separated by internal partitions, which are slightly larger than the internal partitions in 3D-LS liner (see 3.1).

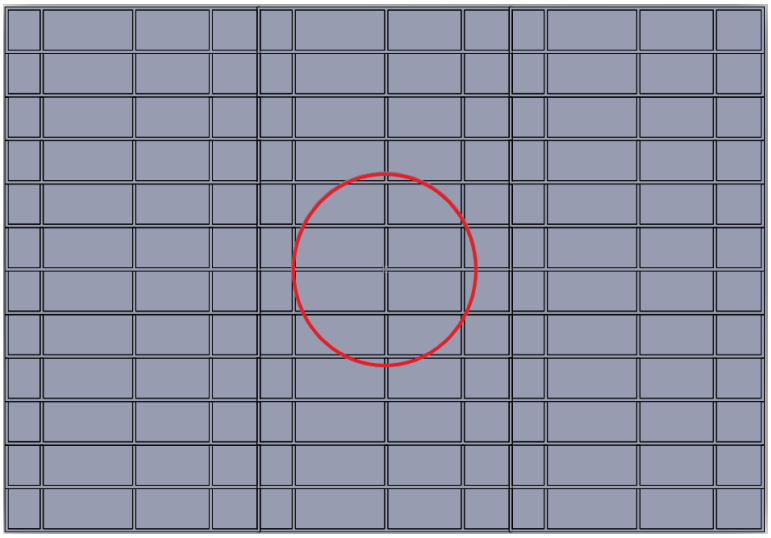

Figure 4.51. Top view of 50 mm height sample and area covered by the 29 mm diameter impedance tube (Drawing not in scale)

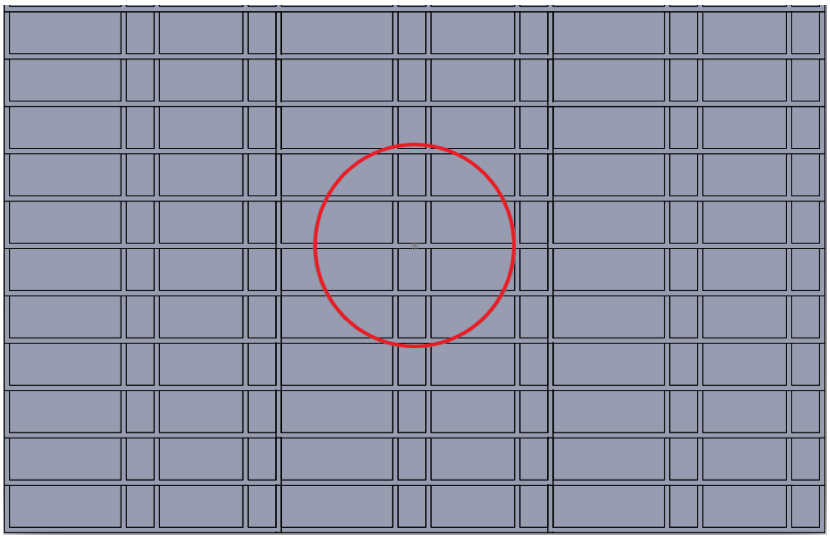

Figure 4.52. Top view of 100 mm height sample and area covered by the 29 mm diameter impedance tube (Drawing not in scale).

The reduction of the axial dimensions is not expected to significantly alter the impedance of the original full-scale optimal liners. The possible effects of the geometry scaling on OPT-1 and OPT-2 impedance are shown in Figure 4.53 and Figure 4.55. The figures compare the predicted impedance of the full-scale optimal liners with the predicted impedance of their scaled counterparts. These are respectively referred to as "OPT-1-60%" and "OPT-2-60%"and their impedances are calculated with the analytical routine introduced in 4.1.

In OPT-1-60% and OPT-2-60%, the contribution of the admittance of the internal partitions to the liner impedance is accounted for and the normalized admittance of the internal walls is set to $A_{hw} = 1e-7$. The impedance of the scaled liners is calculated using the same face sheet resistance R_{fs} of the corresponding original full-scale liners OPT-1 and OPT-2 ($R_{fs} \approx 0.4-0.5$). Figure 4.53 and Figure 4.55 clarify that the difference between the impedances of the full-scale and the scaled liners is expected to be of second order below 4000 Hz. In both OPT-1-60% and OPT-2-60%, the resistance remains close to unity and the reactance close to zero, so the scaled models are expected to provide good sound absorption at normal incidence.

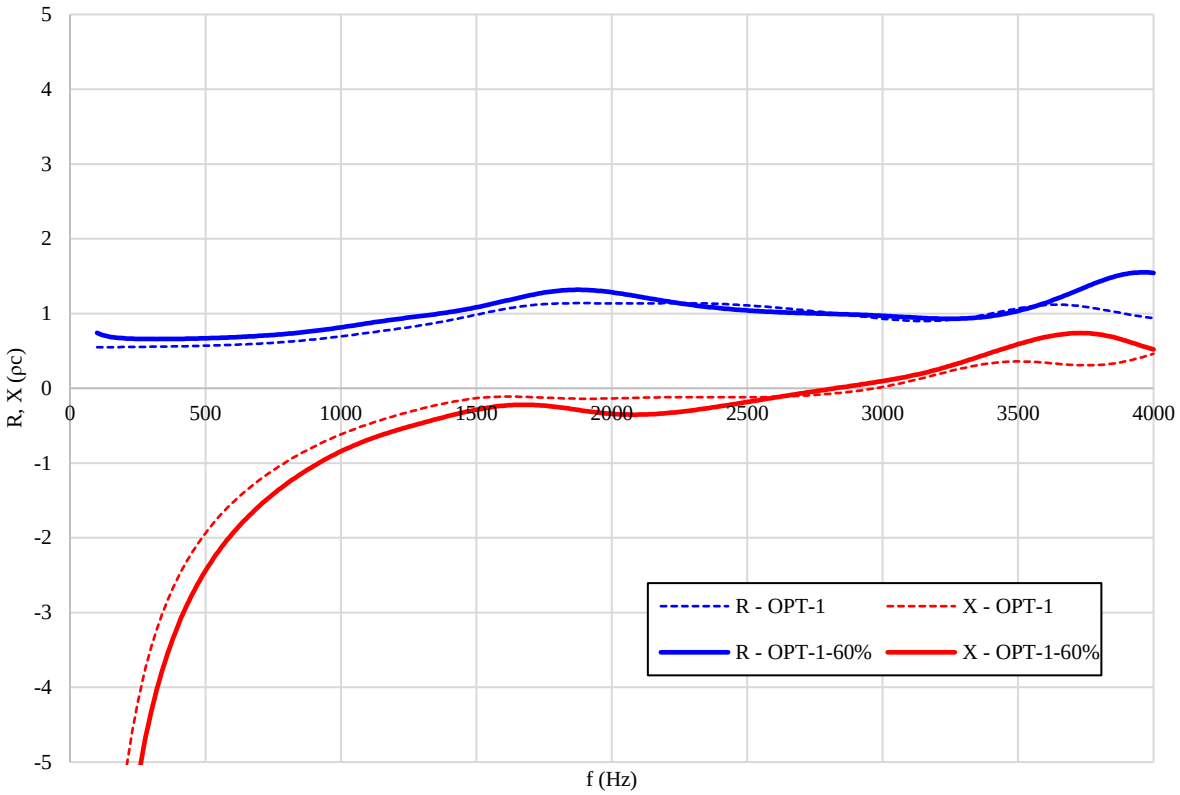

Figure 4.53. OPT-1 and OPT-1-60% normalized impedance

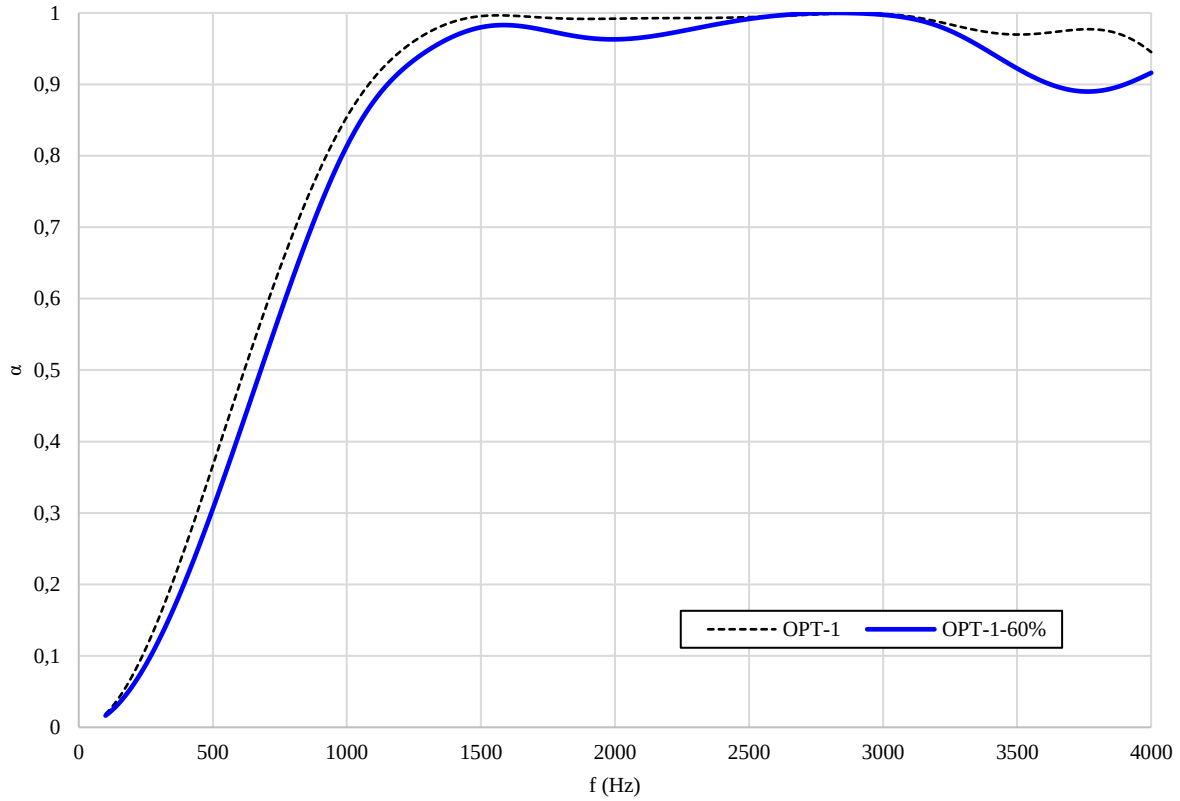

Figure 4.54. OPT-1 and OPT-1-60% normal sound absorption coefficient α

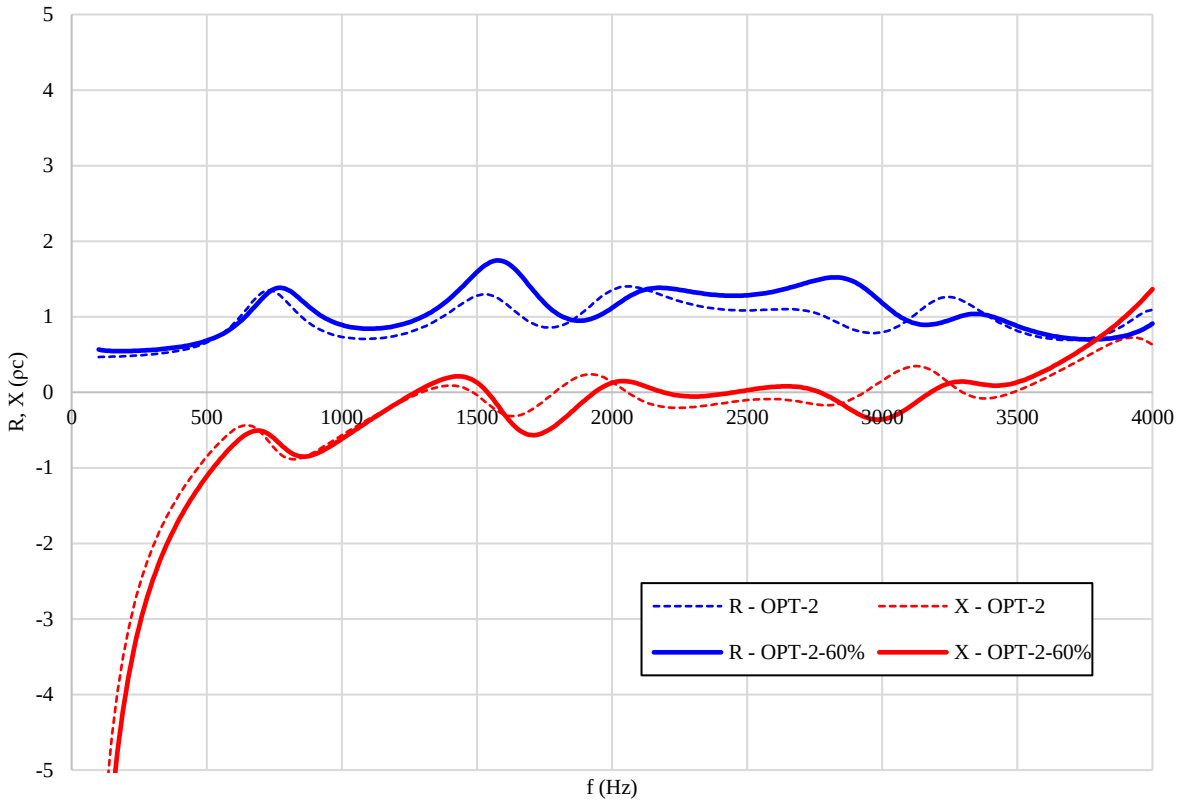

Figure 4.55. OPT-2 and OPT-2-60% normalized impedance

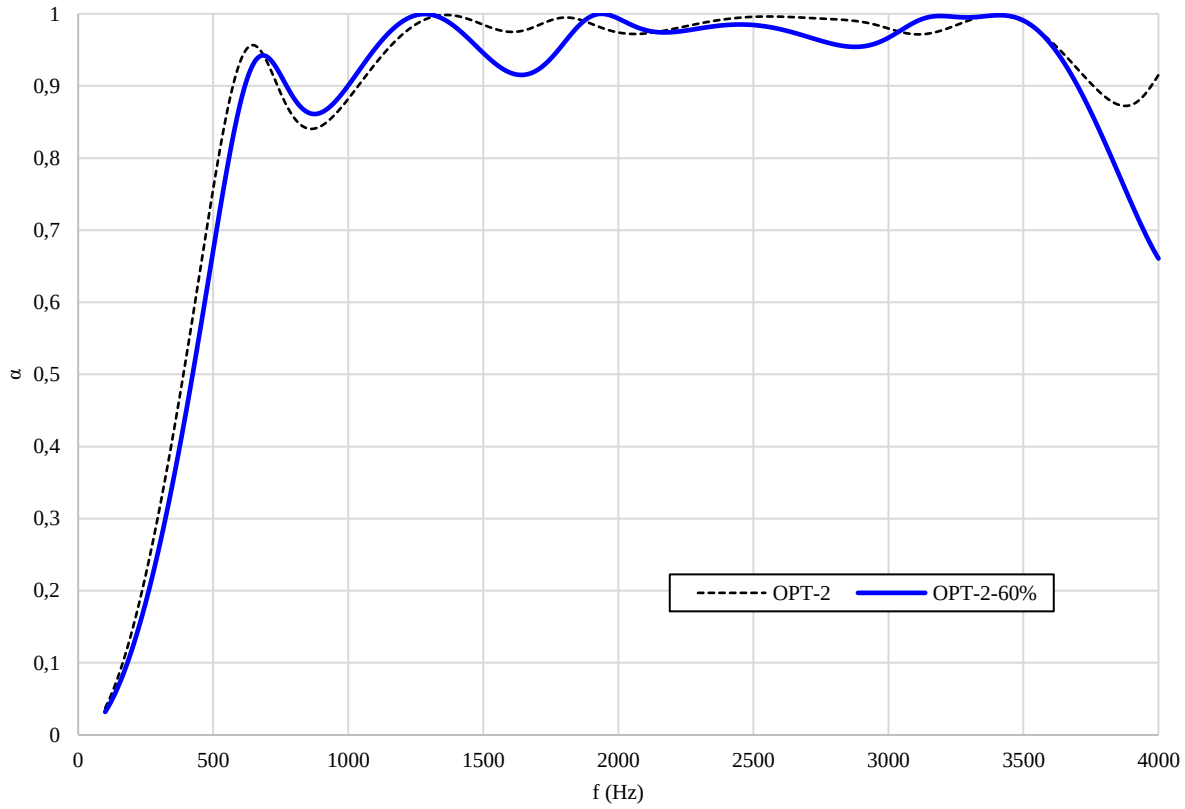

Figure 4.56. OPT-2 and OPT-2-60% normal sound absorption coefficient α

The negligible differences (below 4000Hz) expected between the acoustic properties of the original and the scaled liners is confirmed in Figure 4.54 and Figure 4.56. There, the normal sound absorption coefficient of the full optimal liners is compared with that of the corresponding scaled models. The figures show that the sound absorption of the scaled liners is almost similar to the original or just slightly poorer. Hence, the OPT-1-60% and OPT-2-60% printed samples may not replicate the sound absorption of the full optimal liners perfectly. However, OPT-1-60% still provides excellent sound absorption between 1200 Hz and 4000 Hz, while OPT-2-60% performs well between 600 Hz and 3700 Hz. The scaled liners allow the impedance tube to capture enough cells, so that their acoustic properties can be adequately measured. This cannot be achieved with samples that replicate the full dimensions of the optimal liners.

Two samples of OPT-1-60% were manufactured with two different 3D printers. They are referred to "OPT-1-60%-A" and "OPT-1-60%-B". A single sample of OPT-2-60% was realized. The acoustic impedance of the printed models was measured with the flanged normal impedance tube in the absence of mean flow. A 130dB OASPL broadband signal was used, ranging from 8 Hz to 6400 Hz, with output at a resolution of 8Hz. In each sample, the impedance was measured in five different positions, randomly chosen across the liner surface. Figure 4.57-Figure 4.61 provide the experimental results of the three liner samples.

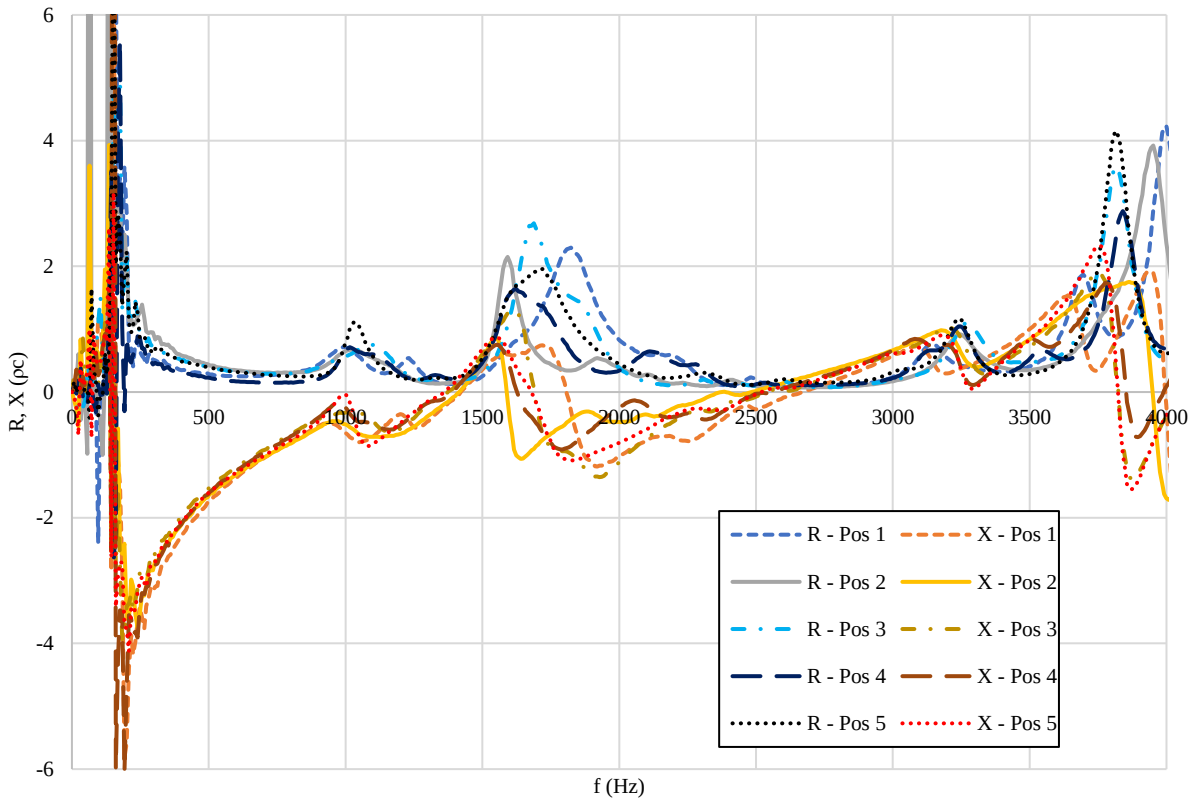

Figure 4.57. R, X of OPT-1-60%-A, OASPL 130 dB – Experimental results

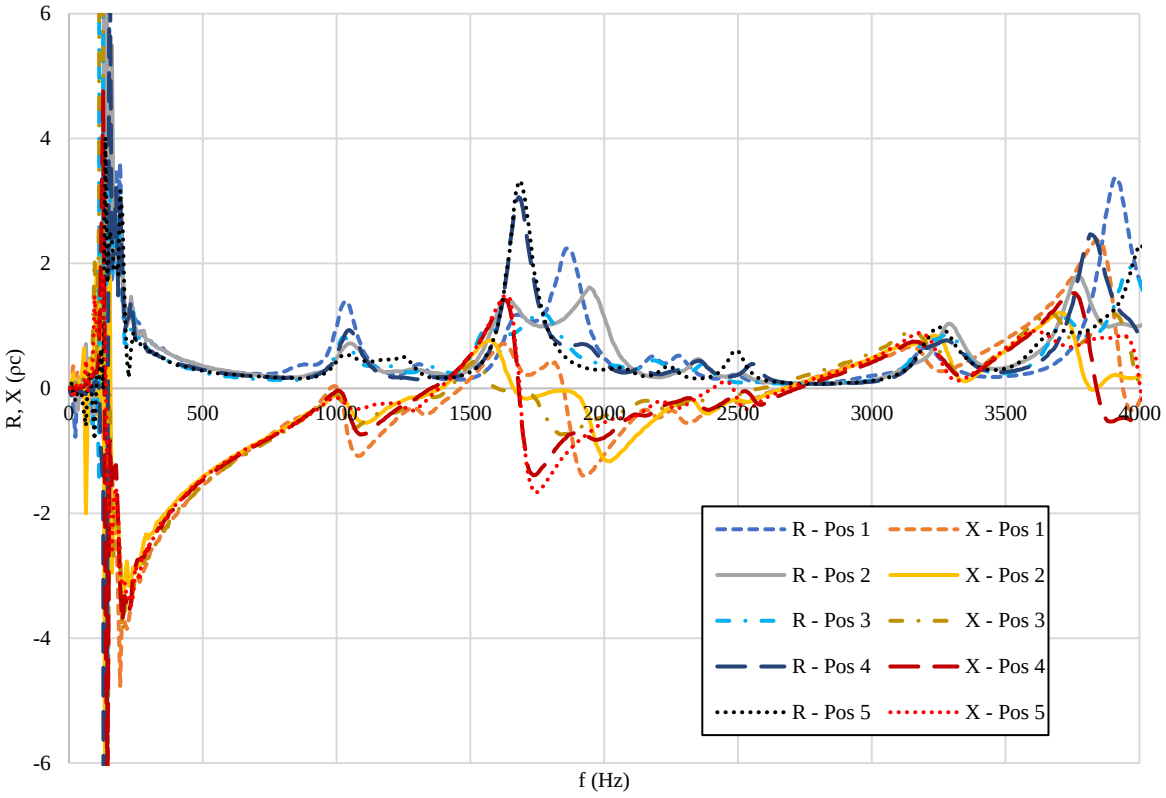

Figure 4.58. R, X of OPT-1-60%-B, OASPL 130 dB – Experimental results

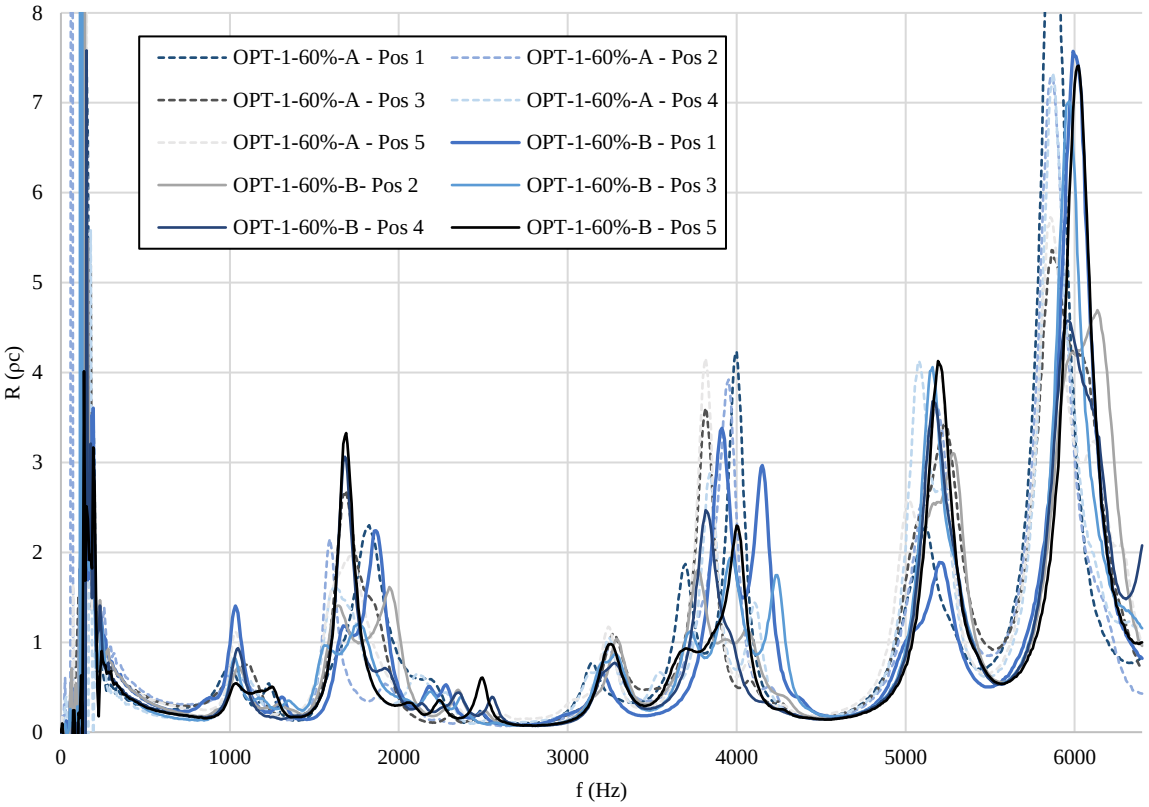

Figure 4.59. R of OPT-1-60%-A and OPT-1-60%-B, OASPL 130 dB – Comparison between experimental results

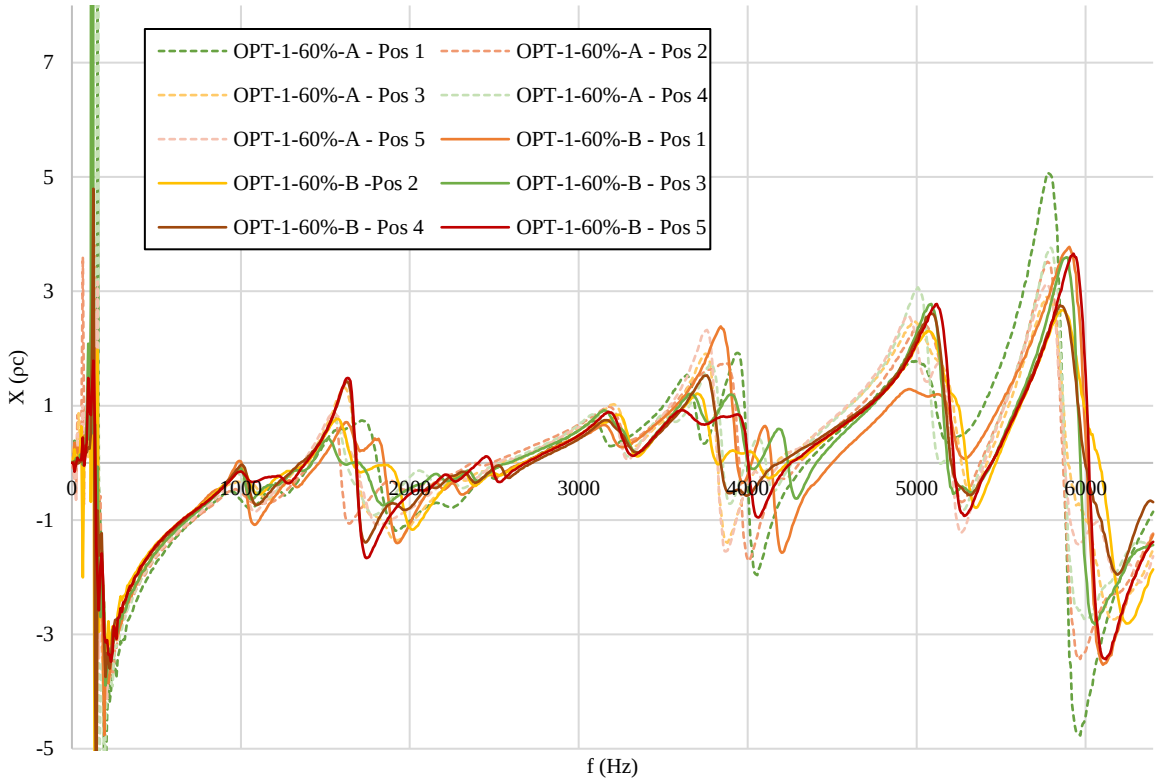

Figure 4.60. X of OPT-1-60%-A and OPT-1-60%-B, OASPL 130 dB – Comparison between experimental results

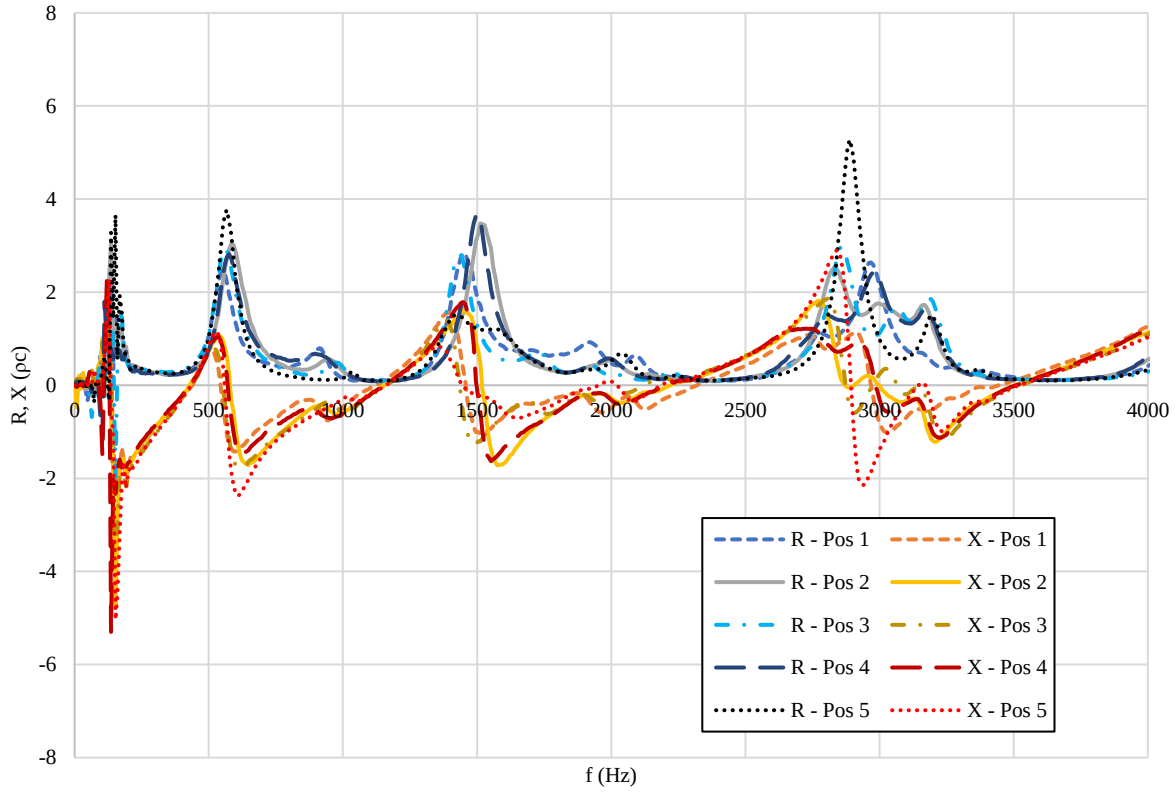

Figure 4.61. R, X of OPT-2-60%, OASPL 130 dB – Experimental results

Figure 4.57 and Figure 4.58 show that the measured impedance does not vary significantly across the surface. The main differences are seen at the locations of the impedance peaks and troughs between 1500 Hz and 2500 Hz and above 3100 Hz. They are mainly due to the variability of the liner geometry across the surface covered by the 29 mm diameter NIT and they are slightly more pronounced for OPT-1-60%-A. However, the differences are reasonably limited for both of the scaled designs, and they can be ignored. The mismatch between the measurements at different positions resembles those found in the measured impedance of 3D-LS sample (see Figure 3.4), but in Figure 4.57 and in Figure 4.58 it is somewhat greater. It is noted that, despite of the geometry scaling, the width of some cavities in OPT-1-60%-A and OPT-1-60%-B is larger than the width of the cavities in 3D-LS. Hence, the 29 mm diameter tube does not capture the four cavities of the baseline cluster as efficiently, and the measurements are more sensitive to the variability of the liner geometry across the surface. Similar conclusions are deduced in Figure 4.61 for OPT-2-60%. In this case, the main differences between the measurements correspond to the locations of the impedance peaks and troughs and are emphasised between 2700 Hz and 3500 Hz. However, the mismatch is of second order and can be neglected. Therefore, the acoustic properties of each of the samples can be approximated as being uniform across the surface, as also deduced in the case of the 3D-LS liner (see 3.1). It may also be concluded that, while scaling of the cavity widths to match the impedance tube diameter is necessary in order to assess liner performance for "large" cavity widths, this does not preclude using full-scale liners for duct applications.

In the figures above, the resistance ranges between $0.1\ \rho c$ and $0.2\ \rho c$ away from the peaks and troughs of the impedance, while the reactance of each sample oscillates around zero. Hence, the reactive performances confirm that the attenuation bandwidth is widened as expected and the sound absorption can be improved by bonding a face sheet of an appropriate resistance onto the liner samples (adding resistance and further damping the oscillations). The measurements also confirm that the designed optimal geometries (see Figure 4.45 and Figure 4.46) can be effectively manufactured using stereolithography and that the complex configurations can be used to attain optimal broadband sound absorption at normal incidence. Moreover, in case of the 50 mm deep liner, it was verified that the sample can be realized with different 3D printers, without varying its acoustic performances across the surface significantly (see Figure 4.59 and Figure 4.60).

In Figure 4.62-Figure 4.65, the measured impedances are compared to the predicted impedances of the corresponding full-scale and downscaled models. The impedances of these liners are calculated using the analytical routine, adjusting the face sheet resistance in order to match the measured level of the panel. This is set equal to $R_{fs} = 0.08\ \rho c$ and $R_{fs} = 0.11\ \rho c$ in the case of the scaled optimal liners OPT-1-60% and OPT-2-60%, while is set equal to $R_{fs} = 0.05\ \rho c$ and $R_{fs} = 0.08\ \rho c$ respectively in the simulation of the full-size optimal liners. These predictions are referred to "OPT-1-60%-R0.08" and "OPT-2-60%-R0.11" for the scaled optimal liners as "OPT-1-R0.05" and "OPT-2-R0.08" for the full-size optimal liners. It is noted that the impedance of the full-size optimal liners is predicted with a lower face sheet resistance rather than the corresponding scaled optimal liners. This is not surprising because the cavities of the full-size optimal liners are larger than the cavities of the corresponding scaled optimal liners. As discussed in [32], 3D printed liners with wide cavities may largely eliminate viscous losses and the damping of the acoustic energy can be reduced. On the contrary, 3D printed liners with narrow cavities damp the acoustic energy more intensely because of the viscous losses that arise within them.

In the following figures, the analytical predictions OPT-1-60%-R0.08, OPT-2-60%-R0.11, OPT-1-R0.05 and OPT-2-R0.08 are presented for the frequency range between 100 Hz and 4000 Hz, with a 100 Hz resolution.

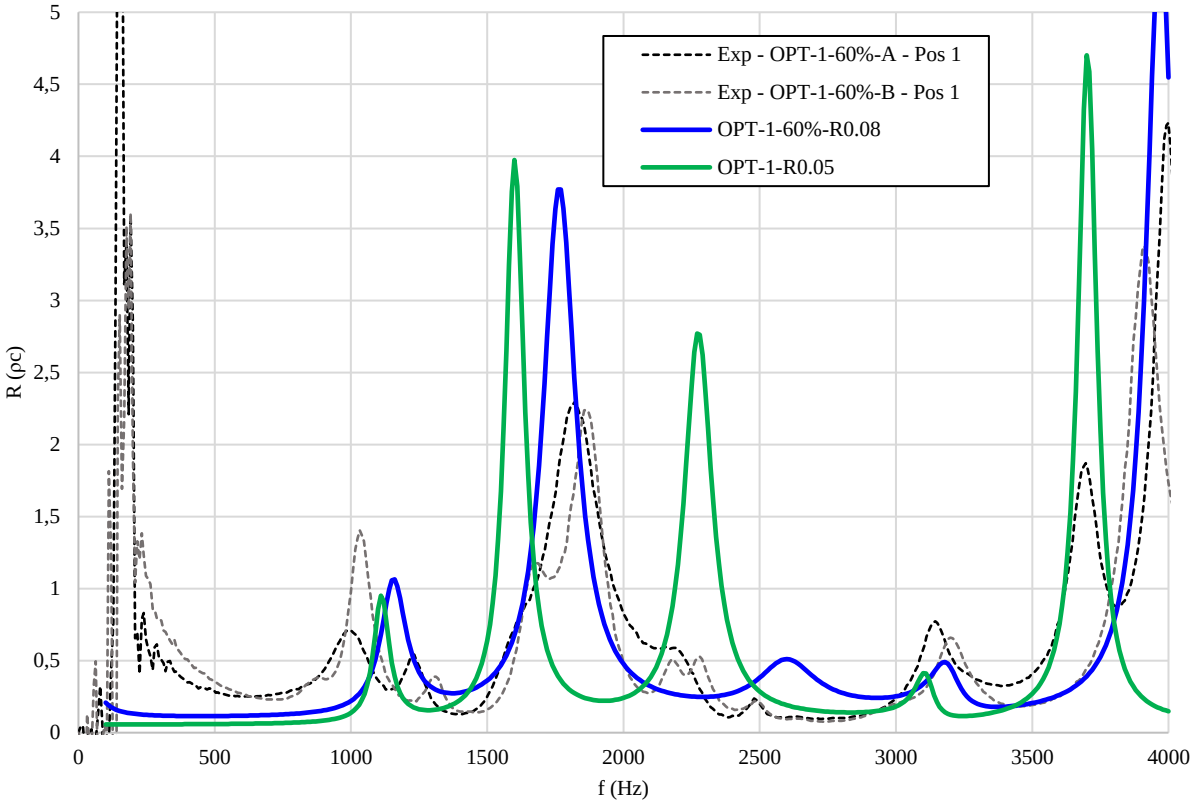

Figure 4.62. OPT-1 Normalized resistance, R

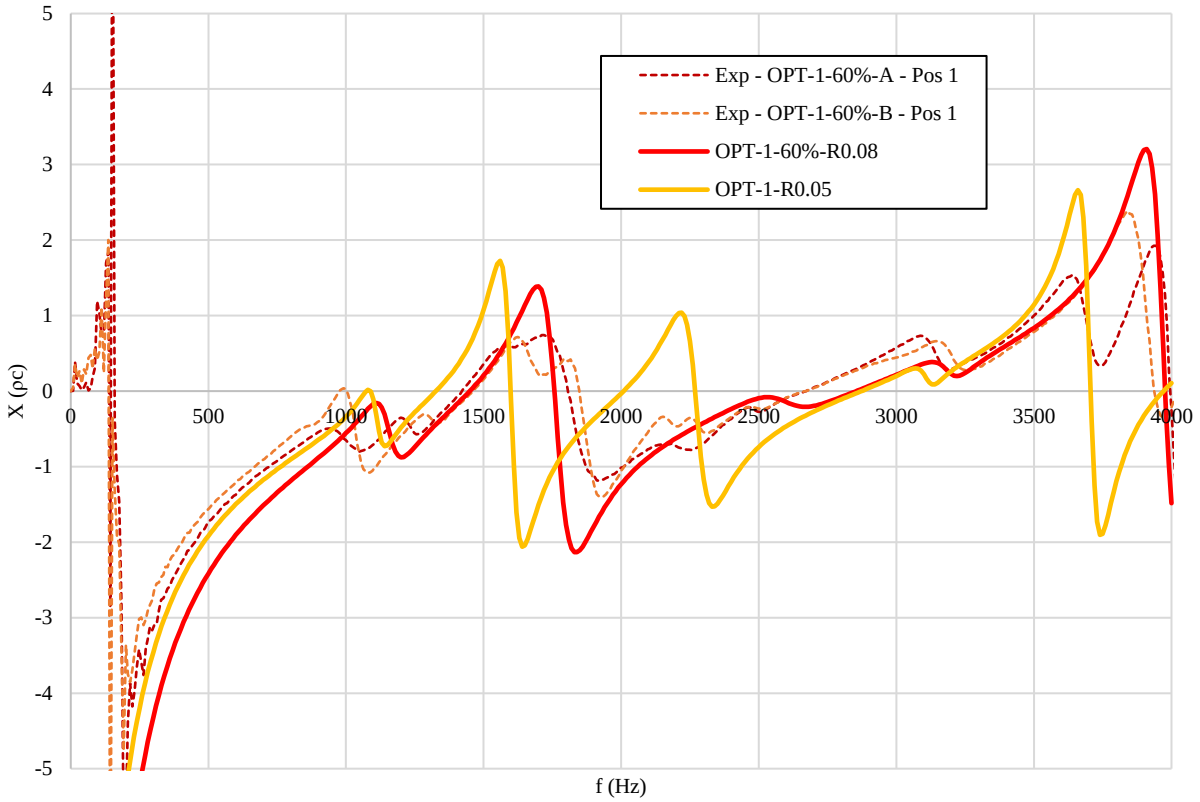

Figure 4.63. OPT-1 Normalized reactance, X

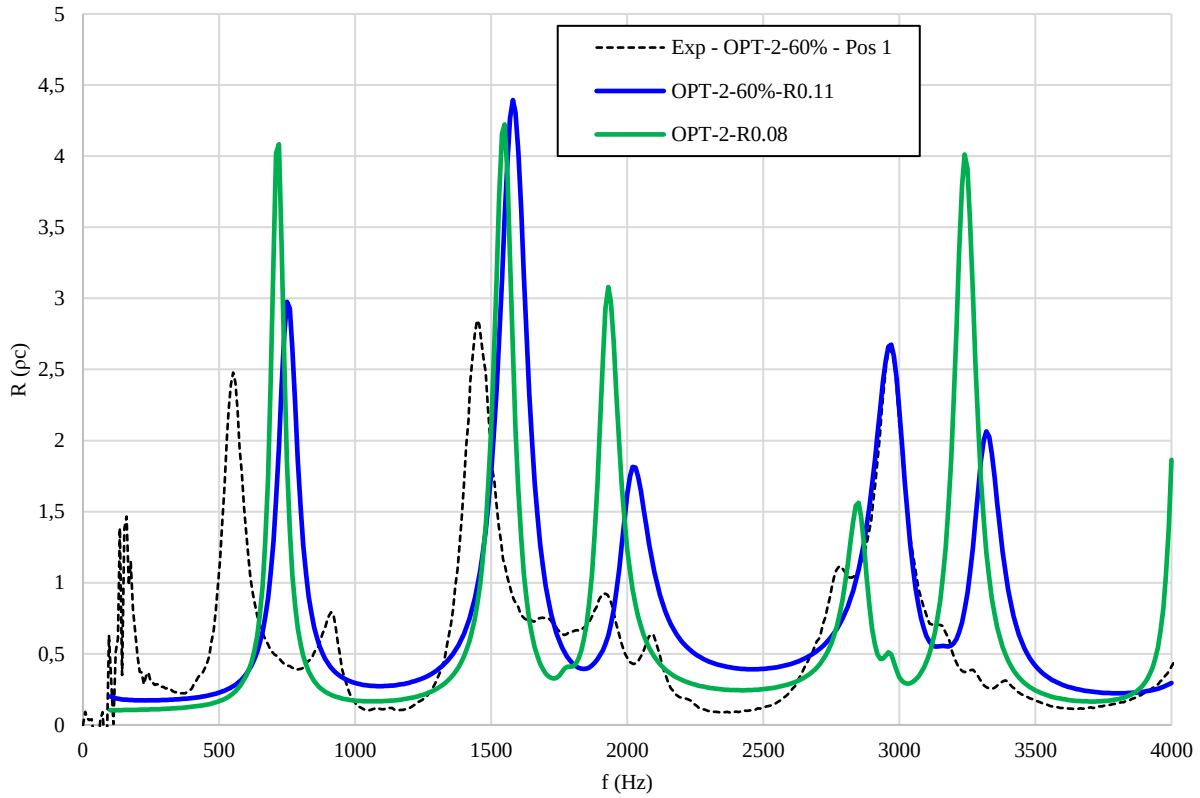

Figure 4.64. OPT-2 Normalized resistance, R

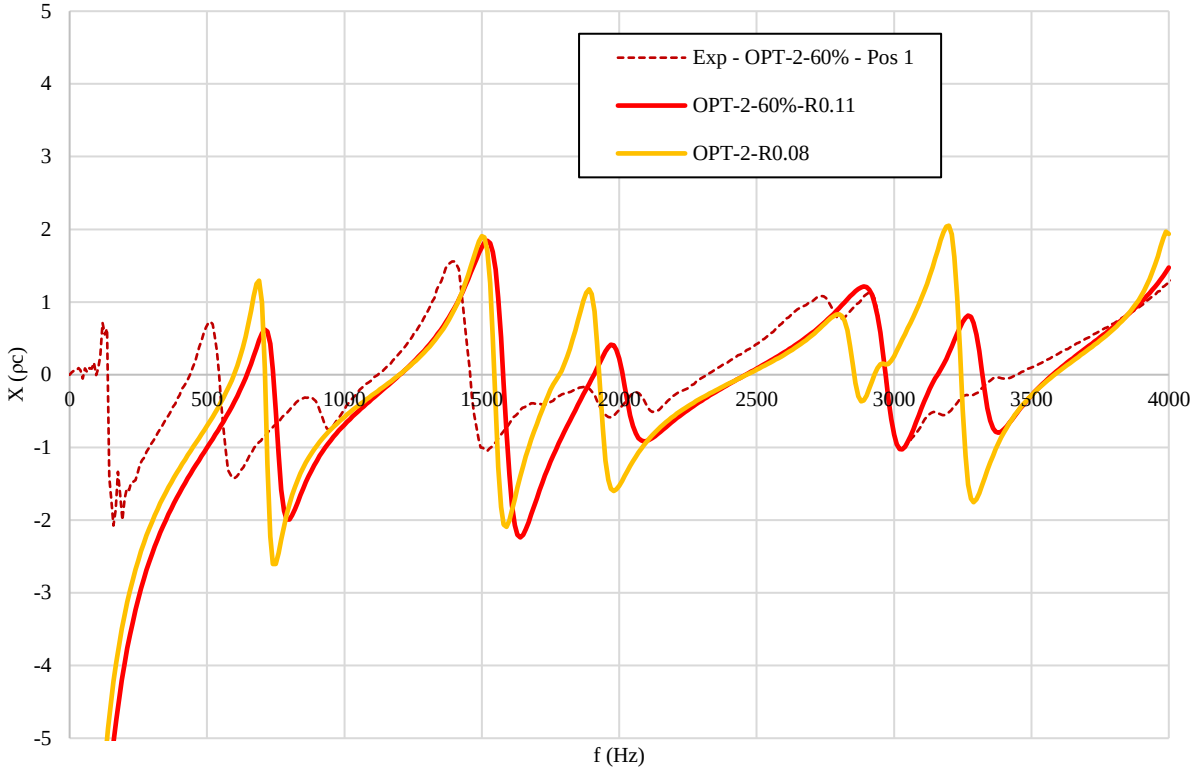

Figure 4.65. OPT-2 Normalized reactance, X

Figure 4.62 and Figure 4.63 show good agreement between the predictions (OPT-1-60%-R0.08) and the measurements, for both the sample tested (OPT-1-60%-A/B). The agreement degrades around the peaks and troughs of the impedance and at low frequencies (< 1000 Hz), where the measurements are altered by the edge effects. Nonetheless, the differences are relatively small and may be neglected to a first order. The measured impedance is considered sufficiently correlated with the analytical prediction (OPT-1-60%-R0.08).

On the contrary, the agreement is poorer between the measurements of the scaled samples (OPT-1-60%-A/B) and the predicted impedance of the full-size liner (OPT-1-R0.05). The spectral shape of the optimal impedance (OPT-1-R0.05) is not well captured between 1200 Hz and 2700 Hz, and the samples (OPT-1-60%-A/B) seems not to have the designed sound absorption in that frequency range. This is likely due to the compromises introduced for the scaled liners which had reduced heights (~ 7-8% reduction) for the longest cavities. However, the addition of a face sheet will improve the performance of the samples. The predictions in Figure 4.53 and Figure 4.54 suggests that the differences between the impedance of the scaled sample and the full-size liner will be reduced if a face sheet resistance is bonded on the liner surface. It is recalled that the acoustic properties (OPT-1-60%-R0.08 and OPT-1-R0.05) in Figure 4.62 and Figure 4.63 were calculated with the face sheet resistance set to match the measured level of the sample, but their values are low ($R_{fs} = 0.08\ \rho c$ and $R_{fs} = 0.05\ \rho c$) and are just a fraction of the desired optimal face sheet resistance ($R_{fs} \approx 0.4 - 0.5\ \rho c$).

The favourable comparison between the measured and the predicted data verifies that the analytical routine can effectively be used to design and optimize the acoustic properties of the 50 mm height liner. Clearly, the required alterations in cavity centreline depths of the scaled liner samples OPT-1-60%-A/B lead to a slightly less efficient design, so they cannot replicate the improved acoustic properties of the optimal liner OPT-1 fully. The full-scale

properties can be measured only with a tube of wider diameter, to adequately capture the four cells of baseline cluster ($d_{tube} > w = 40\ mm$). However, from the favourable agreement between the measurements and the predictions of the scaled liners, it is deduced that a similar good agreement can be obtained in the case of the full-size optimal liners.

Similar considerations can be drawn in the case of the 100mm-high liner. Figure 4.64 and Figure 4.65 show good agreement between the measured (OPT-2-60%) and the predicted impedance of the downscaled liner (OPT-2-60%-R0.11). The main differences occur at the peaks and troughs of the impedance and at lower frequencies (< 1000 Hz), where the results are influenced by the edge effects. However, the mismatch can be neglected, and the measurements and the predictions are well correlated to a first order. To a first approximation, the measurements of the scaled sample (OPT-2-60%) compare well also with the predictions of the full-size liner (OPT-2-R0.08), if not at lower frequencies (< 1000 Hz) and at the peaks and troughs of the impedance. The difference is more significant between 1600 Hz and 2100 Hz, and between 2800 Hz and 3400 Hz. Again, the scaled liner has reduced centreline lengths for the two longest cavities (9% and 2.5% reductions). Nonetheless, it is expected that bonding a face sheet on the sample can further improve the acoustic performances of the scaled model (see Figure 4.55 and Figure 4.56).

The good comparison between the measured and the predicted data confirms that the analytical routine can effectively be used to design and optimize liners of extended height (100 mm). The OPT-2 acoustic performance may be accurately investigated using an impedance tube only if a tube of wider diameter ($d_{tube} > w = 40\ mm$) is available. Although OPT-2-60% partially replicates the OPT-2 impedance, the favourable agreement between the measurements and predictions suggests that a printed sample of the full-size liner may have the expected sound absorption of the designed optimal configuration.

Figure 4.63 and Figure 4.65 confirm the gain in sound absorption at lower frequencies achievable with a liner of extended depth (i.e. 100 mm). In the 100mm-high liner, the measured reactance oscillates close to zero as in case of the 50mm-high liner, but in this case the first measured resonance frequency (OPT-2-60%) is well below 1000 Hz (around 440 Hz, while in OPT-1-60% is about 1000 Hz).

For completeness, the analytical routine is used to calculate the impedance of the 3D-LS sample (see 3.1). The analytical routine is expected to be effective in modelling the acoustic properties of the sample. The comparison between the measured and the predicted impedance of 3D-LS is provided in Figure 4.66 and Figure 4.67. The 3D-LS impedance is predicted analytically using the four-cavity baseline cluster replicated by 2D-4CC-TH0.2-I and its face sheet resistance is set to $R_{fs} = 0.2\ \rho c$. The analytical predictions are referred to as "3D-LS-A" and do not account for the contribution of the hard wall admittance. The contribution of the hard wall admittance is neglected because the width of the cells was widened according to the expression in Equation 3.10. It is recalled that the analytical model of the smallest portion in which the 3D-LS geometry varies can capture the 3D-LS impedance, because the size of the smallest portion is lower than a third of the minimum wavelength considered ($w < \lambda_{min}/3$).

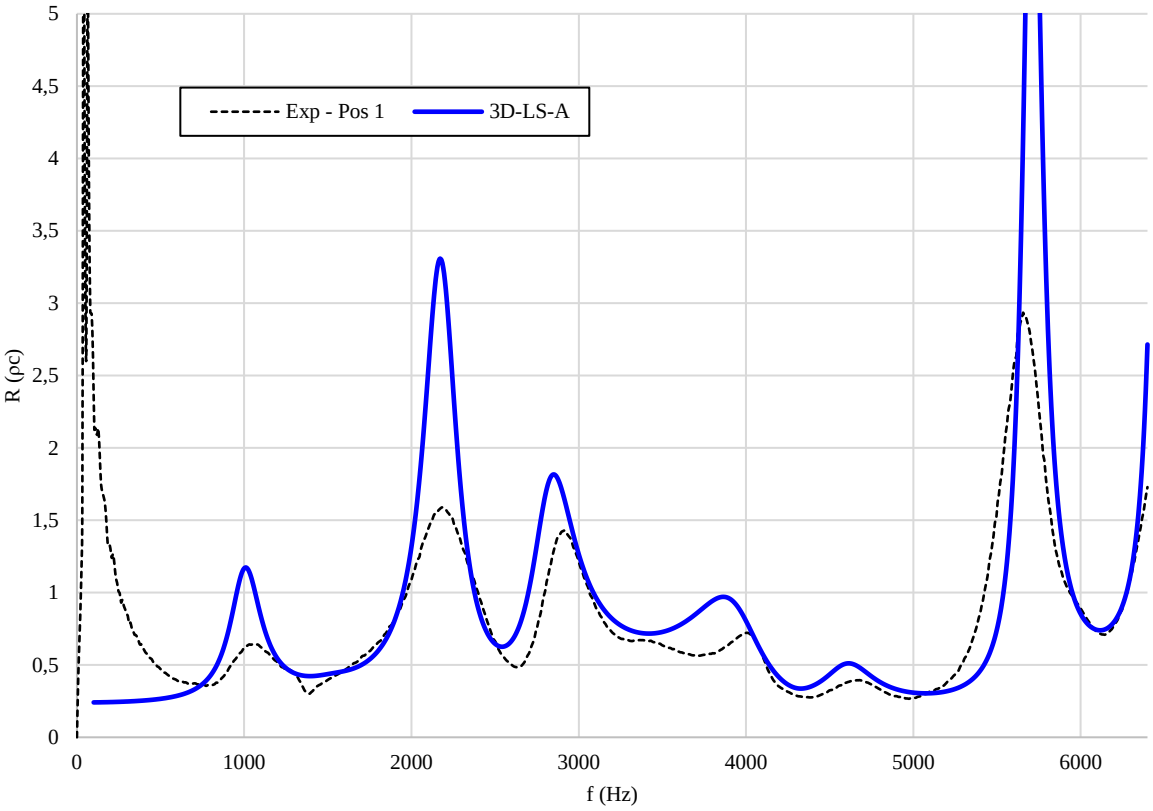

Figure 4.66. 3D-LS Normalized resistance, R

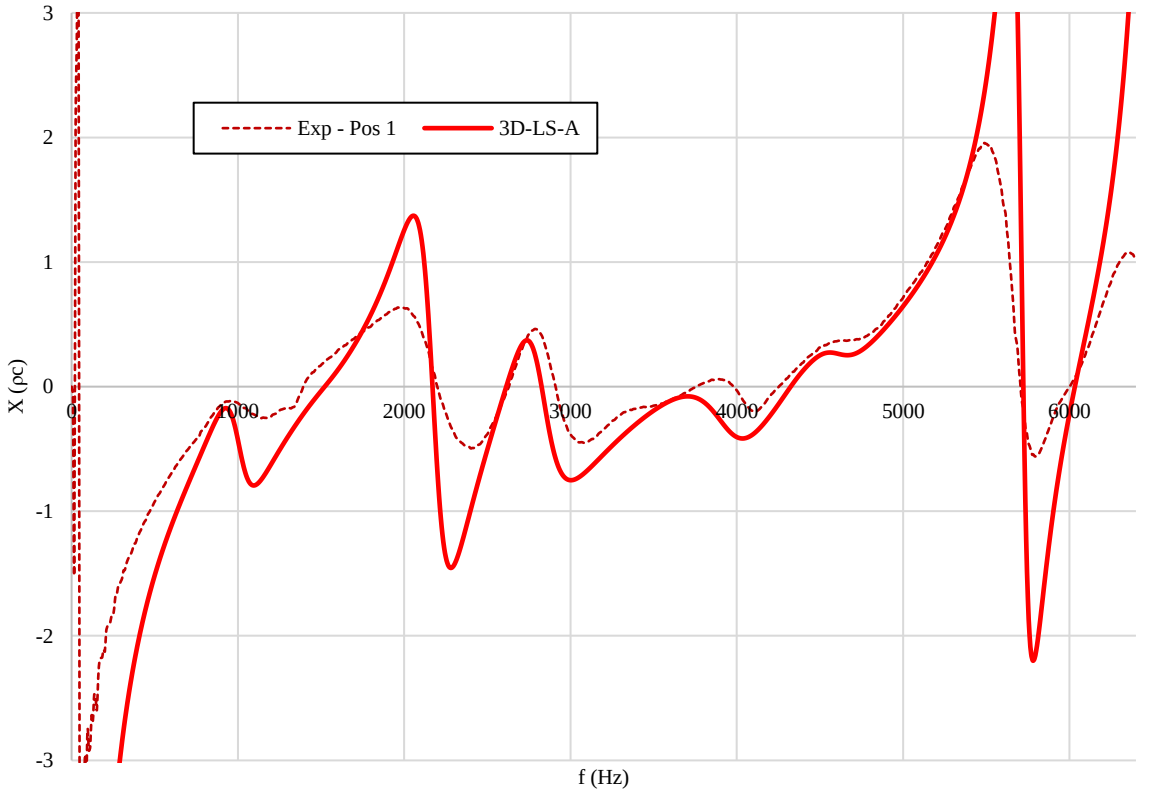

Figure 4.67. 3D-LS Normalized reactance, X

The figures above show a favourable comparison between the measurements and the analytical predictions. The main differences are in correspondence of the impedance peaks and troughs, and at lower frequencies (< 1000 Hz), where the edge effects influence the measured data. The mismatch is similar to that of Figure 4.62-Figure 4.65 and the spectral shape of the liner impedance is well captured. Therefore, this consideration confirms that the analytical routine can be effectively used to model, design, and optimise, acoustic liners with complex configurations and different overall depths, provided that it captures the smallest portion over which the liner geometry varies.

As a side note, it should be recalled that an impedance test using a normal impedance tube with a closed termination can enhance the accuracy of the measurements at low frequencies if a sample is cut and sealed inside the sample holder with the same diameter as the tube. The edge effects would be eliminated and the good correlation between the analytical predictions and the measured impedance at low frequencies can be further investigated (below 1000 Hz for the previous 3D printed samples). Hence, only the scaled models could be tested, but, due to the large cavities still present, the tube may not accurately capture the four cavities of the baseline cluster. As a conclusion, only an impedance tube of larger diameter can measure the sound absorption performance of the optimal liners adequately. However, the performance of a full-scale design may be investigated by inserting a large panel in a grazing incidence duct, and matching the predicted to measured attenuation by iterating on the baseline wall impedance.

4.6 Chapter IV: Final remarks

The current study introduced an innovative configuration of broadband liner, which was used to design two optimal broadband liners with different overall depths. The innovative configuration derives from the baseline cluster of the 3D-LS liner (see Chapter 3) and it is aimed at driving an efficient abatement of noise over a wide frequency bandwidth. It consists of a cluster of four cavities, both folded and straight, whose dimensions respect the geometrical constraints in Eqs.4.1-4.3. The cavities are packaged to minimize the overall height and to enable cavities to be designed with a long effective centreline length, to significantly exceed the maximum height. The proposed configuration can be adjusted to whatever space is reserved for the acoustic liners in a given nacelle.

The acoustic properties of the baseline cluster were investigated using numerical and analytical models and the primary design variables were sought that may be used to control the impedance of the liner. The study led to some interesting outcomes, that are recapped below.

- To a first order, if not in the region of the reactance peaks and troughs and for few points at high frequencies, the simplified predictions of liner sound absorption are not greatly affected by the presence of folded cavities. The impedance of a baseline cluster with folded cavities can be effectively estimated using the numerical model with straight cavities with the same effective centreline lengths.
- Under certain conditions, the acoustic properties of the liner can be assessed using an analytical routine and the analytical predictions are not influenced significantly by the order of the cavities.
- Liner absorption can be tuned by controlling the width of the cells and their number, alongside their effective centreline lengths. However, comparing the effects of cavity width and number of cavities, varying the cavity width provides relatively greater control on the liner optimisation. Moreover, the impedance of the liner can be optimised by choosing an appropriate face sheet resistance in order to match the panel impedance to the optimum for a given application. This does not influence the general spectral

shape of the impedance, in terms of where oscillation occur, but it improves the sound absorption performance.

Clearly, these considerations were deduced for the specific configuration considered and further investigations must be performed for the simulation of other liners. However, they confirm what was demonstrated in previous studies [40] [34] and they can be effectively considered as a starting point for future analyses. These future studies may also consider the influence of varying the facing sheet resistance of each cavity, in addition to varying cavity centreline length and width.

The proposed configuration was optimised in MATLAB using the Genetic Algorithm (GA) to maximise the sound absorption in the frequency bandwidth ranging between 500 Hz and 4000 Hz, for the no-grazing flow condition and for a normally incident pressure wave. Two optimal acoustic liners were found for two different overall liner heights. The former has the depth of 50 mm, which is a typical maximum dimension of current aircraft liners. The latter has the depth of 100 mm, to explore the theoretical gains in absorption at lower frequencies which may be realised from an increased liner core height. Scaled samples of the optimal liners were 3-D printed using stereolithography to match the reduced dimension of the impedance tube. A face sheet was not bonded on the liner surface and the sample impedances were tested using a flanged normal incidence set-up, in the absence of mean flow. The comparison between the measured and the predicted data showed favourable agreement and the expected acoustic properties were verified. The measured reactive performances confirmed the scaled optimal liners to be effective in abating noise over a wide frequency bandwidth. Moreover, it was demonstrated that an analytical routine may be used for calculating and optimizing liner impedance in a normal incidence set-up, in the absence of mean flow.

Clearly, the validity of these conclusions is limited to the scaled samples of the optimal liners. The acoustic performance of the full-size optimal liners were not tested, as they can be effectively verified at normal incidence only with an impedance tube of wider dimensions ($d_{tube} > 40\ mm$). However, the favourable agreement between the measurements and the predictions of the scaled models gives confidence that a good correlation between measured and predicted data may also be obtained in case of the full-size optimal liner. Furthermore, the differences between the acoustic properties of the downscaled and the full-size optimal liners is expected to decrease if a face sheet is bonded to the liner surface.

5. Conclusions and recommendations

Over the last few decades, advances in propulsion system bypass ratio accompanied by improvements in sound-absorbing manufacturing and modelling have led to significant reductions in radiated fan noise. However, these improvements have changed the source duct noise source spectra from being tone dominated to being mostly broadband in nature and they have pushed the frequency content of fan noise towards lower frequencies. The challenges presented by the change in source content cannot be addressed using conventional acoustic treatments with single or double layers, because their sound absorption performance is effective only in relatively narrow frequency ranges. Moreover, the restricted space reserved for traditional liners in current aircraft nacelles restricts any improvement in sound absorption at lower frequencies. Hence, alternative liner concepts must be developed, while maintaining a reasonable thickness that avoids a significant weight penalty.

This study has presented an innovative liner concept that can provide promising sound absorption performance over a wide frequency bandwidth and which may also target low frequencies. The typical honeycomb core is substituted with a core of complex configuration, manufactured using stereolithography. The liner core includes a combination of straight and folded cavities of variable depths, some of which can be designed with long effective centreline lengths, significantly exceeding the overall liner thickness. The cavities are packaged to minimise the unused volume and the configuration can be adjusted easily to fit any space reserved for acoustic liners in a given aircraft nacelle.

The acoustic properties of this liner concept have been investigated in a no-flow environment and with a normally incident sound wave. Many noteworthy outcomes have been realised. The most important are briefly recapped below:

- COMSOL 5.4 was validated for predicting the measured impedance of traditional acoustic liners and it was used to numerically simulate the impact of a flanged impedance tube on the measured data. The physics of prediction and measurement of conventional sound-absorbing treatments was analysed in detail and some interesting considerations were highlighted which must be accounted for in their simulation.
- COMSOL 5.4 was also validated for the prediction and measurement of the impedance of liners with complex cavities. The numerical study investigated the physics of arrays of clustered cells and outlined a simplified mean for modelling these liner types. In the absence of mean flow and for a normally incident sound wave, it was found that liners with clusters of varying cavity types can respond as if having an average impedance for which the wavelength of the incident sound is greater than three times the maximum dimension of the repeating cluster.
- The acoustic features of liners with a complex configuration have been analysed extensively. It was found that the liner absorption can be tuned to a given engine noise source spectrum by controlling the width of the cavities, their number, and their effective centreline lengths. Varying the width of the cavities was shown to be more powerful than introducing additional cavities. The application of a face sheet resistance, selected to match the optimum duct wall impedance, can further improve the acoustic performance by increasing the average panel resistance and also damping the impedance oscillations.

The configurations of the proposed liner concept were optimized to maximise sound absorption over the frequency range from 500 Hz to 4000 Hz, for two overall liner depths (50 mm and 100 mm). The optimization was performed for the no-flow condition and for a normally incident sound wave. Scaled samples of the optimal configurations were manufactured and their impedances were measured. The favourable correlation between measurements and predictions confirmed the expected enhanced broadband sound absorption. The differences that persist, are expected to decrease when a face sheet is bonded to the liner surface, and improved further when the edge effect is removed. Moreover, it was demonstrated that the 100mm-high optimal liner can target low-frequency noise more efficiently than the 50mm-high counterpart.

- These results proved that the stereolithography is a valid manufacturing process to fabricate liners with complex configurations. Furthermore, an analytical routine was validated for preliminarily modelling and optimizing the acoustic impedance of this type of liner.

Clearly, further investigations are required in order to prove the general validity of these conclusions. Nonetheless, they represent a firm starting point for future simulations. Furthermore, it may be concluded that the knowledge and methodology realised in this study can be adopted in the design and optimization of broadband liners with similar complex configurations.

The favourable agreement between the measured and the predicted impedance of the scaled optimal liners suggests that a comparable agreement can be also obtained in the case of the full-size optimal liners. This result gives confidence that the full-size optimal liners can be adopted in aircraft nacelles to effectively abate low-frequency, broadband noise sources. However, the expected sound absorption has been designed in a laboratory environment (no-flow condition and normal sound wave), whereas the acoustic performance must be demonstrated in a relevant environment (grazing flow and multi-modal propagation of the acoustic energy), that simulates real working conditions. The following notes summarizes the most significant suggestions to consider in the prosecution of this work:

- The liner response should be simulated in COMSOL, in the presence of representative grazing flow and sound source, and with multi-modal propagation.
- The liner impedance should be assessed in grazing incidence tests, under representative flow conditions and high sound pressure levels. It should be noted that these tests are planned to be performed in the near future.

  The average response of the liner design above a minimum wavelength ($\lambda_{min} = 3w$, where w is the maximum cluster width) should be assessed under grazing incidence and grazing flow conditions and for different Mach numbers and directions of sound propagation. It is recalled that this result was demonstrated in previous studies [33], but considering liners with parallel-element, variable-depth cavities. The analysis should focus on understanding the liner response at both lower and higher frequencies, both in the no-flow condition and in the presence of mean flow.
- This study can investigate to what frequency the average response persists, and when the response for a given cluster is influenced by the variability of the liner geometry across the surface.
- The full-size optimal liner configurations may require some changes in order to match the optimum impedance that maximises the sound absorption for a given duct geometry and flow condition.

6. References

[1] International Civil Aviation Organization, “Annex 16 (to the Convention on International Civil Aviation),” in *Environmental Protection - Aircraft Noise*, 2008.

[2] J. R. Astley, “Can technology deliver acceptable levels of aircraft noise?,” in *Inter.noise 2014*, Melbourne, 2014.

[3] M. Versaevel, L. Moreau and E. Lacouture, “Folded spiral-shaped cavities for nacelle acoustic liners: Impedance and attenuation modelling and comparison to experimental results,” in *3AF Greener Aviation 2016*, 2016.

[4] D. P. Lockard and G. M. Lilley, “The Airframe Noise Reduction Challenge,” 2004.

[5] J. F. Groeneweg, T. G. Sofrin, E. J. Rice and P. R. Gliebe, “Turbomachinery Noise,” in *Aeroacoustics of Flight Vehicles, Theory and Practice*, vol. I, Hampton, NASA Langley Research Center: Harvey H. Hubbard, 1991, pp. 151-209.

[6] R. Sugimoto, P. B. Murray and R. J. Astley, “Folded Cavity Liners for Turbofan Engine Intakes,” in *AIAA Paper 2012-2291*, 2012.

[7] The Royal Aeronautical Society, “An introduction to aircraft noise,” in *ESDU 02020*, 2007.

[8] J. M. Tyler and T. G. Sofrin, “Axial Flow Compressor Noise Studies,” in *SAE Trans.*, vol. 70, 1962, pp. 309-332.

[9] P. F. Joseph and M. G. Smith, “Aircraft Noise,” in *Advanced Applications in Acoustics, Noise and Vibration*, New York, Spon Press, 2004, pp. 292-346.

[10] A. Hirschberg and S. W. Rienstrra, An introduction to aeroacoustics, Eindhoven University of Technology, 2004.

[11] F. Fahy, Foundations of Engineering Acoustics, Academic Press - Elsevier Science, 2001.

[12] E. Envia, “Fan Broadband Noise generation and Suppression,” in *Aviation 2015*, 2015.

[13] Adamson, “Integrated Gas Turbine Engine-Nacelle”. Patent 4,055,041, 1977.

[14] M. G. Jones, W. R. Watson, D. M. Nark, B. M. Howerton and M. C. Brown, “A Review of Acoustic Liner Experimental Characterization at NASA Langley,” NASA/TP-2020-220583, 2020.

[15] B. Howerton, “Experimental Characterization of Acoustic Liners,” 2019.

[16] R. E. Motsinger and R. E. Kraft, “Design and Performance of Duct Acoustic Treatment,” in *Aeroacoustics of Flight Vehicles, Theory and Practice*, vol. II, Hampton, NASA Langley Research Center: Harvey H. Hubbard, 1991, pp. 91-112.

[17] H. Batard, “The Zero Splice Engine Intake Liner: An Efficient Way of Reducing Aircraft Noise without any Weight or Aerodynamic Penalty,” in *ICAS 2004*, 2004.

[18] B. J. Tester, C. J. Powles, N. J. Baker and A. J. Kempton, “Scattering of Sound by Liner Splices: A Kirchoff Modell with Numerical Verification,” *AIAA Journal,* vol. 44, no. 9, pp. 2009-2017, 2006.

[19] F. Bake, “Experimental techniques for duct acoustics,” 2019.

[20] A. Cummings, “Transient and Multiple Frequency Sound Transmission Through Perforated Plates at High Amplitude,” in *AIAA 84-2311*, 1984.

[21] P. M. Morse and K. U. Ingard, Theoretical Acoustics, New York: McGraw-Hill, 1968.

[22] Y. Aurégan and CNRS, “Modelling of liners (physics, impedance models),” in *LAUM Mat&FLow Winter School*, 2019.

[23] COMSOL, “COMSOL 5.4 - Acoustics Module, User's Guide”.

[24] C. K. W. Tam and K. A. Kurbatskii, “Microfluid Dynamics and Acoustics of Resonant Liners,” *AIAA Journal,* vol. 38, no. 8, pp. 1331-1339, 2000.

[25] P. B. Murray and J. R. Astley, “Development of a single degree of freedom perforate impedance model under grazing flow and high SPL,” in *AIAA 2012-2294*, 2012.

[26] P. G. Serrano, “Measurement and prediction of nonlinear acoustic liners in the presence of high level multiple tones,” ISVR PhD thesis, 2018.

[27] I. D. J. Dupère and A. P. Dowling, “The Absorption of Sound by Helmholtz Resonators with and without Flow,” in *AIAA 2002-2590,* 2002.

[28] J. W. Kooi and S. L. Sarin, “An Experimental Study of the Acoustic Impedance of Helmholtz Resonator Arrays Under a Turbulent Boundary Layer,” in *AIAA 81-1998*, 1981.

[29] Q. Zhang and D. J. Bodony, “Numerical Simulation of Two-Dimensional Acoustic Liners with High-Speed Grazing Flow,” *AIAA Journal,* vol. 49, no. 2, 2011.

[30] P. Ferrante, W. De Roeck, W. Desmet and N. Magnino, “Back-to-back comparison of impedance measurement techniques applied to the characterization of aero-engine nacelle acoustic liners,” *Applied Acoustic,* no. 105, pp. 129-142, 2015.

[31] ISO, “ISO-10534-2. Acoustics - Determination of sound absorption coefficient and impedance in impedance tubes,” 1998.

[32] M. G. Jones, B. M. Howerton and E. Ayle, "Evaluation of Parallel-Element, Variable-Impedance, Broadband Acoustic Liner Concepts," in *AIAA Paper 2012-2194*, 2012.

[33] M. G. Jones, W. R. Watson, D. M. Nark, N. H. Schiller and J. C. Born, "Optimization of Variable-Depth Liner Configurations for Increased Broadband Noise Reduction," in *AIAA Paper 2016-2783*, 2016.

[34] M. G. Jones, D. M. Nark, W. R. Watson and B. M. Howerton, "Variable-Depth Liner Evaluation Using Two NASA Flows Ducts," in *AIAA Paper 2017-3022*, 2017.

[35] M. G. Jones, D. M. Nark, A. Baca and C. R. Smith, "Applications of Parallel-Element, Embedded Mesh-Cap Acoustic Liner Concepts," in *AIAA 2018-3445*, 2018.

[36] B. M. Howerton and T. L. Parrott, "Validation of an Acoustic Impedance Prediction Model for Skewed Resonators," in *AIAA 2009-3143*, 2009.

[37] A. T. Chambers, J. M. Manimala and M. G. Jones, "Design and Optimization of 3D Folded-Core Acoustic Liners for Enhanced Low-Frequency Performance," *AIAA Journal,* vol. 58, no. 1, pp. 1-13, 2019.

[38] B. S. Beck, N. H. Schiller and M. G. Jones, "Impedance assessment of a dual-resonance acoustic liner," *Applied Acoustics,* no. 93, pp. 15-22, 2015.

[39] N. H. Schiller and M. G. Jones, "Smeared Impedance Model for Variable Depth Liners," in *AIAA Paper 2018-3774*, 2018.

[40] M. G. Jones, W. R. Watson, D. M. Nark and N. H. Schiller, "Evaluation of Spanwise Variable Impedance Liners with Three-Dimensional Aeroacoustics Propagation Codes," in *AIAA Paper 2017-3021*, 2017.

[41] D. M. Nark, M. G. Jones, D. L. Sutliff, E. Ayle and F. Ichihashi, "Improved Broadband Liner Optimization Applied to the Advanced Noise Control Fan," in *AIAA 2014-3103*, 2014.

[42] D. N. Nark, M. G. Jones and D. L. Sutliff, "Further Development and Assessment of a Broadband Liner Optimization Process," in *AIAA Paper 2016-2784*, 2016.

[43] P. B. Murray, P. Ferrante and A. Scofano, "Manufacturing Process and Boundary Layer Influences on Perforate Liner Impedance," in *AIAA 2005-2849*, 2005.

[44] P. B. Murray, P. Ferrante and A. Scofano, "The Influence of Aircraft Nacelle Acoustic Panel Drainage Slots on Duct Attenuation," in *AIAA 2007-3548*, 2007.

[45] Bruel & Kjaer, "Technical Documentation - Portable Impedance Meter System Type 9737 - User Manual".

[46] M. C. Brown and M. G. Jones, "Effects of Cavity Diameter on Acoustic Impedance of Perforate-Over-Honeycomb Liners," in *AIAA 2017-4189*, 2017.

[47] A. Scofano, P. B. Murray and P. Ferrante, "Back-Calculation of Liner impedance using Duct Insertion Loss," in *AIAA Paper 2007-3534*, 2007.

[48] F. Gantie, H. Batard, N. J. Baker and P. J. G. Schwaller, “Zero Splice Intake Technology and Acoustic Benefits,” in *AIAA 2006-2455*, 2006.